Biochemical characterisation of the interaction of the myosin light chain phosphatase with the regulatory subunits of protein kinase A in cells of the circulatory system

Paulo André Cardoso Bicho da Silva Saldanha

Doctor of Philosophy in Medical Sciences

The University of Hull and The University of York

Hull York Medical School (HYMS)

July,2023

Dedications

To my father,
(Para o meu pai)

Acknowledgements

First and foremost, I express my heartfelt gratitude to all the remarkable individuals within my family and circle of friends who have supported me throughout my PhD journey. Without their unwavering support and constant assistance, completing this thesis would not have been possible. I am deeply thankful for the consistent guidance and expertise offered by my supervisors, Dr. Francisco Rivero and Dr. Leonid Nikitenko. Their valuable insights and continuous support have been instrumental in shaping my development as a researcher.

I would like to extend my appreciation to my colleagues at the University of Hull. Their collaboration, constructive discussions, and shared experiences have played a crucial role in broadening my perspective and enhancing the quality of this thesis. I am grateful for their intellectual contributions and the stimulating environment they have fostered. Furthermore, I would like to acknowledge the technical support provided by the dedicated individuals who have assisted me throughout this research endeavour. Their expertise and assistance in navigating various technical challenges have been invaluable, and I am sincerely thankful for their contributions. Those I am thankful for include Dr Azhis Ashgar for all the support and extra time he spent on my project, and thanks to the staff and technicians from Glasgow University from Professor George Baillie's laboratory.

I would like to thank my colleagues from the Health*GDP - Health Global Data Pipeline for biomedical research and clinical applications. Thank you, Matthew, Shirin, Eamon, Dimitiros, and Adam for your time and shared knowledge.

On a personal note, I would like to thank several individual people that crossed my path since I remember.

Quero agradecer à minha familia. Desde os meus avós, com os quais aprendi imenso como ser humano, aos meus tios, primos. Ao meu pai e à minha mãe que desde pequenino me ensinaram a respeitar todas as pessoas por igual. Eles , que sempre me apoiaram, com toda a paciencia do mundo, para vocês o meu muito obrigado por

sempre acreditarem em mim. Às minhas irmãs por todas as rebeldias, amuos e sorrisos, obrigado.

This journey was not possible without my teachers from primary school until my PhD, but amongst all these talented people my research adventure started in Portugal with my master's degree.
O meu obrigado, Professora Elisa e Professor Ignacio.

To the one that made me move from the comfort of my country to do research out there. Merci Romuald d'avoir cru en moi. To Dr Mentaverri's team upon my stay in Amiens/UPJV, Merci Lucie et Cedric.

A todos mis amigos que conocí en España, la familia BQ: Gabriel, María, Maider, Marina, Alicia, Ana, los juegos de futbol. A vosotros gracias por todos los momentos que pasamos.

Aos meus melhores amigos na vida, João Baltazar, Renato Leitão, José Sereno, João Pedro Azoia Lopes, entre muitos outros que cruzaram-se comigo. O meu obrigado por compreenderem aqueles inumeros dias sem nos vermos. Obrigado por estarem sempre lá quando é preciso.

I could not finish without being grateful to someone special who has helped me go throw the last stage of my PhD. To my love Amber, I want to thank you for the care, love, attention and all the brightest days you can pull when we pass through cloudy moments. I cannot express how much I owe you and I want you to know that I appreciate you for all the support through all my grumpiest times while writing the thesis. Thank you for being the "Portuguese sunny daylight on this British cloudy weather". Thank you for being my support and filling me with love throughout this time.

Finally, because family is the key to all unwavering support in the world, I would like to dedicate this thesis to my late father, Carlos Saldanha. His untiring support and wisdom always ensured that support and taught me that I could do and be whatever I wanted if I put my heart and soul into it. Your life wisdom has been a source of

immense strength and inspiration. I miss you lot (Tenho muitas saudades tuas), I dedicate this thesis to you (dedico-te a minha tese, por tudo o que fizeste por mim). I am forever grateful for his guidance and encouragement.

Abstract

Regulation of actomyosin-driven contraction is important for numerous cardiovascular cell functions, including smooth muscle tone, endothelial cell permeability and platelet shape change and spreading. These processes are primarily regulated by the phosphorylation and dephosphorylation of the myosin light chain, catalysed by myosin light chain kinase (MLCK) and myosin light chain phosphatase (MLCP), respectively. MLCP is composed of a 38-kDa protein phosphatase catalytic subunit (PP1c) and a 130-kDa myosin phosphatase targeting subunit 1 (MYPT1). MYPT1 serves as a scaffold that positions PP1c in proximity to its substrates. The activity, protein-protein interactions and localisation of MLCP are fine-tuned by the phosphorylation status of MYPT1, which is targeted by multiple protein kinases. Notably, phosphorylation by protein kinase A (PKA) can counteract the inhibition of MLCP elicited by ROCK phosphorylation.

Several isoforms of MYPT1 have been identified, resulting from cassette-type alternative splicing of exons E13, E14, E22, and E24 of the *PPP1R12A* gene. An analysis of public databases reveals a greater transcriptional complexity of this gene than previously appreciated. Many studies on *PPP1R12A* expression and transcription variants have focused on a limited number of organs and tissues, often composed of mixed cell types. There is a scarcity of studies on specific cell lines or individual cell types. To address this gap, a comprehensive examination of the transcriptional landscape of the *PPP1R12A* gene, emphasising protein-coding transcripts was conducted. This *in silico* analysis of public EST and mRNA databases revealed that *PPP1R12A* comprises 32 exons, 29 of which are used in 11 protein-coding transcripts. Using publicly available RNAseq data and reverse transcription PCR, the relative abundance of each transcript in human umbilical vein endothelial cells (HUVEC), human saphenous vein smooth muscle cells (HSVSMC), and platelets were determined. HUVECs and HSVSMCs were found to predominantly express the full-length variant (58.3% and 64.3%, respectively), with the E13-skipping variant being the second most common (33.7% and 23.1%, respectively). Variants including E24 account for 5.4% of transcripts in platelets but are rare in HUVECs and HSVSMCs.

These insights set the stage for future studies on the specific roles of MYPT1 isoforms in physiology and pathology.

MYPT1 is part of a complex signalling node involving PP1c, kinases, and other enzymes, and previous studies have unravelled a direct interaction between MYPT1 and the regulatory subunits of PKA. The hypothesis in this study was that MYPT1 and PKA subunits interact directly in vascular cells, potentially functioning as an A-kinase anchoring protein (AKAP) to target PKA to the MLCP signalling node. Using immunoprecipitation, affinity pulldown, and in situ proximity ligation assays in human platelets and endothelial cells, it was demonstrated that MYPT1 directly interacts with all four PKA regulatory subunit variants. Peptide array overlays identified K595, E676, and the PKA/ROCK kinase substrate motif R693/R694/S695/T696 as critical for this interaction. Substitution of S695, T696, or both with aspartic acid or the corresponding phosphorylated residues abolished binding. A model is proposed where MYPT1 functions as a non-canonical AKAP, anchoring PKA near non-phosphorylated S695/T696 to prevent PKA catalytic subunits and potentially ROCK from phosphorylating MYPT1. Collectively, these findings provide valuable insights into the anchoring role of MYPT1 and lay the groundwork for future research into the specific roles of MYPT1 isoforms in cardiovascular function.

Table of Contents

List of figures

List of tables

Abbreviations

Abbreviation	Name
a.a.	Amino acid
8-AHA-cAMP	8-(6-aminohexylamino) adenosine-3',5'-cyclic monophosphate
ACD	Acid Citrate Dextrose
ADP	Adenosine diphosphate
AKAPs	A-kinase Anchoring Proteins
APS	Ammonium persulfate
Arp2/3	Actin-related proteins 2/3
ATP	Adenosine triphosphate
BCA	Bicinchoninic Acid Assay
bp	Base pair
BRET	Bioluminescence Resonance Energy Transfer
BSA	Bovine Serum Albumin
cAMP	3',5'-cyclic monophosphate
Cdc42	Cell division control protein 42 homologue
CI	Central Insert
CREB	cAMP Response Element-Binding Protein
CRISPR	Clustered Regularly Interspaced Short Palindromic Repeats
Cryo-TEM	Cryogenic transmission electron microscopy
DAPI	4′,6-diamidino-2-phenylindole
DMF	Dimethylformamide
DMSO	Dimethylsulfoxide
DNA	Deoxyribonucleic acid
dNTPs	Deoxynucleoside triphosphate
DTT	Dithiothreitol
EC	Endothelial cells
EDTA	Ethylenediaminetetraacetic acid
EST	Expressed sequence tag

EtOH-NH	Ethanolamine
FBS	Foetal Bovine Serum
FL	Full Length
FRET	Fluorescence Resonance Energy Transfer
GAPDH	Glyceraldehyde 3-phosphate dehydrogenase
GST	Glutathione S-transferase
GTP	Guanosine-5'-triphosphate
HDBEC	Human Dermal Blood Endothelial Cells
HEK 293T	Human Embryonic Kidney 293
HRP	Horseradish peroxidase
HSVSMC	Human Saphenous Veins Smooth Muscle Cells
HUVEC	Human Umbilical Vein Endothelial Cells
IFs	Intermediate Filaments
IgG	Immunoglobulin G
IP	Immunoprecipitation
IPTG	Isopropyl ß-D-1-thiogalactopyranoside
Kb	Kilo base
LB	Lysogeny Broth (as known as Luria-Bertani)
LZ	Leucine Zipper
$MgCl_2$	Magnesium chloride
MLCK	Myosin Light Chain Kinase
MLCP	Myosin Light Chain Phosphatase
MP	Myosin Phosphatase
mRNA	Messenger Ribonucleic Acid
MS	Mass spectrometry
MYPT	Myosin Phosphatase Targeting Protein
MYPT1	Myosin Phosphatase Targeting Protein 1
NaCl	Sodium chloride
Ni-NTA	Nickel-Nitrilotriacetic acid (NTA)
NM	Non-Myosin

NM II	Non-Myosin II
NMDA	N-methyl-D-aspartate
NO	Nitric Oxide
NPFs	Nucleation-Promoting Factors
PBS	Phosphate-buffered Saline
PBS-T	Phosphate-buffered Saline with Triton X-100
PCR	Polymerase Chain Reaction
PDB	Protein Data Bank
PDEs	Phosphodiesterases
PFA	Paraformaldehyde
PGI_2	Prostacyclin
PIC	Protease Inhibitor cocktail
PKA	Protein Kinase A
PKAcat	Protein Kinase A Catalytic
PKA-R	Protein Kinase A Regulatory
PKA-RI	Protein Kinase A Regulatory I
PKA-RII	Protein Kinase A Regulatory II
PKC	Protein Kinase C
PKG	Protein Kinase G
PLA	Proximity Ligation Assay
PMSF	Phenylmethylsulphonyl fluoride
PP1c	Protein Phosphatase 1c
PRP	Platelet Rich Plasma
PVDF	Polyvinylidene fluoride
Rac1	Ras-related C3 botulinum toxin substrate 1
RhoA	Ras homologue family member A
RLC	Regulatory Light Chain
RNA	Ribonucleic Acid
RNAseq	Ribonucleic Acid Sequencing
ROCK	Rho-associated protein kinase

ROS	Reactive Oxygen Species
RT-PCR	Reverse Transcription Polymerase Chain Reaction
SDS	Sodium dodecyl-sulphate
SDS-PAGE	Sodium dodecyl-sulphate polyacrylamide gel electrophoresis
SMC	Smooth Muscle Cell
SOC	Super Optimal broth with Catabolite repression
SPR	Surface Plasmon Resonance
TAE	Tris-Acetate-EDTA
TBS	Tris-buffered Saline
TBS-T	Tris-buffered Saline with Tween™20
TCCF	Total Corrected Cellular Fluorescence
TEMED	N,N,N',N'-tetramethylethylenediamine
TGF	Transforming Growth Factor
TIMAP	TGF-ß-inhibited membrane associated protein
UTR	Untranslated Region
UV	Ultraviolet
X-Gal	5-bromo-4-chloro-3-indolyl-ß-D-galactopyranoside

Author's declaration

I confirm that this work is original and that if any passage(s) or diagram(s) have been copied from academic papers, books, the internet or any other sources these are clearly identified by the use of quotation marks and the reference(s) is fully cited. I certify that, other than where indicated, this is my own work and does not breach the regulations of HYMS, the University of Hull or the University of York regarding plagiarism or academic conduct in examinations. I have read the Hull-York Medical School Code of Practice on Academic Misconduct, and state that this piece of work is my own and does not contain any unacknowledged work from any other sources.

Publications

- Saldanha PA, Bolanle IO, Palmer TM, Nikitenko LL, Rivero F. Complex Transcriptional Profiles of the *PPP1R12A* Gene in Cells of the Circulatory System as Revealed by In Silico Analysis and Reverse Transcription PCR. Cells. 2022;11(15):2315. Published 2022 Jul 27. doi:10.3390/cells11152315

- Khalil JS, Saldanha PA, Blair CM, Ling J, Ji W, Baillie GS, Naseem KM, Nikitenko LL, Rivero F. MYPT1 is a non-canonical AKAP that tethers PKA to the MLCP signaling node. bioRxiv 2023.04.27.538407; doi: https://doi.org/10.1101/2023.04.27.538407 (Preprint 27/04/2023)

Chapter 1. General Introduction

1.1. Cell Cytoskeleton and Extracellular Matrix

The eukaryotic cell cytoskeleton is a complex network of interconnected filaments and tubules that extends mainly throughout the cytosol. It gives shape to the cell, mediates anchoring to the substrate and to other cells, facilitates cell movements and movement of organelles, and is necessary for cell division. The cytoskeleton is formed by three main types of polymers: microtubules, intermediate filaments (IFs), and microfilaments (Figure 1.1) (Rivero F., 2017). The three cytoskeletal polymers have distinctive structure and mechanical properties relating to their function in the cytoskeleton (Pollard and Goldman, 2018).

Numerous classes of associated proteins are responsible for the dynamic properties and the formation of links to organelles, plasma membrane components and cytoskeleton systems. They also constitute the targets of signalling networks that control the spatial and temporal remodelling of the cytoskeleton (Rivero F., 2017, Pollard and Goldman, 2018).

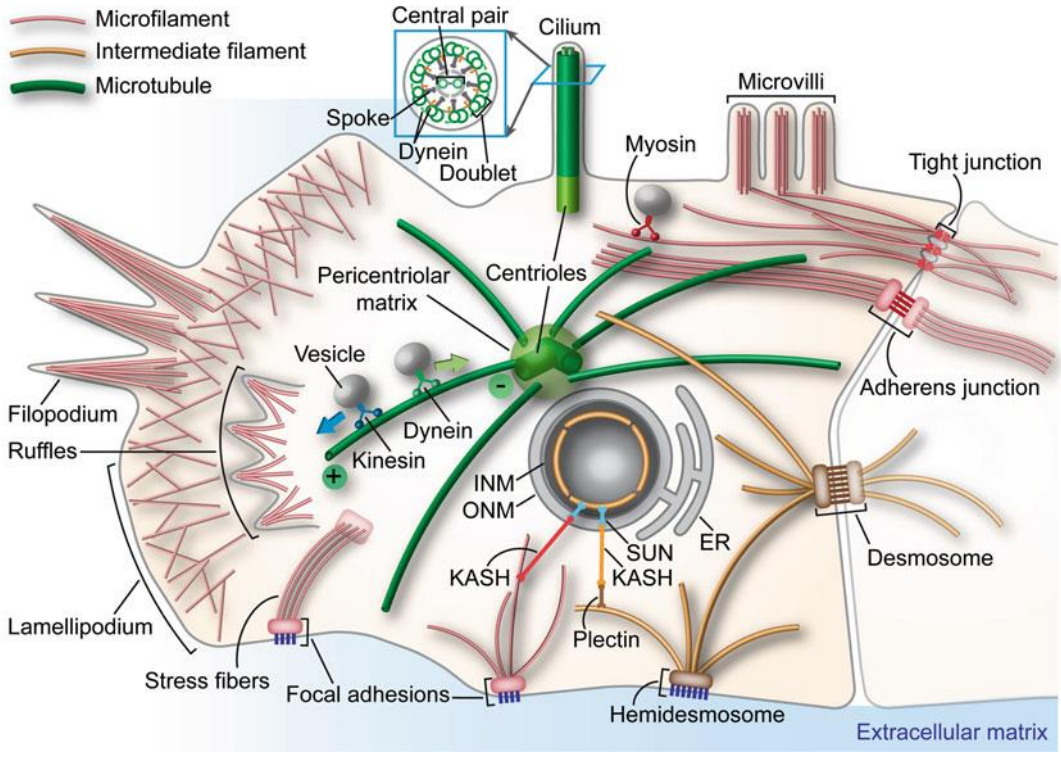

Figure 1.1 Schematic of the three cytoskeleton systems and some specialised structures. Hypothetical cell displaying features of an epithelial cell on the right side and of a mesenchymal cell on the left side. Examples of microtubule and microfilament-associated motor proteins carrying a vesicle are depicted. ONM, outer nuclear membrane; INM, inner nuclear membrane; ER, endoplasmic reticulum. Figure 2, page 1296, from: (Rivero F., 2017).

1.1.1. Extracellular matrix and cell-cell adhesions

The extracellular matrix (ECM) is a complex and dynamic network of macromolecules that provides structural and biochemical support to surrounding cells. The primary components of the ECM include proteins like collagen, elastin, fibronectin, and laminins, as well as glycoproteins and proteoglycans. Collagen, the most abundant ECM protein, forms fibrillar structures that provide tensile strength and structural integrity to tissues (Shoulders and Raines, 2009). Elastin imparts elasticity, allowing tissues such as skin, lungs, and blood vessels to resume their shape after stretching or contracting (Vrhovski and Weiss, 1998). Fibronectin, a glycoprotein, binds to integrins and other ECM components, playing a critical role in cell adhesion, migration, and wound healing (Pankov and Yamada, 2002). Laminins, found

predominantly in the basal lamina, influence cell differentiation, migration, and adhesion, crucial for tissue maintenance and repair (Durbeej, 2010). Proteoglycans, consisting of a core protein and covalently attached glycosaminoglycans (GAGs), regulate the movement of molecules within the ECM and affect cell behaviour through interactions with growth factors (Iozzo and Schaefer, 2015).

Integrins are transmembrane receptors that mediate cell-ECM adhesion, connecting the ECM to the actin cytoskeleton. They transmit mechanical and chemical signals between the ECM and the cell interior influencing bidirectional signal transduction (Hynes, 2002), cell shape, motility, and signalling pathways. These signals also influence cellular responses to the microenvironment, playing a pivotal role in processes like wound healing, where cells migrate and proliferate to repair tissue damage immune responses, and development (Hynes, 2002, Chen et al., 2003). Together, these components ensure the structural and functional coherence of tissues, enabling dynamic responses to physiological changes. Dysregulation of these interactions can lead to pathological conditions such as fibrosis, characterised by excessive ECM deposition and tissue stiffening, or cancer, where altered cell adhesion and signalling contribute to tumour invasion and metastasis (Leask and Abraham, 2004, Hynes, 2009).

Intercellular junctions are specialised structures that maintain the integrity and function of tissues by facilitating adhesion and communication between adjacent cells.

Tight junctions (TJs) form a seal that regulates the paracellular transport of molecules, preserving the distinct composition of the cellular environment (Tsukita et al., 2001). Tight junctions are essential for creating selective barriers between epithelial and endothelial cells, regulating paracellular transport, and maintaining cell polarity. They are formed by transmembrane proteins such as claudins, occludins, and junctional adhesion molecules, which interact with cytoplasmic scaffolding proteins to link TJs to the actin cytoskeleton (Zihni et al., 2016).

Adherens junctions (AJs) are critical for maintaining cell-cell adhesion and tissue integrity. They are composed of cadherins, which are transmembrane proteins that mediate cell adhesion through calcium-dependent interactions. These junctions link the actin cytoskeleton of adjacent cells, facilitating coordinated cellular movements and mechanical stability (Niessen et al., 2011). They are linked to the actin cytoskeleton, provide mechanical stability, and play a role in signal transduction, essential for maintaining tissue architecture and transmitting signals that control cell behaviour (Gumbiner, 2005). Desmosomes, connected to intermediate filaments, offer strong adhesion, particularly in tissues subjected to mechanical stress such as the skin and heart, ensuring tissue cohesion and resilience (Garrod and Chidgey, 2008). Gap junctions allow direct chemical and electrical communication between cells through connexin protein channels, coordinating cellular activities such as cardiac muscle contraction and embryonic development (Naus and Laird, 2010). Dysfunction in these junctions can lead to diseases, including arrhythmias in the heart due to impaired electrical coupling and compromised skin integrity due to weakened cellular adhesion (Delmar and McKenna, 2010, Kottke et al., 2006).

Vinculin is a cytoskeletal protein that reinforces cell-matrix and cell-cell adhesions. It associates with integrins and cadherins, providing mechanical linkage to the actin cytoskeleton and stabilising adhesions under mechanical stress (Bays and DeMali, 2017).

In summary, the ECM, along with adherens junctions, tight junctions, vinculin, and integrins plays pivotal roles in maintaining cellular structure, function, and communication behaviour including proliferation, differentiation and migration, and its composition varies between tissues to meet specific functional demands (Frantz et al., 2010).

1.1.2. Microtubules

Microtubules are tubular structures formed of polymers of heterodimeric subunits of α and ß tubulin. They serve as pathways for the transportation of membrane-bound vesicles, ribonucleoprotein particles, and intermediate filaments by the motor proteins dynein and kinesin. These motor proteins enable the movement of cargo over long distances within the crowded cytoplasm (Barlan and Gelfand, 2017). They also play a crucial role in forming the structural framework of axonemes found in cilia and flagella (Viswanadha et al., 2017), as well as the mitotic apparatus during cell division (McIntosh, 2016). They provide the necessary support and organisation for the proper functioning of these cellular structures.

The polymerisation and depolymerisation of the microtubules are responsible for their stability. Once started, microtubules undergo elongation at both ends through the addition GTP-tubulin dimers. Specifically, plus ends of microtubules exhibit faster growth rates compared to their respective opposite ends (Pollard and Goldman, 2018)

1.1.3. Intermediate filaments (IFs)

Intermediate filaments are 10 nm diameter protein structures made up of homopolymers or heteropolymers, which are encoded by a diverse family of approximately 70 genes (van Bodegraven and Etienne-Manneville, 2020). IFs are composed of subunits that form tetramers consisting of four polypeptides. These tetramers are assembled from two dimeric molecules, where their rod domains interact alongside each other with opposite polarity (Herrmann and Aebi, 2016).

From all the cytoskeleton main types of polymers, IFs demonstrate the greatest flexibility, with a persistence length spanning from 0.3 to 1.0 mm. They exhibit exceptional tensile strength, allowing them to withstand stretching despite their natural flexibility (Pollard and Goldman, 2018). It is believed that the principal function of IFs is to provide structural support and strength to the internal cytoplasm and cell surface, stabilising connections formed by the actin filaments (Yuan and

Rigor, 2010, Pegoraro et al., 2017). Additionally, they are actively involved in shaping the cell and modulating signal transduction processes, as comprehensively reviewed by (Herrmann and Aebi, 2016, Cheng and Eriksson, 2017).

The IFs are classified into six families based on their primary structure, gene organisation, assembly properties, and developmentally regulated, tissue-specific expression patterns (Strelkov et al., 2003).

The types I, acidic keratins, and II, basic keratins, are the primary intermediate filaments in epithelial cells. They form heteropolymers essential for mechanical stability and resilience against physical stress, helping maintain the integrity of tissues such as the skin and other epithelia (Chang and Goldman, 2004).

The type III encompasses desmin, glial fibrillary acidic protein (GFAP), peripherin, vimentin, and syncoilin (van Bodegraven and Etienne-Manneville, 2020). Desmin is predominantly found in muscle cells. It is crucial for the integrity and alignment of myofibrils, aiding in muscle contraction and strength. Mutations in desmin are linked to myopathies and cardiac diseases (Paulin and Li, 2004). GFAP is characteristic of astrocytes in the central nervous system, providing structural support and maintaining the blood-brain barrier. It also plays a role in the response to central nervous system injuries (Chang and Goldman, 2004). Peripherin is specifically expressed in the peripheral nervous system. Its cell-type-specific expression is influenced by epigenetic modifications, and it plays important roles in neurite outgrowth and stability, axonal transport, and axonal myelination. Additionally, it interacts with various proteins involved in vesicular trafficking, signal transduction, DNA/RNA processing, protein folding, and mitochondrial metabolism (Romano et al., 2022).Vimentin is found in mesenchymal cells, supporting cellular integrity, and participating in cell migration, proliferation, and signalling. It is prominently expressed in fibroblasts, endothelial cells, and macrophages (Chang and Goldman, 2004).

The type IV includes nestin, neurofilaments, synemins, and internexin (van Bodegraven and Etienne-Manneville, 2020). Nestin is transiently expressed in

neuronal precursor cells during development and is involved in cell proliferation and differentiation (Chang and Goldman, 2004). Neurofilaments are imperative for maintaining axonal calibre and proper nerve impulse transmission. They consist of light, medium, and heavy chains, essential for neuronal function and stability (Yuan et al., 2012). Synemin is predominantly found in skeletal, cardiac, and smooth muscle tissues, as well as in neurons and glial cells. It plays a critical role in maintaining cellular integrity by integrating into the intermediate filament network, which supports cellular stability and resilience against mechanical stress (Capetanaki et al., 2007). In muscle cells, synemin is essential for force transmission, linking the cytoskeleton to the extracellular matrix, especially at the Z-discs and myotendinous junctions (Capetanaki et al., 2007). Internexin plays a critical role in the development and maintenance of the nervous system. It is predominantly expressed in neurons of the central and peripheral nervous systems. It contributes to the formation and stabilisation of the neuronal cytoskeleton, facilitating proper neuronal function and resilience against stress. Studies have shown that it can co-assemble with neurofilament triplet proteins (low, medium and heavy chains) to form IFs, which are essential for maintaining neuronal structure and function. This cooperative assembly helps in the stabilisation of axonal structures, supporting efficient nerve transmission and plasticity (Ching and Liem, 1998, Yuan et al., 2006).

The type V are lamins. Lamins are found in the nucleus, they provide structural support to the nuclear envelope and are involved in DNA replication, RNA transcription, and nuclear organisation. They are divided into A and B types, playing distinct roles in nuclear mechanics and genome stability (Dechat et al., 2008, Gruenbaum et al., 2005). Lamins share structural similarities with cytoplasmic intermediate filaments but form thinner filaments approximately 3.5 nm in diameter and contain a nuclear localisation signal (Saez and Gonzalez-Granado, 2022).

Type VI of IFs are phakinin and filensin. These are specific to the lens of the eye and contribute to the transparency and refractive properties of the lens, forming a unique cytoskeletal network essential for maintaining lens structure (Chang and Goldman, 2004).

1.1.4. Actin filaments

Actin filaments are protein filaments primarily composed by two strands of polymers of actin that interact with other proteins, including myosins. Their functions vary from their role in cytokinesis, cell motility, endocytosis and exocytosis, cell contractility to provide mechanical stability to the cells. Actin filaments possess flexibility and considerable strength, resisting to compressive and tensile forces (Alberts, 2022). Actin amino acid sequences across various eukaryotic species typically exhibit approximately 90% similarity. Even slight deviations in actin amino acid composition can yield notable functional distinctions. For instance, vertebrates possess three actin isoforms—α, ß, and γ—each with slight variations in sequence and unique roles. Specifically, α-Actin is exclusive to muscle cells, whereas ß- and γ-actins coexist in nearly all non-muscle cells (Alberts, 2022).

Actin filaments are linear polymers of filamentous (F)-actin, and their stability is dependent upon the concentration of monomeric globular (G)-actin within the cell. (Yuan and Rigor, 2010). Actin filament polymerisation is a rapid process *in vitro*, resulting in the formation of polar filaments with distinct fast-growing barbed (+) and slower-growing pointed (-) ends. However, cells have evolved mechanisms to tightly regulate actin filament dynamics to suit their needs. The majority of actin monomers within cells are sequestered or bound by proteins like thymosin ß4 and profilin. Profilin drives the addition of actin monomers towards the barbed end, increasing filament length, with the ultimate result of reducing the pool of actin available for polymerisation (Skruber et al., 2018, Schaks et al., 2019).

Nucleation, the critical initial step in filament formation, involves the assembly of a trimer or tetramer mimicked by actin nucleators. Regulatory complexes, referred to as “nucleators”, control the nucleation of actin filaments in cells. Two types of actin filaments are formed by nucleators, branched filament networks (formed by the Arp2/3 complex) and linear filament bundles (formed by formins). Branched filament networks are abundant at the leading-edge lamellipodium of migrating cells and are also found at sites of endocytosis and organelle dynamics, such as fusion and fission.

In contrast, elongating linear actin filament bundles are characteristic of filopodia protruding from the leading edge (Lappalainen et al., 2022).

The Arp2/3 (actin-related proteins) complex, composed of actin-related proteins Arp2 and Arp3 and five scaffolding subunits (ArpC1 to ArpC5) (Gautreau et al., 2022), is activated by nucleation-promoting factors (NPFs) (Machesky et al., 1999) like the WASP and WAVE protein families. These NPFs, anchored to lipid membranes and activated by GTPases such as Rac1 (Ras-related C3 botulinum toxin substrate 1) and Cdc42 (Cell division control protein 42 homologue), expose their C-terminal WCA domains, which bind actin monomers and the Arp2/3 complex (Bieling et al., 2018, Lappalainen et al., 2022). This interaction causes a conformational change in Arp2/3, allowing it to attach to an existing filament and form a branch at a 70° angle. This branching is crucial for the polarised growth of actin networks essential for cell migration and endocytosis (Lappalainen et al., 2022).

Formins are homodimeric proteins that control actin filament elongation by binding to filament barbed ends with their formin homology 2 (FH2) domains, allowing continuous actin monomer incorporation. The formin homology 1 (FH1) domain binds profilin–actin, accelerating filament growth (Kovar and Pollard, 2004, Romero et al., 2004). Formins can be activated by Rho GTPases and phosphatidylinositol-4,5-bisphosphate, and work with other proteins to enhance actin nucleation and polymerisation (Gorelik et al., 2011, Ramalingam et al., 2010, Watanabe et al., 1999, Lappalainen et al., 2022).

Cells exhibit three modes of protrusion, relying on polarisation for forward movement. One mechanism of plasma membrane protrusion, lamellipodium, is the formation by continuous Arp2/3 complex branching at the cell periphery, overcoming membrane tension to move the plasma membrane forward. The lamellipodium is a flat structure that protrudes on solid surfaces *in vitro* and *in vivo* but can lift into the third dimension depending on signalling and adhesion to the substratum. These 3D structures, also called ruffles, have similar actin turnover mechanisms as flat lamellipodia (Small et al., 2002, Oakes et al., 2018, Rottner et al., 2017, Rottner and Schaks, 2019, Schaks et al., 2019).

A second mechanism of plasma membrane protrusion involves the growth of small linear bundles of actin filaments, known as filopodia, which generate forces towards the membrane through filament polymerisation independent of the Arp2/3 complex. The spaces between filopodial bundles are typically filled by myosin II-mediated contractile activity. Various types of these bundled structures exist, ranging from dynamically protrusive and retractile filopodia to the more static microvilli of epithelial cells and stereocilia in cochlear hair cells (Suraneni et al., 2015, Steffen et al., 2006, Wu et al., 2012, Nicholson-Dykstra and Higgs, 2008, Jacquemet et al., 2015, Bornschlogl, 2013, Fischer et al., 2019, Schaks et al., 2019).

A third mechanism is one that does not require active actin polymerisation (Paluch and Raz, 2013, Charras and Paluch, 2008). The plasma membrane of eukaryotic cells is attached to a thin actin cortex with contractile properties due to myosin II activity, creating hydrostatic pressure (Charras et al., 2005). Bleb formation occurs via cortex-plasma membrane detachment or actin cortex rupture, driven by myosin II activity, facilitating amoeboid motility (Paluch and Raz, 2013, Charras and Paluch, 2008, Schaks et al., 2019).

The small GTPases Rac1 and RhoA are crucial for initiating and maintaining cell polarity and directed movement, though they play opposing roles (Iseppon et al., 2015, Martin et al., 2016, Machacek et al., 2009, Isogai and Danuser, 2018). Their spatiotemporal activities, studied using fluorescence resonance energy transfer microscopy, show differential patterns at the leading edge and cell rear (Iseppon et al., 2015, Martin et al., 2016, Machacek et al., 2009, Isogai and Danuser, 2018). RhoA signalling is enhanced at retraction sites, with mutual inhibition between Rac1 and RhoA leading to a bistable system (Machacek et al., 2009, Isogai and Danuser, 2018, Isogai et al., 2015, Pertz et al., 2006, Byrne et al., 2016, Schaks et al., 2019).

A wide range of regulatory proteins enable actin filaments to form diverse structures involved in cellular motility, cytokinesis, membrane trafficking, and maintenance of cellular integrity (Pollard and Goldman, 2018). Actin filaments are a major player in facilitating short-range movements of vesicles and cables, which are contracted by myosin motors during processes such as locomotion, cytokinesis, and changes in cell

shape (Yuan and Rigor, 2010). Myosin, a key actin-binding protein, interacts with actin filaments to generate the contractile forces necessary for these essential cellular processes (Schaks et al., 2019, Lappalainen et al., 2022, Jegou and Romet-Lemonne, 2021).

The actomyosin contractile machinery serves as a fundamental system involved in various cellular processes, including muscle contraction, cell migration, cytokinesis, and tissue morphogenesis. It relies on the intricate interaction between actin filaments and myosin motor proteins that will be described next (Masters et al., 2017).

1.2. Myosin

The myosin superfamily is a large and diverse protein family that contains more than 40 known classes. Of these, there are 12 myosin classes that are expressed in humans including myosins I, II, III, V, VI, VII, IX, X, XV, XVI, XVIII, and XIX (Masters et al., 2017, Foth et al., 2006), which are coded by 40 genes (Pollard, 2020). All myosins contain three domains. The N-terminus contains a highly conserved catalytic motor domain (80-100 kDa) where the actin binding and ATPase sites are located. This domain is followed by a central "lever-arm" region with one to six motifs. This arm binds to either light chains (regulatory or essential light chain) or calmodulin, which stabilise the lever arm. The C-terminal region is termed the tail and typically contains α-helical coiled-coil regions for dimerisation (Sellers, 2000, Masters et al., 2017).

Myosins are a diverse family of motor proteins essential for numerous cellular processes. They are involved in plasma membrane tension regulation, endocytosis, organisation of actin filaments in sensory cells, mediation of vesicle transport and intracellular trafficking, cell motility and regulation of mitochondrial dynamics (Coluccio, 2020).

Class I myosins are monomeric membrane-associated motor proteins that interact with actin filaments to produce movement and force. They are involved in plasma membrane tension regulation, endocytosis, exocytosis, and cell-cell contact

(Coluccio, 2018, McIntosh, 2016). Humans have eight isoforms (MYO1A-H), which feature an ATP-binding motor domain, a light chain-binding domain, and a C-terminal tail with a PH domain for membrane binding (Bahler et al., 1994, Hokanson et al., 2006).

Skeletal muscle myosin-II was identified over 150 years ago by (Kühne, 1864) being previously called simply myosin. Only many years later Huxley proved his previously proposed sliding filament theory, in which filaments of acting and myosin overlap each other leading to muscle contraction (Huxley, 1957). Myosin II will be discussed in detail later.

Myosin III proteins are predominantly found in sensory cells such as retinal photoreceptors and inner ear hair cells. They stabilise actin filaments at sensory protrusions (Dose et al., 2003, Schneider et al., 2006). Vertebrates have two genes for myosin III: MYO3A and MYO3B, essential for sensory function (Salles et al., 2009, Merritt et al., 2012).

Myosins V, including MYO5A, MYO5B, and MYO5C, mediate membrane trafficking and are expressed in almost all human cells (Rodriguez and Cheney, 2002). These motors interact with Rab GTPases, facilitating vesicle movement along actin filaments (Roland et al., 2007). Defects in MYO5 lead to neurological and intestinal issues, cholestasis, and cancer.

The Myosin VI MYO6, unique for moving toward the minus end of actin filaments, functions as both a monomer and a dimer upon cargo binding, playing roles in vesicle trafficking, Golgi morphology, and cell motility ((Wells et al., 1999, Yu et al., 2009). MYO6 mutations are linked to cardiomyopathy, deafness, and cancer (Buss et al., 1998, Sahlender et al., 2005).

Human myosin VII isoforms, MYO7A and MYO7B, are crucial for transport and maintenance of cell structures. MYO7A mutations cause Usher syndrome and nonsyndromic hearing loss (Hasson et al., 1995). MYO7B maintains microvilli structure in epithelial cells (Chen et al., 2016, Li et al., 2016).

MYO9A and MYO9B, class IX myosins, play roles in brain, testis, and immune cells. MYO9A deficiency leads to hydrocephalus and renal disease (Abouhamed et al., 2009). MYO9B is essential for macrophage motility and immune responses (Hanley et al., 2010).

The class X myosin MYO10, with a motor domain, three calmodulin-binding IQ domains, and a MyTH4-FERM domain, facilitates filopodia formation and cellular migration by transporting integrins and other cargo (Divito and Cheney, 2008, Zhang et al., 2004a).

The class XV myosin MYO15A is critical for stereocilia formation and maintenance in the inner ear, necessary for hearing and balance (Bird et al., 2014, Fang et al., 2015). Mutations in MYO15A cause deafness and vestibular defects (Probst et al., 1998).

Class XVI myosins, including MYO16A and MYO16B, are primarily expressed in the brain and regulate actin dynamics and cell cycle progression (Cameron et al., 2013).

Class XIX myosins, especially MYO19, interact with mitochondria and regulate mitochondrial dynamics, facilitating mitochondrial positioning and cell division (Quintero et al., 2009, Rohn et al., 2014).

1.2.1. Class II myosin

The class II myosins are hexamers consisting of two heavy chains (205 kDa) and two pairs of light chains (essential and regulatory light chains, 16-20 kDa) (Masters et al., 2017). The class II myosins are double-headed molecules that form bipolar filaments, playing crucial roles in muscle contraction and various cellular processes. In humans the myosin II can be divided into two main groups: the sarcomeric skeletal and cardiac muscle myosins II and the non-sarcomeric smooth muscle and non-muscle myosin II (Berg et al., 2001).

These myosins are encoded by 15 genes in humans, designated as MYH1 through MYH15. They mediate skeletal muscle contraction (MYH1, MYH2, MYH3, MYH4, MYH7b, MYH8, MYH13, and MYH15), cardiac muscle contraction (MYH6 and MYH7), and smooth muscle contraction (MYH11), which is essential for maintaining visceral

activities like blood pressure regulation ((Simons et al., 1991, Berg et al., 2001, Marigo et al., 2004, Conti et al., 2008, Masters et al., 2017).

Class II myosins exhibit structural and functional heterogeneity to support their diverse roles (Reggiani and Bottinelli, 2008). Striated muscles, including skeletal and cardiac muscles, show alternating light and dark bands due to the sarcomere arrangement, with different myosin II isoforms present in various muscle fibre types (Schiaffino and Reggiani, 2011, Schiaffino et al., 2015). For instance, skeletal muscle myosin 2X/D is found in fast-twitch type 2X fibres, while myosin 2A is in fast-twitch oxidative glycolytic type 2A fibres, and myosin 2B in fast-twitch glycolytic type 2B fibres (Rossi et al., 2010). Cardiac muscle expresses β- and α-cardiac myosin II, with β-cardiac myosin II also known as slow skeletal myosin II.

Smooth muscle myosins lack the striated appearance of sarcomeric muscles due to their non-aligned contractile units. There are four isoforms of smooth muscle myosin II (SM1A, SM1B, SM2A, and SM2B) generated by splicing of the MYH11 gene (Eddinger and Meer, 2007). Regulation differs between muscle types, with skeletal muscle contraction controlled by thin filament proteins like troponin and tropomyosin, and smooth muscle contraction mediated by myosin light chain phosphorylation (Coluccio, 2020). Class II myosins also include non-muscle myosin IIA, IIB, and IIC (MYH9, MYH10, and MYH14, respectively), expressed in all eukaryotic cells, where they are involved in cytokinesis, cell migration, adhesion, and signalling (Simons et al., 1991, Berg et al., 2001). These myosins function as fast movers (fast skeletal muscle myosin 2A), efficient force holders (slow skeletal myosin II, β-cardiac myosin II), and strain sensors (NMIIa, NMIIb) (Berg et al., 2001, Bloemink and Geeves, 2011).

NMIIa is a motor protein that plays a critical role in various cellular processes including cell division, adhesion, migration, and maintenance of cell shape. NMIIa generates contractile forces within cells by interacting with actin filaments, contributing to the mechanical properties and dynamic remodelling of the cytoskeleton. It is particularly important in processes such as cytokinesis, where it helps to physically separate daughter cells, and in cell migration, where it aids in

the formation of the leading edge and rear contraction necessary for cell movement (Vicente-Manzanares et al., 2009).

NMIIa interacts with a variety of proteins to perform its functions. These interactions include interaction with actin filaments: NMIIa binds to actin filaments to produce tension through ATP-dependent motor activity. This interaction is crucial for the formation of stress fibres and the maintenance of cellular tension (Vicente-Manzanares et al., 2009); interaction with focal adhesions: NMIIa anchors to the extracellular matrix via focal adhesions, allowing cells to sense and respond to the mechanical properties of their environment (Weißenbruch et al., 2021); interaction with other NMII isoforms: NMIIa can co-assemble with NMIIb to form heterotypic filaments, creating a gradient along the cell's front to rear that regulates contractility during cell polarisation, migration, and cytokinesis (Weißenbruch et al., 2021).

The mechanism of NMII's motor activity involves the hydrolysis of ATP, which provides the energy needed for its motor functions (Figure 1.2). ATP Binding: ATP binds to the ATPase domain of NMII, causing a conformational change that detaches NMII from actin (Juanes-García et al., 2017, Brito and Sousa, 2020). ATP Hydrolysis: The hydrolysis of ATP into ADP and inorganic phosphate (Pi) leads to another conformational change, preparing NMII for reattachment to actin (Brito and Sousa, 2020). Power Stroke: The release of Pi triggers a conformational change in the NMII neck domain, generating a power stroke that moves the actin filament. This is accompanied by a rotation of the neck domain, translating chemical energy into mechanical force (Holmes, 2008). ADP Release: The final step involves the release of ADP from the actin bound NMII, allowing a new cycle of ATP binding and force generation to begin (Juanes-García et al., 2017, Brito and Sousa, 2020).

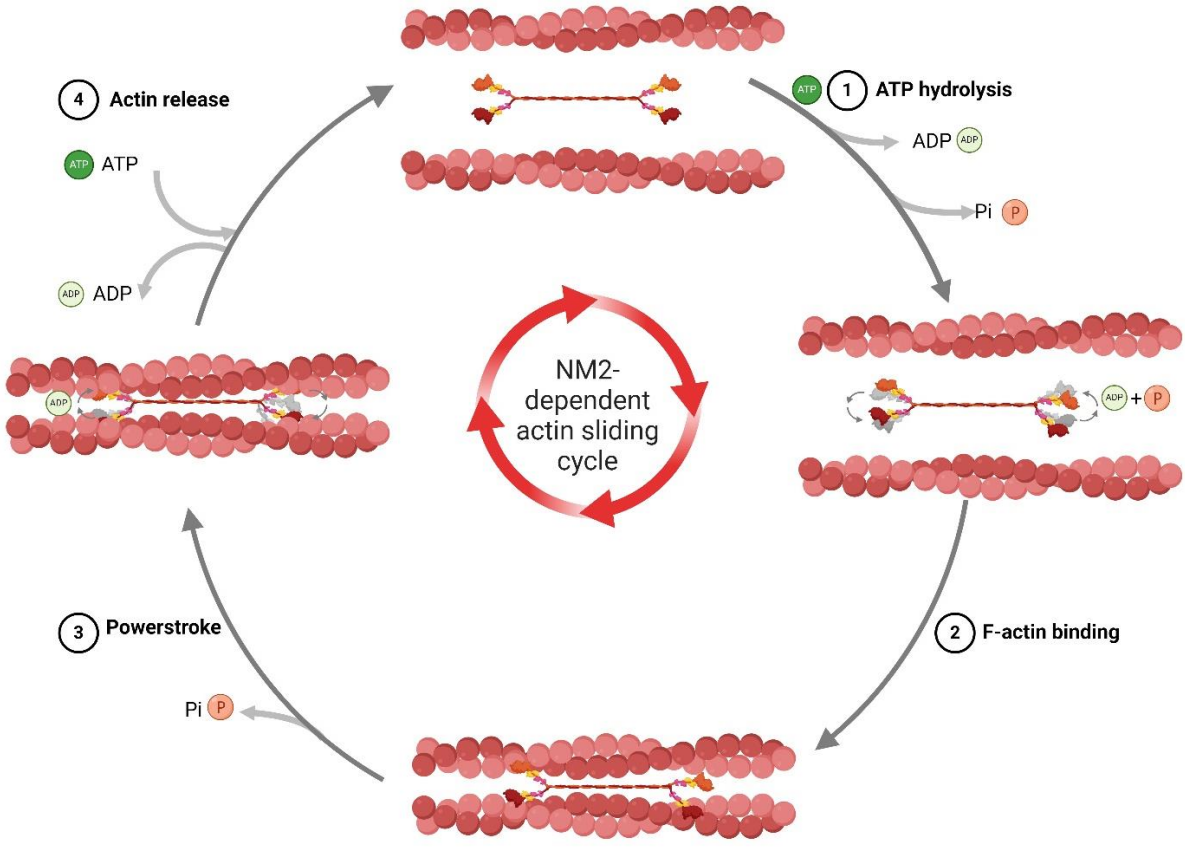

Figure 1.2 Schematic model for NMII-dependent actin sliding cycle. ATP binding dissociates NMII from actin (actin release). **(1)** Myosin motor head hydrolyses ATP and **(2)** re-attaches to actin. **(3)** The release of the phosphate (Pi) triggers a conformational change that promotes movement and powers the contraction of actin filaments (power stroke). The coloured region corresponds to the portion of the cycle during which the NMII motor head is strongly bound to actin, this is called duty ratio. **(4)** The exchange of ADP by ATP restarts the cycle (Created with Biorender.com).

The globular head domains of NMII contain binding sites for both ATP and actin, followed by neck regions that interact with two distinct light chains, serving as lever arms to amplify the head domains' rotation during the conversion of ATP's chemical energy into mechanical movement (Figure 1.3).

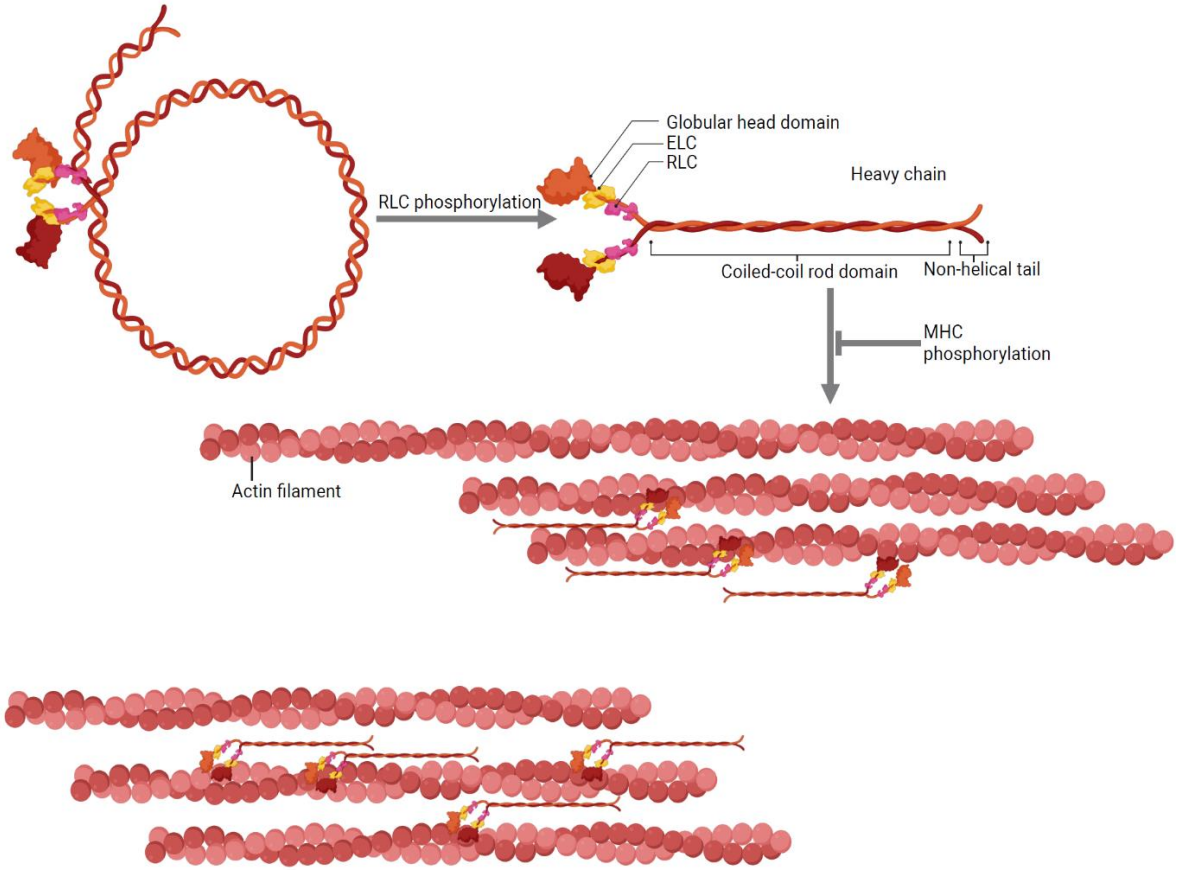

Figure 1.3 Domain structure of NMII. Non-muscle myosin II exhibits a distinct subunit and domain structure, characterised by the formation of a dimer through interactions between the α-helical coiled-coil rod domains. The globular head domain of NM II contains actin-binding regions and enzymatic Mg^{2+}-ATPase motor domains. The heavy chains of NM II interact with essential light chains (ELCs) and regulatory light chains (RLCs) at the lever arms, which serve as linkers between the head and rod domains. In the absence of RLC phosphorylation, NM II adopts a compact conformation through a head-to-tail interaction. NM II molecules form bipolar filaments by interacting with each other through their rod domains, and these filaments bind to actin through their head domains, where the ATPase activity induces a conformational change that enables the movement of actin filaments in an anti-parallel fashion, ultimately leading to the assembly of thick bundles such as stress fibres that connect actin filaments together. **(**Created with Biorender.com).

Beyond the neck domain, NMII features a long α-helical coiled coil that forms an elongated rod-shaped domain responsible for dimerisation between the heavy chains, concluding with a relatively shorter non-helical tail region (Holmes, 2008). NMII activity and assembly into filaments are regulated by the phosphorylation of the regulatory light chain (RLC) on serine 19 by various kinases. This phosphorylation

activates NMII's ATPase activity and promotes its filament assembly, enhancing its ability to generate force and maintain cellular tension (Masters et al., 2017, Vicente-Manzanares et al., 2009, Juanes-García et al., 2017).

1.2.2. Actomyosin contractile machinery - Regulation by MLCP/MLCK

Cytoskeletal rearrangements are an integral component of actin-myosin binding and contraction, inextricably linked to the generation of cytoskeletal tension, while changes in this tension profoundly impact the structure and function of the cellular barrier, particularly in endothelial cells (ECs) (Masters et al., 2017).

The regulation of actomyosin contractility is achieved through the delicate equilibrium between myosin phosphorylation by myosin light chain kinase (MLCK) and dephosphorylation by myosin light chain phosphatase (MLCP) (Figure 1.4). Myosin light chain (MLC) phosphorylation is essential in various cellular functions such as cellular morphogenesis, motility, and smooth muscle contraction and is important for MLC dephosphorylation. MLC phosphorylation is determined by the MLCK, which promotes actomyosin cross-bridge formation by phosphorylating the regulatory light chains (RLCs) of myosin, enhancing myosin's ATPase activity, and promoting actin-myosin cross-bridge formation (Cole and Welsh, 2011). Conversely, MLCP catalyses the dephosphorylation of the RLCs, leading to relaxation and the cessation of contractile activity in the actomyosin complex (Masters et al., 2017). The balance between MLCK and MLCP activity is critical for regulating various cellular functions, including contraction in smooth muscle cells, motility in non-muscle cells, and cytokinesis (Hartshorne, 1989, Cole and Welsh, 2011).

Rho cycles between inactive GDP-bound and active GTP-bound states (Amano et al., 2010, Heasman and Ridley, 2008, Hall and Lalli, 2010), functioning through specific effectors, including Rho-kinase, which directly phosphorylates MLC (Ishizaki et al., 1996, Leung et al., 1995, Matsui et al., 1996, Amano et al., 1996). This phosphorylation is also regulated by myosin phosphatase, composed of MYPT1, M20, and PP1δ subunits (Figure 1.6) (Alessi et al., 1992, Shirazi et al., 1994, Shimizu et al., 1994). Rho-kinase phosphorylates MYPT1, inhibiting myosin phosphatase (Kimura

et al., 1998) and enhancing actomyosin contraction by both direct MLC phosphorylation and phosphatase inhibition (Amano et al., 2010). Disruptions in this regulation can lead to conditions such as hypertension and asthma, where abnormal smooth muscle contraction is implicated. For example, thrombin induces sustained MLC phosphorylation, maintaining endothelial permeability, even though Rho activation is transient. Additional pathways, including potential auto-dephosphorylation of myosin phosphatase, might contribute to sustained MLC phosphorylation, highlighting the intricate regulatory mechanisms involved (Kaneko-Kawano et al., 2012).

Several signalling molecules and pathways have been implicated in the regulation of MLCP and MLCK. Calcium signalling has an important messenger role, initiating actomyosin contraction through MLCK activation. Increased cytosolic calcium levels bind to calmodulin, which in turn activates MLCK, resulting in myosin phosphorylation and actin-myosin interaction in muscle and non-muscle cells (Hartshorne, 1989, Somlyo and Somlyo, 2003, Mizuno et al., 2008, Cole and Welsh, 2011).

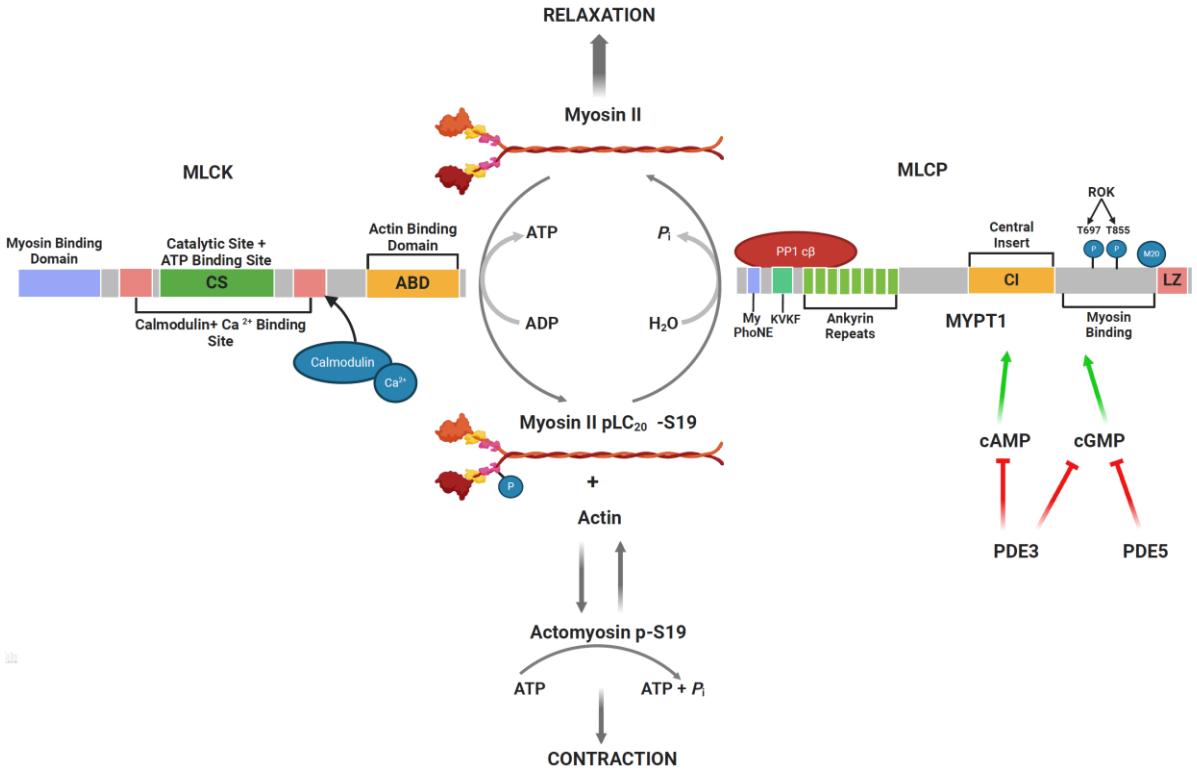

Figure 1.4 Mechanism of regulation of myosin light chain. Reversible phosphorylation-dephosphorylation of the regulatory light chain (LC_{20}) of myosin II. Myosin light chain kinase (MLCK) is activated by the binding of Ca^{2+}-calmodulin ($(Ca^{2+})_4$-CaM) leading to the phosphorylation of LC_{20} at serine-19 that permits actin interaction, the activation of myosin ATPase activity and in the presence of ATP, cross-bridge cycling, and contraction. LC_{20} is dephosphorylated by myosin light chain phosphatase to induce relaxation. The balance of MLCK and MLCP activities determines the level of LC_{20} phosphorylation and force generation in the steady state (Created with Biorender.com).

Integrins, which are transmembrane receptors that mediate cell adhesion to the extracellular matrix (see section 1.1.1), have been implicated in actomyosin regulation. Integrin-mediated signalling can activate MLCK and promote actomyosin contraction (Chrzanowska-Wodnicka and Burridge, 1996). The engagement of integrins with the extracellular matrix triggers intracellular signalling cascades that ultimately regulate MLCK activity and actomyosin contractility (Vicente-Manzanares et al., 2009). Although an increase in intracellular Ca^{2+} is necessary for MLCK activation, MLC20 can be phosphorylated by integrin-linked kinase (ILK) without an increase in Ca^{2+} (Williams et al., 1987). Likewise, ILK can inhibit MLCP by phosphorylating MYPT1 at Thr^{696} or through the activation of endogenous inhibitors

of PP1c, such as CPI-17 and PHI-1(Kiss et al., 2019, Sun et al., 2019, Deng et al., 2002).Furthermore, signalling pathways such as PKC can phosphorylation MLC and affects the ability of MLCK to phosphorylate MLC.PKC-mediated phosphorylation of MLCK can also modulate its activity and impact actomyosin contractility (Vicente-Manzanares et al., 2009).

Research has also revealed the involvement of other regulatory mechanisms in actomyosin contractility and the MLCP/MLCK pathway. For instance, myosin binding protein-C (MyBP-C), a component of the sarcomere in striated muscle, has been shown to modulate myosin phosphorylation through its interaction with MLCK (Colson et al., 2012). Additionally, phosphorylation of the myosin phosphatase targeting subunit 1 (MYPT1) at specific sites, such as Thr^{696} and Thr^{853}, can influence MLCP activity and actomyosin contractility (Figure 1.5) (Khromov et al., 2009). The inhibition of MYPT1 activity by ROCK1/2 and ZIPK, through phosphorylation at these sites, leads to the activation of MLCK, causing Ca^{2+} release and subsequent smooth muscle cell contraction or non-smooth muscle cell migration. Additionally, CPI-17 and PHI-1 can directly inhibit MYPT1 (Hudson et al., 2012, Singh et al., 2011, Wu et al., 2013). Conversely, protein kinase A (PKA) and protein kinase G (PKG) promote the phosphorylation of MYPT1 at Ser^{695}, and Ser^{852}, which activates MYPT1 and thus plays a role in regulating smooth muscle and non-muscle cell functions (Wang and Sun, 2018) (Figure 1.5).

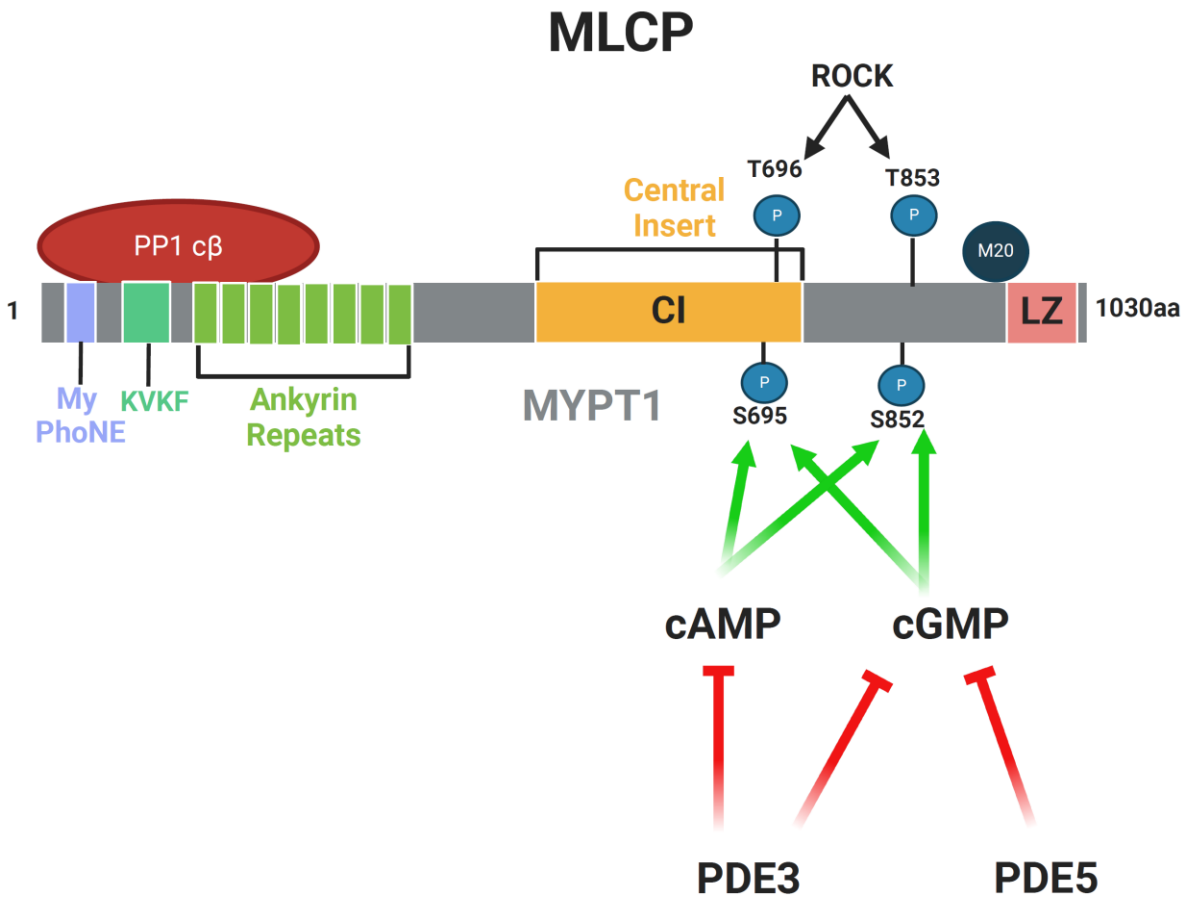

Figure 1.5 Phosphorylation sites of MYPT1. Phosphorylation of MYPT1 by ROCK predominantly occurs at Thr^{696} and Thr^{853}, which plays a crucial role in smooth muscle cell contraction and non-myocyte movement (Khasnis et al., 2014, Khromov et al., 2009). PKA and PKG promote the phosphorylation of MYPT1 at Ser^{695}, and Ser^{852}, which activates MYPT1 and thus plays a role in regulating smooth muscle and non-muscle cell functions (Wang and Sun, 2018) (Created with Biorender.com).

1.2.3. Myosin Light Chain Phosphatase (MLCP)

Myosin phosphatase (MP) was first isolated from chicken gizzard (Alessi et al., 1992); (Shimizu et al., 1994) and later from pig bladder (Shirazi et al., 1994). These independent studies confirmed that MP/MLCP holoenzyme consists of three subunits: a protein phosphatase-1 catalytic subunit (PP1c) of about 38kDa; a large myosin binding subunit of 110-133 kDa later defined as myosin phosphatase targeting subunit-1 (MYPT1); and a small subunit of about 20kDa (M20/21) (Figure 1.6) (Kiss et al., 2019). M20/21 is a protein of unknown physiological function (Hartshorne et al., 2004) but appears to be involved in regulating microtubule dynamics (Takizawa et al., 2003, Kiss et al., 2019).

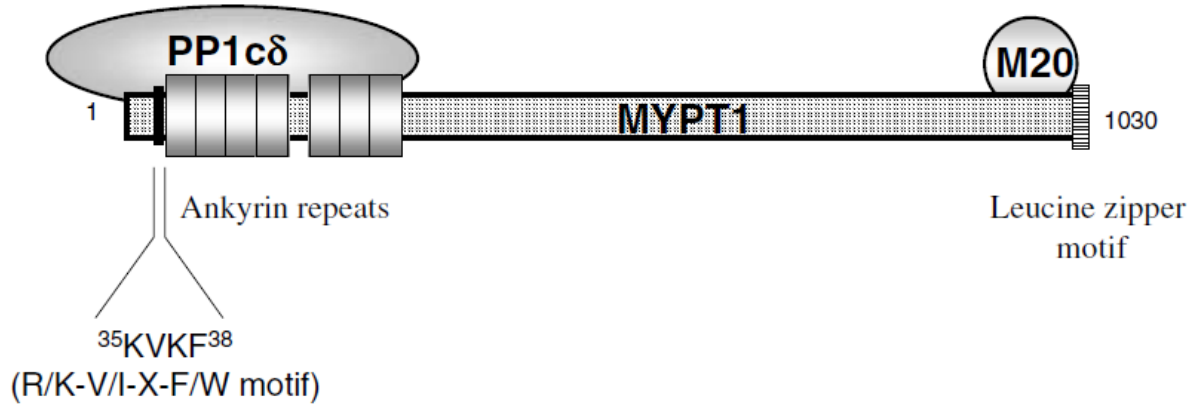

Figure 1.6 Subunit structure of smooth muscle myosin phosphatase. Includes RVxF PPP1-c binding motif ($K^{35}VKF^{38}$) which is essential for the interaction of PP1c with MYPT1. MyPhoNE (myosin phosphatase N-terminal element, not shown) (10-17 residues) and ankyrin repeats are also PP1c interaction sites. taken from (Ito et al., 2004).

It was established that out of three major PP1c isoforms (α, ß/δ, γ1) expressed in mammalian cells MYPT1 exclusively interacted with PP1c ß/δ (Scotto-Lavino et al., 2010, Kiss et al., 2019).

1.3. Myosin Phosphatase Targeting Subunit 1 (MYPT1)

1.3.1. MYPT family

MYPT1 is responsible for bringing PP1c in the proximity of its target, the myosin light chain. MYPT1 is a member of a larger family consisting of five gene products: MYPT1 (Shimizu et al., 1994); MYPT2 (Fujioka et al., 1998); MYPT3 (Skinner and Saltiel, 2001); protein phosphatase 1 myosin binding subunit of 85kDa (MBS85) and the TGF-ß1-inhibited, membrane-associated protein (TIMAP) (Tan et al., 2001). The family members have been ascribed to following genes: MYPT1= *PPP1R12A*, MYPT2 = *PPP1R12B*, MYPT 3 = *PPP14R16A*, MBS85 = *PPP1R12C* and TIMAP = *PPP1R16B* (Grassie et al., 2011).

A striking feature of all MYPT proteins is the presence of N-terminal ankyrin repeats (Hartshorne et al., 2004). In MYPT1 each of the 7 or 8 repeats contains ~33 residues with 20 conserved residues (Hartshorne et al., 2004). Sequence comparison of MYPT family members reveals high similarity in structural and functional domains, such as the RVxF motif for PP1c binding near the N-terminus (residues 1-296), followed by ankyrin repeats that bind various proteins, including phosphorylated myosin. MYPT1's interaction with myosin demonstrates the localisation of PP1c near its substrate (Terrak et al., 2004). Crystal structure studies show that MYPT1 contacts PP1c's conserved central region via the RVxF motif and MyPhoNE (residues 10-17) (Terrak et al., 2004, MacDonald and Walsh, 2018) and a K35VKF38 binding motif which facilitates binding of the 8 ankyrin repeats (residues 40 -296) to the PP1c (Toth et al., 2000, Terrak et al., 2004). MYPT1 also interacts with the C-terminus of PP1c via specific ankyrin repeats, explaining its specificity for PP1c isoforms, (Scotto-Lavino et al., 2010) involving Tyr305 and Tyr307 residues (Terrak et al., 2004). There are two nuclear localisation sequences located in the N-terminal (27-33) and C-terminal (845-854) regions. These motifs are responsible for directing the subcellular distribution of MYPT1 (Wu et al., 2005). The central region following the ankyrin repeats, containing conserved sequences, regulates MYPT functions primarily through phosphorylation by various kinases. Phosphorylation of MYPT1 at T696 and

T853 by ROCK is well understood, decreasing MLCP activity and inducing MYPT1 dissociation from myosin (as describe above on section 1.2.2, Figure 1.5) (Kimura et al., 1996, Ichikawa et al., 1996, Velasco et al., 2002, Muranyi et al., 2005, Grassie et al., 2011). The sequences around T696 and T853 of MYPT1 resemble the LC20 sequence in the vicinity of S19, consistent with a pseudo substrate mechanism of inhibition of PP1c activity, whereby phosphorylation of T696 or T853 results in docking of this region of MYPT1 into the PP1c active site, blocking access to the substrate (Khromov et al., 2009). MYPT1, MYPT2, and MBS85 contain C-terminal leucine zipper sequences for dimerisation and protein interaction, while MYPT3 and TIMAP have a C-terminal CaaX box (Figure 1.7) for membrane targeting (Cao et al., 2002, Ceulemans et al., 2002, Fu and Casey, 1999)..

At the C-terminal half of MYPT1 binds M20 (Shimizu et al., 1994, Hirano et al., 1997, Johnson et al., 1997) (between amino acids 934 and 1006) which is involved in regulating microtubule dynamics (Takizawa et al., 2003, Kiss et al., 2019), GTP-bound RhoA (Kimura et al., 1996), acidic phospholipids (Ito et al., 1997), and arachidonic acid (Gailly et al., 1996, Grassie et al., 2011).

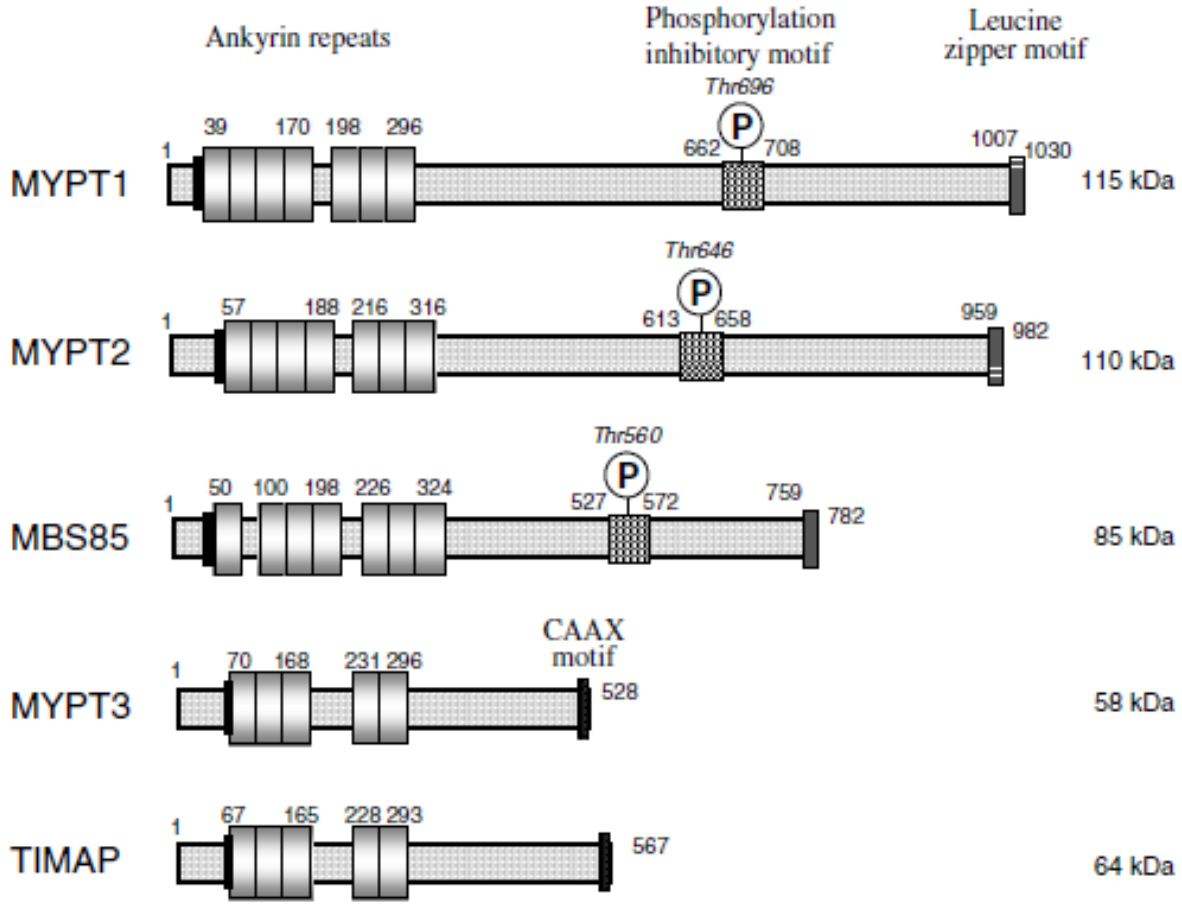

Figure 1.7 Domain structure of mammalian MYPT family members. PP1c binding motif indicated as bold black line near the N-terminus followed by 8 ankyrin repeats indicated as rectangular boxes and a central sequence containing inhibitory phosphorylation residue conserved in MYPT1, MYPT2 and MBS85. The leucine zipper domain of MYPT1, MYPT2 and MBS85 is located at the C-terminus are indicated. A CAAX box (prenylation motif) at the C-terminus of MYPT3 and TIMAP is shown as bold black line. Taken from (Ito et al., 2004).

1.3.2. MYPT1 structure

MYPT1 contains several structural motifs (Figure 1.8). The N-terminal region is common to all members of the MYPT family (Khromov et al., 2009) and has been described in the previous section. The central insert region (552-608) exhibits high variability, this region undergoes alternative splicing in different species leading to the generation of MYPT1 isoforms. The LZ motifs at the C-terminus are important for the phosphorylation of MYPT1 mediated by PKG (Butler et al., 2013, MacDonald and Walsh, 2018). There are splice variants lacking the LZ motifs. The LZ^- splice variant is subject to developmental regulation, is predominantly expressed in phasic

(rhythmically contracting) smooth muscle cells like in the bladder but is less abundant in the tonic (continuously contracted) smooth muscle cells of the large arteries and is absent in most other tissues (Dirksen et al., 2000, Payne et al., 2006, Oslin et al., 2022). Several interactions involving the LZ motifs in specific isoforms of MYPT1 have been identified. These interactions include: 1) the interaction between the LZ motifs of cGMP-dependent kinase (cGKI) and MYPT1 (Surks et al., 1999); 2) the binding of the PDZ2 domain of interleukin-16 precursor proteins to the C-terminal 30 residues of MYPT (Bannert et al., 2003); and 3) the interaction between a coiled-coil domain in RhoA-interacting protein (expressed in vascular smooth muscle) and the LZ motifs of MYPT1 (Surks et al., 2003).

The MYPT1 C-terminal region plays a crucial role in inhibiting MP activity through phosphorylation. MYPT1 contains multiple consensus sites for various protein kinases, and among them, phosphorylation at Thr^{696} and/or Thr^{853} (in human orthologue numbering) leads to the inhibition of MP activity. These phosphorylation events on MYPT1 regulate the function of MP and its ability to dephosphorylate myosin, thereby modulating actomyosin contractility (Kiss et al., 2019).

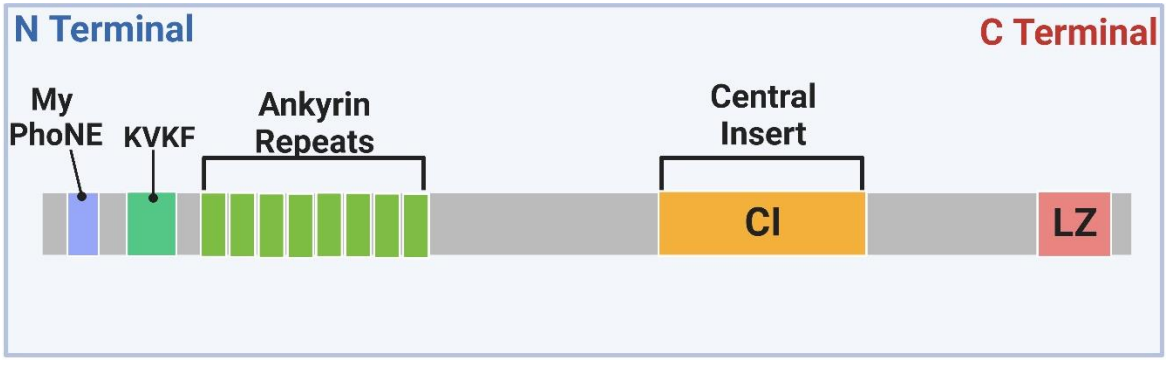

Figure 1.8 Structural domains of MYPT1. MYPT1 is constituted of for MyPhoNE (10-17 amino acid residues) the KVKF motif and 8 ankyrin repeats. All these regions facilitate binding of PP1c. There is also a central insert and a leucine zipper domain at the C-terminus.

1.3.3. Functional studies of MYPT1

Previous studies have shown that the knockout of *Mypt1* was performed by flanking the regions of exon 1 in mice that resulted in embryo lethality in mice. A critical region of the N-terminal sequence of MYPT1 is the PP1c-binding motif (RVxF) at residues 35–38 (Hartshorne et al., 2004, Ito et al., 2004). The homozygous embryos were not detected at 7.5 – 16.5 days of development (Okamoto et al., 2005). The mechanism(s) responsible for the lethality of the *Ppp1r12a*$^{-/-}$ mouse remain(s) to be identified. Evidence indicates that even at 7.5 days of development, no overt resorption of decidual swellings were found, thus the point of embryonic lethality is before 7.5 days of development. Although homozygosity was lethal, the heterozygous male and female mice (presented in equal frequency) were healthy and fertile. The MYPT1 expression levels had no substantial difference in the aorta, lung, and kidney between heterozygous and wild type animals (Okamoto et al., 2005).

In zebrafish (*Danio rerio*), knockdown of both maternal and zygotic expression of *ppp1r12a* using morpholino antisense oligonucleotides resulted in morphant embryos with hypercontractile mesodermal cells that failed to undergo proper morphogenetic cell movement during gastrulation, including convergent extension of the presomatic mesoderm (Weiser et al., 2009, Diz-Muñoz et al., 2010). Convergent extension is a cellular process by which cells first migrate toward the future dorsal side of the embryo and subsequently intercalate between neighbouring cells, resulting in an overall dorsal-ventral narrowing (convergence) and anterior–posterior lengthening (extension) of the embryonic tissue (Keller, 2002, Tada and Heisenberg, 2012, LaFlamme et al., 2018).

In a phosphoproteomics study to investigate Ser/Thr phosphorylation events regulated by MYPT1 gene in the L6 skeletal muscle cell line the knock down of the *PPP1R12A* gene increased overall phosphorylation at basal conditions. This knockdown also led to changes in phosphorylation levels for 698 sites, assigned to 295 phosphoproteins at the basal and/or insulin-stimulated conditions thus showing that MYPT1 has several Ser/Thr regions that can be phosphorylated (Zhang et al., 2014).

1.3.4. Regulation of MLCP by phosphorylation

Some aspects of MLCP regulation by phosphorylation were explained above on section 1.2.3. MYPT1 interacts with PP1c and M20 to form the trimeric holoenzyme and with phosphorylated myosin (Hartshorne et al., 1998) to enhance phosphatase activity towards phosphorylated myosin. The signalling pathways converging on MLCP can increase phosphatase activity to decrease MLC phosphorylation and myosin force through Ca^{2+} desensitisation. They can conversely decrease phosphatase activity to increase MLC phosphorylation and myosin force through Ca^{2+} sensitisation (Somlyo and Somlyo, 2003).

MYPT1, a target of multiple protein kinases, undergoes phosphorylation at various sites, with S^{695}, T^{696}, S^{852}, and T^{853} being the most extensively studied ones (Figure 1.5)(MacDonald and Walsh, 2018). Other protein kinases like zipper-interacting protein kinase (ZIPK), but not MLCK are known to indirectly phosphorylate MYPT1 atT696 (Yuen et al., 2014).

Both inhibitory phosphorylation sites, T^{696} and T^{853}, are immediately preceded in the sequence by serine residues S^{695} and S^{852} that match the cAMP- and cGMP-dependent protein kinase (PKA and PKG) phosphorylation consensus motif (Grassie et al., 2011). The term consensus sequence refers to those sequence elements immediately surrounding the site(s) phosphorylated by a given protein kinase that are considered essential for its recognition and phosphorylation by that kinase (Kennelly and Krebs, 1991). Phosphorylation by PKA and PKG at those sites is believed to counteract or prevent the inhibition of MLCP induced by ROCK phosphorylation, leading to disinhibition (Wooldridge et al., 2004).

1.4. Protein kinase A (PKA)

1.4.1. PKA

Protein kinase A (PKA), also known as cyclic AMP-dependent protein kinase, is an enzyme essential for regulation of cellular processes, by potentiating the signals from a wide range of ligands that bind G-protein coupled receptors (GPCRs) (London et al., 2020) in eukaryotes It is a type of serine/threonine kinase, activated by cyclic AMP (cAMP), and involved in numerous cellular functions including metabolism, gene expression, and cell proliferation (Taylor et al., 2012, Torres-Quesada et al., 2017).

The PKA holoenzyme is a tetramer composed of two regulatory (R) and two catalytic (C) subunits. The regulatory subunits bind cAMP, leading to the dissociation and activation of the catalytic subunits. The genes encoding these subunits have different isoforms, which allow for tissue-specific expression and functional diversity (Skalhegg and Tasken, 2000, Taskén et al., 1997). There are four regulatory subunit genes in mammals: *PRKAR1A* and *PRKAR1B* that encode the RIα and RIß isoforms, respectively; *PRKAR2A* and *PRKAR2B*, encoding the RIIα and RIIß isoforms, respectively. RIα (*PRKAR1A*) is ubiquitously expressed and involved in various cellular processes. Mutations in RIα are linked to Carney complex, a disorder characterised by multiple neoplasias (Bossis and Stratakis, 2004). RIß (*PRKAR1B*) is predominantly found in the brain, particularly the hippocampus and cortex, indicating a role in neural signalling (Brandon et al., 1998). RIIα (PRKAR2A) is also ubiquitously expressed and involved in found in a wide range of tissues (Scott et al., 1987). RIIß (*PRKAR2B*) is primarily expressed in adipose tissue and the brain, suggesting roles in energy metabolism and neurophysiology (Cadd and McKnight, 1989). The catalytic subunit genes include *PRKACA* that encodes the Cα isoform (Guthrie et al., 1997), *PRKACB* that encodes the Cß isoform (Uhler et al., 1986), and *PRKACG* encoding the Cγ isoform, which is primarily found in the testis (Beebe et al., 1990, Zhang et al., 2004b, Soberg et al., 2017). Alternative splicing of these genes gives rise to multiple isoforms of both the regulatory and catalytic subunits, leading to functional diversity of PKA.

1.4.2. Regulation and function of PKA

1.4.2.1 Function of PKA

The primary function of PKA is to mediate cellular responses to the second messenger cAMP. In response to extracellular signals, such as hormones or neurotransmitters, adenylate cyclase is activated, leading to increased cAMP levels. Elevated cAMP levels bind to the regulatory subunits of PKA, resulting in their dissociation from the catalytic subunits and subsequent activation of PKA (Figure 1.9) (Taylor et al., 2012, Tasken and Aandahl, 2004). Once activated, PKA phosphorylates a wide range of target proteins, including enzymes, ion channels, and transcription factors, thereby regulating their activity and function. PKA has been implicated in the modulation of diverse cellular processes, such as metabolism, gene expression, cell growth and proliferation, and neuronal signalling (Francis et al., 2011, Lefkimmiatis and Zaccolo, 2014).

All isoforms of the R subunits of PKA share the same structural features, including a Dimerisation/Docking (D/D) domain, a small inhibitory segment, and two cyclic nucleotide-binding (CNB) domains, referred to as CNB-A (more N-terminal) and CNB-B (more C-terminal). The ratio of Type I and Type II PKA holoenzymes varies across tissues. Proliferating or differentiating tissues express higher ratios of Type I holoenzymes, while terminally differentiated tissues exhibit higher levels of Type II holoenzymes (Cho-Chung et al., 1995).

The D/D domain serves two critical roles: it facilitates the dimerisation of two regulatory subunits and docks the PKA holoenzyme into specific subcellular compartments by binding to an amphipathic α-helix in A-kinase anchoring proteins (AKAPs) (Gold et al., 2006, Sarma et al., 2010). The specificity of AKAPs to R subunits is determined by amino acids within the D/D domain (Figure 1.9) (Gold et al., 2006), enabling the compartmentalisation of PKA C subunits for specific cAMP signalling.

The α and β isoforms of Type I and Type II R subunits form isoform-specific heterodimers, with no significant evidence of heterodimerisation between Type I and Type II R subunits. Holoenzymes tend to form homodimers of α and β R subunits

of the same isoform (Ogreid et al., 1985, Carlson et al., 2003, Tasken et al., 1993), adding a layer of regulation in PKA signalling based on isoform expression levels in tissues.

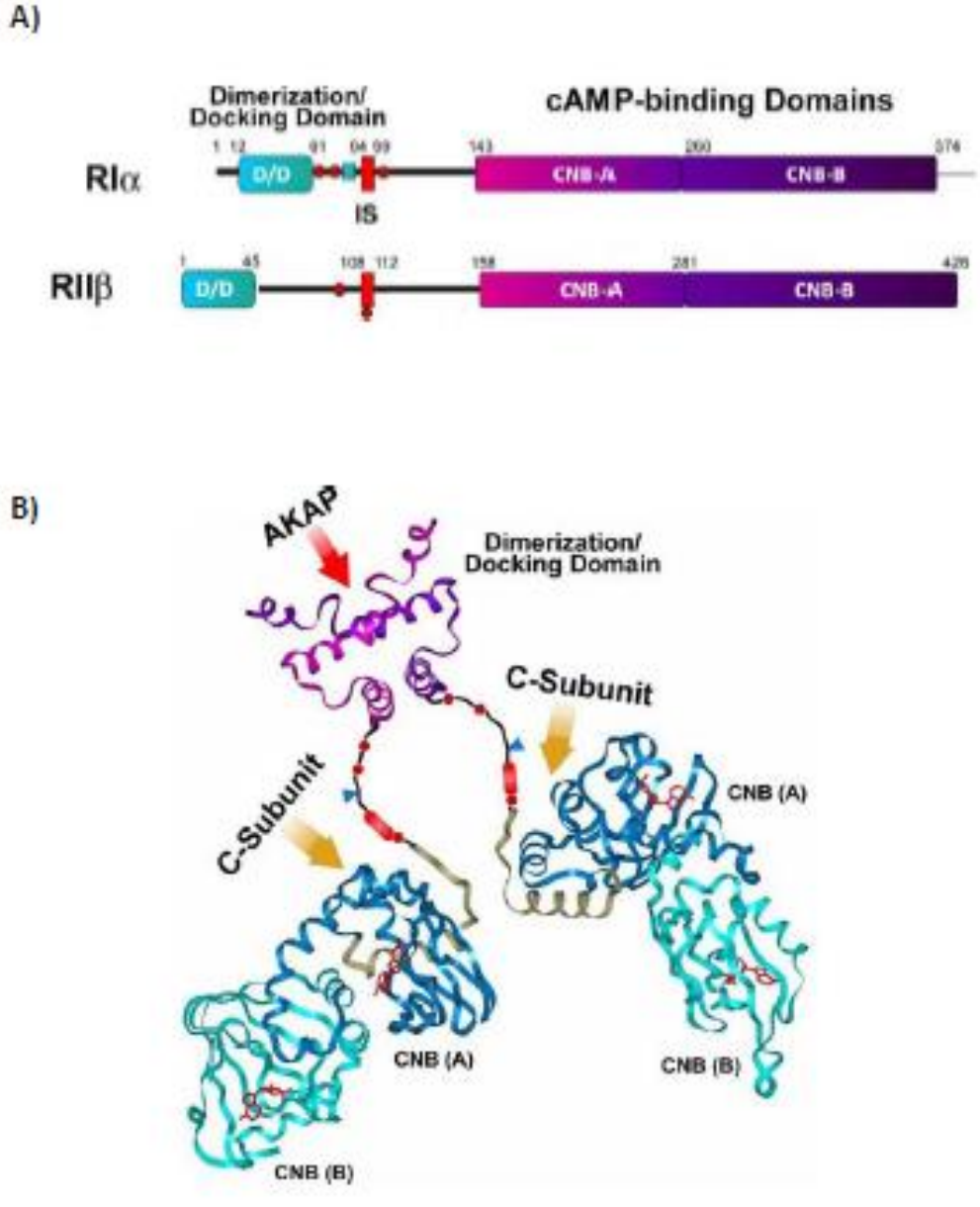

Figure 1.9 Schematic representation of PKA regulatory subunit. (A) Domain organisation of PKA regulatory subunits RIα and RIIß: N-terminal dimerisation and docking domain (D/D), followed by a linker region housing phosphorylation residue, serine (red circles), a proline box (**blue** square), inhibitor site (IS) (red rectangle) and two C-terminal cyclic nucleotide binding domains (CNB-A and CNB-B). **(B)** Ribbon illustration of the NMR structure of PKA RIα dimer including AKAP binding site D/D domain, inhibitor sites (red rectangular box), serine residues (red circles) in the linker region followed by four cyclic nucleotide binding domains designated as CNB-A and CNB-B. Modified from (Taylor et al., 2012).

The CNB domains have different affinities for cAMP, with the A-site exhibiting faster on and off rates. The CNB domains form an allosteric network that facilitates cooperative activation of PKA by cAMP. Binding of cAMP to the A-site induces a conformational change that modulates cAMP binding to the B-site. Phosphorylation of downstream PKA targets occurs only after cAMP binds to both sites, leading to the dissociation of C subunits from R subunits (Figure 1.10). The distinct conformations of the A- and B-sites in Type I and Type II R subunits' crystal structures may explain the differences in cooperativity and sensitivity to activation by cAMP between these holoenzymes (Gibbs et al., 1992, Taylor et al., 1990, Anand et al., 2007).

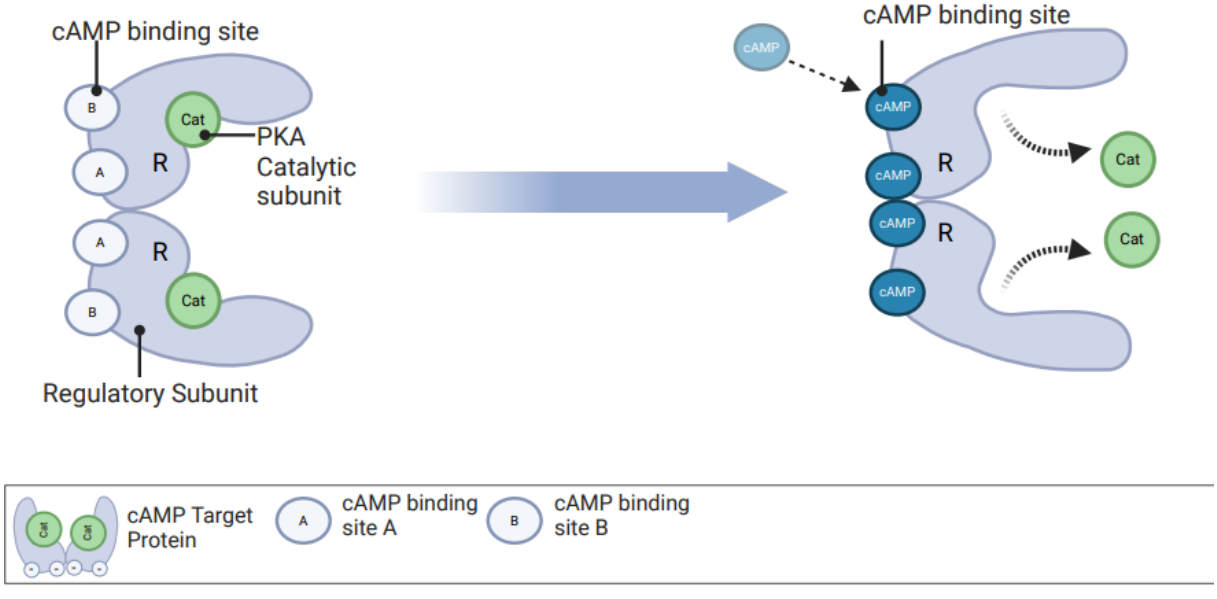

Figure 1.10 cAMP-mediated activation of PKA. PKA holoenzyme is composed of two regulatory (R) and two catalytic subunits (C). Each regulatory subunit has two cAMP binding sites (A and B). When four cAMP molecules bind to regulatory subunits, unleash the catalytic subunits and result in PKA activation. (Created with Biorender.com).

A recent review by Gold (2019) has summarised experiments in support of the mechanism of PKA activation via cAMP-induced dissociation of PKA-C from PKA-R as well as other lines of evidence that suggest that PKA-Cat subunits do not fully dissociate from PKA-R. Experiments have shown that cAMP releases C subunits from RI and RII according to cation exchange chromatography (Beavo et al., 1974), affinity

to casein-sepharose (Reimann et al., 1971) and cAMP agarose (Dills et al., 1975, Corbin et al., 1978), size-exclusion chromatography (Erlichman et al., 1971, Kumon et al., 1972), and sucrose gradient ultracentrifugation (Hofmann et al., 1975). Further in vitro data by small-angle X-ray scattering (Vigil et al., 2004), and AlphaScreen experiments (Moll et al., 2006), in live cell FRET experiments, two-photon fluorescence lifetime imaging microscopy (2p-FLIM) (Tillo et al., 2017), UV cross-linking (Walker-Gray et al., 2017), proximity ligation assays (Smith et al., 2013) and bioluminescence resonance energy transfer (BRET) experiments (Moll et al., 2006, Isensee et al., 2018) support that PKA-C dissociates from PKA-R upon cAMP binding. In support of the non-dissociative model, cAMP co-immunoprecipitations with either AKAP79-RII (Smith et al., 2013, Smith et al., 2017) or AKAP18-RII (Smith et al., 2013) complexes is not reduced by the ß-adrenergic receptor agonist isoproterenol. Physiological agonists cause the dissociation of C subunits from PKA holoenzymes in cells. However, there is no conclusive evidence indicating that phosphorylation by cAMP-activated intact type II PKA holoenzymes plays a major role (Isensee et al., 2018, Gold, 2019).

PKA role in cellular metabolism is one of its well-known functions. PKA regulates glucose and lipid metabolism in various tissues, including adipocytes and skeletal muscle (London et al., 2020). It modulates the activity of key enzymes involved in metabolic pathways, influencing processes like glycogenolysis, gluconeogenesis, and lipolysis. PKA is essential in the regulation of gene expression. It phosphorylates transcription factors, such as cAMP response element-binding protein (CREB), leading to the activation of expression of target genes (Wang et al., 2018). Through this mechanism, PKA influences cellular processes such as cell differentiation, development, and synaptic plasticity. PKA activity is tightly regulated by several mechanisms. In addition to cAMP synthesis, the activity of PKA is regulated by phosphodiesterases (PDEs), which hydrolyse cAMP and terminate its signalling (Francis et al., 2011, Krishnamurthy et al., 2014).

1.4.2.2 Compartmentalisation of PKA signalling: A-Kinase Anchoring Proteins (AKAPs)

Early studies by (Hayes et al., 1979, Hayes et al., 1980) and later by (Buxton and Brunton, 1983) provided initial indirect evidence for the compartmentalisation of cAMP signals in whole tissues and cell preparations, respectively. Nearly two decades later, direct evidence emerged, substantiating the functional relevance of subcellular cAMP signalling events. Pioneering work by (Zaccolo and Pozzan, 2002) and (Nikolaev et al., 2006) reinforced the model of compartmentalised cAMP signalling, establishing its critical role in cellular function (Di Benedetto et al., 2008, Zaccolo and Pozzan, 2002).

The advent of molecular tools capable of detecting cAMP changes in real-time within intact living cells marked a significant advancement. Tools developed by (Berrera et al., 2008, Gesellchen et al., 2011, Stangherlin et al., 2014) were instrumental in this regard. These tools utilised Fluorescence Resonance Energy Transfer (FRET)-based probes sensitive to cAMP and PKA, revolutionising the study of cAMP signalling. By leveraging the cAMP binding domains in PKA (Zaccolo et al., 2000, Zaccolo and Pozzan, 2002) or exchange protein activated by cAMP (EPAC) (Ponsioen et al., 2004, Nikolaev et al., 2004), these sensors achieved high spatial and temporal resolution, crucial for detecting physiological changes in cAMP levels. Being genetically encoded, these probes could be targeted to specific cellular compartments, enabling real-time detection of cAMP at distinct intracellular sites. The high-resolution capabilities of these probes demonstrated that cAMP achieves specificity of action through the precise organisation of its pathway's molecular components into complex "signalosomes" located at defined cellular locations (Stangherlin and Zaccolo, 2012).

Compartmentalisation of cAMP is primarily achieved through the action of phosphodiesterases (PDEs), which are enzymes that degrade cAMP into AMP, thereby limiting the spread of cAMP within the cell. Different PDE isoforms are localised to distinct cellular regions, creating microdomains with varying cAMP concentrations

(Baillie et al., 2005). This localisation is further refined by anchoring proteins such as A-kinase anchoring proteins (AKAPs), which tether PKA and other signalling molecules to specific locations within the cell. By anchoring PKA near its substrates and cAMP sources, AKAPs ensure that cAMP signals can be quickly and efficiently transduced (Wong and Scott, 2004).

Additionally, the distribution of adenylyl cyclases (ACs), which synthesise cAMP from ATP, contributes to the compartmentalisation. Different ACs isoforms are expressed in various cellular locations, such as the plasma membrane, Golgi apparatus, or even in mitochondria, generating localised pools of cAMP in response to specific signals (Dessauer, 2009). This spatial organisation is key for the selective activation of downstream effectors like PKA, EPAC, and cyclic nucleotide-gated ion channels.

Moreover, cell-type-specific expression of PDEs, ACs, and AKAPs further diversifies the compartmentalisation of cAMP. For instance, in cardiac myocytes, the precise regulation of cAMP signalling is essential for the modulation of heart rate and contraction strength. Disruptions in cAMP compartmentalisation can lead to pathological conditions, highlighting the importance of this regulatory mechanism (Lefkimmiatis and Zaccolo, 2014).

AKAPs are characterised by the presence of a structurally conserved domain known as the A-kinase anchoring domain (AKAD) (Figure 1.11) (Scott and Santana, 2010). This domain facilitates the interaction between AKAPs and regulatory subunits of PKA, enabling the assembly of PKA holoenzymes at specific subcellular locations (Feliciello et al., 2001, Scott and Santana, 2010).

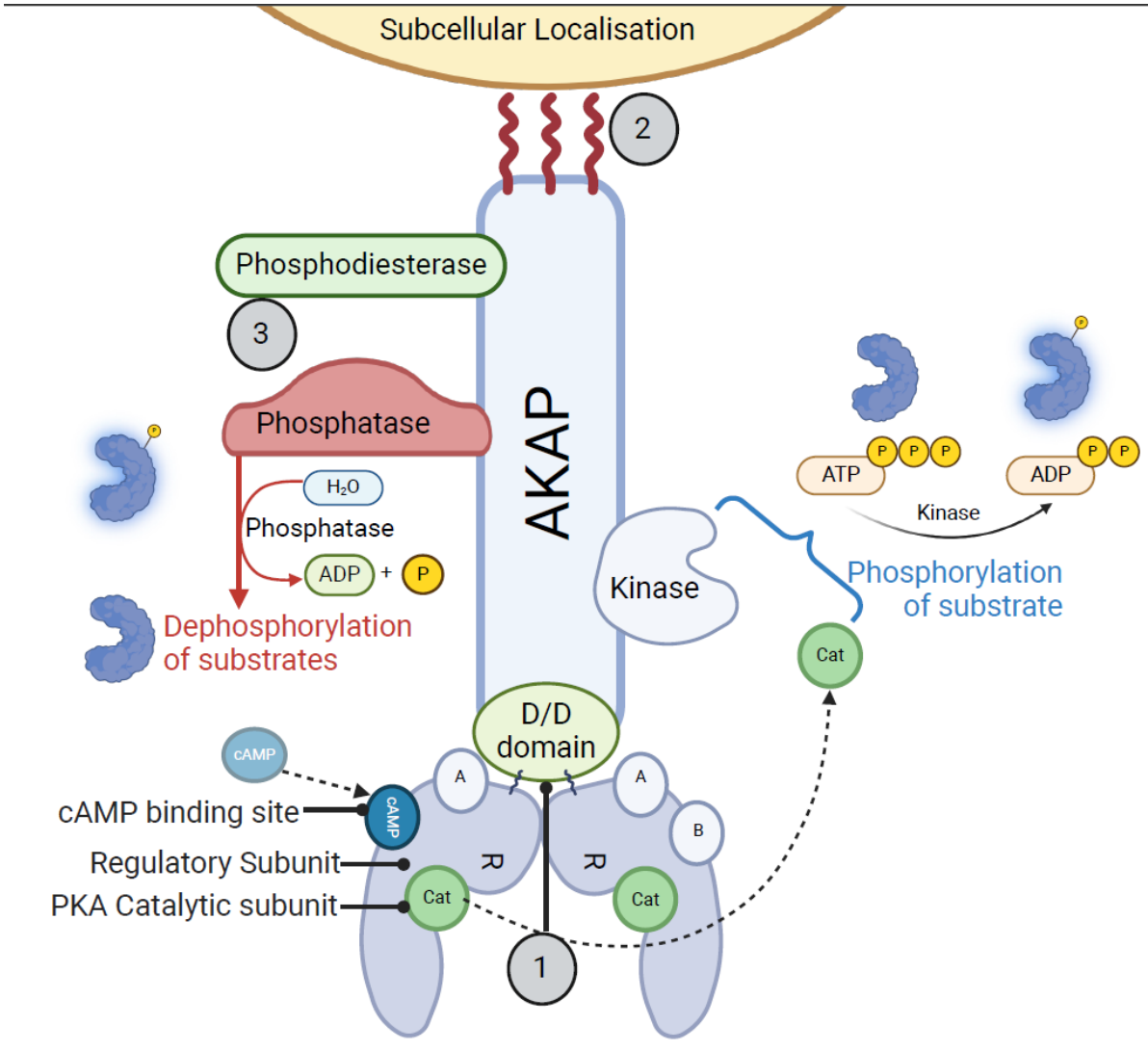

Figure 1.11 Properties of AKAPs. AKAPs regulate the subcellular localisation of PKA, generating substrate specificity for PKA. All AKAPs possess three properties: **(1)** A conserved PKA anchoring domain; **(2)** Localisation signals to direct AKAP complexes to subcellular locations; **(3)** Interaction with other signalling molecules, including phosphodiesterases, phosphatases, and kinases. Adapted from (Gabrovsek et al., 2018).

AKAPs integrate signal transduction processes both spatially and temporally. Depending on their subcellular localization and specific protein interactors, a single AKAP can regulate multiple pathways (Dema et al., 2015). For example, WAVE-1 is located at the actin cytoskeleton in neurons, where it regulates actin crosslinking (Soderling et al., 2007). In breast cancer cells, WAVE-1 is involved in the formation of cellular protrusions, facilitating cell migration and invasion (Frugtniet et al., 2015). In leukaemia cells, WAVE-1 is found at mitochondria, where it regulates apoptosis (Kang et al., 2010). Another notable example is Optic Atrophy 1 (Opa-1), which is best known for its role in controlling mitochondrial fusion when localised to mitochondria (Frezza et al., 2006, Song et al., 2009). Additionally, Opa-1 has been suggested to function as an AKAP involved in adrenoceptor-induced lipolysis when located on lipid droplets (Pidoux et al., 2011). However, this interpretation has been contested, as Opa-1 may have been detected on lipid droplets as a mitochondrial contaminant (Belenguer and Pellegrini, 2013). Canonical AKAPs interact with the dimerised N-terminal D/D domains of PKA-R subunits through their structurally conserved A kinase-binding (AKB) domains. These AKB domains are 14–25 amino acids in length and form amphipathic helices. The hydrophobic face of these helices docks into a hydrophobic pocket formed by the D/D domain (Newlon et al., 1999, Newlon et al., 2001). Through these interactions, AKAPs enable precise regulation of PKA activity and other associated signalling pathways, contributing to the intricate control of cellular processes. The ability of AKAPs to form complexes with multiple proteins and localise to various cellular compartments underscores their critical role in cellular signalling dynamics (Dema et al., 2015).

AKAPs exhibit distinct subcellular localisations, allowing for compartmentalised signalling by directing PKA to specific substrates and effectors. This localisation allows for precise and efficient phosphorylation events. For example, AKAP79/150 is localised to the plasma membrane and is involved in anchoring PKA, phosphodiesterases, and other signalling proteins at the cell cortex (Dell'Acqua et al., 2002), it binds to PDE4, regulating cAMP levels and modulating PKA signalling

(Bauman et al., 2006). This interaction provides a mechanism for AKAPs to fine-tune cAMP-mediated signalling pathways.

AKAPs are involved in numerous physiological processes. AKAP150 is a critical regulator of synaptic plasticity and memory formation in the brain. It localises PKA, N-methyl-D-aspartate (NMDA) receptors, and ACs to the postsynaptic density, facilitating the phosphorylation of synaptic proteins and modulating synaptic strength (Dell'Acqua et al., 1998). AKAPs also have a role in cellular adhesion and migration. AKAP12 (Gravin) acts as a signalling scaffold at focal adhesions and contributes to the regulation of cell motility and adhesion (Benz et al., 2020). Dysregulation of AKAP-mediated signalling has been implicated in various diseases. Alterations in AKAP signalling have been associated with cardiac dysfunction, neurodegenerative disorders, cancer progression, and diabetes. In heart failure, disruption of AKAP-mediated PKA signalling contributes to contractile dysfunction and arrhythmogenesis (Hulme et al., 2006). AKAP-Lbc mediates the activation of PKA and the small GTPase Ras, which is critical in cardiac hypertrophy (Diviani et al., 2004). By organising PKA and Ras signalling, AKAP-Lbc modulates the hypertrophic response of cardiac myocytes. AKAP dysregulation has also been implicated in neurodegenerative diseases such as Alzheimer's and Parkinson's, where synaptic dysfunction and cognitive deficits occur (Dagda and Das Banerjee, 2015). For a comprehensive account on AKAPs please refer to the comprehensive review by, (Omar and Scott, 2020).

While the majority of AKAPs recruit PKA-R subunits via a characteristic amphipathic helix that engages with the D/D domain, several proteins exhibit a different mode of interaction. Examples of non-canonical AKAPs include pericentrin (Diviani et al., 2000), RSK1 (Chaturvedi et al., 2006), neurochondrin (Hermann et al., 2015), tubulin (Kurosu et al., 2009), actin (Rivard et al., 2009), and α4 integrin (Lim et al., 2007). These proteins interact with PKA-R without involving an amphipathic helix or the D/D domain of PKA-R (Dema et al., 2015).

The critical role of AKAPs in cellular signalling pathways presents them as potential therapeutic targets. Modulating AKAP-dependent signalling may offer new avenues

for developing targeted therapies. For instance, disrupting specific AKAP-protein interactions through small molecules or peptides could selectively inhibit pathological signalling pathways. Conversely, drugs that enhance AKAP-mediated signalling could be employed to restore normal cellular functions in disease states (Bucko and Scott, 2021).

1.5. The vasculature

The vasculature refers to the intricate network of blood vessels in an organism, encompassing arteries, veins, and capillaries, which facilitate the circulation of blood throughout the body. In the human vasculature, the intricate dynamic interplay between platelets, endothelial cells and smooth muscle cells plays a crucial role in maintaining vascular homeostasis and regulating various physiological processes (Figure 1.2) (Sena et al., 2013).

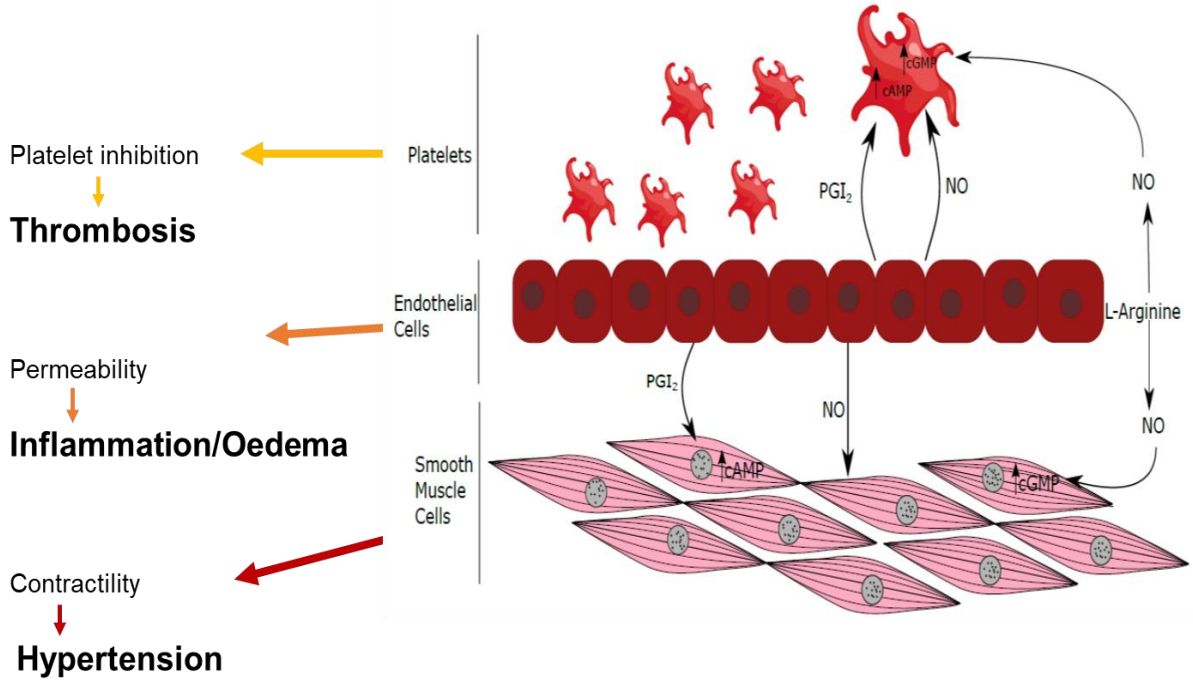

Figure 1.12 Signalling interaction between smooth muscle cells, endothelial cells, and platelets. Modified from (Norton et al., 2012).

The cardiovascular (CV) system is the first functional organ system formed during vertebrate development. Its primary function is to enable gas exchange, supply nutrients, and remove waste from tissues, thus ensuring proper cellular nourishment and organism growth (Udan et al., 2013). As the embryo develops, the CV system also becomes integral to lymph regulation, endocrine system functions, immunological surveillance, and inflammation. In mammals, the CV system comprises a four-chambered heart connected to the vasculature via pulmonary arteries and veins, dorsal aorta, and sinus venosus. The vasculature is divided into three main systems: arteries, veins, and lymphatics. Arteries transport blood from the heart to tissues, veins return blood to the heart apart from pulmonary (Suresh and Shimoda, 2016) and umbilical cord circulations (Murphy, 2005), and lymphatic vessels manage interstitial fluid. Vessels consist of multiple cell types, including endothelial cells forming the inner lining, supported by vascular smooth muscle cells and pericytes. Larger vessels have additional layers, such as the tunica media and tunica adventitia, providing stability and flexibility. The development and remodelling of the vasculature involve vasculogenesis and angiogenesis, processes that remain active throughout life to adapt to physiological changes and pathological conditions. Advances in understanding these mechanisms are highlighted by studies utilising various vertebrate models (Udan et al., 2013).

After vessel formation and remodelling are complete, ensuring vessel stability and tissue homeostasis becomes essential. This stability is partially achieved by recruiting mural cells, which smooth muscle cells and pericytes are part of, to the vessel wall (Rossant and Howard, 2002). During maturation, endothelial cells secrete platelet-derived growth factor subunit B (PDGFB), which binds PDGFRB (PDGF receptor ß) on mural cell precursors, promoting their recruitment and proliferation. These precursors then engage in reciprocal signalling by secreting angiopoietin 1 (ANGPT1), which binds to the TEK receptor (Angiopoietin-1 receptor also known as CD202B (cluster of differentiation 202B)) on endothelial cells, facilitating the formation of cell-cell adhesions and mural cell association with the vessel wall (Lindahl et al., 1997, Sato et al., 1995, Suri et al., 1996). Mural cell differentiation

is dependent on endothelial contact, involving gap junction communication via gap junction protein alpha 1 (GJA1), also known as connexin 43 and gap junction protein, gamma 1 (GJC1), known as connexin 45, and transforming growth factor ß1 (TGFB1) signalling (Hirschi et al., 2003, Kruger et al., 2000, Carvalho et al., 2004). Vessel homeostasis disruption is regulated by ANGPT2, antagonising ANGPT1/TEK signalling. Mural cells maintain vessel integrity, with smooth muscle cells coordinating with endothelial cells to regulate blood flow. Their diverse developmental origins contribute to functional heterogeneity, with ongoing research exploring varied TGFB1 responses (Udan et al., 2013).

Organ homeostasis is critically dependent on the coordinated function of two hierarchically branched vessel networks: the blood vasculature and the lymphatic vasculature. The blood vasculature operates as a closed circulatory system composed of arteries, veins, and interconnecting capillaries. This system is essential for the transportation of gases, nutrients, metabolites, and cells, as well as the delivery of paracrine signalling molecules to surrounding tissues. In contrast, the lymphatic system is characterised by its blind-ended and unidirectional structure, comprising lymphatic vessels, lymph nodes, and associated lymphoid organs. This 'secondary vascular system' is integrally connected to the blood vasculature, facilitating the return of extravasated fluid and macromolecules back into the blood circulation. Furthermore, lymphatic vessels play crucial roles in fat absorption, tissue cholesterol clearance and immune cell trafficking (Aspelund et al., 2016, Potente and Makinen, 2017).

Focusing on blood vasculature, blood vessels originate from the mesodermal embryonic layer. The development of embryonic vessels and the heart starts in the middle of the third week of gestation, in humans, with foetal circulation beginning around the eighth week. Blood vessels originate from the mesodermal embryonic layer (Tucker et al., 2024).

Blood vessel formation occurs through two main mechanisms: vasculogenesis and angiogenesis. Vasculogenesis refers to the process by which blood vessels form in the embryo. This process is driven by interactions between precursor cells and various

growth factors, leading to cellular differentiation. Mesodermal precursor cells, in response to fibroblast growth factor 2 (FGF2), differentiate into haemangioblasts. These haemangioblasts, upon interaction with vascular endothelial growth factor (VEGF), further differentiate into endothelial cells. These endothelial cells then aggregate to form the initial hollow blood vessels. The first vessels formed through vasculogenesis include the dorsal aorta and the cardinal veins. In contrast, all other vasculature in the human body forms through angiogenesis(Potente and Makinen, 2017).

Angiogenesis is the process by which new blood vessels arise from the endothelial layer of pre-existing vessels. This process, primarily driven by interactions involving VEGF, is the predominant form of neovascularisation in adults. Angiogenesis is crucial for expanding the vascular network beyond the initial structures formed during vasculogenesis, supporting growth, and responding to tissue demands throughout life (Potente and Makinen, 2017, Tucker et al., 2024).

1.5.1. Blood vessel structure

1.5.1.1 Arteries

Arteries play a crucial role in delivering oxygenated blood and nutrients to various organs. Due to the high-pressure conditions, they endure, arteries are rich in elastic tissue and possess relatively less smooth muscle. This abundance of elastin in large arteries allows these vessels to expand and contract efficiently, accommodating dynamic changes in blood flow. As arteries approach target organs, they branch into smaller vessels characterised by increased smooth muscle and reduced elastic tissue, leading to a decrease in blood flow velocity. Approximately 10% to 15% of the total blood volume resides within the arterial system, which is typified by high systemic pressure and low volume. There are two primary types of arteries: elastic and muscular arteries. Muscular arteries, such as the brachial, radial, and femoral arteries, contain a higher proportion of smooth muscle in the tunica media compared to elastic arteries. Elastic arteries, including the aorta and pulmonary arteries, are

located proximal to the heart and have a higher content of elastic tissue. This structural feature enables elastic arteries to maintain a consistent pressure gradient despite the heart's continuous pumping (Tucker et al., 2024).

1.5.1.2 Arterioles

Arterioles, primarily composed of smooth muscle, deliver blood to organs and are significantly influenced by the autonomic nervous system. These small vessels respond to the metabolic demands of tissues, adjusting their diameter accordingly. Due to their minimal elastic tissue, arterioles play a pivotal role in systemic vascular resistance. They range from 8 to 60 micrometres in diameter and further subdivide into metarterioles (Gao, 2022, Tucker et al., 2024)

1.5.1.3 Capillaries

Capillaries, the smallest and thinnest blood vessels, consist of a single endothelial cell layer, facilitating the exchange of nutrients and metabolites through diffusion (Tucker et al., 2024).

1.5.1.4 Venules

Venules are small veins that collect blood from capillaries and participate in the exchange of oxygen, nutrients, and waste products. Venules are thin-walled and susceptible to rupture under excessive volume or pressure. Blood from venules flows into larger veins, which, like arteries, consist of three layers (Gao, 2022, Tucker et al., 2024).

1.5.1.5 Veins

However, veins have lower pressure, thinner walls, and greater elasticity. This allows veins to accommodate a large volume of blood at low pressure, known as high capacitance. Approximately three-fourths of the circulating blood volume is contained within the venous system. One-way valves in veins ensure unidirectional blood flow toward the heart, aided by muscle contractions and respiratory-induced pressure changes(Gao, 2022).

1.5.2. Smooth muscle cells

In arteries, smooth muscle cells are located in the middle layer of blood vessel walls and are responsible for regulating vascular tone and remodelling. They respond to signals from platelets and endothelial cells, undergoing contraction or relaxation to modulate blood flow and maintain blood pressure. Smooth muscle cells present high elasticity, they contribute to vascular repair processes by proliferating and migrating in response to injury or growth factors released by platelets and endothelial cells (Sena et al., 2013).

1.5.3. Pericytes

Pericytes are located around the capillaries and are able to modify the capillary diameter, regulate the amount of blood flow through the microcirculation during functional hyperaemia. Pericytes are crucial components of the vascular system, playing a significant role in vessel maturation and stability. These cells are located along the endothelial cells of capillaries and small vessels, where they regulate blood flow, contribute to the blood-brain barrier, and aid in the formation and maintenance of the extracellular matrix. Pericytes communicate with endothelial cells through direct contact and paracrine signalling, influencing vascular development and remodelling. Their dysfunction is associated with various pathologies, including diabetic retinopathy and tumour angiogenesis (Alarcon-Martinez et al., 2021).

1.5.4. Platelets

Platelets are not part of the physical vasculature but intervene in supporting regeneration of blood vessels after vascular injury. Platelets are small, circulating cell fragments that become activated upon vascular injury or inflammation. They adhere on the vessel side of ECs components, such as von Willebrand factor, forming a primary haemostatic plug. Platelets also release prothrombotic factors and chemokines, which recruit other platelets and inflammatory cells to the site of injury or inflammation. Moreover, platelets interact with endothelial cells through

adhesion molecules, contributing to vascular inflammation and endothelial dysfunction (Sena et al., 2013).

1.5.5. Endothelial cells

Endothelial cells (**ECs**), also known as the endothelium, are the inner cell layer of blood and lymphatic vessels (Potente and Makinen, 2017). There are various theories about the origin of endothelial cells, but the mesoderm has been reported to generate an endothelial cell progenitor (angioblast) and a common progenitor of haematopoietic cells and endothelial cells (haemangioblast). The mesoderm is one of the three germinal layers, the others being the ectoderm and endoderm which forms in the third week of the embryonic development through a process called gastrulation (Sharma et al., 2017) (Tsuji-Tamura and Ogawa, 2018).

Endothelial specification into arterial and venous ECs is established prior to forming complete blood vessel structures and appears to occur from the microenvironment and subsequent transcriptional programming (Potente and Makinen, 2017, Tsuji-Tamura and Ogawa, 2018, Schimmel and Gordon, 2018).

Depending on the type of vessel or organ in which they reside, ECs exhibit a large amount of heterogeneity shown through their distinct molecular and functional properties. This specialisation is important as ECs are known to have numerous functions and are widely distributed across the human body (Plein et al., 2018). One example of this is the variance among the different vascular beds. In the brain, for example, ECs establish the highly selective blood brain barrier (BBB) which protects neurons from pathogens by having tighter junctions and less transcytosis than other ECs. Compare this to the EC structure and formation found in the glomeruli of the kidney, which is less selective and easier for molecules to traverse (Potente and Makinen, 2017)

To reach this specialised morphology and vessel heterogeneity there are several endothelial cell progenitors that undergo maturation until reaching the mature and

well differentiated state. Endothelial progenitor cells (EPCs) are housed in bone marrow, peripheral blood and umbilical cord blood or produced by transdifferentiation from various sources under the influence of microenvironments suitable for endothelial differentiation. The four phases of neovascularisation include differentiation, proliferation, migration and attachment of EPCs to form tubes (Chopra et al., 2018). The origin of the EPCs and their role to form the differentiated heterogenous endothelial cells is important for future therapies.

The ECs have several functions. The main function of endothelial cells, especially vascular endothelial cells, are to be a semi-selective barrier for macromolecule transport across the vessel wall. ECs respond to external stimuli by cytoskeletal rearrangements, also can be selective effects on junctional proteins (e.g. phosphorylation of VE-cadherin, without actin cytoskeletal changes) and activation or inhibition of contractile machinery, which determine the barrier enhancing or barrier disruptive EC response (Plein et al., 2018).

Normal adult ECs remain largely quiescent in health but can become rapidly activated in response to injury or pathological conditions. A consistent and reliable blood supply is required to facilitate delivery of oxygen and nutrients to tissues. The process, called angiogenesis, generates three different EC subtypes: the migratory tip cells, which guide the growing vascular sprout in respond to growth factors; stalk cells which proliferate and elongate the sprout; and quiescent phalanx cells, identified by their cobblestone-like shape, which are present in established vessels and function to regulate vascular homeostasis and endothelial barrier function. (Wong et al., 2017, Bierhansl et al., 2017).

These modifications to the ECs occur while maintaining a functional vascular barrier to prevent leakage from vessels. This highly dynamic and plastic nature of cell–cell adhesions is mediated through the junctional properties of the cells, primarily mediated by vascular endothelial cadherin (VE-cadherin)-based adherens junctions and other junctional proteins, e.g PECAM1, that connect junctions with the actin cytoskeleton. The importance of these interactions during morphogenesis was

demonstrated by early experiments where VE-cadherin was deleted in the mouse (Carmeliet et al., 1999, Gory-Faure et al., 1999), resulting in embryonic lethality due to defects in vascular patterning (Schimmel and Gordon, 2018).

Cell-cell adhesions are the more critical part of the formation, maintenance, and function of the blood vasculature. VE-cadherin, a key component of adherens junctions can be regulated by a range of factors, such as kinases, phosphatases, and hemodynamic forces, all of which guide its stability at the cell junctions (Figure 1.13) (Schimmel and Gordon, 2018)

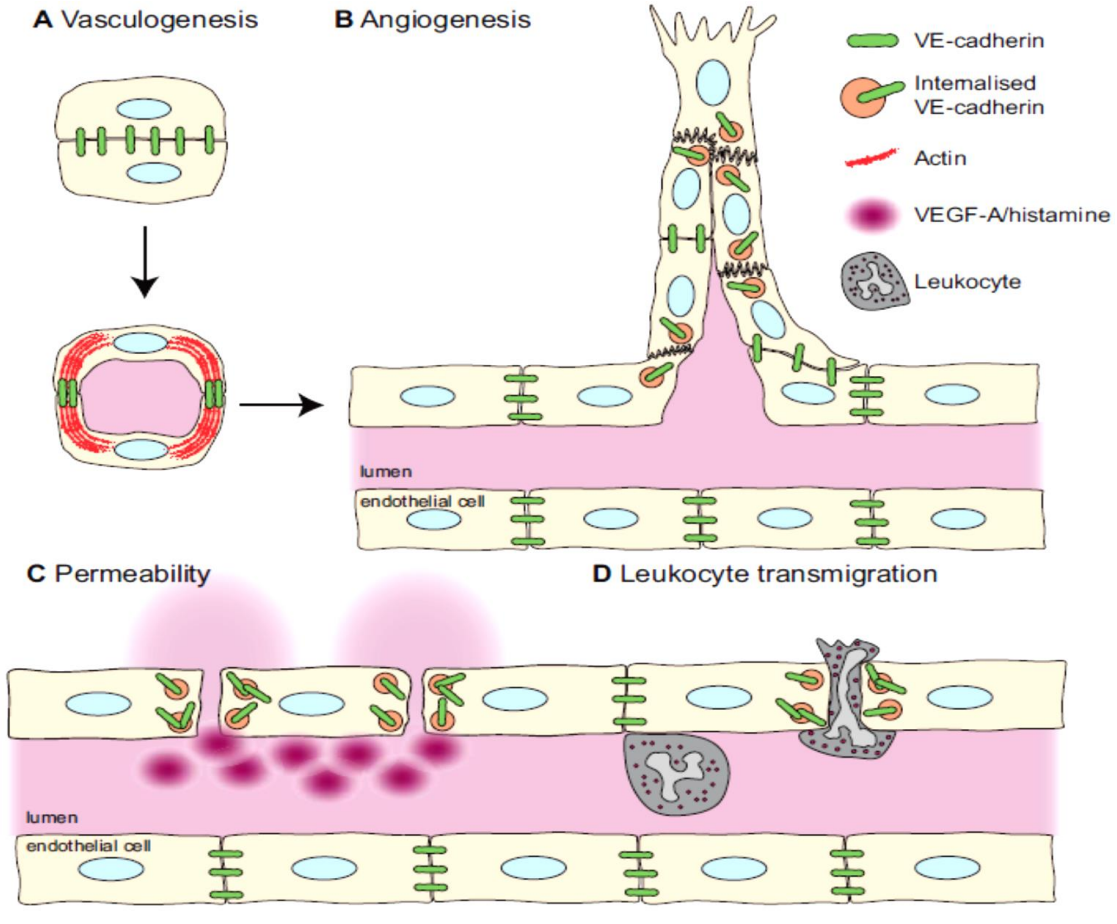

Figure 1.13 Adhesion within the cell wall. Cell adhesion plays a critical role in the development of the vascular system, regulating **(A)** vasculogenesis, **(B)** regulate angiogenesis, **(C)** Responsible for the vascular permeability and **(D)** transmigration of leukocytes across the vessel wall. From (Schimmel and Gordon, 2018).

1.5.6. Endothelial cells and disease

The disease types impacting ECs are not limited by type, due to the risk factors associated with disease can cause a secondary effect. Different diseases ranging from cancer to cardiovascular disease and obesity have all been linked to EC damage. The are several cardiovascular diseases that have origin in ECs, such as: atherosclerosis and hypercholesterolemia; ischemic disease (stroke, heart attack); aneurysm; aortic dissection and pulmonary hypertension. Ischemia-reperfusion (I/R) injury refers to tissue damage that occurs after blood supply returns to previous ischemic areas. I/R injury is often accompanied by oxidative stress due to overproduction of reactive oxygen species (ROS), which damage endothelial barrier integrity and disrupt endothelial cell-cell junctions leading to microvascular hyperpermeability (Yuan and Rigor, 2010).

Solid tumours require a reliable and large supply of oxygen to grow. Because of this, the tumour vasculature is characterised by excessive formation of neovessels, which are tortuous and have a discontinuous EC lining and basement membrane with sparse pericyte coverage, causing the vessels to be leaky. Tumour ECs express pro-angiogenic genes to a higher degree than normal ECs, have higher proliferation rates and are resistant to serum starvation-induced apoptosis. ECs use glycolysis for ATP production. It was reported recently that tumour ECs are hyperglycolytic compared with normal ECs from the same organ and divert more glycolytic intermediates into the pentose phosphate pathway serine biosynthesis pathway for the nucleotide synthesis being one of the reasons for the higher metabolic rate of cancer cells (Bierhansl et al., 2017).

1.6. Knowledge gaps, hypothesis and aims

Regulation of actomyosin-driven contraction is critical for numerous cell functions in the cardiovascular system, including smooth muscle tone, changes in permeability of endothelial cell monolayers and platelet shape change and spreading. The principal regulatory mechanism of these processes involves the phosphorylation and dephosphorylation of MLC, catalysed by MLCK and MLCP respectively (MacDonald and Walsh, 2018, Alvarez-Santos et al., 2020). Other kinases also phosphorylate MLC. ROCK and PKC both play crucial roles in the phosphorylation of myosin light chain (MLC), impacting cellular functions like migration and adhesion. ROCK directly phosphorylates MLC and inhibits myosin phosphatase activity, leading to increased MLC phosphorylation and enhanced contractility. It is a vital component of the Rho/ROCK signalling pathway, influencing various cellular activities. Similarly, PKC phosphorylates MLC in response to certain stimuli, regulating cytoskeletal dynamics and cell motility. Both this kinases directly phosphorylate MLC (Kaneko-Kawano et al., 2012). Therefore, MLC constitutes a crucial node that integrates and channels activatory and inhibitory stimuli towards myosin II function.

The relevance of antagonistic regulation of MLCP by cyclic nucleotides and ROCK is widely recognised. cAMP signalling promotes endothelial cell monolayer barrier integrity, is the most potent endogenous mechanism for the control of platelet function and is also an important mediator of smooth muscle relaxation (Wooldridge et al., 2004, Aburima et al., 2013, Aslam et al., 2010, Batori et al., 2019). Understandably, the role of MYPT1 in smooth muscle contraction has been broadly studied and is covered by more than 380 papers. In platelets, cAMP signalling inhibits morphological changes driven by a dynamic remodelling of their actin cytoskeleton by targeting the RhoA/ROCK/MLCP pathway (Aburima et al., 2013). More specifically, PKA phosphorylates RhoA and prevents its translocation and subsequent activation of ROCK (Qiao et al., 2003). A search conducted on PubMed in May 2023 using the terms "MYPT1" and "endothelial cells" yielded only 48 research articles focused on studies involving endothelial cells from humans and other mammals.

There is evidence for cAMP signalling compartmentalisation in platelets, where moesin, the first functionally validated AKAP in those cells, targets type I PKA to lipid rafts (Raslan et al., 2015). Because MYPT1 is part of a complex signalling node that includes PP1c, kinases, and other enzymes involved in signal transduction (Kiss et al., 2019), a previous study investigated whether MYPT1 could function as an AKAP (Khalil, 2018). In this PhD thesis from Dr Rivero's laboratory, immunoprecipitation, affinity cAMP pull-down and co-localisation approaches were used to confirm the interaction of MYPT1 and PKA-R subunits in platelets and to map the interaction region to a central region of MYPT1 (aa 501-706), and it showed that this region interacts directly in vitro with PKA-R subunits (Khalil, 2018). These observations can be generalised to endothelial and possibly also smooth muscle cells, leading to the hypothesis that:

MYPT1 and PKA subunits interact directly in cells of the vasculature

To address this hypothesis, this thesis covers following aims:

1. To use an *in silico* and RT-PCR approach to determine transcriptional variants of *PPP1R12A* in cells of the vasculature.
2. To verify the existence of protein complexes of MYPT1 and PKA subunits in vivo and determine their co-localisation and interaction *in situ*.
3. To determine the interaction site of PKA-R subunits on MYPT1 and determine which residues are important for the interaction.

Chapter 2. Materials and Methods

2.1. Materials

2.1.1. Laboratory materials and reagents

Common laboratory reagents were obtained from the following suppliers: Amersham, BioRad, Fluka, Invitrogen, Melford Laboratories, Merck, Promega, Roche and Roth. Consumables are shown in Table 2.1. Specialised reagents and kits are shown in Table 2.2 to Table 2.7.

Table 2.1 Consumables used in this study and their suppliers.

Name	Source
6-well plates	Nunc
T75 Flasks	Nunc
Serological pipettes: 5 ml, 10 ml, 25 ml	Sarstedt
Cell scraper 25 cm	Sarstedt
PCR reaction tubes: 0.2 ml	VWR
Filters: 0.20 µm, 0.45 µm	Millipore
Falcon tubes: 15 ml, 50 ml	Starsted
Eppendorf tubes: 0.5 ml, 1.5 ml, 2 ml	Eppendorf
Pipette tips (10, 200, 1000 µl)	Starlab, Starsted
Parafilm	Pechiney
Cryotubes 2 ml	Nunc
PVDF transfer membrane	Bio-Rad, GE Healthcare Life Sciences
Hyperfilm ECL 18x24 cm	GE Healthcare Life Sciences
Pipettes: 1-10 µl, 1-20 µl, 20-200 µl und 200-1000 µl	Gilson
Needles	BD Plastipak
Syringes	BD Plastipak
Filters 0.22 µm	Sartorius

Table 2.2 Inhibitors used in this study.

Name	Source
Phenylmethylsulfonyl fluoride (PMSF)	Sigma
Protease Inhibitor Cocktail cOmplete™, Mini, EDTA-free Protease Inhibitor Cocktail	Roche
PhosSTOP	Roche
Latrunculin B	Calbiochem
Sodium orthovanadate (Na_3VO_4)	Sigma

Table 2.3 Antibiotics.

Name	Source
Ampicilin	Sigma
Kanamycin	Melford Laboratories
Penicillin/Streptomycin	Gibco

Table 2.4 Molecular biology enzymes used in this study.

Name	Source
Q5 High fidelity DNA polymerase	New England BioLabs
Pfu DNA polymerase	New England BioLabs
OneTaq DNA polymerase	New England BioLabs
Ribonuclease A (RNAse A)	Macherey-Nagel
GoScript™ reverse transcriptase	Promega
T4 DNA ligase	Promega
Shrimp alkaline phosphatase	Roche

Table 2.5 Transfection reagent.

Name	Source
Oligofectamine™ Transfection Reagent	Invitrogen™, Thermofisher Scientific

Table 2.6 Molecular Weight Markers.

Name	Sizes	Source
EZ-Run™ Prestained Rec protein ladder	170/130/95/72/55/43/34/26/17/10 kDa	Fisher Scientific
Precision Plus protein standards (Dual Colour)	250/150/100/75/50/37/25/20/15/10 kDa	Bio-Rad
1 kb Full scale DNA Ladder	10000/8000/6000/5000/4000/3000/2000/1500/1200/ 1000/900/ 800/ 700/ 600/ 500/ 400/ 300/ 200/ 100 bp	New England Biolabs
100 bp scale DNA Ladder	1517/ 1200/ 1000/ 900/ 800/ 700/ 600/ 500/517/ 400/ 300/ 200/ 100 bp	New England Biolabs
DNA Ladder III	1500/ 1200/ 1000/ 900/ 800/ 700/ 600/ 500/ 450/ 400/ 350 / 300/ 250/ 200/ 150/ 100/ 50 bp	PCR Biosystems
DNA Ladder IV	1500/1000/900/800/700/600/500/400/300/200/100 bp	PCR Biosystems

Table 2.7 Kits

Name	Source
pGEM-T easy cloning kit	Promega
High Pure plasmid purification kit (for mini prep)	Roche
NucleoSpin gel and PCR cleanup Kit	Macherey Nagel
Pierce® BCA protein assay kit	Pierce (ThermoScientific)
ECL	BioRad
Dynabeads™ Protein A	Invitrogen (Thermofisher Scientific)
mirVana™ miRNA Isolation Kit, without phenol	Invitrogen (Thermofisher Scientific)
Duolink® *in situ* red starter kit mouse/rabbit (Merck, Dorset, UK)	Merck

2.1.2. Antibodies and fluorescent dyes used in this study

All antibodies and fluorescence dyes used in this thesis are shown in Table 2.8, Table 2.9 and Table 2.10.

Table 2.8 Primary antibodies used for immunofluorescence, immunoprecipitation and western blotting.

Antibody	Host	Concentration	Blocking		Dilution		Source
			WB	IF	WB	IF	
IgG1	Rabbit mAb	3134 µg/ml	5% Milk	10% DS	N/A	1:80	Cell Signalling (DA1E) #3900
MYPT1(*)	Rabbit mAb	83 µg/ml	5% Milk	10% DS	1:1000 in 5% BSA	1:80	Cell Signalling (D6C1) #8574
MYPT1	Mouse mAb	200 µg/ml	5% Milk	10% DS	N/A	1:40	Santa Cruz SC-514261
MYPT1	Rabbit pAb	500 µg/ml	5% Milk	N/A	1:1000 Milk	N/A	Merk Millipore 07-672-I
MYPT1	Rabbit pAb	500 µg/ml	5% Milk	N/A	1:500 in	N/A	Merk Millipore ABS1495
IgG 2b	Mouse mAb	500 µg/ml	5% Milk	10% DS	N/A	1:100	BD BioSciences 557351
PKA cat subunit	Mouse mAb	250 µg/ml	5% Milk	10% DS	1:1000 in 2%BSA	1:50	BD BioSciences 610980
PKA RI	Mouse mAb	250 µg/ml	5% Milk	10% DS	1:1000 in 2%BSA	1:50	BD BioSciences 610166
IgG 1κ	Mouse mAb	500 µg/ml	5% Milk	10% DS	N/A	1:100	BD BioSciences 555868
PKA RIIα	Mouse mAb	250 µg/ml	5% Milk	10% DS	1:1000 in 2%BSA	1:50	BD BioSciences 612243
PKA RIIß	Mouse mAb	250 µg/mL	5% Milk	10% DS	1:1000 in 2%BSA	1:50	BD BioSciences 610626
GAPDH	Mouse mAb	6.6 mg /ml	5% Milk	N/A	1:6000 in 5% Milk	N/A	Calbiochem (Finland) CB1001-500UG (6C5)
ß-Actin	Mouse mAb	2.1 mg / ml	5% Milk	N/A	1:300000 in 5% Milk	N/A	Abcam (Abs6276)
GAPDH	Mouse mAb	N/A	5% Milk	N/A	1:150000 in 5% Milk	N/A	Advanced Immunochemica 2-RGM2l
GST	Rabbit pAb	N/A	5% Milk	N/A	1:5000	N/A	Angelika A. Noegel (U. of Cologne)
Non-SMC myosin IIa	Rabbit pAb	1.0 mg / ml	N/A	10% DS	N/A	1:100	Novus Biologicals NB600-1083
6-his HRP-conjugated	Mouse mAb	1.0 mg / ml	5% Milk	N/A	1:10,000 in 5% Milk	N/A	HRP-66005, Proteintech (1B7G5)

Blocking Solution solvent WB = TBS T-0.1%; Blocking solution solvent IF = PBS T-0.1%; Diluent solvent WB = TBS T-0.1%; Diluent solvent IF = 2% Donkey serum PBS T0.1%. DS – Donkey serum; N/A – non applicable; * MYPT1 antibody used in this study.

Table 2.9 Secondary antibodies used in this study.

Antibody	Host	Concentration	Dilution		Source
			WB	IF	
HRP-conjugated	Goat anti-Mouse	N/A	1:2000 in 5% Milk	N/A	DAKO – PO447
HRP-conjugated	Goat anti-Rabbit	N/A	1:2000 in 5% Milk	N/A	DAKO – PO448
IgG Light Chain Specific HRP conjugated	Goat anti-Rabbit	N/A	1:10000 in 5% Milk	N/A	Novus Biologicals NBP2-75935
IgG Light Chain Specific HRP conjugated	Goat anti-Mouse	0.8 mg / ml	1:2000 in 5% Milk	N/A	Jackson ImmunoResearch 112-035-175
Alexa Fluor 488 (Green)	Donkey anti-Mouse	2 mg / ml	N/A	1:600 2% DS	Invitrogen A21202
Alexa Fluor 594 (Red)	Donkey anti-Rabbit	2 mg / ml	N/A	1:600 2% DS	Invitrogen A21207

Diluent solvent WB = TBS T-0.1%; Diluent solvent IF = 2% Donkey serum PBS T0.1%. DS – Donkey serum;

Table 2.10 Fluorescent dyes.

Name	Source
VECTASHIELD® Antifade Mounting Medium with DAPI	2bscientific
Phalloidin - TRITC	Sigma P19851
Phalloidin - FITC	Sigma P5282
Alexa Fluor™ 647 Phalloidin	Invitrogen - Thermofisher Scientific (A22287)

TRITC - Tetramethylrhodamine B isothiocyanate**; FITC -** Fluorescein Isothiocyanate

2.1.3. Oligonucleotides

Oligonucleotides used in this study are shown in tables 2.11 to 2.14. All primers were custom made by Eurofins Genomics (Cologne, Germany)

Table 2.11 Oligonucleotides for cloning purposes. Built-in restriction enzyme sites are underlined, start, or stop codons are bold. Bases are grouped by codons according to the reading frame in both forward and reverse primers. In black, the sequence that anneals with MYPT1; in blue, added sequences for cloning.

PCR amplicon	Forward primer (5' to 3')	Reverse primer (5' to 3')
HsMYPT1-C2 Extended	aattcCATATGtatgttgcacctacaatacc	gccgCTCGACagtggttgaacttgaagttg

Table 2.12 Oligonucleotides for sequencing.

Vector	Forward primer
pGEX	GGGCTGGCAAGCCACGTTTGGTG
pQE	CCCGAAAAGTGCCACCTG

Table 2.13 Oligonucleotide pairs used for control RT-PCR reactions. Primer pairs are given as forward (top)-reverse (bottom). In the amplicon size column (g) indicates that the primers were tested using genomic DNA as template; (p) indicates that the primers were tested using a plasmid containing the *PPP1R12A* variant encoding the FL MYPT1 variant as a template. The position of the primer pairs and their respective amplicons are shown in Fig. 3.9A. Primers in blue characters were used exclusively for testing the other member of the pair and not further used in RT-PCR reactions. E19 and E26' were used in combination to test each other and subsequently in separate RT-PCR reactions. Annealing temperature and number of cycles for the PCR reactions are indicated. Where the PCR buffer departed from the standard this is also indicated.

Primer pair	Sequence (5'-3')	Amplicon size (bp)	PCR conditions
$E1^{-}$–E1	ATCTGCCCTGTAGAGCCTTG TTCACCTGGTCTTCTGGCGC	632 (g)	55.4°C, 42x, GC-enriched buffer + DMSO
E1–E1	GGATACTGGAAGTCTCGAGCG TTCACCTGGTCTTCTGGCGC	265 (g)	55.4°C, 42x, GC-enriched buffer + DMSO
$E1^{+}$–I1	AGGGGCTAAGAGAAACACTGA CACAAACAGACAATGCACACA	158 (g)	58°C, 42x
E1'–E2	ATGAAATGGCGGACGCG GGTATCCAGCCTTCATTATCAGG	326 (p)	60°C, 35x
E4–E8	CGGCATGCAAAATCTGGAGG TCCTTCTTCTTCTTCATCAACC	465 (p)	52°C, 35x
E4'–E8	TACAGCACTTCACGTTGC TCCTTCTTCTTCTTCATCAACC	445 (p)	61°C, 35x
E8–E10	AGACGTTGATTATTGAACCAGAG GGGACTTGAAGCTGAACGTG	461 (p)	58°C, 35x
I9–$E9^{+}$	TGTTTGGTGGGGAAATCAGTAAA CCTTACTGGGCACAAGAACAATG	523 (g)	58°C, 42x
E11-E14	TGCACCTACAATACCAAGACGA CAGGAATGGTCACTGCCGTA	410 (p)	56ºC, 35X
E12–E16	AGGAGAAAATGGGAAGATGATC CTCATCATACGTTCTGGAGTAC	705 (p)	56°C, 35x
E21–E26	AGAAAACCTTACAGCAGCAGG TCAAGGCCCCATTTTCATCC	316 (p)	56°C, 35x
E19–E26'	CAGACACAGAAGAGGGATCCA ATAACTCTGATCAAGGCCCC	463 (p)	56°C, 35x
MYPT1 FL-E1	**ATG**AAATGGCGGACGCG TTCACCTTGGTCTTCTGGCG	109 (p)	60ºC, 35X
MYPT1 FL-E2	**ATG**AAATGGCGGACGCG GGTATCCAGCCTTCATTATCAGG	325 (p)	60ºC, 35X

Table 2.14 Oligonucleotide pairs used for RT-PCR reactions. Primer pairs are given as forward (top)-reverse (bottom). The position of the primer pairs and expected amplicons for each variant are shownin Figure 3.10, Figure **3.12**,Figure **3.13**,Figure **3.14**. In primers spanning exon boundaries the side of the upstream exon is underlined. Annealing temperature and number of cycles for the PCR reactions are indicated.

Primer pair	Sequence (5'-3')	Variants (amplicon sizes in bp)	PCR conditions
E1$^-$–E2	ATCTGCCCTGTAGAGCCTTG TTCACTTGGTCTTCTGGCGC	E1$^-$ in (447) E1$^-$ out (0)	55°C, 35x
E1–E2	GGATACTGGAAGTCTCGAGCG TTCACTTGGTCTTCTGGCGC	E1 in (481) E1 out (0)	56°C, 35x
E1$^+$–E2	AGGGGCTAAGAGAAACACTGA GGTATCCAGCCTTCATTATCAGG	E1$^+$ in (159) E1$^+$ out (0)	55°C, 35x
E4–E8	CGGCATGCAAAATCTGGAGG TCCTTCTTCTTCTTCATCAACC	E6 in (465) E6 out (389)	52°C, 35x
E8–E10	AGACGTTGATTATTGAACCAGAG GGGACTTGAAGCTGAACGTG	E9$^+$ in (578) E9$^+$ out (461)	58°C, 35x
E8–E9$^+$	AGACGTTGATTATTGAACCAGAG CCTTACTGGGCACAAGAACAATG	E9$^+$ in (381) E9$^+$ out (0)	58°C, 42x
E11-E14	TGCACCTACAATACCAAGACGA CAGGAATGGTCACTGCCGTA	E13 in - E14 in (410) E13b in - E14 in (374) E13a out - E14 in (278) E13 out - E14 in (242)	54ºC, 35X
E12–E16	AGGAGAAAATGGGAAGATGATC CTCATCATACGTTCTGGAGTAC	E13 in–E14 in (705) E13b in–E14 in (669) E13 out–E14 in (537) E13 in–E14 out (528) E13 out–E14 out (360)	54°C, 35x
E21–E26	AGAAAACCTTACAGCAGCAGG TCAAGGCCCCATTTTCATCC	E22 in–E24 in (347) E22 in–E24b in (329) E22 in–E24 out (316) E22 out–E24 out (211)	58°C, 35x
E4'–E5.7	TACAGCACTTCACGTTGC CCGTTTTTCACTATGGAGCACT	E6 in (0) E6 out (211)	61°C, 42x
E11–E12.13b	TGCACCTACAATACCAAGACGA GCTTGGAACACTAGAACTTTTATG	E13 in (0) E13b in (181)	53°C, 42x
E19–E21.23	CAGACACAGAAGAGGGATCCA CAGCAAATCTTTCTTGTCTCTTT	E22 in (0) E22 out (210)	55°C, 42x
E23.24–E26'	GAAAAAAGGGTGACCGGCAAG ATAACTCTGATCAAGGCCCC	E24 in (159) E24b in (141)	56°C, 42x

2.1.4. Plasmids

Plasmids in this study are shown in table 2.15.

Table 2.15 Plasmids used in this study. The cloned fragments and corresponding amino acid position as well as the vector backbone are given in the table. All tags are placed atthe N-terminus of the protein of interest.

Insert	Amino acids	Tag	Backbone	Source
HsPKARIß	1-381	GST	pGEX-3X	Pharmacia (GEHealthcare, Munich, Germany)
HsPKARIIß	1-418	GST	pGEX-3X	
HsPKARIß	1-381	His	pQE32	Qiagen (Hilden,Germany)
HsPKARIIß	1-418	His	pQE32	
MYPT1 C2 Ext	497-780	His	pET40b(+)	Novagen EMD Millipore (Hertfordshire, United Kingdom)

2.1.5. Human cells and bacterial strains

Human cells and bacterial strains used in this study are shown in table 2.16.

Table 2.16 Mammalian cells and cell lines and bacterial strains used in this study.

	Name	Origin	Description
Mammalian cell	HUVECs (C-12208, lot 447Z015; Promocell, Heidelberg, Germany)	*Homo sapiens*	Human umbilical vein endothelial cells
	HSV-SMC	*Homo sapiens*	Human saphenous vein smooth muscle cells
	Platelets	*Homo sapiens*	Human platelets
Bacterial Strains	XL1-Blue	*Escherichia coli*	For routine cloning
	BL21	*Escherichia coli*	For general protein expression
	Rosetta-gami	*Escherichia coli*	Enhanced expression of eukaryotic proteins

2.1.6. Laboratory equipment used in this study.

Equipment	Source
Autoclave	Prestige Medical
Thermocycler	Techne Prime
Thermocycler	Bio Rad
Thermocycler	Applied Biosystems
Laminar Flow Class II Hood	Esco
ChemiDoc	Bio Rad
Sonicator	Hilscher
Tecan Plate Reader	Tecan Infinite M200
Shaking incubator	Stuart SI500
Shaking incubator	Innova 40
Zeiss LSM confocal microscope	Zeiss
Nanodrop	Thermofisher Scientific
Ultracentrifuge	Sorvall RC-5B
VersaDoc 1000 imaging Versa	Bio Rad
French Press	Custom made

2.1.7. Sterilisation

Glassware, buffers, agar, and media were sterilised by autoclaving at 120ºC, 15psi. If sterilisation was not possible, 0.22 µm or 0.45 µm filter units were used. Open media were always filtered before use with 0.22 µm filter units.

2.2. *In silico* analyses

2.2.1. Sequence databases

Data for *in silico* analyses of *PPP1R12A* transcripts was obtained from GenBank® (https://www.ncbi.nlm.nih.gov/genbank/), Ensembl (https://www.ensembl.org/index.html), the Genotype-Tissue Expression (GTEx) project portal (https://www.gtexportal.org/home/), and the AceView portal (https://www.ncbi.nlm.nih.gov/IEB/Research/Acembly/index.html). AceView collates all public mRNA sequences: mRNAs from GenBank or RefSeq, single pass cDNA sequences from dbEST and Trace and deep transcriptomics sequences from the Sequence Read Archive (SRA) and Gene Expression Omnibus (GEO) (Thierry-Mieg and Thierry-Mieg, 2006). It was last updated in October 2012. GTEx is a resource to study tissue specific gene expression and regulation from samples collected from 54 non-diseased tissue sites across nearly 1000 individuals (Consortium, 2013). Data from the release V8 of August 2019 was used.

RNAseq data from GenBank was collected from the RNAseq intron features window of the *PPP1R12A* gene page (update 8 April 2022). Because the data from AceView, GTEx and GenBank do not overlap, they were combined to calculate the frequency of alternative splicing of exons of interest.

2.2.2. Transcription factor binding site identification

PROMO (http://alggen.lsi.upc.es/cgi-bin/promo_v3/promo/promoinit.cgi?dirDB=TF_8.3) was used for transcription factor binding site identification using version 8.3 of TRANSFAC (Messeguer et al., 2002).

2.2.3. Sequence database searches

The non-redundant, EST database was interrogated with Blastn searches (https://blast.ncbi.nlm.nih.gov/Blast.cgi) with the query sequences indicated in the

corresponding figure or table legend using default parameters unless indicated otherwise.

2.2.4. Generation of multiple alignments

Multiple alignments were generated using the Clustal Omega program at Uniprot (https://www.uniprot.org/help/sequence-alignments).

2.2.5. Calculation of the frequency of splicing variants

The frequency of exon usage or skipping and the frequency of splicing variants were calculated as reported by (Qin and Zhang, 2017) with some modifications as described here.

To account for the fact that in many cases the RNAseq reads are not distributed uniformly along the *PPP1R12A* cDNA, calculations were made relative to the regions where splicing events take place. Consider the following example where exon E_c can be alternatively spliced.

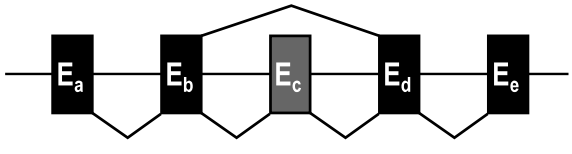

For each region, first the average number of reads spanning constitutive exon junctions was calculated using the following formula:

$$N = [E_aE_b + (E_bE_c + E_bE_d) + (E_cE_d + E_bE_d) + E_dE_e] / 4$$

where E_aE_b is the number of reads spanning exons E_a and E_b, and so on. Variations of the above formula were used for alternative splicing donor or acceptor sites and in

regions involving splicing of more than one exon. The frequency (expressed as percentage) of skipping or splicing in of E_c is calculated as:

$$\%\text{Splicing out} = 100 * E_bE_d / N$$

$$\%\text{Splicing in} = 100 * [(E_bE_c + E_cE_d) / 2] / N$$

To calculate the frequency (expressed as percentage) of each variant we assumed only one exon is alternatively spliced in every variant, as there is no evidence of *PPP1R12A* variants resulting from simultaneous splicing of two or more exons other than E13+E14. The frequency of LZ^- variants was taken as the frequency of splicing in of E24 (LZ^-a) and E24b (LZ^-b). The frequency of all other (LZ^+) variants was calculated relative to (100 - LZ^-a - LZ^-b). For example, the frequency of the ΔE14 variant was calculated as:

$$\%\Delta E14 = \%\text{Splicing out E14} * (100-LZ^-a-LZ^-b) / 100$$

Finally, the frequency of the FL variant was calculated as 100 minus the sum of frequencies of all other variants.

2.3. Molecular biology methods

The molecular biology techniques used to manipulate DNA and RNA applied in this study are described below.

2.3.1. DNA extraction

HUVECs were lysed with TRIzol® Reagent following the manufacturer's instructions. The lysate was mixed with chloroform and centrifuged at 12,000x*g* for 15 minutes at 4ºC. The aqueous phase was discarded, and the DNA was precipitated with 100% ethanol by centrifugation at 2000x*g* for 5 min at 4ºC. The DNA pellet was resuspended in sodium citrate/ethanol solution (0.1M sodium citrate in 10% (*v*/*v*) ethanol, pH=8.5) and centrifuged again for 30 min at 4ºC. The washing step was repeated, and the pellet was resuspended in 75% ethanol (*v*/*v*) for 10-20 min. The DNA was centrifuged again at 2000x*g* for 5 min at 4ºC and the pellet was air dried. The DNA was redissolved in pre-warmed (70ºC) TE Buffer (10mM Tris, 1mM EDTA pH = 8.0). The concentration and quality of DNA samples were assessed with a NanoDrop 1000 spectrophotometer.

2.3.2. RNA extraction

Total RNA was acquired using Invitrogen™ mirVana™ miRNA Isolation Kit, with phenol. The cells were washed with PBS and lysed directly with 600 µL of lysis solution. Cells were scraped and recovered to a 1.5 mL tube. The protocol was continued according to the manufacturer's instructions. The concentration and quality of the RNA samples were assessed with a NanoDrop 1000 spectrophotometer.

2.3.3. Determination of DNA and RNA concentration

For quantification of DNA and RNA concentration, spectrophotometry was employed using a Thermofisher Nanodrop 1000 instrument at a wavelength of λ = 260 nm. The purity of the DNA sample was evaluated by analysing the absorbance ratio at 260 nm and 280 nm. A ratio approaching 1.8 indicates the presence of pure DNA, while a significantly lower ratio suggests contamination with proteins or other substances that exhibit strong absorbance around 280 nm (Lucena-Aguilar et al., 2016). RNA, DNA and siRNAs were measured using their specific ratio; DNA-50 and RNA-40.

2.3.4. DNA agarose gel electrophoresis

Agarose gel electrophoresis is used to resolve and purify DNA fragments after rt-PCR or restriction endonuclease digestions. Gels were prepared by boiling 1 - 2% (*w/v*) agarose in TAE buffer. Once the gel was cooled ethidium bromide was added (final concentration 5 µg/l). The gel was poured in a casting chamber containing the appropriate size of combs. After agarose reached room temperature the gel was submerged in a horizontal electrophoresis tank containing TAE buffer. The reactions were mixed with loading buffer (30% glycerol, 0.1% bromophenol blue) and 40% of the reaction was separated by gel electrophoresis on agarose gels stained with ethidium bromide. The sizes of amplicons obtained from the reactions were assessed using gel electrophoresis and a suitable gel ladder. Gels were run until the bromophenol blue dye present in the DNA-loading buffer had migrated the appropriate distance through the gel. The gels were imaged on a Bio-Rad VersaDoc 1000 imaging system.

DNA loading buffer
30% (v/v) Glycerol
0.25% (w/v) Bromophenol blue
Add H_2O up to 10 mL

TAE buffer, pH 8.5
40 mM Tris acetate
mM EDTA (pH 8.0)

2.3.5. Recovery and purification of PCR amplified products from agarose gels

To clean the PCR product, from the agarose gel, after electrophoresis a commercial NucleoSpin™ Extraction Kit was used. A UV transilluminator was used to visualise the desired DNA fragment. The fragment was cut out from the agarose gel with a clean scalpel. The excised piece of gel was transferred to a 1.5ml tube containing buffer (200 µl NT1 buffer/100 mg of gel) and was heated for 10 minutes at 50ºC. Eppendorf tubes were vortexed several times to ensure the gel to be completely dissolved. The melted gel with buffer was loaded into a PCR clean-up column with 1.5 ml collection tube before spinning at 11,000x*g* for 30 seconds. The flow-through was discarded

and the DNA bound column was washed three times with NT3 buffer. Prior to elution the column was dried at 70ºC for 2 minutes. The quality and the eluted DNA concentration were tested by NanoDrop 1000 spectrophotometer (see 2.3.3) and by running 1-2 µl of the aliquot on an agarose gel.

2.3.6. cDNA synthesis for reverse transcriptase polymerase chain reaction (rt-PCR)

The total RNA (1 µg) was used for cDNA synthesis using a GoScript™ Reverse Transcriptase kit from Promega, following the manufacturer's instructions. It is shown in the Table 2.17, the PCR mix per each reaction. Table 2.18. shows the PCR conditions used for RT-PCR while Table 2.19 and Table 2.20 show the PCR mix and PCR conditions that were used for the Q5 High Fidelity Polymerase (cloning purposes).

Table 2.17 PCR mix per reaction.

Reagent	Amount per reaction
5X One Taq® Standard Reaction Buffer	5 µl
10 mM deoxynucleotide triphosphates (dNTPs)	0.5 µl
5 pmol/µl forward primer	0.5 µl
5 pmol/µl reverse primer	0.5 µl
One Taq® Polymerase	0.125 µl
Purified water	17.375 µl
cDNA template	1 µl

Inactivation of reverse transcriptase was performed before proceeding with PCR, heating in a heat block at 70ºC for 15 minutes. cDNA samples were stored at -20ºC before use. Negative control reactions used no template or a mock reverse transcriptase reaction as a template.
Both reactions were performed to create a final volume of 20 µL.

Table 2.18 RT-PCR conditions.

Step	Temperature	Time
Initial Denaturation	95ºC	2 minutes
Cycles 25-42 Cycles	95ºC	30 seconds
	45-68ºC	30 seconds
	68ºC	1 minute /kb
Final Extension	68ºC	5 minutes
Hold	4ºC	∞

For cloning purposes specific Taq Polymerase was used. Mix and PCR conditions were composed by:

Table 2.19 PCR mix and conditions for using Q5 Polymerase.

Reagent	Volume per reaction
5x Q5® Reaction Buffer	10 µl
10 mM deoxynucleotide triphosphates (dNTPs)	1 µl
5 pmol/µl forward primer	5 µl
5 pmol/µl reverse primer	5 µl
Q5® High-Fidelity DNA polymerase	0.5 µl
Nuclease-Free water	to 50 µl
Template	1 µl

Table 2.20 Thermocycler Program.

Step	Temperature	Time
Initial Denaturation	98ºC	30 seconds
Cycles 25-42 Cycles	98ºC	10 seconds
	50-72ºC	30 seconds
	72ºC	30 seconds/ kb
Final Extension	72ºC	2 minutes
Hold	4ºC	∞

2.3.7. DNA sequencing

Newly generated plasmids and most of the PCR amplified products were verified by sequencing with specific primers. DNA sequencing was performed by Eurofins Genomics.

2.3.8. Dephosphorylation of plasmid DNA 5´- ends

Linearised plasmid DNA was dephosphorylated to prevent self-ligation and facilitate ligation of the insert. 1U of shrimp alkaline phosphatase (SAP), 10x SAP buffer and ultrapure water were added to the linearised plasmid to the final reaction volume of 10 µl. The reaction was mixed gently and incubated for 10 min at 37ºC. The reaction was stopped by heat inactivating the enzyme at 65ºC for 15 min.

10x SAP buffer
0.5 M Tris-HCl, pH 8.5
10 mM $MgCl_2$

2.3.9. Ligation of vector and insert

After the dephosphorylation of the plasmid DNA the purified DNA fragments were added. T4 DNA ligase, T4 DNA ligase buffer and ATP were added to the mix. The ligation reaction was gently mixed, left for 30 minutes at room temperature or for sticky ends overnight at room temperature. This reaction was stopped by heat inactivation of the enzyme by heating at 65ºC for 10 minutes. Chill on ice for 5 minutes and transform the reaction with the addition of 200 µL of competent cells.

Ligation Reaction	
Linearised plasmid DNA (vector)	1 µl
Purified DNA fragment (insert)	14 µl
T4 DNA ligase	2 µl
10x T4 DNA ligase buffer	2 µl
ATP (100 mM)	1 µl
Ultrapure H_2O	Up to 20 µl

10x Ligase buffer
660 mM Tris-HCl, pH 7.5
50 mM MgCl2
50 mM DTT
10 mM ATP

2.3.10. Preparation of medium for *E. coli* culture

The LB (Luria Bertani) medium is a nutritional medium for bacterial growth and was prepared with deionised water, then autoclaved at 120ºC. When the medium is cooled down (<55ºC), ampicillin (0.1 mg/ml) or kanamycin (0.05 mg/mL) are added (Sambrook et al., 1989).

For LB agar plates, 1.5% of agar was added to the LB medium and then autoclaved at 120ºC. The medium was cooled down to approximately 55ºC, antibiotic was added (specific to the resistant gene that the vector expresses) and the medium was poured in Petri dishes.

LB medium (pH 7.0 at 37˚C) (Sambrook et al., 1989)
1% (w/v) Bacto-Tryptone
0.5 % (w/v) Yeast Extract
0.5 % (w/v) NaCl
Add dH_2O to make 1 litre

LB agar plates (pH 7.0 at 37˚C)
1 % (w/v) Bacto-tryptone
0.5 % (w/v) Yeast extract
0.5 % (w/v) NaCl
1.5 % (w/v) Agar-agar
Add dH_20 to make 1 litre

2.3.11. Transformation of *E. coli*

XL-1 blue competent cells (100 µl) were thawed on ice for 30 minutes. DNA from the ligation method (2.3.9) was added to the cell suspension, mixed gently and left incubating on ice for 1 hour. A 42ºC heat shot was applied to the cells with ligation for 1-2 minutes. Immediately after the heat shock cells with DNA was placed on ice for 2 minutes. Subsequently 1 ml of pre-warmed at 37ºC of SOC (Super Optimal broth with Catabolite repression) medium was added to the mixture and incubated for 1 hour at 37ºC with shaking at 200 rpm before harvest by centrifugation at 10000x*g* for 1 minute. The majority of the supernatant was discarded, and pellet was resuspended in 50 µl of remaining medium. This new suspension was then transferred to a LB-agar plate, previously pre-coated with 20 µl of each IPTG (Isopropyl ß-D-1-

thiogalactopyranoside) (1 M) and X-Gal (20 mg/ml stock in DMF) The plate was left incubating at 37ºC overnight.

SOC medium (pH 7 at 37˚C) (Autoclaved at 121˚C and filtered through 0.2 µm filter unit) (Sambrook et al., 1989)
2 % (w/v) Bacto-trypton
0.5 % (w/v) Yeast Extract
10 mM NaCl
2.5 mM KCl
20 mM Mg^{2+} (1:1 $MgCl_2 \cdot 6H_2O$ and $MgSO_4 \cdot 7H_2O$)
20 mM glucose

2.3.1. Plasmid Isolation

To obtain high-quality plasmid DNA for sequencing, PCR, and transformation, a commercially available High Pure Plasmid Isolation Kit was utilised. A flask containing 5 ml of LB medium supplemented with antibiotic was inoculated with the bacterial suspension or a glycerol stock of interest and incubated overnight at 37˚C and 200 rpm. The following day, the overnight culture was centrifuged at 6000x*g* for 2 minutes at 4˚C, resulting in the formation of a bacterial pellet. The pellet was then resuspended in 250 µl of suspension buffer containing RNase. Subsequently, 250 µl of lysis buffer were added, and the mixture was incubated at room temperature for 5 minutes. To neutralise the lysate, 350 µl of ice-cold binding buffer was added and allowed to sit on ice for 5 minutes, after which the mix was centrifuged at >15,000x*g* for 10 minutes at 4˚C. The supernatant, containing the plasmid DNA, was passed through a filter column containing a silica matrix, washed with buffer I and buffer II containing ethanol, and finally eluted with 50 µl of elution buffer.

Suspension buffer, pH 8.0
50 mM Tris-HCl,
10 mM EDTA
100 µg/ml RNase A

Lysis buffer
0.2 M NaOH
1%SDS

Binding buffer, pH 4.2
4 M guanidine hydrochloride
0.5 M potassium acetate

Wash buffer I, pH 6.6
5M guanidine hydrochloride
20mM Tris-HCl
20ml absolute ethanol

Wash buffer II, pH 7.5
5M guanidine hydrochloride
2mM Tris-HCl
20mM NaCl
Add 40ml absolute ethanol

Elution buffer, pH 8.5
10mM Tris-HCl

2.3.2. Colony PCR

After transformation, colony PCR was implemented on bacterial colonies to rapidly determine the incorporation of insert DNA within the plasmid. 50 µl of LB medium with the appropriate antibiotic was added to each labelled microcentrifuge tube. Single colonies were picked up with a micropipette tip and transferred to the pre-prepared tubes. The tubes were incubated for 1 hour at 37°C. Following this, a PCR reaction of each colony was prepared as described in the following Table 2.21.

Table 2.21 Colony PCR (implemented on bacterial colonies).

Colony PCR Mix	
10x PCR buffer	2.5 µl
25 mM $MgCl_2$	1 µl
10 mM dNTPs	0.5 µl
Forward primer 5 mM (5 pmol/µl)	0.5 µl
Reverse primer 5 mM (5 pmol/µl)	0.5 µl
Taq polymerase 5U/µl	0.5 µl
Purified H_2O	18.5 µl
Template (bacterial culture)	1 µl

The tubes were transferred to a thermocycler and the reaction was conducted using following parameters:

Colony PCR programme	
95°C - 2 min	1 cycle
95°C - 15 sec	30 cycles
55°C - 15 sec	
72°C - 1 min /kb	
72°C - 5 min	1 cycle
4 °C	hold

Each 10 µL of PCR reaction was mixed with 2 µL of loading buffer and loaded on an agarose gel. Subsequently, the gel was examined using a UV transilluminator, and the colonies displaying positive results were expanded through inoculation into a substantial quantity of LB medium supplemented with the suitable antibiotic. This was done to facilitate additional analysis or subsequent applications.

2.3.3. Preparation of glycerol stocks

An overnight culture was mixed with 87 % glycerol on a proportion (34:6) and frozen in a 1.5 ml tube clearly labelled with date, stock number, plasmid name and number before stored at -80ºC. To recover bacteria from glycerol stock a micropipette tip was scratched on the surface of the frozen mixture and inoculated on a flask with LB medium containing appropriate antibiotics.

2.4. Protein biochemistry

2.4.1. Expression and purification of recombinant GST-tagged proteins

A starter of LB medium containing ampicillin (0.1 mg/ml) was inoculated with an *E. coli* XL-1 blue strain carrying a pGEX plasmid for expression of the GST fusion protein of interest. The medium was grown overnight at 37ºC at 200 rpm. Starter culture was added to fresh LB medium containing ampicillin to an OD_{600} = 0.1. and was allowed to grow at 37ºC to reach an optical density of OD_{600} = 0.7. This culture was induced with IPTG (0.5 mM) and incubated for 12-16 hours at 20ºC. After the induction the cells were centrifuged at 6000x*g* for 30 minutes at 4ºC. The supernatant was discarded, and the pellet was lysed immediately or frozen at -80ºC. Cells were resuspended in lysis buffer and lysed using lysis and either an ice-cold French press or a sonicator. For the French press, 2 to 4 repeats were made to ensure efficient bacterial lysis. To ensure efficient lysis cycles of sonicator, 3 cycles of 1 minute at 0.5 amplitude and followed by 3 cycles of 30 second at 0.8 amplitude were used. The lysate was centrifuged at 17,000x*g* for 30 minutes at 4ºC to separate insoluble from soluble proteins. Pellet and supernatant were kept for monitoring of the process. The supernatant was incubated with pre-equilibrated glutathione-Sepharose bead slurry for 1 hour at 4ºC on a rotating wheel at 10 rpm, to purify the GST fusion proteins. After 1 hour the beads with the bound proteins were washed 4 times with lysis buffer. The proteins were eluted using elution buffer containing reduced glutathione. The elution step was repeated several times, and the eluates were inserted into dialysis tubing and dialysed overnight to ensure removal of reduced glutathione. Samples kept for monitoring the purification process were supplemented with 2x Laemmli Buffer and boiled for 5 minutes at 95ºC.

Lysis buffer (and washing buffer)
20 mM Tris-HCl (pH variable, depending on the recombinant protein)
300 mM NaCl
0.5% Triton X-100
10 mM DTT (add fresh)
1 mM PMSF (add fresh)
PIC (added fresh)

Elution buffer
50 mM Tris-HCl, pH variable
100 mM NaCl
10 mM reduced glutathione

Dialysis Buffer (Enough for 2x)
20mM Tris-HCl (pH variable)
100m NaCl

2.4.2. Expression and purification of recombinant His tagged proteins

Inoculation, induction, and lysis were performed essentially as described in 2.4.1. The bacterial pellet was reconstituted with lysis buffer containing 10 mM imidazole (to minimise nonspecific binding) and left to incubate on ice for a duration of 30 minutes. Subsequently, the cell suspension was subjected to lysis using a sonicator, and the resulting lysate was centrifuged to separate the insoluble fraction. The supernatant was mixed with a 50% pre-equilibrated Ni-NTA bead slurry and incubated for 1 hour at 4ºC on a rotating wheel at 10 rpm, to purify the his-tagged fusion protein. The beads were subsequently washed three times using wash buffer, and the proteins that had bound to the beads were eluted using elution buffer. The elution step was repeated several times, and the eluates were inserted into dialysis tubing and dialysed overnight to ensure removal of imidazole. Samples kept for monitoring the purification process were supplemented with 2x Laemmli Buffer and boiled for 5 minutes at 95ºC.

Lysis buffer, pH 8.0
50 mM NaH_2PO_4
300 mM NaCl
10 mM imidazole

Wash buffer, pH 8.0
50 mM NaH_2PO_4
300 mM NaCl
20 mM imidazole

Elution buffer, pH 8.0
50 mM NaH_2PO_4
300 mM NaCl
250 mM imidazole

2.4.3. Determination of protein concentration

The protein concentration was determined utilising a detergent-compatible Pierce BCA protein assay kit, which is based on the Lowry method (Lowry et al., 1951). This colorimetric assay involves two distinct steps. In the first step, known as the Biuret reaction, proteins reduce cupric ions (Cu^{+2}) to cuprous ions (Cu^{+1}) in an alkaline environment, resulting in the formation of a light blue complex. Subsequently, in the second step, bicinchoninic acid (BCA) reacts with the cuprous ions, producing an intense purple colour that is soluble in water and exhibits maximum light absorbance at 562 nm. The change in light absorption can be detected using spectrophotometry.

Various concentrations (100, 200, 400, 600, 800, 1000, 1200, 1400, 1500 µg/µl) of bovine serum albumin (BSA) were prepared in lysis buffer to serve as protein standards. Simultaneously, an aliquot of the sample suspension was diluted in the same lysis buffer. For quantification purposes, the samples were diluted at ratios of 1:2, 1:5, and 1:10. 10 µl of each protein standard and lysate were added in triplicate to the corresponding wells of a 96-well Nunc microplate. Subsequently, 200 µl of the BCA reagent mix was added to each well, followed by thorough mixing on a plate shaker for 30 seconds. The microplate was then incubated at 37°C for 30 minutes.

The plate was then cooled to room temperature and light absorbance was measured at 562 nm using a Tecan plate reader. A standard curve was plotted by using absorption values from the protein standards and protein concentrations were calculated from the curve.

2.4.4. Immunoprecipitation

Immunoprecipitation (IP) is a widely accepted technique to investigate protein-protein interactions and it is widely used in cell biology (van Andel et al., 2022). IP uses a specific antibody that binds to the protein on interest. This antibody is separated, along with the attached immune complexes, by using protein A or G coupled to magnetic beads (Figure 2.1).

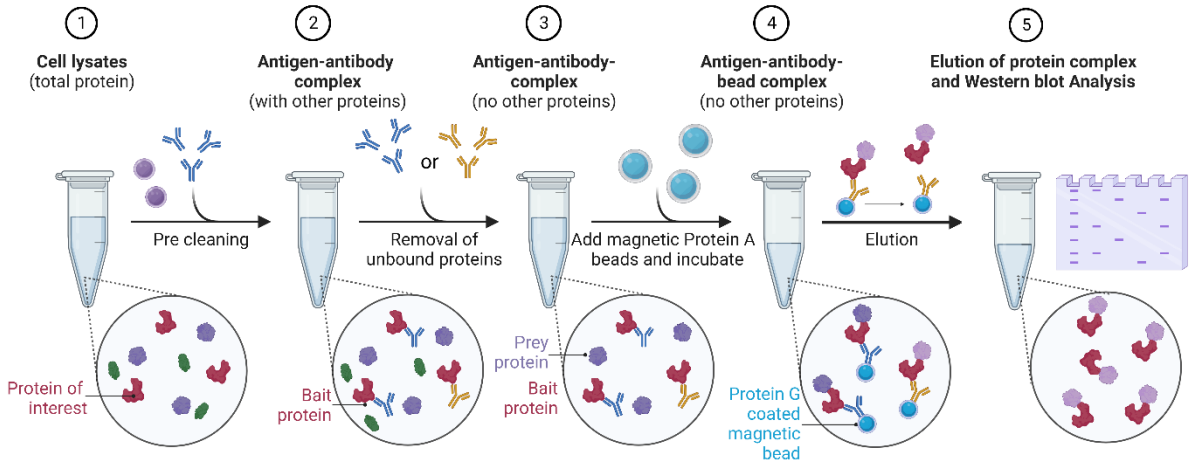

Figure 2.1 Immunoprecipitation workflow. The schematic of immunoprecipitation used in this work to evaluate. IgG was used as isotype matching control antibody.**1**, collection of protein lysate. Before reach the complex with antibodies dynabeads with IgG are added to pre-clean the lysate with 2 µg of immunoglobulin G (IgG). After pre-cleaning split sample for each tube; **2**, add MYPT1 and/or IgG antibody; **3**, add dynabeads to capture the immunocomplex; **4**, dynabeads-antibody-protein (dynabeads coated with protein A binding MYPT1 or IgG antibodies; **5**, elution of proteins bound to the dynabeads and electrophoresed on SDS-PAGE. (Created with Biorender.com)

T75 flasks with HUVECs cells grown to a 90-95% confluence and human washed platelets (1x109/ml) were lysed with ice cold immunoprecipitation lysis buffer (10 mM Tris-HCl pH 7.4, 150 mM NaCl, 5 mM EDTA, 10% glycerol, 1% NP-40) containing protease and phosphatase inhibitors (cOmplete™ and PhosTOP™, Roche/Merck, Dorset, UK), 1 mM sodium orthovanadate and 1 mM phenylmethylsulphonyl fluoride and incubated for 30 min on ice.

Cell lysates were centrifuged at 13,000x*g* for 15min. The supernatant was transferred to a fresh sterilised 1.5 ml tube and the protein concentration was determined. Lysate (500 µl) was pre-cleaned by adding isotype-specific control antibody (2.0 µg for every 1.0 µg/µl protein. Pre-cleaning proceeded for 30 minutes at 4ºC on a rotating wheel at 10 rpm. Pre-equilibrated Dynabeads™ Protein G bead slurry (20 µl) were added to capture the control antibody and the beads were removed by magnetic force. The pre-cleaned supernatant was split into two different tubes to which 1.0 µg of capture antibody or 1.0 µg of control antibody

were added, respectively. Both tubes were incubated for 1 hour at 4ºC on a rotation wheel at 10 rpm. Fresh beads were washed and prepared the same way as described before. Each control and capture antibody tube lysates were transferred into the new ones with washed beads and were left overnight at 4ºC on a rotation wheel at 10 rpm. The next day the beads were washed three times with lysis buffer. An aliquot of 2x reducing sample buffer and the same volume of PBS were added to achieve a final concentration of 1x reducing sample buffer. The samples were heated at 70ºC for 10 minutes. The eluted samples were separated from the beads, transferred to a fresh tube and frozen at -20ºC until analysis by SDS-PAGE gel.

Buffers for immunoblotting, immunoprecipitation and cAMP pull down assays:

Solubilisation Buffer	
Tris/HCl pH 7.4 (10mM) Stock solution (1M)	0.5 ml
NaCl (150mM) Stock solution 1M	7.5 ml
EDTA (5mM) Stock solution 0.5 M	0.5 ml
Glycerol (10%) (bidistilled)	5 ml
Sodium azide (0,02%) Stock solution 10%	100 µl
Distilled water	36.5 ml
Total Volume	50 ml

Lysis Buffer 1%	Volume
Solubilisation buffer	840 µL
NP40 10%	100 µL
PMSF (0.1 M)	10 µL
Vanadate (200 mM)	10 µL
Protease inhibitor 25x	40 µL
Total Volume	1 mL

2.4.5. cAMP pull down assay

HUVEC cells and human washed platelets were lysed with ice-cold lysis buffer supplemented with PIC and PMSF. Lysates were centrifuged at 13000x g for 15min. The supernatant was collected and transferred to a new tube. Next, pre-equilibrated 8-(6-aminohexylamino) adenosine-3',5'-cyclic monophosphate (8-AHA-cAMP) cAMP agarose beads and control (ethanolamine) agarose beads (Biolog, Life Science Institute, Germany) slurries were incubated with 350-500 µg of lysate at 4°C overnight with rotation at 10 rpm. Beads were collected by centrifugation at 500xg, washed twice with lysis buffer and boiled in 2X Laemmli buffer at 95°C for 5 min. The eluted proteins were run on SDS-PAGE and analysed by western blotting (see section 2.4.8). This procedure is depicted schematically in Figure 2.2.

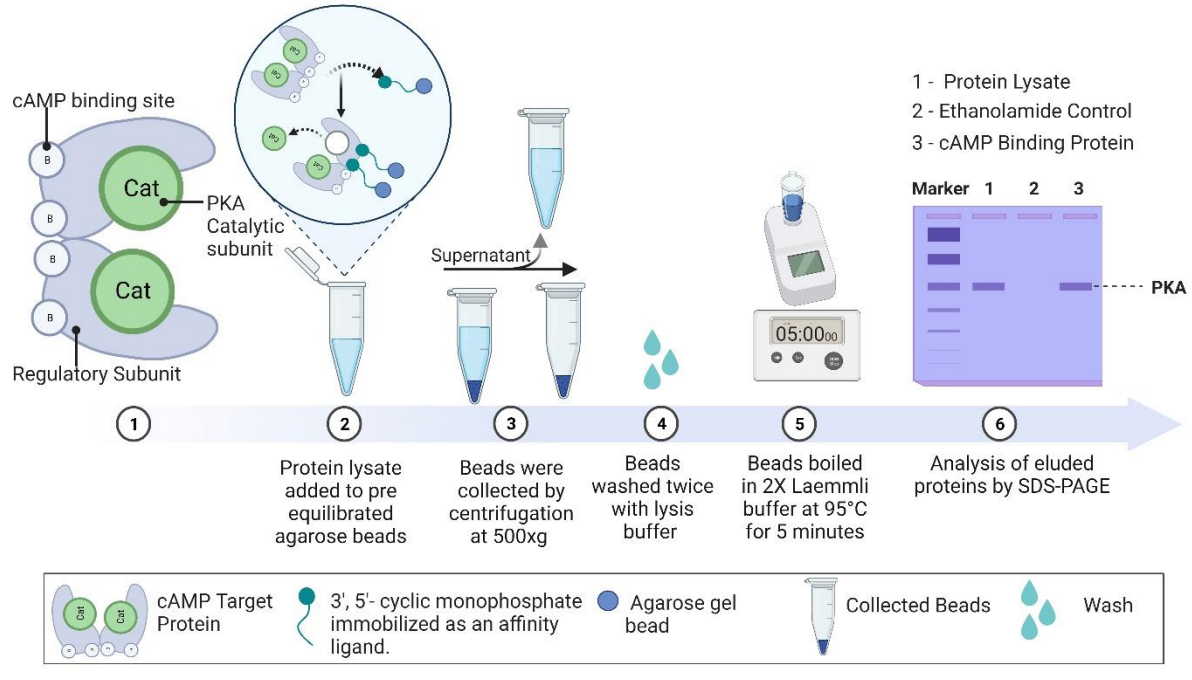

Figure 2.2 Principle of cAMP pull-down assay. Schematic showing the various steps involved in the method. **1**, PKA proteins are on its free state on lysate; **2**, Pre-equilibration of lysate with beads containing 8-(6-aminohexylamino) adenosine-3',5'-cyclic monophosphate (8-AHA-cAMP) or ethanolamine (EtOH-N); **3** beads are collected; **4**, beads are washed; **5**, beads are boiled to facilitate the elution of PKA from the beads, **6** the complexes are analysed by SDS-PAGE. (Created with Biorender.com).

2.4.6. Sodium dodecyl sulphate-polyacrylamide gel electrophoresis (SDS-PAGE)

Sodium dodecyl sulphate-polyacrylamide gel electrophoresis (SDS-PAGE) is a technique employed to separate proteins based on their molecular masses under the influence of an electric current. Polyacrylamide gels are created by polymerisation of acrylamide and bis-acrylamide monomers, initiated by ammonium persulfate (APS) (Shi and Jackowski, 1998) and catalysed by N,N,N',N'-tetramethylethylenediamine (TEMED). During gel manufacturing, alternative pore sizes are corresponded to the percentage of acrylamide used, thereby enabling separation of proteins within the mixture. To ensure a consistent negative charge, SDS is added to the protein mixture (Shapiro et al., 1967), effectively concealing the inherent net charge of the proteins. Furthermore, the introduction of a reducing agent like 2-mercaptoethanol serves to disrupt disulphide bridges and linearise the proteins, thereby facilitating their separation based exclusively on molecular weight.

2.4.6.1 Procedure for SDS-PAGE

In all experiments conducted for this thesis, the samples were subjected to electrophoresis using a Mini PROTEAN® 3 system (Bio-Rad) and a discontinuous buffer system. This particular buffer system, initially described by (Laemmli, 1970), is commonly utilised in SDS-PAGE. It necessitates the inclusion of specific buffers in both the gel and electrophoresis tank. For the experiments, polyacrylamide gels with a thickness of 1.5 mm were prepared, comprising of a separating gel (pH 8.8) ranging from 7-12% and a stacking gel (pH 6.8) consisting of 4%, as indicated below.

The gels were loaded with a pre-stained protein ladder and protein samples ranging from 20-60 µg. These loaded gels were then placed into the electrophoresis tank, which contained running buffer in both the upper and lower chambers. Electrophoresis was carried out at an initial voltage of 70 V for the first 30 minutes, followed by an increase in voltage to 120 V for a duration of 1.5 to 2.5 hours, depending on the size of the protein under investigation. Upon completion of

electrophoresis, the resolved proteins were analysed either by Coomassie staining or by western blotting, depending on the specific experimental requirements.

10X Tris-Glycine (1 litre)
Tris (250 mM) -30.28g
Glycine (1.92 M) – 144.15g
Dissolve and add up to 1 litre with ultrapure H_2O

1X Running Buffer (1 litre)
Tris- Glycine – 100 ml
SDS (10%) – 10 ml
H_2O – 890 ml

Separation Gel (Lower Gel)		
7%	H_2O	4.97 ml
	Acrylamide/bisacrylamide 30%	2.33 ml
	Tris 1.5M (pH=8.8)	2.5 ml
	SDS 10%	100 µl
	APS (ammonium persulfate)10%	100 µl
	TEMED	10 µl
8%	H_2O	4.83 ml
	Acrylamide 30%	2.67 ml
	Tris 1.5M (pH=8.8)	2.5 ml
	SDS 10%	100 µl
	APS (ammonium persulfate)10%	100 µl
	TEMED	10 µl
10%	H_2O	4.17 ml
	Acrylamide 30%	3.33 ml
	Tris 1.5M (pH=8.8)	2.5 ml
	SDS 10%	100 µl
	APS (ammonium persulfate)10%	100 µl
	TEMED	10 µl
12%	H_2O	3.5 ml
	Acrylamide 30%	4 ml
	Tris 1.5M (pH=8.8)	2.5 ml
	SDS 10%	100 µl
	APS (ammonium persulfate)10%	100 µl
	TEMED	10 µl

Stacking Gel (4%)	
H_2O	2.817 ml
Acrylamide/bisacrylamide 30%	0.833 ml
Tris 0.5 M (pH=6.8)	1.25 ml
SDS 10%	50 µl
APS (ammonium persulfate)10%	50 µl
TEMED	5 µL

2.4.7. Coomassie blue staining of polyacrylamide gels

Following SDS-PAGE transfer, Coomassie-Brilliant-Blue R250 staining was implemented to provide visualisation of protein bands in the gel. The volume and concentration of Coomassie-Brilliant-Blue R250 added to a protein sample is between 0.1% to 0.5% (w/v) of the total sample volume and was based upon the type of protein being analysed and the desirability of the sensitivity of the specific assay. Staining was allowed to proceed overnight at room temperature with gentle shaking.

The following day, the gel was subjected to either room temperature destaining with shaking using a destaining solution or boiled in distilled water three times using a microwave until the protein bands became visible. Subsequently, the destained gel was either imaged using an Odyssey CLx imaging machine (Li-Cor, Germany) or scanned with a flatbed scanner.

Coomassie Staining Solution (1 litre)	
0.05%Coomassie Brilliant Blue R-250	0.5 g
10% Acetic acid	100 ml
50% Methanol	500 ml
40% H_2O	400 ml

Coomassie Destaining Solution (1litre)	
10% Acetic acid 10%	100 ml
50% Methanol (or ethanol)	500 ml
40% H_2O	400 ml

2.4.7.1 Protein quantification from acrylamide gels

The determination of recombinant GST and His-Tag protein purity was performed by using Image J software. This software allowed to quantify the band intensity on all columns. The expected protein size was quantified and considered intact protein (in box in black), while the rest of the peaks (bands) were also quantified but considered degradation products as shown inside box in red in Figure 2.3A. This method of quantification was performed for all recombinant proteins ran on SDS-PAGE gels. As show on panel B of Figure 2.3 to quantify each protein it was laid a rectangle that occupied all are where the eluted proteins would run. To differentiate the protein of interest and its degraded products the area of the peaks for each intensity curves were determined as shown in Figure 2.3 C. From this quantification results were considered as % of intact protein shown on Appendix Table 8.3-1, Appendix Table 8.3-2 and Appendix Table 8.3-3.

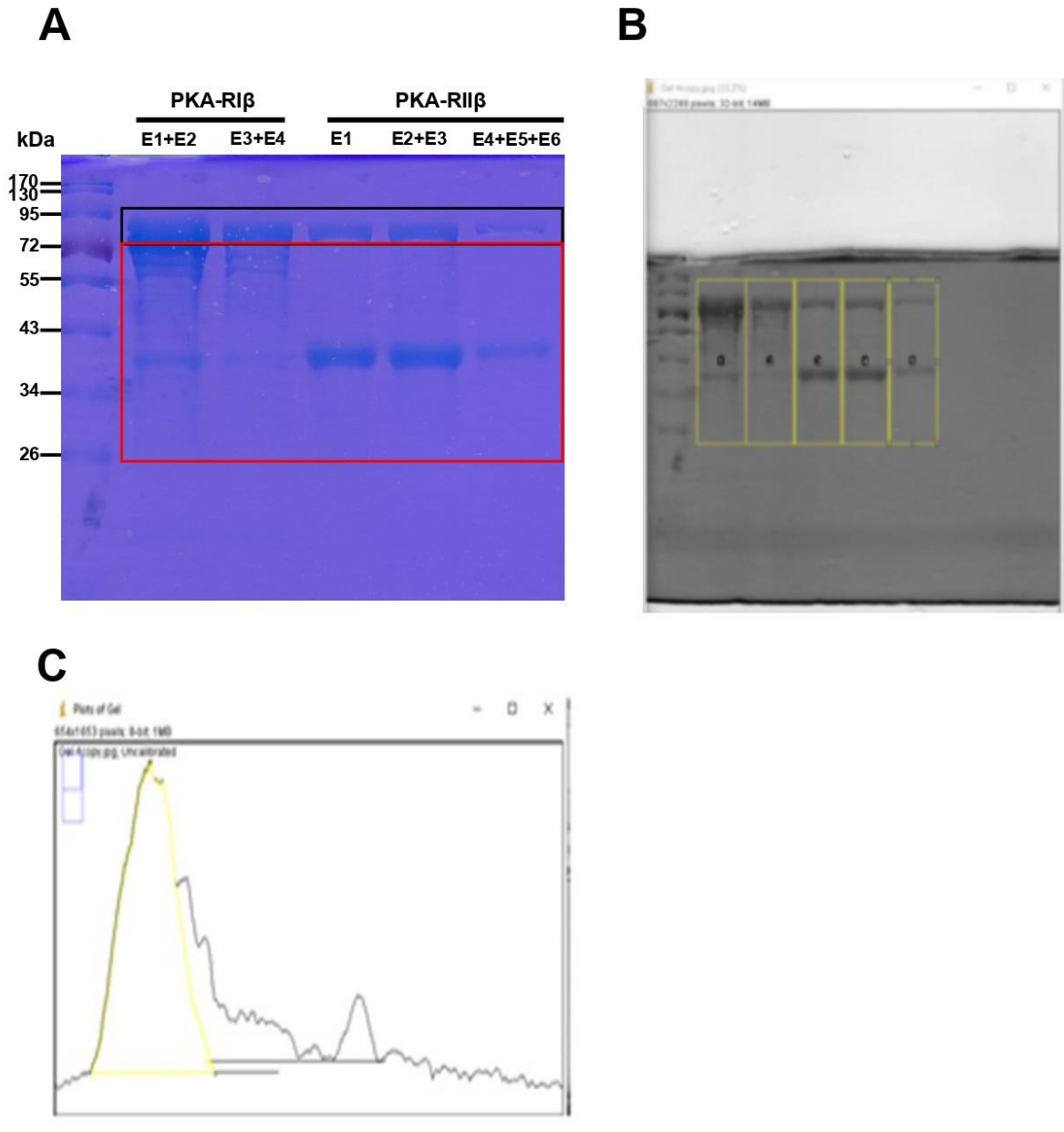

Figure 2.3 Protein purity determination using Image J software. (A) Protein eluates were run on 10% SDS-PAGE and stained with Coomassie staining solution. The protein of interest was located around 72 kDa. **(B)** Representation of how protein was determined for all recombinant proteins. A rectangle was drawn for each eluate. **(C)** Intensity peaks represent protein intensity inside each rectangle. The highest peak represents the protein of interest while the others are degraded protein products.

2.4.8. Western Blotting

Western blotting is a technique used to detect specific proteins extracted from cells. This method utilises the transfer and immobilisation of these specific proteins from an SDS-PAGE gel onto an adhesive support matrix such as nitrocellulose or polyvinylidene fluoride (PVDF) membranes. The membranes are probes using specific primary antibodies which form protein antibody complexes via specific epitopes. Following the primary antibody incubation and washing steps, a secondary antibody that targets the primary antibody is subsequently added to the membrane (Figure 2.4).

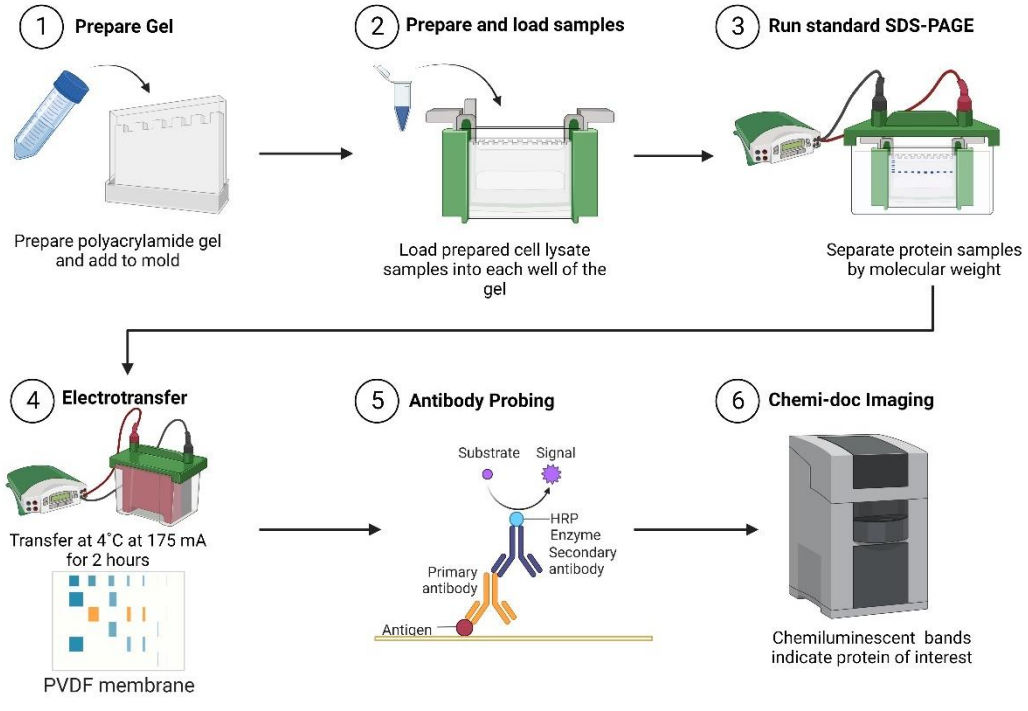

Figure 2.4 Schematic of the Western blotting procedure including SDS-PAGE, electrotransfer and immunoblotting steps. **1**, Preparation of gels according to the percentage of acrylamide (section 2.4.6 separation and stacking gels); **2**, preparation and loading of samples into the wells; **3**, running SDS-PAGE gel at 4ºC 120V (1.5 to 2.5 h); **4**, electrotransfer done at 4ºC 175 mA for 2hours; **5**, previous to incubation overnight with primary antibody block with 5% milk overnight at 4 degrees. Incubate 1hour with secondary HRP antibody; **6**, Chemiluminescent bands due to the reaction of ECL with HRP. (Created with Biorender.com)

Detection molecules, such as horseradish peroxidase (HRP) enzyme are typically conjugated to secondary antibodies to enable their detection on the membrane during imaging. Throughout this thesis HRP is commonly used. The addition of luminol, coumaric acid and H_2O_2 to the HRP linked secondary antibodies results in the emission of light (425 nm) that can be detected by an X-ray film or a CCD camera.

2.4.8.1 Western Blotting methodology

After separation by SDS-PAGE, proteins were transferred to a PVDF membrane using an electrotransfer system (Bio-Rad laboratories, Hertfordshire, UK) for 2 hours at constant amperage (175 mA) at 4ºC. In this method, filter papers, polyacrylamide gel and methanol activated PVDF membrane were submerged in transfer buffer before arranged in the correct order in the Bio-Rad transfer system, such as sponge, bottom double western blotting filter paper square, PVDF membrane, acrylamide gel on top of the membrane followed double wester botting paper and sponge. This "sandwich" order is then loaded vertically into the support grid with the gel facing the white part of the grid. The grid is inside the tank transfer system with transfer buffer.

1X Transfer Buffer (1 litre)
Tris- Glycine – 100 ml
Methanol – 200 ml
H_2O – 700 ml

Care was taken not to trap any air bubbles between PVDF membrane and gel. Under these conditions, proteins migrating towards the anode were captured by the PVDF membrane. Following transfer, membranes were blocked for 1 hr at room temperature with 5% (w/v) BSA/TBS-T or 5% (w/v) semi-skimmed milk/TBS-T depending on the primary antibody to be used, in order to prevent non-specific antibody binding. After blocking, membranes were incubated with the appropriately diluted primary antibody in TBS-T containing 2% BSA, 2% or 5% milk (w/v) overnight at 4°C with gentle agitation. After incubation with primary antibody, membranes

were rinsed twice with TBS-T for 8 min with gentle agitation and incubated either with HRP-conjugated secondary antibodies.

2.4.9. Ponceau Red staining of PVDF membranes

Proteins transferred to PVDF membranes were visualised by staining Ponceau S following by distaining with distilled water. This staining served as a control of protein transfer after the blotting. The staining was removed by washing with TBS-T.

Ponceau Red
0.1% Ponceau S
1% Acetic acid

2.4.10. Stripping and re-probing of PVDF membranes

Membranes were washed with TBS-T (0.1%) three times for 8min prior to incubation with 10 ml of Restore™ PLUS Western Blot Stripping for 30min at room temperature with continued shacking. The stripping buffer was removed, and the membrane was washed with TBS for 8 minutes, followed by three washes with TBS-T (0.1%), 8 minutes each. If membranes are going to be stored, they must be washed with TBS before allowed to dry. Stripped membranes are ready to be probed with another antibody.

10x TBS (pH = 7.5)
Tris -24 g
NaCl -88 g
Water up to 1L

1x TBS	
10X Tris	100 ml
ddH_2O	900 ml

1x TBS -T (0.1%)	
1x TBS	1000 ml
Tween 20	1ml

2.4.11. Peptide Array

Peptide array experiments were conducted following the methodology outlined in (Brown et al., 2013). Briefly, peptides spanning residues 501-706 of MYPT1 were synthesised using automatic SPOT synthesis (Frank, 1992, Amartely et al., 2014). Synthesis was performed on continuous cellulose membrane supports utilising 9-fluorenylmethyloxycarbonyl chemistry (Fmoc) via a MultiPep RSi Robot (Intavis, Cologne, Germany). Prior to use, arrays were pre-activated in absolute ethanol and then blocked with 5% dehydrated milk in TBST for 4 hours at room temperature. Following blocking, MYPT1 arrays were incubated overnight at 4°C with 10 µg/ml of His-tagged PKA-RIß or PKA-RIIß diluted in a buffer containing 150 mM NaCl, 5% glycerol, and 50 mM Tris pH 7.4. PKA-R binding to MYPT1 peptides was assessed by incubating the array for 4 hours at 4°C with an HRP-conjugated anti-6His antibody (1:2000, Sigma, A7058) in TBST, followed by detection using enhanced chemiluminescence. Throughout the experiment, all protein and antibody incubation steps were conducted under gentle agitation, with arrays washed after each incubation step in 1X TBST (these experiments were performed at Professor George Baillie's laboratory in Glasgow University).

2.4.12. Quantification of Blots

Immunoblots were imaged using a ChemiDoc XRS+ Imaging System (Bio-Rad Laboratories, Watford, UK) or a LI-COR Odyssey CLx Imaging System (LI-COR Biosciences, Lincoln, USA). Images were acquired at several exposure times within the linear range of the signal. Protein band densities were analysed with Image Lab software (Bio-Rad Laboratories, Watford, UK)

2.4.13. Quantification of pulldowns

The depletion ratios for the cAMP affinity pulldown were calculated as for the immunoprecipitation. Pulldowns were calculated as the band intensities of the eluate lanes divided by the b-actin normalised intensity of the respective protein in the total lysate.

2.4.14. Quantification of IP

To calculate immunoprecipitation depletion ratios, first the density of each b-actin normalised band in the post-beads lysates were calculated. Next, the normalised density in the lysate incubated with anti-MYPT1 antibody was divided by the normalised density in the lysate incubated with IgG. The result was subtracted from 1 to produce the depletion ratio. To calculate co-immunoprecipitation ratios, the band intensities of the immunoprecipitation lanes were normalised to their respective IgG light chain signal. Next, the normalised values for the IgG and anti-MYPT1 lanes were added, and the value of each lane was divided by the sum.

2.5. Cell biology methods

2.5.1. Cell cultivation

2.5.1.1 Mammalian cell culture

Human umbilical vein endothelial cells, (HUVECs) (C-12208, lot 447Z015; Promocell, Heidelberg, Germany) were grown at 37ºC in a humidified incubator supplied with 5% CO_2. The cells were grown in endothelial cell growth medium MV2 supplemented with 5% (v/v) foetal bovine serum, 5 ng/mL epidermal growth factor, 10 ng/mL basic fibroblast growth factor, 20 ng/mL insulin-like growth factor-1, 0.5 ng/mL vascular endothelial growth factor 165, 1 µg/mL ascorbic acid, and 0.2 µg/mL hydrocortisone (Promocell, Heidelberg, Germany). The cells were grown at 37ºC in a humidified incubator supplied with 5% CO_2.

HSVSMCs were provided by fellow colleague Olapeju Bolanle (Professor Tim Palmer's group, Centre for Biomedicine). HSVSMCs were isolated from surplus vein tissue from consenting subjects undergoing coronary artery bypass graft surgery under ethical approval by the NHS Health Research Authority (ref. 15/NE/0138, IRAS project ID 170899), and cultivated in smooth muscle cell growth medium 2 supplemented with 5% (v/v) foetal bovine serum, 0.5 ng/mL epidermal growth factor, 2 ng/mL basic fibroblast growth factor, and 5 µg/mL insulin (Promocell, Heidelberg, Germany). SMC integrity was verified by the presence of SMC markers myosin heavy chain and α-actin and the absence of the endothelial marker PECAM1 (CD31). Cultures were maintained at 37ºC in a humidified atmosphere containing 5% (v/v) CO_2.

2.5.1.2 Thawing of mammalian cell stocks

A cryovial containing frozen mammalian cells was removed from liquid nitrogen storage and immediately thawed in a 37ºC water bath. The cell suspension was added to 10 ml of pre-warmed supplemented endothelial cell growth medium MV2 and centrifuged at 425x*g* for 3 minutes. The supernatant was removed, and the cell pellet was resuspended in fresh medium and transferred to 75 cm^2 flasks.

2.5.1.3 Subculturing of human cells

HUVECs were grown in a 75 cm^2 flask until they reached 90-95% confluence. Medium was removed from the flask and cells were washed with pre-warmed PBS. The PBS was then removed, and a volume of trypsin (0.05%) was added to the cells. The flask was transferred to the incubator for 1-2 minutes. Cell detachment was checked under a microscope. A volume PBS was added. the suspension was transferred to a 15 ml conical tube and centrifuged at 425x*g* at room temperature for 3 minutes. The supernatant was removed, and the cell pellet carefully resuspended with supplemented endothelial cell growth medium MV2. Cells were counted using a haemocytometer under an inverted microscope. Cells were seeded according to the particular experiment in a fresh labelled flask containing pre-warmed growth medium and incubated at 37ºC, 5% CO_2.

2.5.1.4 Cryopreservation of human cells

To prepare mammalian cells for cryopreservation in liquid nitrogen, a 90-95% confluent 75cm^2 flask was trypsinised, centrifuged and resuspended in a freezing solution containing 90% FBS and 10% DMSO. 1 ml of the pellet resuspended in this cryopreservative solution was transferred to a sterile labelled cryotube. The tubes were then placed into a cryorack (Nalgene Mr FrostyTM Cryo) with isopropanol filling and left at -80ºC overnight. Following day, the cryotubes were transferred to liquid nitrogen for storage until further use.

2.5.1.5 Preparation of human washed platelets

Blood extraction occurred by piercing of the median-cubital vein using a 21- gauge sterile butterfly needle mounted on 20cm of plastic tubing directly into a 20ml plastic syringe preloaded with the anticoagulant acid citrate dextrose (ACD) at a ratio of 1:5 (4ml of ACD to 20ml blood). ACD is previously filtered through a 0.22 µm filter. The first 4ml of blood was discarded to a avoid potential contamination of

tissue factors and trace thrombin to prevent platelet activation. The citrated blood is then decanted into a 50ml conical tube and centrifuged 200x*g* for 15 minutes at room temperature. Pre-warm Tyrode's buffer with 0.045 g of glucose on the incubator. The top layer consists of platelet-rich plasma (PRP), this layer was carefully transferred into a 15 ml conical tube using a pasteur pipette without disturbing the blood layers. To separate the PRP from the solution 0.3 M citric acid (20 µl/ml of PRP) was added to precent platelet activation. Tubes were centrifuged at 800x*g* for 12 minutes at room temperature. Platelet poor plasma (PPP) was gently removed then discarded, and the platelet pellet was gently resuspended in 1ml of wash buffer then an additional 4ml of wash buffer and centrifuged at 1000x*g* for 10 minutes. The supernatant was removed, and remaining pellet was resuspended at the desired concentration in modified Tyrode's buffer (an iso-osmotic phosphate buffer).

Platelet counting was carried out using a Beckman Coulter Z1 Particle Counter by combining 5µl of platelet suspension to 10 ml of isotonic buffer within a Beckman Coulter Accuvette. The machine counts cells per millilitre by measuring the electrical resistance of cells as they are passed through a micro-aperture. Platelets were then allowed to rest at 37°C for 30 min before experimentation.

Human blood was taken after informed consent from healthy, drug-free volunteers under approval of the Hull York Medical School ethic committee. Prior to donation volunteers confirmed they had not taken any medication that affects platelet activity such as antihistamines two weeks prior to donation date.

2.5.2. Immunofluorescence

HUVECs were processed for immunofluorescence using established protocols (Nikitenko et al., 2006). HUVECs were seeded at 5,000-10,000 cells per well in 8-well plates (Nunc™ Lab-Tek™ II Chamber Slide™ System, Thermofisher) and cultivated for 48 hours. For acetone methanol (A/M) fixation the medium was tapped off, each well was washed with PBS and the buffer discarded. 300 µl of acetone/methanol

(2:3) were added to each well. After 3 minutes, the fixation liquid was removed, and the slide allowed to air dry for 30 min. If incubation with primary antibodies was not performed right, the slide was stored at -20ºC and left to thaw at room temperature for 5 minutes before washing with PBS. For paraformaldehyde (PFA) fixation, the wells were washed as above and 4% of PFA was added and allowed to incubate for 7 minutes. The fixative was removed, and the wells were washed with PBS. PBS was added to the wells and the slide was stored at 4ºC until use.

Before primary antibody incubation, the wells were blocked with 10% donkey serum in PBS-T (0.1%) for 30 min at room temperature. Antibodies were diluted in PBS-T (0.1%) containing 2% donkey serum with the required concentration, added to the wells and the plate was placed in a humidified chamber protected from light at 4ºC overnight. Next day the wells were washed with PBS-T (0.1%) and secondary antibody also diluted in PBS-T (0.1%) was added to each well for 45 min at room temperature away from the light. The wells were washed, and Vectashield® antifade mounting medium containing DAPI (2BScientific, Kidlington, UK) was added. A coverslip was placed on top, and the 8 well slide was stored at 4ºC away from the light until imaged.

This protocol was also employed for dual labelling. It involves simultaneous incubation of two primary antibodies derived from distinct species. Subsequently, two secondary antibodies labelled with fluorescent tags are introduced, each binding specifically to its respective species.

Composition of PBS-T (0.1 %) pH 7.45	
NaCl	140.0 mM
KCl	2.68 mM
Na_2HPO_4, and 2 mM KH_2PO_4	10.0 mM
Add 500 µLTriton X-100 to reach 0.1% final concentration	

2.5.2.1 Image acquisition and processing

Slides were imaged with a ZEISS LSM710 confocal microscope equipped with a 10x and 20×/0.5 ECPlan-NEOFLUAR objective fl (ZEISS, Cambridge, UK). Images were processed with ZEISS Zen software.

2.5.2.2 Quantification of co-localisation images

For co-localisation analysis, regions of interest (125x125 pixel) were extracted from double staining images and were used to calculate the Pearson's correlation coefficient with the ImageJ plugin JACoP (Bolte and Cordelieres, 2006). A set of images in which one of the channels was rotated 90° was used as a negative control.

2.5.2.3 *In situ* proximity ligation assay (Duolink®)

In situ proximity ligation assays (PLAs) were carried out using a Duolink® in situ red starter kit mouse/rabbit (Merck, Dorset, UK). Previously seeded HUVECs in 8-well chambers were fixed with 4% PFA, permeabilised and blocked as described above in section 2.5.2. Cells were then incubated with matching concentrations of the relevant primary antibody or isotype specific immunoglobulin (mouse and rabbit) pairs (section 4.6, Figure 4.11). This was followed by incubation with anti-mouse and anti-rabbit probes and for the fluorescence-producing reaction as per the manufacturer's instructions.

Briefly, PLUS and MINUS PLA probes were diluted (1:5) in 2% donkey serum PBS-Triton X-100 0.1% (PBS-Triton). Upon removing the primary antibody solution from the slides, two washes of 5 minutes were performed in PBS-Triton at room temperature. The probes were added to each well and the slides were incubated in a pre-heated humidity chamber for 1 hour at 37°C. Probes were removed and the wells were washed 2x 5 minutes each in PBS-Triton at room temperature, followed by a wash with PBS. Ligation buffer was diluted 1:5 in high purity water and ligase was added at a final 1:40 dilution. The solution was added to the wells and the slides were incubated in a pre-heated humidity chamber for 30 minutes at 37°C. Ligation solution was removed, the wells washed with PBS-Triton and PBS as before.

Amplification buffer was diluted 1:5 in high purity water and polymerase was added at a 1:80 dilution. The solution was added to the wells and the slides were incubated in a pre-heated humidity chamber for 100 minutes at 37°C (Figure 2.5).

Once the polymerase reaction was completed, slides were washed 2 times 10 minutes each in 1x Wash Buffer B at room temperature followed by one wash with 0.01X Wash Buffer B. The samples were incubated with fluorescein isothiocyanate (FITC) labelled phalloidin for 30 min prior to mounting with Vectashield® antifade mounting medium containing DAPI (2BScientific, Kidlington, UK). Samples were imaged as described in the previous section. Fluorescence density was calculated using ImageJ because the high density of dots made counting impractical. For each individual HUVEC the background subtracted intensity was normalised to the cell area and the result expressed as arbitrary units.

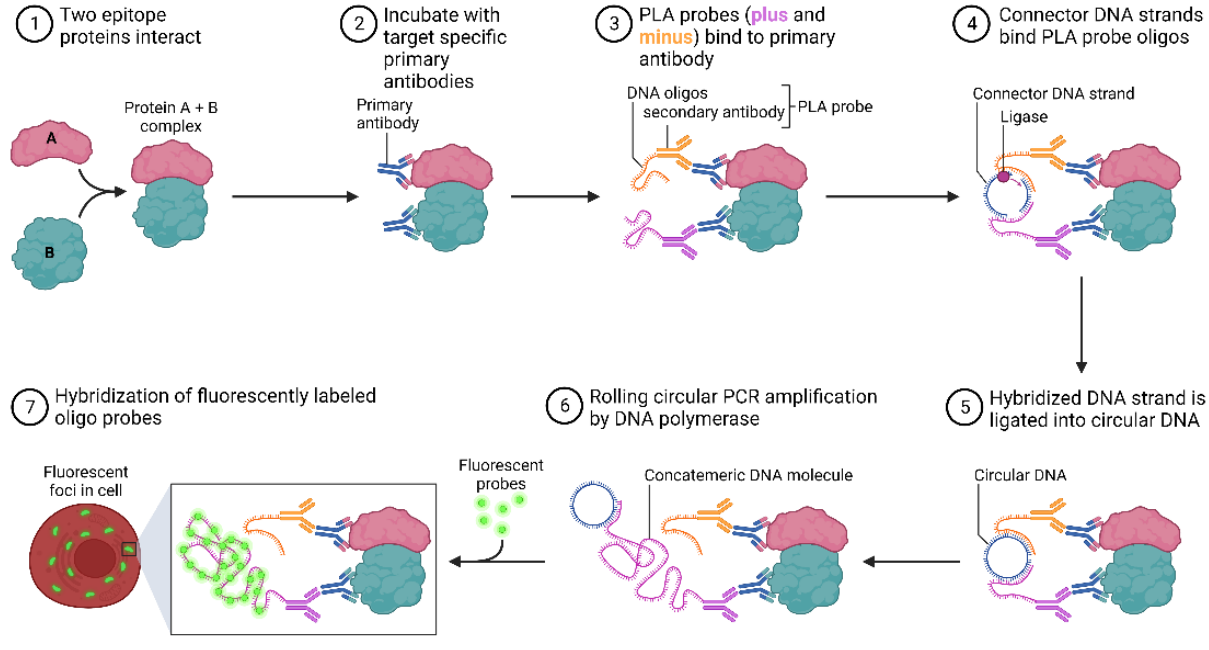

Figure 2.5 Principle of in situ proximity ligation assay. Schematics of proximity ligation assay technique used in this study. **1** Two epitopes of two proteins interact; **2** Incubation with target specific primary antibodies from different host species; **3** PLA probes (Minus and Plus) bind to primary antibodies; **4** Connector DNA strands bind to PLA probe oligos; **5** Hybridised DNA strand is ligated into circular DNA; **6** Rolling circular PCR amplification by DNA polymerase; **7** Hybridisation of fluorescently labelled oligo probes **(**Created with Biorender.com).

2.5.2.4 Quantification of proximity ligation assay

Fluorescence density was calculated using ImageJ (v1.53, NIH) because the high density of coalescent dots makes counting of individual dots impractical. Outlines were drawn around each cell area and integrated density were measured along with several adjacent background region outside the cells. A mean background fluorescence was calculated as the integrated density of the background region divided by its area. The total corrected cellular fluorescence (TCCF) for each cell was calculated as follows:

TCCF = integrated density – (area × mean background fluorescence)

The result was expressed as arbitrary units (McCloy et al., 2014).

2.5.3. Gene silencing

The RNA interference (RNAi) method has been used to study the loss of function analysis in basic cell biological research and for developing of novel therapeutic methods (Agrawal et al., 2003). Small interfering RNA (siRNA) is a type of nucleic acid that is used for gene silencing. It is delivered as duplexes comprising a sense and antisense strand. Once in the cytoplasm, siRNA complexes with RNA interference (RNAi) enzymes, during which the passenger strand is degraded and the mature RNA-induced silencing complex (RISC) forms. This RISC complex is now capable of degrading mRNA that is recognised by the guide strand (Aagaard and Rossi, 2007).

Prior to perform the knockdown experiment the siRNAs were quantified by spectrophotometry (Nanodrop). siRNAs were brought up to a stock concentration of 20 µM. 75,000 HUVEC cells were seeded in each well of a six well cell culture plate with 1 ml of full medium containing 1% penicillin/streptomycin. For each silencing reaction, a master mix (MM1) containing Opti-MEM™ and siRNA oligonucleotide (500nM) and a second master mix (MM2) containing Opti-MEM™ and 20% Oligofectamine™ were prepared at room temperature. Oligofectamine was dropped

into the Opti-MEM™ without touching the tube walls and left incubating at room temperature for 10 minutes.

A set of master mixes 3 (MM3) was prepared by combining half volume of MM1 with half volume of for each siRNA with an aliquot of MM2 and incubating for 20 minutes at room temperature. 200 µl of medium were removed from each well and 200 µl of MM3 were added, to reach a final concentration of oligonucleotide of 50mM.

After 4 hours 0.5 mL of full medium containing 1% penicillin/streptomycin were added gently to each well, avoiding stressing the cells. After 24 hours the steps including MM1, MM2 and MM3 were repeated. 72h after the first transfection the medium was removed, the cells were washed with 1 ml PBS and trypsinised with 0.5 ml of trypsin for 1 min at 37ºC. Trypsinisation was stopped with 0.5 ml FBS. Cells were collected and centrifuged at 423x*g* for 3 min and cell pellets were resuspended in 1ml of complete medium containing 1% penicillin/streptomycin. Transfected cells were seeded in a new six well cell culture plate (100,000 cells per well) for lysate preparation and eight well slide for immunofluorescence staining (20000 cells per well). 24 hours after the last seeding, the 8 well slides were fixed with 4% PFA and processed for immunostaining (section 2.5.2), and complete medium with 1% penicillin/streptomycin was added to the 6 well plates. Next day the cells of the 6 well plates were washed with PBS and lysed with 30 µL of lysis buffer (section 2.4.4). Lysates were quantified by BCA kit (section 2.1.1, Table 2.7) prior to processing for western blotting analysis.

2.6. Statistical analysis

All analyses were performed using R (version 4.1.3) and R Studio (version 02.2.485). All data was tested for normality distribution using the Shapiro-Wilk test, then subsequent parametric and non-parametric tests were applied based upon normality. For normally distributed data, parametric tests including paired and non-paired t-test or one-way analysis of variance (ANOVA) with Tukey's post hoc test were used. For non-parametric data, Mann-Whitney U, Wilcoxon Signed Rank or Kruskal Wallis Rank sum tests were used. Statistical significance was accepted at a P-value of 0.05 or 5%, calculated at a confidence level of 95%. For graphical representation of statistical results, the statistical software GraphPad Prism 7 was utilised, then significance added using analysis from RStudio. Data are expressed as median ± first and third quartile of the distribution unless otherwise indicated in the figure legend. Complete output tables derived from statistical analyses can be found in 8.1 Appendix A and 8.2 Appendix B.

Chapter 3. Transcriptional profiles of the *PPP1R12A* gene in cells of the circulatory system

3.1. Introduction

The gene encoding MYPT1 (*PPP1R12A* in humans) consists of at least 26 protein coding exons in vertebrates (Dippold and Fisher, 2014a). MYPT1 isoforms have been described as the product of cassette-type alternative splicing of exons at two regions, the central part (often referred to as the central insert, CI) and the 3'-end of the transcript (involving exon 24, E24) (Dirksen et al., 2000, Payne et al., 2006, Oslin et al., 2022, Khatri et al., 2001, Htet et al., 2021, Dordea et al., 2013, Lartey et al., 2016, Shimizu et al., 1994, Twomey et al., 2010, Payne et al., 2004). Skipping of E24 results in an isoform with a C-terminal leucine zipper (LZ) motif, whereas inclusion of the exon causes a reading frame shift and a premature stop codon. The result is a shorter isoform (LZ-) that lacks the LZ motif and is less sensitive to nitric oxide (Dippold and Fisher, 2014b). The LZ- splice variant is subject to developmental regulation, is predominantly expressed in phasic (rhythmically contracting) smooth muscle cells like in the bladder but is less abundant in the tonic (continuously contracted) smooth muscle cells of the large arteries and is absent in most other tissues (Dirksen et al., 2000, Payne et al., 2006, Oslin et al., 2022). In chicken and rodents, E24 variants have been extensively studied for their role in smooth muscle physiology (Dippold and Fisher, 2014b, Khatri et al., 2001, Htet et al., 2021). In humans, the LZ- variant, although not annotated in GenBank, has been reported in the smooth muscle of blood vessels, bladder, and uterus (Oslin et al., 2022, Dordea et al., 2013, Lartey et al., 2016).

CI splice variants were initially reported in chicken (involving E12), where MYPT1 was first characterised (Shimizu et al., 1994), and subsequently in rat (involving E13 and E14) and human cells (involving E13) (Xia et al., 2005, Twomey et al., 2010). Five rat CI variants arising by cassette-type alternative splicing and usage of

alternative splicing acceptor sites have been described (Dirksen et al., 2000, Payne et al., 2004). CI variants have not been extensively studied and their functional relevance is unclear, but a lower rate of PKG-mediated phosphorylation *in vitro* has been reported in the chicken isoform skipping E12 (Yuen et al., 2011) and a human isoform skipping E13 was proposed to have lower binding affinity for radixin (Kim et al., 2012) compared to the full-length isoform. No other *PPP1R12A* variants have been reported other than a splice variant of E22 in a GenBank submission that was found absent in HeLa and vascular endothelial cells using a PCR approach (Kim et al., 2012). In addition, Machida et al. (2001)analysed the 5' region of *PPP1R12A* in aortic smooth muscle and experimentally determined a transcription initiation site (Machida et al., 2001).

The existence of alternative splicing variants of *PPP1R12A* and orthologous genes is well documented. However, inspection of the information available in public databases indicates a to date unappreciated transcriptional complexity of this gene. GenBank reports just five *PPP1R12A* transcripts encoding four protein isoforms, whereas Ensemble (accession number ENSG00000058272) collates the sequence information from EST and mRNA submissions into 23 transcripts categorised as protein coding, nonsense-mediated decay and retained intron (section 3.2, Figure 3.2). In addition, much of the published information on *PPP1R12A* expression and transcription variants has been obtained from studies in a limited number of organs and tissues, which consist of a mixture of cell types. Studies on cell lines or individual cell types are scarce and of limited scope (Xia et al., 2005, Kim et al., 2012, Twomey et al., 2010). Very little has been done to fully clarify the transcriptional landscape of the human *PPP1R12A* gene. The purpose of this chapter is to begin filling this knowledge gap.

Aims of this chapter:

1. To use an *in silico* approach to interrogate public sequence databases about transcriptional variants of *PPP1R12A* towards verifying the accuracy of the transcript predictions, in particular the alternative splicing.

2. To set up and validate a RT-PCR approach for identification of transcriptional variants of *PPP1R12A* in human RNA samples.

3. To use the RT-PCR approach to identify transcripts experimentally in cells of the vasculature in which MYPT1 is known to play important roles, namely endothelial cells (represented by HUVECs) and smooth muscle cells (represented by HSVSMCs) using RT-PCR.

3.2. *In silico* analysis of *PPP1R12A* transcription variants

3.2.1. MYPT1 transcripts and isoforms

PPP1R12A gene encodes several MYPT1 isoforms. Kimura et al. (1996) mapped the MYPT1 gene to the long arm of chromosome 12q15-q21.2 (Kimura et al., 1996). It is expressed in many tissues, most abundantly in smooth muscles (Takahashi et al., 1997). The gene has 26 exons and 25 introns. The locus also contains 2 RNA pseudogenes, 3 antisense gene transcripts, 6 long non-coding RNAs and miRNAs. (Figure 3.1).

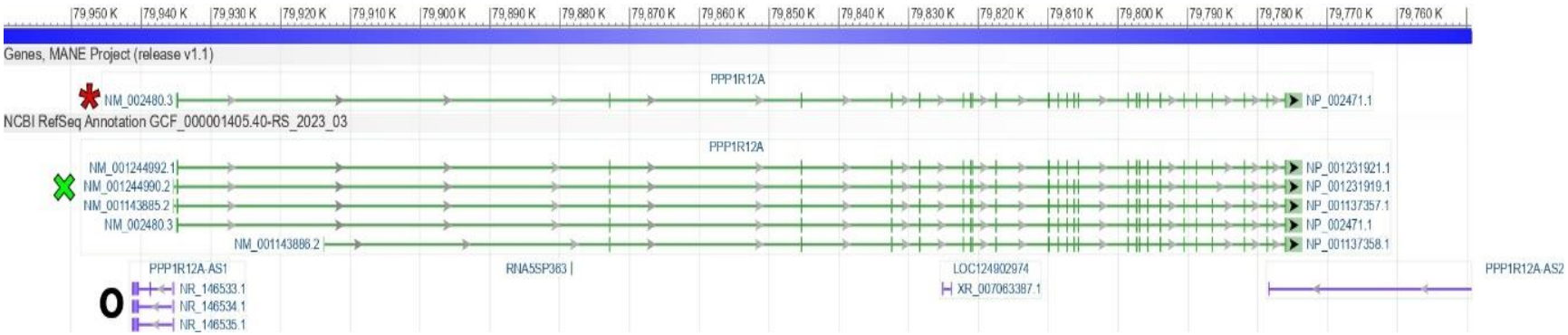

Figure 3.1 Features of the human *PPP1R12A* locus in GenBank. Image was taken from GenBank (https://www.ncbi.nlm.nih.gov/gene/4659 22/06/2022). The * (in red) indicates the canonical transcript of *PPP1R12A*. The x (in green) indicates the alternative splicing transcripts. The "o" (in black) indicates 3 antisense transcripts.

MYPT1 isoforms have been described as the product of cassette-type alternative splicing of *PPP1R12A* exons at two regions, the central part (often referred to as the central insert, CI) and the 3'-end of the transcript (involving exon 24, E24, and affecting the LZ domain) (Dirksen et al., 2000, Payne et al., 2006, Oslin et al., 2022, Khatri et al., 2001, Htet et al., 2021, Dordea et al., 2013, Lartey et al., 2016, Shimizu et al., 1994, Twomey et al., 2010, Payne et al., 2004). GenBank reports just five *PPP1R12A* transcripts encoding four protein isoforms, suggesting that the gene's transcriptional complexity may not be reflected in the current annotation thus prompting to examine the available information in public databases to seek clarity (Saldanha et al., 2022).

The Ensemble database collates the sequence and expression information of *PPP1R12A* into 23 transcripts distributed into three types: protein coding, nonsense-mediated decay and retained intron (Figure 3.2 and Table 3.1Table 3.1 *PPP1R12A* transcripts and protein variants as annotated in Ensemble and GenBank.). Four transcripts predict exons not annotated in GenBank within introns 2, 9, 20 and 22 that were named $E2^+$, $E9^+$, $E20^+$ and $E22^+$, in order to preserve the exon nomenclature commonly used in the literature (Appendix Figure 8.1-1). Transcripts including $E20^+$ (PPP1R12A-217) and $E22^+$ (PPP1R12A-205) are annotated as nonsense-mediated decay, whereas transcripts including $E2^+$ (PPP1R12A-209) and $E9^+$ (PPP1R12A-223) are annotated as protein coding. However, careful inspection showed that PPP1R12A-209 is more likely a nonsense-mediated decay transcript because splicing in of an additional exon causes a frame shift and results in a premature stop.

Transcript ID	Name	bp	Protein	Biotype	CCDS	UniProt Match	RefSeq Match	Flags
ENST00000450142.7	PPP1R12A-203	5620	1030aa	Protein coding	CCDS44947	O14974-1	NM_002480.3	MANE Select Ensembl Canonical GENCODE basic APPRIS P3 TSL:1
ENST00000261207.9	PPP1R12A-201	5582	1030aa	Protein coding	CCDS44947	O14974-1	-	GENCODE basic APPRIS P3 TSL:5
ENST00000437004.6	PPP1R12A-202	4639	995aa	Protein coding	CCDS58260	O14974-2	-	GENCODE basic TSL:1
ENST00000546369.5	PPP1R12A-204	2977	943aa	Protein coding	CCDS44948	O14974-5	-	GENCODE basic TSL:2
ENST00000550107.5	PPP1R12A-213	2925	974aa	Protein coding	CCDS58259	O14974-3	-	GENCODE basic APPRIS ALT1 TSL:1
ENST00000547330.5	PPP1R12A-208	2275	692aa	Protein coding		F8VZN8	-	TSL:1 CDS 3' incomplete
ENST00000650220.1	PPP1R12A-223	1143	381aa	Protein coding		A0A3B3ISH4	-	CDS 5' and 3' incomplete
ENST00000553081.5	PPP1R12A-221	1101	367aa	Protein coding		H0YHI8	-	TSL:5 CDS 5' and 3' incomplete
ENST00000547131.1	PPP1R12A-206	897	299aa	Protein coding		H0YIS4	-	TSL:5 CDS 5' and 3' incomplete
ENST00000550299.5	PPP1R12A-214	683	188aa	Protein coding		H0YIM2	-	TSL:5 CDS 5' incomplete
ENST00000550510.5	PPP1R12A-216	631	210aa	Protein coding		H0YHL8	-	TSL:5 CDS 5' and 3' incomplete
ENST00000548318.1	PPP1R12A-209	582	97aa	Protein coding		F8VW28	-	TSL:3 CDS 3' incomplete
ENST00000634739.1	PPP1R12A-222	560	100aa	Protein coding		A0A0U1RQZ1	-	TSL:2 CDS 5' incomplete
ENST00000546762.5	PPP1R12A-205	1257	234aa	Nonsense mediated decay		H0YIS3	-	TSL:5 CDS 5' incomplete
ENST00000550903.5	PPP1R12A-217	959	161aa	Nonsense mediated decay		H0YIL7	-	TSL:5 CDS 5' incomplete
ENST00000548908.3	PPP1R12A-210	3064	No protein	Retained intron		-	-	TSL:5
ENST00000552892.1	PPP1R12A-220	2277	No protein	Retained intron		-	-	TSL:2
ENST00000550351.5	PPP1R12A-215	738	No protein	Retained intron		-	-	TSL:2
ENST00000547253.5	PPP1R12A-207	676	No protein	Retained intron		-	-	TSL:2
ENST00000550001.1	PPP1R12A-211	631	No protein	Retained intron		-	-	TSL:5
ENST00000551781.2	PPP1R12A-219	629	No protein	Retained intron		-	-	TSL:5
ENST00000551191.1	PPP1R12A-218	602	No protein	Retained intron		-	-	TSL:3
ENST00000550007.1	PPP1R12A-212	443	No protein	Retained intron		-	-	TSL:2

Figure 3.2 Ensemble Genome Browser of *PPP1R12A* gene transcripts. Image taken from ensemble gene browser (https://www.ensembl.org/Homo_sapiens/Gene/Splice?db=core;g=ENSG00000058272;r=12:79773563-79935460). This database lists the alternative splicing transcripts, nonsense mediated decay transcripts and retained intron transcripts.

Table 3.1 *PPP1R12A* transcripts and protein variants as annotated in Ensemble and GenBank. All transcripts are supported by EST and/or mRNA sequences and for the protein coding variants also by RNAseq data, with the exception of transcript PPP1R12A-223, which is only supported by RNAseq data. The variant considered canonical in Uniprot uses all coding exons except $E9^+$, E24 and exons only found in nonsense-mediated decay transcripts ($E2^+$, $E20^+$ and $E22^+$). Transcript PPP1R12A-209 is annotated as protein coding but is more likely a nonsense-mediated decay transcript. Most Ensemble transcripts are incomplete and have been extended as shown in Figure 3.3 to calculate the predicted protein isoforms.

Ensembl (GenBank) transcript	Type	Splicing	Protein isoform (predicted length) (GenBank isoform)
PPP1R12A-201 (NM_001143885.2, variant 2)	Protein coding	Canonical, start at $E1^-$	FL (1030) (isoform a)
PPP1R12A-202 (NM_001244990.2, variant 4)	Protein coding	E22 out, start at $E1^-$	ΔE22 (995) (isoform c)
PPP1R12A-203 (NM_002480.3, variant 1)	Protein coding	Canonical, start at E1	FL (1030) (isoform a)
PPP1R12A-204 (NM_001143886.2, variant 3)	Protein coding	Start at $E1^+$	ΔN (943) (isoform b)
PPP1R12A-205	Nonsense-mediated decay	$E22^+$ in	
PPP1R12A-206	Protein coding	E13+E14 out	ΔE13+14 (915)
PPP1R12A-207	Retained intron		
PPP1R12A-208	Protein coding	E14 out	ΔE14 (971)
PPP1R12A-209	Protein coding (Nonsense-mediated decay)	$E2^+$ in	
PPP1R12A-210	Retained intron		
PPP1R12A-211	Retained intron		
PPP1R12A-212	Retained intron		
PPP1R12A-213 (NM_001244992.1, variant 5)	Protein coding	E13 out	ΔE13 (974) (isoform d)
PPP1R12A-214	Protein coding	E24 in (31 bp variant)	LZ^-a (1005)
PPP1R12A-215	Retained intron		
PPP1R12A-216	Protein coding	E6 out	ΔE6 (1005)
PPP1R12A-217	Nonsense-mediated decay	$E20^+$ in	
PPP1R12A-218	Retained intron		
PPP1R12A-219	Retained intron		
PPP1R12A-220	Retained intron		
PPP1R12A-221	Protein coding	Alternative splicing acceptor site in E13	E13b (1018)
PPP1R12A-222	Protein coding	E24 in (13 bp variant)	LZ^-b (999)
PPP1R12A-223	Protein coding	$E9^+$ in	E9+ (1062)

Taking into consideration only protein coding transcripts in Ensemble, 11 were identified, each encoding a predicted MYPT1 isoform. The exon composition of each protein coding transcript and their proposed names are shown in Figure 3.3. A multiple alignment of all predicted isoforms is shown in Figure 3.4. The information available in GenBank does not support the presence of variants simultaneously carrying more than one alternatively spliced coding exon, however that information is restricted to just 14 mRNA or cDNA sequences >1 kb in length along the coding region of *PPP1R12A*. These include complete coding regions for FL, ΔE13, ΔE22 and ΔN and almost complete for ΔE14. No mRNA/cDNA sequences cover ΔE6, E9+, ΔE13+14, LZ$^-$a and LZ$^-$b variants. There is evidence of a transcription start at E1$^-$ in the FL and ΔE22 variants, but the use of the P1$^-$ region by other transcripts cannot be ruled out.

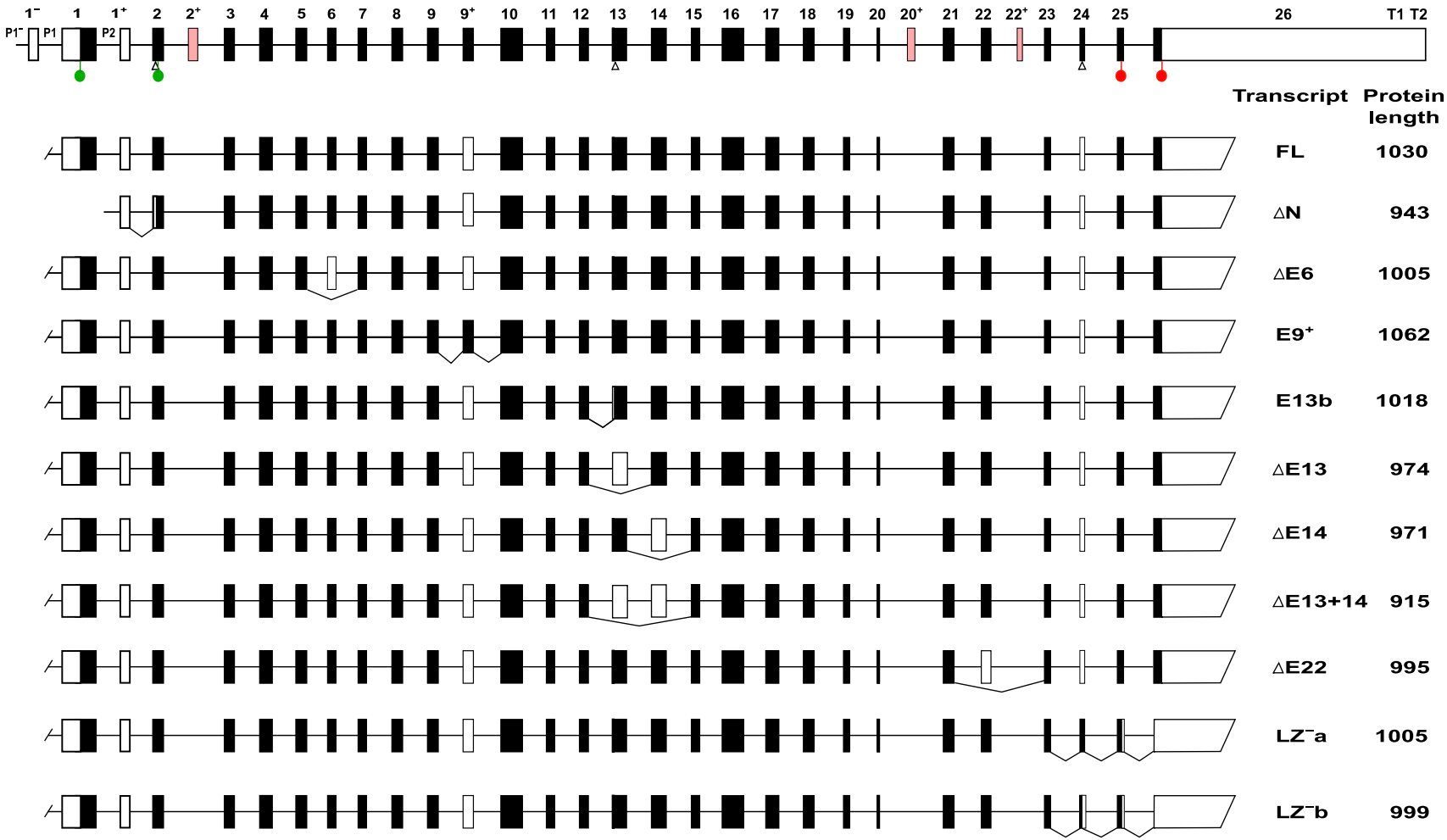

Figure3.3 Figure legend following on the next page.

Figure 3.3 Transcription variants of *PPP1R12A*. The top is a schematic representation of the *PPP1R12A* gene based on our analysis of data from Ensemble and GenBank. Only exons are depicted at scale. White boxes represent UTRs or spliced out exons, black boxes represent translated regions. Salmon boxes are exons found in nonsense-mediated decay transcripts. Triangles below E2, E13 and E24 indicate alternative acceptor splice sites. Green and red circles indicate translation start and stops, respectively. P and T denote promoter and terminator regions. Transcripts are truncated at both ends because there is insufficient information to assign particular promoters or terminators to specific transcripts. The scheme does not take into account possible combinations of alternatively spliced exons, for which there is no support (adapted from Figure 2 from (Saldanha et al., 2022)).


E1
MyPhone
KVKF motif
E2
FL MQMADAKQKRNEQLKRWIGSETDLEPPVVKRQKTKVKFDDGAVFLAACSSGDTDEVLKLLHRGADINYANVDGLTALHQACIDDNVDMVKFLVENGANINQPDNEGWIPLHAAASCGYLD 120
DN ----------MVKFLVENGANINQPDNEGWIPLHAAASCGYLD 33
DE6 MKMADAKQKRNEQLKRWIGSETDLEPPVVKRQKTKVKFDDGAVFLAACSSGDTDEVLKLLHRGADINYANVDGLTALHQACIDDNVDMVKFLVENGANINQPDNEGWIPLHAAASCGYLD 120
E9+ MKMADAKQKRNEQLKRWIGSETDLEPPVVKRQKTKVKFDDGAVFLAACSSGDTDEVLKLLHRGADINYANVDGLTALHQACIDDNVDMVKFLVENGANINQPDNEGWIPLHAAASCGYLD 120
DE13 MKMADAKQKRNEQLKRWIGSETDLEPPVVKRQKTKVKFDDGAVFLAACSSGDTDEVLKLLHRGADINYANVDGLTALHQACIDDNVDMVKFLVENGANINQPDNEGWIPLHAAASCGYLD 120
E13b MKMADAKQKRNEQLKRWIGSETDLEPPVVKRQKTKVKFDDGAVFLAACSSGDTDEVLKLLHRGADINYANVDGLTALHQACIDDNVDMVKFLVENGANINQPDNEGWIPLHAAASCGYLD 120
DE14 MKMADAKQKRNEQLKRWIGSETDLEPPVVKRQKTKVKFDDGAVFLAACSSGDTDEVLKLLHRGADINYANVDGLTALHQACIDDNVDMVKFLVENGANINQPDNEGWIPLHAAASCGYLD 120
DE13+14 MKMADAKQKRNEQLKRWIGSETDLEPPVVKRQKTKVKFDDGAVFLAACSSGDTDEVLKLLHRGADINYANVDGLTALHQACIDDNVDMVKFLVENGANINQPDNEGWIPLHAAASCGYLD 120
DE22 MKMADAKQKRNEQLKRWIGSETDLEPPVVKRQKTKVKFDDGAVFLAACSSGDTDEVLKLLHRGADINYANVDGLTALHQACIDDNVDMVKFLVENGANINQPDNEGWIPLHAAASCGYLD 120
LZ-a MKMADAKQKRNEQLKRWIGSETDLEPPVVKRQKTKVKFDDGAVFLAACSSGDTDEVLKLLHRGADINYANVDGLTALHQACIDDNVDMVKFLVENGANINQPDNEGWIPLHAAASCGYLD 120
LZ-b MKMADAKQKRNEQLKRWIGSETDLEPPVVKRQKTKVKFDDGAVFLAACSSGDTDEVLKLLHRGADINYANVDGLTALHQACIDDNVDMVKFLVENGANINQPDNEGWIPLHAAASCGYLD 120
E3
E4
Ankyrin repeats
E5
FL IAEFLIGQGAHVGAVNSEGDTPLDIAEEEAMEELLQNEVNRQGVDIEAARKEEERIMLRDARQWLNSGHINDVRHAKSGGTALHVAAAKGYTEVLKLLIQAGYDVNIKDYDGWTPLHAAA 240
DN IAEFLIGQGAHVGAVNSEGDTPLDIAEEEAMEELLQNEVNRQGVDIEAARKEEERIMLRDARQWLNSGHINDVRHAKSGGTALHVAAAKGYTEVLKLLIQAGYDVNIKDYDGWTPLHAAA 153
DE6 IAEFLIGQGAHVGAVNSEGDTPLDIAEEEAMEELLQNEVNRQGVDIEAARKEEERIMLRDARQWLNSGHINDVRHAKSGGTALHVAAAKGYTEVLKLLIQAGYDVNIKDYDGWTPLHAAA 240
E9+ IAEFLIGQGAHVGAVNSEGDTPLDIAEEEAMEELLQNEVNRQGVDIEAARKEEERIMLRDARQWLNSGHINDVRHAKSGGTALHVAAAKGYTEVLKLLIQAGYDVNIKDYDGWTPLHAAA 240
DE13 IAEFLIGQGAHVGAVNSEGDTPLDIAEEEAMEELLQNEVNRQGVDIEAARKEEERIMLRDARQWLNSGHINDVRHAKSGGTALHVAAAKGYTEVLKLLIQAGYDVNIKDYDGWTPLHAAA 240
E13b IAEFLIGQGAHVGAVNSEGDTPLDIAEEEAMEELLQNEVNRQGVDIEAARKEEERIMLRDARQWLNSGHINDVRHAKSGGTALHVAAAKGYTEVLKLLIQAGYDVNIKDYDGWTPLHAAA 240
DE14 IAEFLIGQGAHVGAVNSEGDTPLDIAEEEAMEELLQNEVNRQGVDIEAARKEEERIMLRDARQWLNSGHINDVRHAKSGGTALHVAAAKGYTEVLKLLIQAGYDVNIKDYDGWTPLHAAA 240
DE13+14 IAEFLIGQGAHVGAVNSEGDTPLDIAEEEAMEELLQNEVNRQGVDIEAARKEEERIMLRDARQWLNSGHINDVRHAKSGGTALHVAAAKGYTEVLKLLIQAGYDVNIKDYDGWTPLHAAA 240
DE22 IAEFLIGQGAHVGAVNSEGDTPLDIAEEEAMEELLQNEVNRQGVDIEAARKEEERIMLRDARQWLNSGHINDVRHAKSGGTALHVAAAKGYTEVLKLLIQAGYDVNIKDYDGWTPLHAAA 240
LZ-a IAEFLIGQGAHVGAVNSEGDTPLDIAEEEAMEELLQNEVNRQGVDIEAARKEEERIMLRDARQWLNSGHINDVRHAKSGGTALHVAAAKGYTEVLKLLIQAGYDVNIKDYDGWTPLHAAA 240
LZ-b IAEFLIGQGAHVGAVNSEGDTPLDIAEEEAMEELLQNEVNRQGVDIEAARKEEERIMLRDARQWLNSGHINDVRHAKSGGTALHVAAAKGYTEVLKLLIQAGYDVNIKDYDGWTPLHAAA 240

```
                                E6                      E7                      E8
FL        HWGKEEACRILVDNLCDMEMVNKVGQTAFDVADEDILGYLEELQKKQNLLHSEKRDKKSPLIESTANMDNNQSQKTFKNKETLIIEPEKNASRIESLEQEKVDEEEEGKKDESSCSSEED 360
DN        HWGKEEACRILVDNLCDMEMVNKVGQTAFDVADEDILGYLEELQKKQNLLHSEKRDKKSPLIESTANMDNNQSQKTFKNKETLIIEPEKNASRIESLEQEKVDEEEEGKKDESSCSSEED 273
DE6       HWGKEEACRILVDNLCDMEMVNKV------------------------LHSEKRDKKSPLIESTANMDNNQSQKTFKNKETLIIEPEKNASRIESLEQEKVDEEEEGKKDESSCSSEED 335
E9+       HWGKEEACRILVDNLCDMEMVNKVGQTAFDVADEDILGYLEELQKKQNLLHSEKRDKKSPLIESTANMDNNQSQKTFKNKETLIIEPEKNASRIESLEQEKVDEEEEGKKDESSCSSEED 360
DE13      HWGKEEACRILVDNLCDMEMVNKVGQTAFDVADEDILGYLEELQKKQNLLHSEKRDKKSPLIESTANMDNNQSQKTFKNKETLIIEPEKNASRIESLEQEKVDEEEEGKKDESSCSSEED 360
E13b      HWGKEEACRILVDNLCDMEMVNKVGQTAFDVADEDILGYLEELQKKQNLLHSEKRDKKSPLIESTANMDNNQSQKTFKNKETLIIEPEKNASRIESLEQEKVDEEEEGKKDESSCSSEED 360
DE14      HWGKEEACRILVDNLCDMEMVNKVGQTAFDVADEDILGYLEELQKKQNLLHSEKRDKKSPLIESTANMDNNQSQKTFKNKETLIIEPEKNASRIESLEQEKVDEEEEGKKDESSCSSEED 360
DE13+14   HWGKEEACRILVDNLCDMEMVNKVGQTAFDVADEDILGYLEELQKKQNLLHSEKRDKKSPLIESTANMDNNQSQKTFKNKETLIIEPEKNASRIESLEQEKVDEEEEGKKDESSCSSEED 360
DE22      HWGKEEACRILVDNLCDMEMVNKVGQTAFDVADEDILGYLEELQKKQNLLHSEKRDKKSPLIESTANMDNNQSQKTFKNKETLIIEPEKNASRIESLEQEKVDEEEEGKKDESSCSSEED 360
LZ-a      HWGKEEACRILVDNLCDMEMVNKVGQTAFDVADEDILGYLEELQKKQNLLHSEKRDKKSPLIESTANMDNNQSQKTFKNKETLIIEPEKNASRIESLEQEKVDEEEEGKKDESSCSSEED 360
LZ-b      HWGKEEACRILVDNLCDMEMVNKVGQTAFDVADEDILGYLEELQKKQNLLHSEKRDKKSPLIESTANMDNNQSQKTFKNKETLIIEPEKNASRIESLEQEKVDEEEEGKKDESSCSSEED 360

               E9                                      E9+                              E10
FL        EEDDSESEAETDKTKPLASVTNANTSSTQAAPVAVTTPTVSSGQATPTSPIKK---------------------------------FPTTATKISPKEEERKDESPATWRLGLRKTGSYGA 448
DN        EEDDSESEAETDKTKPLASVTNANTSSTQAAPVAVTTPTVSSGQATPTSPIKK---------------------------------FPTTATKISPKEEERKDESPATWRLGLRKTGSYGA 361
DE6       EEDDSESEAETDKTKPLASVTNANTSSTQAAPVAVTTPTVSSGQATPTSPIKK---------------------------------FPTTATKISPKEEERKDESPATWRLGLRKTGSYGA 423
E9+       EEDDSESEAETDKTKPLASVTNANTSSTQAAPVAVTTPTVSSGQATPTSPIKKMPVVESVDPASWRQGLRTKGIVLVPSKGEKSMFPTTATKISPKEEERKDESPATWRLGLRKTGSYGA 480
DE13      EEDDSESEAETDKTKPLASVTNANTSSTQAAPVAVTTPTVSSGQATPTSPIKK---------------------------------FPTTATKISPKEEERKDESPATWRLGLRKTGSYGA 448
E13b      EEDDSESEAETDKTKPLASVTNANTSSTQAAPVAVTTPTVSSGQATPTSPIKK---------------------------------FPTTATKISPKEEERKDESPATWRLGLRKTGSYGA 448
DE14      EEDDSESEAETDKTKPLASVTNANTSSTQAAPVAVTTPTVSSGQATPTSPIKK---------------------------------FPTTATKISPKEEERKDESPATWRLGLRKTGSYGA 448
DE13+14   EEDDSESEAETDKTKPLASVTNANTSSTQAAPVAVTTPTVSSGQATPTSPIKK---------------------------------FPTTATKISPKEEERKDESPATWRLGLRKTGSYGA 448
DE22      EEDDSESEAETDKTKPLASVTNANTSSTQAAPVAVTTPTVSSGQATPTSPIKK---------------------------------FPTTATKISPKEEERKDESPATWRLGLRKTGSYGA 448
LZ-a      EEDDSESEAETDKTKPLASVTNANTSSTQAAPVAVTTPTVSSGQATPTSPIKK---------------------------------FPTTATKISPKEEERKDESPATWRLGLRKTGSYGA 448
LZ-b      EEDDSESEAETDKTKPLASVTNANTSSTQAAPVAVTTPTVSSGQATPTSPIKK---------------------------------FPTTATKISPKEEERKDESPATWRLGLRKTGSYGA 448
```

```
                                                E11                                                 E12                                                 E13         E13b
FL        LAEITASKEGQKEKDTAGVTRSASSPRLSSSLDNKEKEKDSKGTRLAYVAPTIPRRLASTSDIEEKENRDSSSLRTSSSYTRRKWEDDLKKNSSVNEGSTYHKSCSFGRRQDDLISSSVP 568
DN        LAEITASKEGQKEKDTAGVTRSASSPRLSSSLDNKEKEKDSKGTRLAYVAPTIPRRLASTSDIEEKENRDSSSLRTSSSYTRRKWEDDLKKNSSVNEGSTYHKSCSFGRRQDDLISSSVP 481
DE6       LAEITASKEGQKEKDTAGVTRSASSPRLSSSLDNKEKEKDSKGTRLAYVAPTIPRRLASTSDIEEKENRDSSSLRTSSSYTRRKWEDDLKKNSSVNEGSTYHKSCSFGRRQDDLISSSVP 543
E9+       LAEITASKEGQKEKDTAGVTRSASSPRLSSSLDNKEKEKDSKGTRLAYVAPTIPRRLASTSDIEEKENRDSSSLRTSSSYTRRKWEDDLKKNSSVNEGSTYHKSCSFGRRQDDLISSSVP 600
DE13      LAEITASKEGQKEKDTAGVTRSASSPRLSSSLDNKEKEKDSKGTRLAYVAPTIPRRLASTSDIEEKENRDSSSLRTSSSYTRRKWEDDLKKNSSVNEGSTYHK---------------- 551
E13b      LAEITASKEGQKEKDTAGVTRSASSPRLSSSLDNKEKEKDSKGTRLAYVAPTIPRRLASTSDIEEKENRDSSSLRTSSSYTRRKWEDDLKKNSSVNEGSTYHK------------SSSVP 556
DE14      LAEITASKEGQKEKDTAGVTRSASSPRLSSSLDNKEKEKDSKGTRLAYVAPTIPRRLASTSDIEEKENRDSSSLRTSSSYTRRKWEDDLKKNSSVNEGSTYHKSCSFGRRQDDLISSSVP 568
DE13+14   LAEITASKEGQKEKDTAGVTRSASSPRLSSSLDNKEKEKDSKGTRLAYVAPTIPRRLASTSDIEEKENRDSSSLRTSSSYTRRKWEDDLKKNSSVNEGSTYHK---------------- 551
DE22      LAEITASKEGQKEKDTAGVTRSASSPRLSSSLDNKEKEKDSKGTRLAYVAPTIPRRLASTSDIEEKENRDSSSLRTSSSYTRRKWEDDLKKNSSVNEGSTYHKSCSFGRRQDDLISSSVP 568
LZ-a      LAEITASKEGQKEKDTAGVTRSASSPRLSSSLDNKEKEKDSKGTRLAYVAPTIPRRLASTSDIEEKENRDSSSLRTSSSYTRRKWEDDLKKNSSVNEGSTYHKSCSFGRRQDDLISSSVP 568
LZ-b      LAEITASKEGQKEKDTAGVTRSASSPRLSSSLDNKEKEKDSKGTRLAYVAPTIPRRLASTSDIEEKENRDSSSLRTSSSYTRRKWEDDLKKNSSVNEGSTYHKSCSFGRRQDDLISSSVP 568

                                                  E14     Central insert                                                  E15
FL        STTSTPTVTSAAGLQKSLLSSTSTTTKITTGSSSAGTQSSTSNRLWAEDSTEKEKDSVPTAVTIPVAPTVVNAAASTTTLTTTTAGTVSSTTEVRERRRSYLTPVRDEESESQRKARSRQ 688
DN        STTSTPTVTSAAGLQKSLLSSTSTTTKITTGSSSAGTQSSTSNRLWAEDSTEKEKDSVPTAVTIPVAPTVVNAAASTTTLTTTTAGTVSSTTEVRERRRSYLTPVRDEESESQRKARSRQ 601
DE6       STTSTPTVTSAAGLQKSLLSSTSTTTKITTGSSSAGTQSSTSNRLWAEDSTEKEKDSVPTAVTIPVAPTVVNAAASTTTLTTTTAGTVSSTTEVRERRRSYLTPVRDEESESQRKARSRQ 663
E9+       STTSTPTVTSAAGLQKSLLSSTSTTTKITTGSSSAGTQSSTSNRLWAEDSTEKEKDSVPTAVTIPVAPTVVNAAASTTTLTTTTAGTVSSTTEVRERRRSYLTPVRDEESESQRKARSRQ 720
DE13      ----------------------------------------STSNRLWAEDSTEKEKDSVPTAVTIPVAPTVVNAAASTTTLTTTTAGTVSSTTEVRERRRSYLTPVRDEESESQRKARSRQ 632
E13b      STTSTPTVTSAAGLQKSLLSSTSTTTKITTGSSSAGTQSSTSNRLWAEDSTEKEKDSVPTAVTIPVAPTVVNAAASTTTLTTTTAGTVSSTTEVRERRRSYLTPVRDEESESQRKARSRQ 676
DE14      STTSTPTVTSAAGLQKSLLSSTSTTTKITTGSSSAGTQS----------------------------------------------------------------RSYLTPVRDEESESQRKARSRQ 629
DE13+14   ----------------------------------------------------------------------------------------------------RSYLTPVRDEESESQRKARSRQ 573
DE22      STTSTPTVTSAAGLQKSLLSSTSTTTKITTGSSSAGTQSSTSNRLWAEDSTEKEKDSVPTAVTIPVAPTVVNAAASTTTLTTTTAGTVSSTTEVRERRRSYLTPVRDEESESQRKARSRQ 688
LZ-a      STTSTPTVTSAAGLQKSLLSSTSTTTKITTGSSSAGTQSSTSNRLWAEDSTEKEKDSVPTAVTIPVAPTVVNAAASTTTLTTTTAGTVSSTTEVRERRRSYLTPVRDEESESQRKARSRQ 688
LZ-b      STTSTPTVTSAAGLQKSLLSSTSTTTKITTGSSSAGTQSSTSNRLWAEDSTEKEKDSVPTAVTIPVAPTVVNAAASTTTLTTTTAGTVSSTTEVRERRRSYLTPVRDEESESQRKARSRQ 688

                    E16                                                                                                 E17
FL        ARQSRRSTQGVTLTDLQEAEKTIGRSRSTRTREQENEEKEKEEKEKQDKEKQEEKKESETSREDEYKQKYSRTYDETYQRYRPVSTSSSTTPSSSLSTMSSSLYASSQLNRPNSLVGITS 808
DN        ARQSRRSTQGVTLTDLQEAEKTIGRSRSTRTREQENEEKEKEEKEKQDKEKQEEKKESETSREDEYKQKYSRTYDETYQRYRPVSTSSSTTPSSSLSTMSSSLYASSQLNRPNSLVGITS 721
DE6       ARQSRRSTQGVTLTDLQEAEKTIGRSRSTRTREQENEEKEKEEKEKQDKEKQEEKKESETSREDEYKQKYSRTYDETYQRYRPVSTSSSTTPSSSLSTMSSSLYASSQLNRPNSLVGITS 783
E9+       ARQSRRSTQGVTLTDLQEAEKTIGRSRSTRTREQENEEKEKEEKEKQDKEKQEEKKESETSREDEYKQKYSRTYDETYQRYRPVSTSSSTTPSSSLSTMSSSLYASSQLNRPNSLVGITS 840
DE13      ARQSRRSTQGVTLTDLQEAEKTIGRSRSTRTREQENEEKEKEEKEKQDKEKQEEKKESETSREDEYKQKYSRTYDETYQRYRPVSTSSSTTPSSSLSTMSSSLYASSQLNRPNSLVGITS 752
E13b      ARQSRRSTQGVTLTDLQEAEKTIGRSRSTRTREQENEEKEKEEKEKQDKEKQEEKKESETSREDEYKQKYSRTYDETYQRYRPVSTSSSTTPSSSLSTMSSSLYASSQLNRPNSLVGITS 796
DE14      ARQSRRSTQGVTLTDLQEAEKTIGRSRSTRTREQENEEKEKEEKEKQDKEKQEEKKESETSREDEYKQKYSRTYDETYQRYRPVSTSSSTTPSSSLSTMSSSLYASSQLNRPNSLVGITS 749
DE13+14   ARQSRRSTQGVTLTDLQEAEKTIGRSRSTRTREQENEEKEKEEKEKQDKEKQEEKKESETSREDEYKQKYSRTYDETYQRYRPVSTSSSTTPSSSLSTMSSSLYASSQLNRPNSLVGITS 693
DE22      ARQSRRSTQGVTLTDLQEAEKTIGRSRSTRTREQENEEKEKEEKEKQDKEKQEEKKESETSREDEYKQKYSRTYDETYQRYRPVSTSSSTTPSSSLSTMSSSLYASSQLNRPNSLVGITS 808
LZ-a      ARQSRRSTQGVTLTDLQEAEKTIGRSRSTRTREQENEEKEKEEKEKQDKEKQEEKKESETSREDEYKQKYSRTYDETYQRYRPVSTSSSTTPSSSLSTMSSSLYASSQLNRPNSLVGITS 808
LZ-b      ARQSRRSTQGVTLTDLQEAEKTIGRSRSTRTREQENEEKEKEEKEKQDKEKQEEKKESETSREDEYKQKYSRTYDETYQRYRPVSTSSSTTPSSSLSTMSSSLYASSQLNRPNSLVGITS 808
```

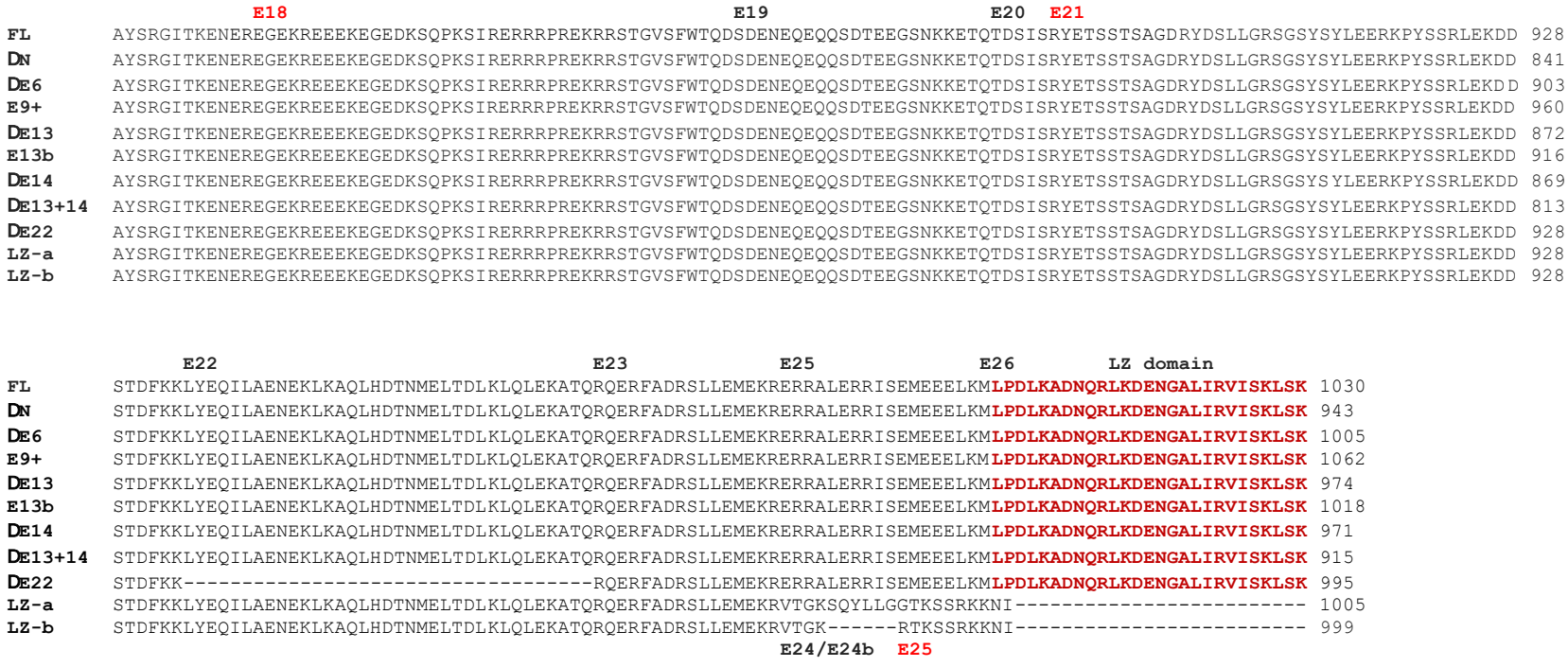

Figure 3.4 Multiple alignment of predicted human MYPT1 protein isoforms. The alignment was constructed using the Clustal Omega program at Uniprot. Exon boundaries are indicated on top of the alignment except for the LZ$^-$ variants, that are at the bottom. Phase 0 exons (between codons) are labelled in black and phase 1 or 2 exons (after the first or second base of a codon) in red. Domains and motifs are shown in different colours (Figure 3 from (Saldanha et al., 2022)).

3.2.2. Transcription of *PPP1R12A* is driven by three promoter regions.

The *Ensembl* database suggests the existence of two transcription initiation sites for *PPP1R12A* in addition to the one reported by Machida et al. (2001) (Figure 3.5 A). The EST database information was examined to gather detailed information of these promoter regions. The analysis started with the transcripts beginning immediately upstream of the first coding exon (E1), PPP1R12A-203 and 208. A BLASTn search with the UTR of the 208 transcript (267 bp) revealed a large number of EST clones (141) in support of this transcription start region, indicating its frequent usage (Figure 3.6 A). Transcription start sites accumulate in a region 166-266 bp upstream of the start codon.

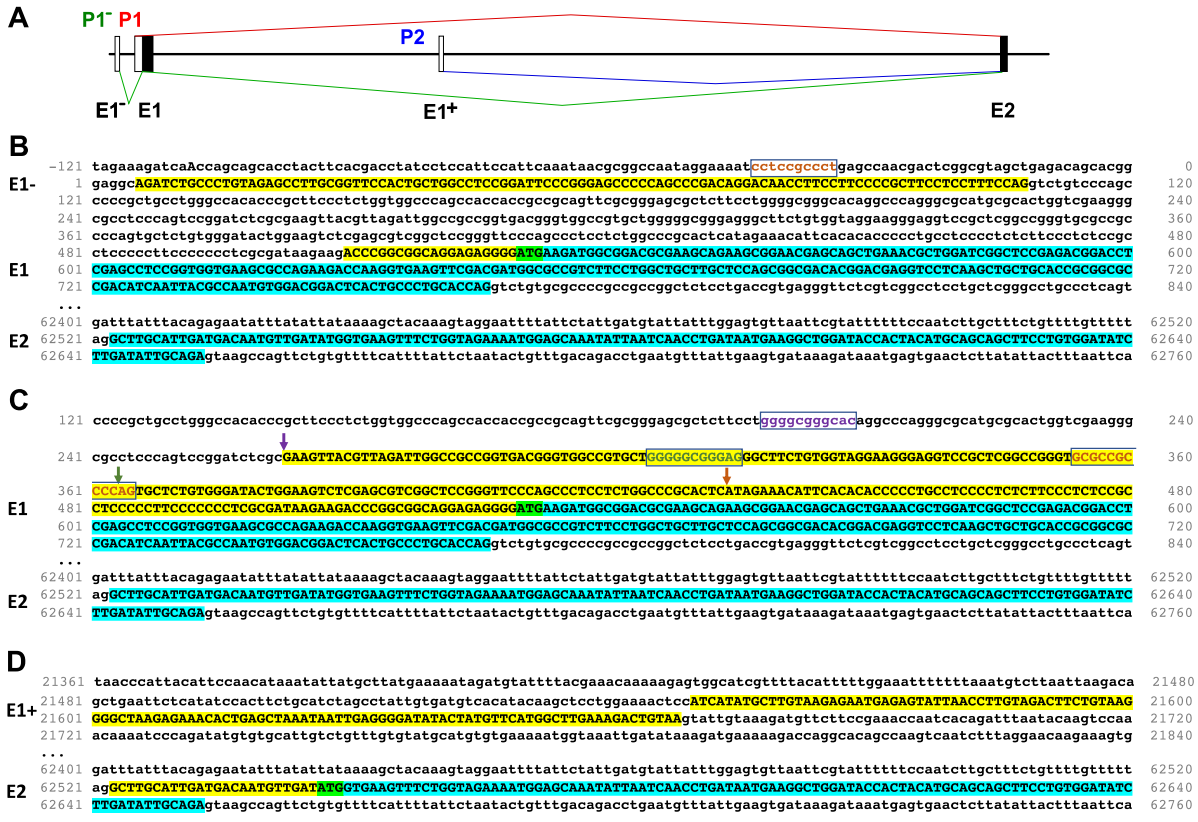

Figure 3.5. Predicted transcription start regions of *PPP1R12A*. (A) Schematic representation of the transcription start regions (P) based on Ensemble annotation. Distances between exons (E) are depicted at scale, except between E1^{-} and E1 for clarity. Black and white boxes represent translated or untranslated regions, respectively. Splicing arising from each promoter is indicated in a different colour**. (B)** Transcription start at the P1^{-} region as per transcripts PPP1R12A-201 and 202. **(C)** Transcription starts at the P1 region as per transcripts PPP1R12A-203 and 208. **(D)** Transcription start at the P2 region as per transcript PPP1R12A-204. Transcribed DNA appears in upper case, of which translated DNA is highlighted in turquoise and untranslated DNA in yellow. Exon numbers are indicated on the left-hand side. Predicted start codons are highlighted in green. Predicted Sp1 binding sites are framed and in coloured fonts. Arrows in B indicate transcription start sites and are coloured like the Sp1 binding site immediately upstream. DNA numbering is as per transcript PPP1R12A-202 (Figure 1 from (Saldanha et al., 2022)).

Three clusters of transcripts starting 96, 166 and 267 bp upstream of the start codon indicate the presence of three alternative transcription start sites in the P1 region (Figure 3.6 A and Figure 3.5 B). Transcripts PPP1R12A-201 and 202 start upstream of E1. This exon, that was denominated E1^{-} (in order to preserve the exon nomenclature commonly used in the literature) is spliced into E1, leaving out a short (401 bp) intron

and using the same translation start as transcripts PPP1R12A-203 and 208 (Figure 3.5 C). A BLASTn search with $E1^-$ plus 20 bp of the E1 UTR showed three clones clearly documenting the existence of an infrequently (<0.1%) used promoter upstream of P1 (Figure 3.6 B, C and Appendix Table 8.1-1) that was named $P1^-$. Of note, the region comprising $P1^-$ and P1 overlaps with transcripts of the antisense gene *PPP1R12A-AS1* that can be distinguished by their opposite orientation. *PPP1R12A-AS1* encodes a long noncoding RNA (lncRNA). Studies have demonstrated lncRNAs role in regulating gene expression through their impact on transcription and mRNA stability. (Pelechano and Steinmetz, 2013, Tufarelli et al., 2003, Latos et al., 2012, Faghihi et al., 2008, Schein et al., 2016). It has been demonstrated by Schein et al. (2016) that this antisense gene functions as a SINEUP (short interspersed nuclear element-containing translation up-regulators) in human cells, increasing the translation of its target *PPP1R12A* mRNA. This study has also shown that this antisense gene is expressed at highest levels in blood cells and neural tissue while limited expression was found within particular cell types, suggesting a potential regulatory role (Schein et al., 2016). Thus, it should not be ruled out that this antisense gene might play a regulatory role on *PP1R12A* expression driven by $P1^-$.

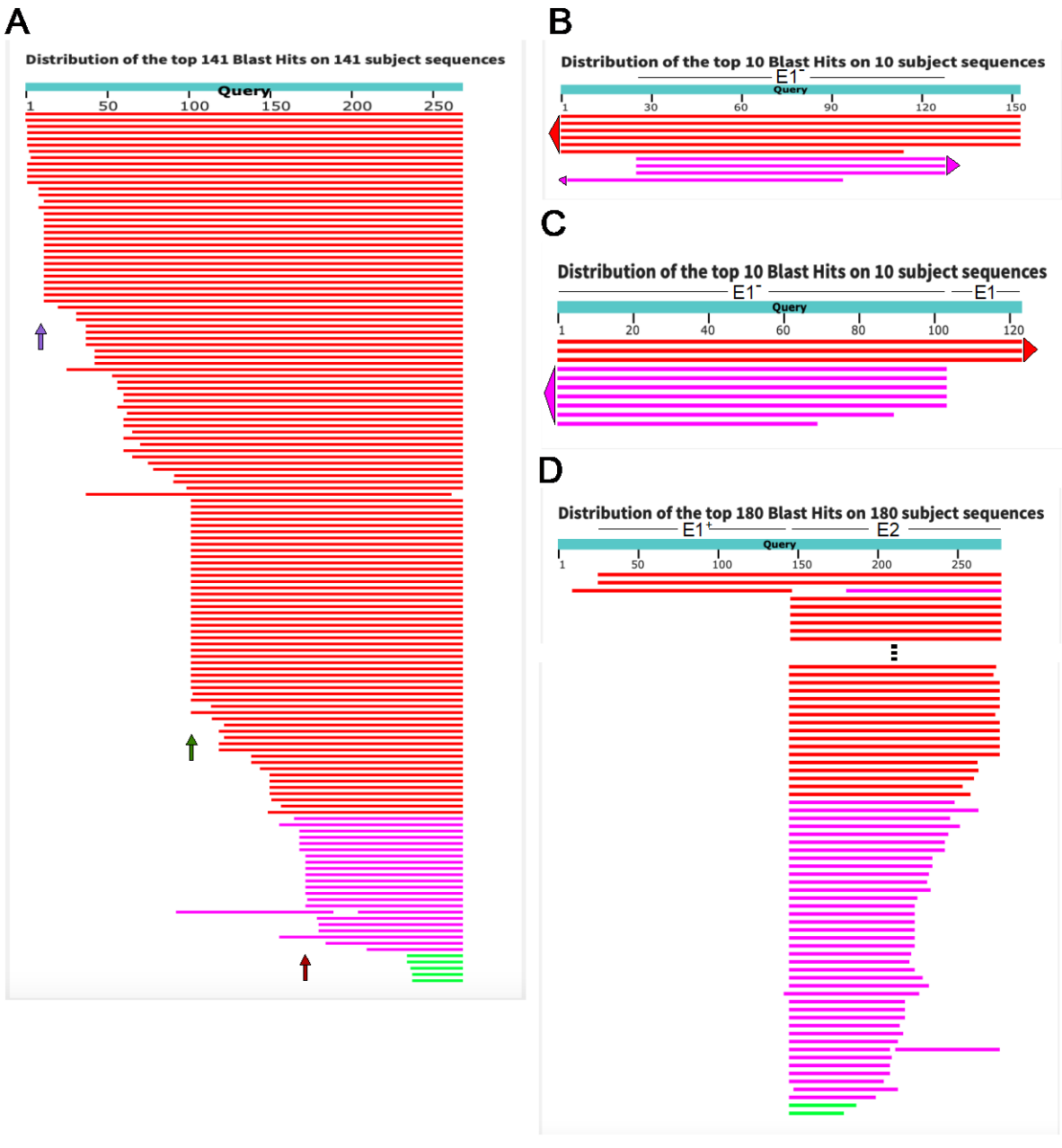

Figure 3.6 Legend on the following page

Figure 3.6 Results of BLASTn searches for ESTs in the transcription start regions of *PPP1R12A*. Horizontal bars represent the extent of the alignment of the database sequences to the query sequence and are colour-coded by score: red, pink, and green from highest to lowest. **(A)** EST support for a transcription start in E1. The human EST database was interrogated with the sequences corresponding to the UTR of E1 as per transcript PPP1PR12-208. Arrows indicate predicted transcription start sites and are coloured like in Figure 3.5 C. (B and C) EST support for a transcription start variant at E1$^-$. In **(B)** the human EST database was interrogated with the sequence corresponding to E1$^-$ flanked by 25 bases of genomic/intron sequence. The arrowheads indicate the directionality of the clones. Three hits read towards the right and encompass only the E1$^-$ sequence. The rest read in the opposite direction and correspond to the overlapping antisense gene *PPP1R12A-AS1*. In **(C)** the human EST database was interrogated with the sequences corresponding to E1$^-$ and 20 bases of E1 as per transcript PPP1R12A-201. The hits are the same as in panel B: the three top ones correspond to EST clones that contain E1$^-$ and splice E1$^-$ into E1, the rest correspond to *PPP1R12A-AS1*. **(D)** Support for a transcription start variant at E1$^+$. The human EST database was interrogated with the sequences corresponding to E1$^+$-E2 flanked by 25 bases of genomic/intron sequence before E1$^+$. The output has been truncated (dashed line). The two top hits correspond to EST clones that include E1$^+$. One EST that covers only E1$^+$ is flanked by intron sequences and may correspond to amplification of contaminating genomic DNA (Figure S2 from (Saldanha et al., 2022)).

The P1$^-$-P1 region is GC-rich and harbours an accumulation of regulatory elements (Ensemble Genome Browser). Sp1 has been shown to bind to this GC-rich promoter region and two Sp1 binding sites were identified (Machida et al., 2001). The region was scanned with the ALGGEN-PROMO website for Sp1 sites and identified a total of four sites with a percentage of dissimilarity below 5%, two in addition to the ones previously recognised by Machida et al. (2001), (Machida et al., 2001). These sites are each placed, approximately 40-60 bases, upstream of one of the transcription start sites in the P1$^-$-P1 region (Figure 3.5 B, C).

Transcript PPP1R12A-204 indicates a transcription start within intron 1, approximately 21 kb downstream of E1. This transcript includes a non-coding exon (that was named E1$^+$) that splices into E2, shifting the start codon 261 bases downstream of the common start and producing a predicted protein lacking the first 87 residues of the full-length protein (Figure 3.5 D). The name for this predicted protein isoform is ΔN. A BLASTn search with the sequences corresponding to E1$^+$ and E2 revealed only two EST clones supporting the existence of an infrequently used promoter region that was called P2 (Figure 3.6 D and Appendix Table 8.1-1). Unlike the P1$^-$-P1 region, the DNA immediately upstream of E1$^+$ is not GC-rich.

3.2.3. *PPP1R12A* transcripts with non-canonical exons

Four *PPP1R12A* transcripts in the Ensembl database predict exons not annotated in GenBank within introns 2, 9, 20 and 22. These exons were named exons E2$^+$, E9$^+$, E20$^+$ and E22$^+$, in order to preserve the exon nomenclature commonly used in the literature (section 3.1.2, Table 3.1, Figure 3.6). Transcripts including E20$^+$ (PPP1R12A-217) and E22$^+$ (PPP1R12A-205) are annotated as nonsense-mediated decay. Transcripts including E2$^+$ (PPP1R12A-209) and E9$^+$ (PPP1R12A-223) are annotated as protein coding, however PPP1R12A-209 also revealed as nonsense-mediated decay transcript, as explained below. Transcripts using E2$^+$, E20$^+$ and E22$^+$ are very rare. PPP1R12A-223 will be considered in the next section on protein coding exons.

Transcript PPP1R12A-209 splices the 144 bp exon E2$^+$. A BLASTn search with the sequences corresponding to E2, E2$^+$ and E3 (Figure 3.7 A) reveal a single ESTs, BP279682.1 that includes the additional E2$^+$ while 90 ESTs in the search do not. The annotation in Ensemble identifies a start codon in E3 that matches the sequence of MYPT1 and interprets the sequences upstream as UTR. Transcript 209 appears to be solely based on the single BP279682.1 clone, which is probably incomplete. It appears more likely that the inclusion of the extra E2$^+$ would cause a shift to the canonical reading frame, introducing a premature stop codon, therefore this variant would be a nonsense mediated decay mRNA.

PPP1R12A-217 is a transcript that splices in the 83 bp exon E20$^+$ and causes a frame shift and a premature stop. To identify EST support for this splicing variant a BLASTn search with E19-E20-E20$^+$-E21. Here E19 was included due to the small size of E20, insufficient for significant alignments. This search revealed two clones that spliced in E20$^+$ (Figure 3.7 B, asterisks). One clone that only covers E20$^+$ (Figure 3.7 B, arrowhead) contains intron sequences upstream and downstream of that exon and may correspond to an intron retain clone.

PPP1R12A-205 splices in the 25 bp exon E22$^+$ and causes a frame shift and a premature stop. A search with E22-E22$^+$-E23 for EST support revealed a single sequence, BG180627.1, containing E22$^+$ (Figure 3.7 C, first hit with asterisk). The

second hit marked with an asterisk in the graph appears to correspond to a clone (BF980059.1) with anomalous splicing at the $E22^{+}$-E23 boundary. One clone that appears to include $E22^{+}$ (Figure 3.7 C, asterisk at bottom) turned out a misaligned sequence and two more that only cover $E22^{+}$ (Figure 3.7 C, arrowheads) contain intron sequences upstream and downstream of that exon and may correspond to intron retain transcripts.

Figure 3.7 Figure Legend on the following page

Figure 3.7 Results of BLASTn searches for ESTs in support of transcripts with non-canonical exons. Horizontal bars represent the extent of the alignment of the database sequences to the query sequence and are color-coded by score: red, pink, and green from highest to lowest. Separate aligned regions on the same database sequence are connected by a thin grey line. **(A)** EST support for a splicing variant with 144 bp exon $E2^+$ (transcript PPP1R12A-209). The EST database was interrogated with the sequences corresponding to E2–$E2^+$–E3. The search was limited to 100 hits and only the top 42 hits are shown. A single EST (asterisk) supports this transcript. **(B)** EST support for a splicing variant with 83 bp exon $E20^+$ (PPP1R12A-217). This exon causes a frame shift and a premature stop. The EST database was interrogated with the sequences corresponding to E19–E20–$E20^+$–E22. Here E19 was included due to the small size of E20, insufficient for significant alignments. This search revealed two clones that spliced in $E20^+$ (asterisks). The clone indicated by an arrowhead contains intron may correspond to an intron retain clone. **(C)** EST support for a splicing variant with 25 bp exon $E22^+$ (PPP1R12A-205). This exon causes a frame shift and a premature stop. The human EST database was interrogated with the sequences corresponding to E22–$E22^+$–E23. This search revealed a single sequence containing $E22^+$ (top hit with an asterisk). The second hit appears to correspond to a clone with anomalous splicing at the $E22^+$–E23 boundary. One clone that appears to include $E22^+$ (at the bottom, asterisk) corresponds to a misaligned sequence and two more that only cover $E22^+$ (arrowheads) may correspond to intron retain transcripts (Figure S3 from (Saldanha et al., 2022)).

3.2.4. *PPP1R12A* protein-coding transcripts

Next it was sought to revise the support for transcription variants of *PPP1R12A* involving coding exons E6, $E9^+$, E13, E14, E22 and E24, most of which have not received attention before. All these splicing variants preserve the reading frame down to the stop codon in E26.

E6 is spliced out in transcript PPP1R12A-216, resulting in the loss of a stretch of 25 amino acids. To find EST support for this variant a BLASTn search with the sequences corresponding to E5-E7 (Figure 3.8 A) was performed. Two ESTs in which E6 was spliced out were identified (Appendix Table 8.1-1). A further BLASTn search with the sequences corresponding to E5-E6-E7 identified one of the two ESTs out of 94, indicating that splicing out of E6 is very rare.

Transcript PPP1R12A-223 splices in the 117 bp exon E9+ and is predicted to result in a protein that is 39 amino acids longer than the FL variant. A BLASTn search with the sequences corresponding to E9, $E9^+$ and E10 revealed one clone (Figure 3.8 B,

arrowhead) apparently lacking most of E10 (BF334095.1). Closer examination revealed that this clone contains 24 bp and 26 bp of the 5' and 3' ends, respectively, of E10, but no canonical splicing sites can be identified that might explain the absence of most of the exon. This apparently anomalous processing results in a frame shift. A further search with the $E9^{+}$ sequence alone failed to reveal any EST or mRNA sequence in support of splicing in of this exon; however, there is clear support by RNAseq data, although it is captured only in the GenBank dataset (Saldanha et al., 2022).

Figure 3.8 Figure Legend on the following page

Figure 3.8 Results of BLASTn searches for ESTs in support of alternatively spliced exons. Separate aligned regions on the same database sequence are connected by a thin grey line. Vertical tick marks indicate intervening sequences not present in the query sequence. **(A)** Splicing of E6. The EST database was interrogated with the sequences corresponding to E5–E7. The boundary between E5 and E7 is placed at bp 145. Two ESTs were found in which E6 was spliced out (asterisks). **(B)** Splicing of 117 bp exon $E9^{+}$ (transcript PPP1R12A-223). The EST database was interrogated with the sequences corresponding to E9–$E9^{+}$–E10. The sequence marked with an arrowhead showed anomalous splicing of E10. **(C)** Splicing of E13. The EST database was interrogated with the sequences corresponding to E12–E14. The boundary between E12 and E14 is placed at bp 105. Twelve ESTs were found in which E13 was spliced out (asterisks). **(D)** An alternative splicing acceptor site in E13. The EST database was interrogated with the sequences corresponding to E12 plus E13b, a 32 bp truncated E13. The boundary between E12 and E13b is placed at bp 105. Four ESTs were found in support of this variant (asterisks). **(E)** Splicing of E14. The EST database was interrogated with the sequences corresponding to E13–E15. The boundary between E13 and E15 is placed at bp 168. One EST was found in which E14 was spliced out (asterisk). **(F)** Splicing of E13+E14. The EST database was interrogated with the sequences corresponding to E2–E15. The boundary between E12 and E15 is placed at bp 105. Four ESTs was found in which E13 and E14 were spliced out together (asterisks). **(G)** Splicing of E22. The EST database was interrogated with the sequences corresponding to E21–E23–E25. The boundary between E21 and E23 is placed at bp 136. Note the absence of EST clones splicing out E22. The clone marked with a black arrowhead is anomalous, it contains E21 in sense fused to a fragment composed of E23+E24+E25 plus part of the coding region of E26 in antisense. The clones marked with red arrow heads splice in the 31 bp variant of E24 (tick mark at bp 184). **(H)** Splicing of E24. The EST database was interrogated with the sequences corresponding to E23–E24–E25 using the 31 bp variant of E24 (nucleotides 49–79 in the graph). Inspection of the six top hit alignments revealed three that include the 31 bp variant and three that include the 13 bp variant (the 18 bp difference is too short to be displayed in the graph). Five ESTs matching almost only E24 at the bottom of the graph (in green) probably correspond to intron-retaining transcripts (PPP1R12A-210 or 220) (Figure S4 from (Saldanha et al., 2022)).

In transcript PPP1R12A-213 E13 is spliced out conserving the reading frame, resulting in a protein that lacks a central stretch of 56 amino acids. To find EST support for this variant, a BLASTn search with the sequences corresponding to E12-E14 (Figure 3.8 C) was performed. 12 ESTs out of 97 were identified (Appendix Table 8.1-1), indicating that splicing out of E13 is relatively frequent, although less than splicing it in.

Transcript PPP1R12A-221 contains a shorter variant of E13 (that was called E13b) that results from the usage of an alternative splicing acceptor site 36 bp into E13. The predicted protein lacks 12 amino acids in its central region. A search with E12 plus the truncated E13 revealed a total of four EST clones supporting this splicing variant (Figure 3.8 D). The use of this alternative acceptor site does not result in changes in the reading frame and the resultant protein would lack 12 amino acids.

In transcript PPP1R12A-208, E14 is spliced out, resulting in a predicted protein that lacks a central stretch of 59 amino acids. A BLASTn search with the sequences corresponding to E13-E15 (Figure 3.8 E) identified a single EST out of 75, suggesting that splicing out of E14 is rare.

In transcript PPP1R12A-206 both E13 and E14 are spliced out simultaneously. In the resulting protein the reading frame is conserved, giving rise to a protein that lacks a central stretch of 115 amino acids. To find EST support for this variant a BLASTn search with the sequences corresponding to E12-E15 (Figure 3.8 F) was performed. Four ESTs bridging E13+E14 out of 83 were identified, indicating that this splicing variant is infrequent (Appendix Table 8.1-1).

In transcript PPP1R12A-202 E22 is spliced out conserving the reading frame, resulting in a protein that lacks 35 amino acids at its C-terminus. A BLASTn search with the sequences corresponding to E21-E23-E25 did not show any EST supporting splicing out of E22 (Figure 3.8 G). EST clones at the E21-E23 boundary all contain E22, either completely or partially. A search in the nucleotide collection yielded only two hits where E22 is spliced out: NM_001244990.1 (the curated model for variant 4/isoform c in GenBank based on alignments) and AF458589.1. This last sequence is a direct submission of a 4631 bp mRNA from liver for which no further information is available. Splicing of E22 appears to be extremely rare. Clone AA715976.1 appears from the BLAST output graph as a clone splicing out E23 (Figure 3.8 G, black arrow). However, upon close inspection its sequence reveals as E22 in sense fused to a fragment composed of E23+E24+E25 plus part of the coding region of E26 in antisense. Two clones, BM669210.1 and AI202675.1 (Figure 3.8 G, red arrows) stand

out in the graph for containing additional sequences in the E23/E25 boundary and are discussed below.

In most transcript variants of *PPP1R12A* E24 is spliced out. However, in two truncated transcripts, PPP1R12A-214 and PPP1R12A-222, this exon is spliced out, causing a frameshift that results in a premature stop and proteins lacking the leucine zipper domain (LZ^- isoforms). E24 can be spliced in in two different ways, to include either a 31 bp exon (transcript 214) or a 13 bp exon (transcript 222). To find EST support for these variants a BLASTn search with the sequences corresponding to E23-E24-E25 was performed, using the 31 bp variant of the exon (Figure 3.8 H). Inspection of the six clones with sequences matching E24 revealed three that include the 31 bp variant and three that include the 13 bp variant (Appendix A table 8.1-1).Figure 3.8 also shows that ESTs in which E24 is spliced out are much more abundant. Five ESTs matching almost only E24 at the bottom of the graph (in green) probably correspond to intron-retaining transcripts (PPP1R12A-210 or 220).

3.2.5. Frequencies of *PPP1R12A* transcripts

In addition to exploring the EST database (Appendix Table 8.1-3) it was collated RNAseq information from GenBank, AceView and GTEx to calculate the frequency of alternative splicing involving protein coding exons and the frequency of each of the 11 transcript variants of *PPP1R12A* (Table 3.2 and Appendix Table 8.1-2). Globally, the most frequent variant is FL, accounting for more than half of the transcripts. Variants that splice E13 or E14 out are relatively frequent (13-15%). Some variants are rare, like ΔE6 (2%), $E9^+$ (5%) and E13b (4%) and other very rare (ΔN, ΔE13-14, ΔE22), all below 1%. Variants that splice E24 in are, on average, relatively uncommon: 1.98% the long (LZ^-a) and 0.55% the short (LZ^-b) variant.

Table 3.2 Frequency of *PPP1R12A* transcripts. Transcript frequency was calculated from combined RNAseq data from AceView, GTEx and GenBank as described in section 2.2.5. Splicing in of E9+ is only recorded in GenBank, therefore the frequency of this variant was calculated relative to the GenBank data only. Details of the analysis are shown in Appendix Table 8.1-2.

Transcript	Protein length(a.a.)	Frequency (%)
FL	1030	56.58
ΔN	943	0.13
ΔE6	1005	2.01
E9$^+$	1069	5.06
E13b	1018	4.00
ΔE13	974	13.43
ΔE14	971	14.87
ΔE13+14	915	0.66
ΔE22	995	0.74
LZ$^-$a	1005	1.98
LZ$^-$b	999	0.55

3.3. Transcription variants of *PPP1R12A* in cells of the vasculature

To dissect the complexity of *PPP1R12A* expression in the circulatory system the focus was directed towards two cell types where MYPT1 is known to play important roles: endothelial cells (Kim et al., 2012), and smooth muscle cells (Payne et al., 2004). To analyse the transcripts, an approach based on reverse transcription (RT) PCR on cDNA prepared from cultured HUVECs and HSVSMCs was used. Real-time PCR was not considered due to unavailability of TaqMan™ probes to study transcripts and the time-consuming process of primer optimisation with SYBR™ Green.

Prior to being used on cDNA, primers were tested either on genomic DNA from HUVECs or on a plasmid containing the coding region of the FL MYPT1 isoform (cDNA sequence of clone MGC: 133042, IMAGE: 40008469, GenBank: BC111752.1) that lacks E24 sequence. Table 2.13 in section 2.1.3 shows the primer pairs, the expected amplicon sizes, and the conditions of the PCR reactions. The positions of each primer pair on the PPPR12A gene or cDNA are depicted in Figure 3.9 A. To test some of the primers (E1$^+$-fwd, E9$^+$-rev) an auxiliary primer was design in adjacent intron. All test PCR reactions yielded a band of the expected size (Figure 3.9 B-L), allowing us to proceed with their use in retrotranscribed RNA samples.

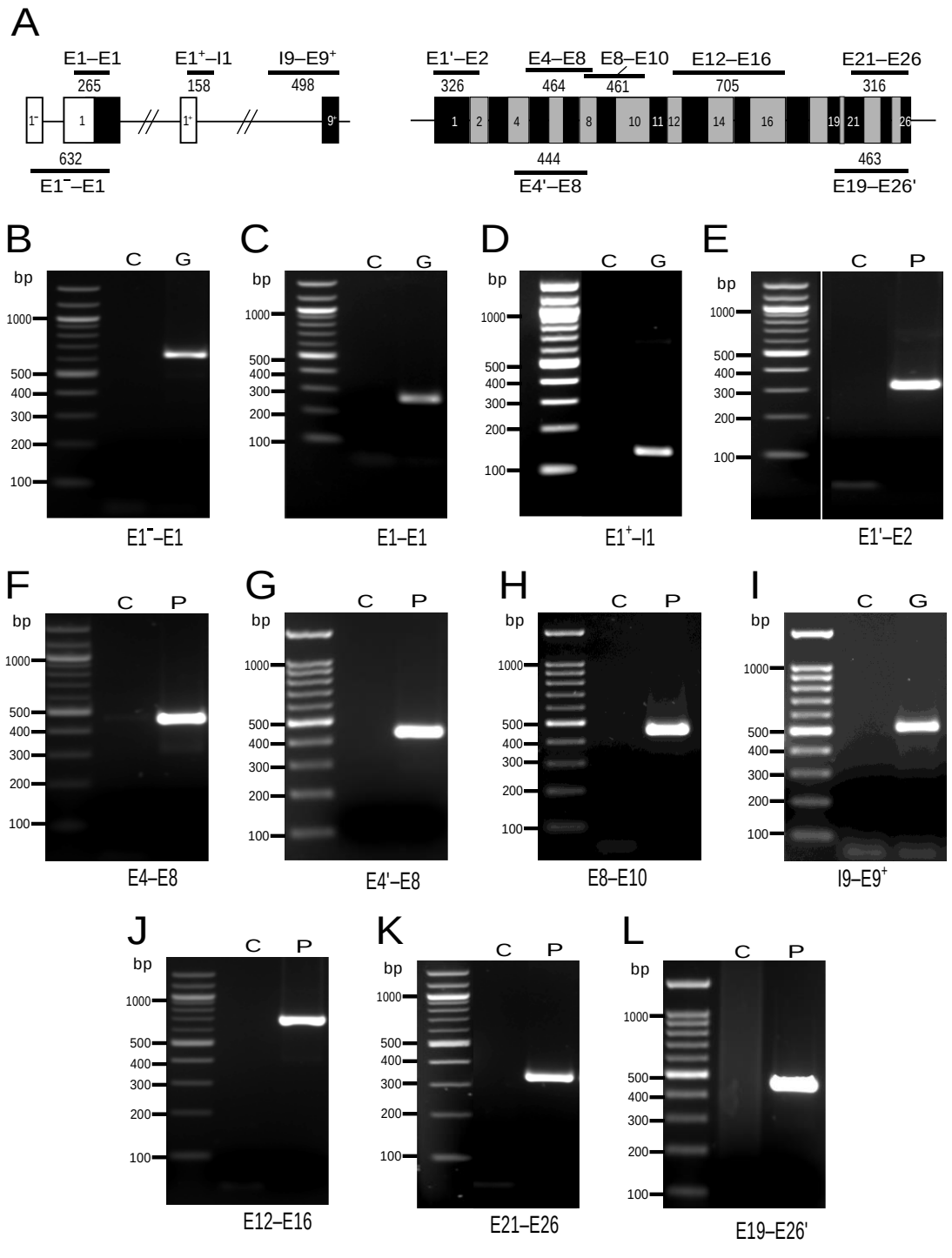

Figure 3.9 Figure Legend on the following page

Figure 3.9 Test PCR reactions of *PPP1R12A* primers. (A) Position and expected size of PCR products. On the left, scheme of the genomic sequence around exons E1 and E9^{+}; white and black boxes represent untranslated and translated regions, respectively. On the right, coding region of the canonical *PPP1R12A* FL variant (lacking E24); exons are shown at scale alternating black and grey. Primer pairs in the forward-reverse sequence and size of expected PCR products are indicated above and under the DNA schemes. Primer sequences and PCR conditions are shown in Table 2.13. (**B-L**) Results of PCR reactions using the primer combinations of the top panel. G, reactions were run using genomic DNA as template; P, reactions were run using a plasmid carrying the coding sequence of the FL *PPP1R12A* variant as template; C, control reaction without template. 40% of each 25 µl reaction was loaded on 1.5% agarose gels (Figure S5 from (Saldanha et al., 2022)).

To determine which main *PPP1R12A* transcripts are presented in HUVECs RT-PCR reactions were performed using the primer pairs and the conditions shown in section 2.1.3, Table 2.14. PCR reactions addressing the three transcription initiation sites indicate that the transcription start on E1 is the only one used by HUVECs (Figure 3.10 A). The PCR reaction targeting alternative splicing of E6 only yielded the band corresponding to E6in variants (Figure 3.10 B), whereas the PCR reaction targeting alternative splicing of E9^{+} only yielded the band corresponding to E9^{+}out variants (Figure 3.10 C).

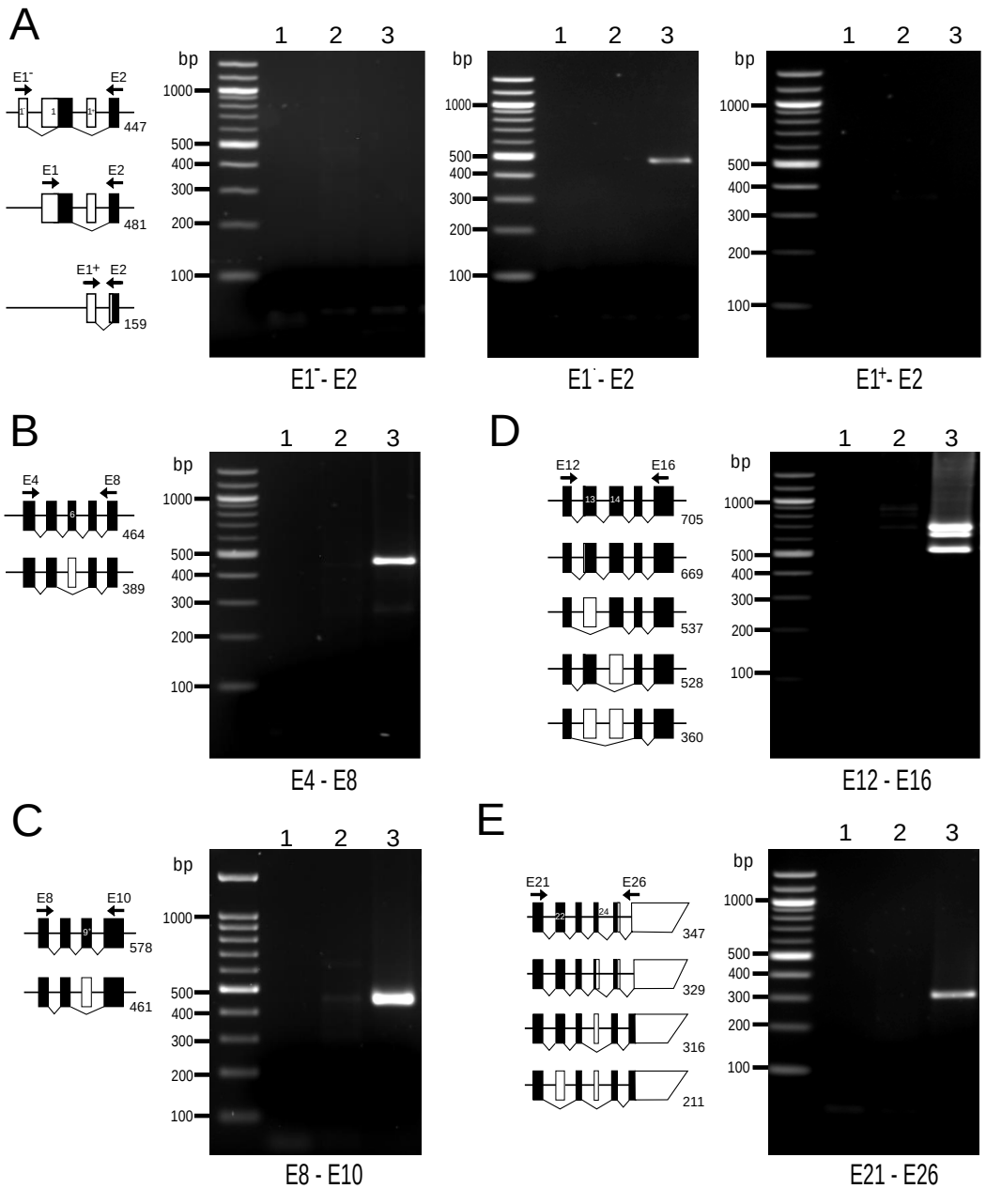

Figure 3.10 *PPP1R12A* transcripts in HUVECs detected by RT-PCR. The diagrams accompanying each panel depict the expected size of PCR products corresponding to all possible alternatively spliced variants sorted by size. White and black boxes represent untranslated and translated exons, respectively. Exons are depicted at scale. Position of primer pairs is indicated schematically. **(A)** PCR reactions targeting alternative transcription start sites. A transcription start on E1 is the only site used by HUVECs. **(B)** PCR reaction targeting E6 splicing variants. **(C)** PCR reaction targeting $E9^{+}$ splicing variants. **(D)** PCR reaction targeting E13 and E14 splicing variants. **(E)** PCR reaction targeting E22 and E24 splicing variants. PCR reactions were run using no template (lane 1), negative control for reverse transcriptase (lane 2) or cDNA (lane 3) as templates. Primer sequences and PCR conditions are shown in Table A2.14. 40% of each 25 µl reaction was loaded on 1.5% agarose gels (Figure 5 from (Saldanha et al., 2022)).

The PCR reaction targeting splicing variants of E13 and E14 yielded three bands (Figure 3.10 D). The top approximately 700 bp band matches in size the more abundant variants including E13 and E14 and was verified by sequencing. The bottom, slightly above 500 bp, band is compatible with both ΔE13 and ΔE14. Sequencing of this amplicon ultimately confirmed it corresponds to ΔE13. The middle, approximately 650 bp, band is compatible with the E13b splicing variant. However, sequencing of this amplicon returned a chromatogram compatible with a mix of E13in and E13out PCR products (Figure 3.11 A). This 650 bp band probably arose by hybridisation of the top and bottom PCR products. This was confirmed in a PCR reaction with same primer E12-E16 pair using a mixture of plasmids containing full length and E13out MYPT1 sequences as template (Figure 3.11 B).

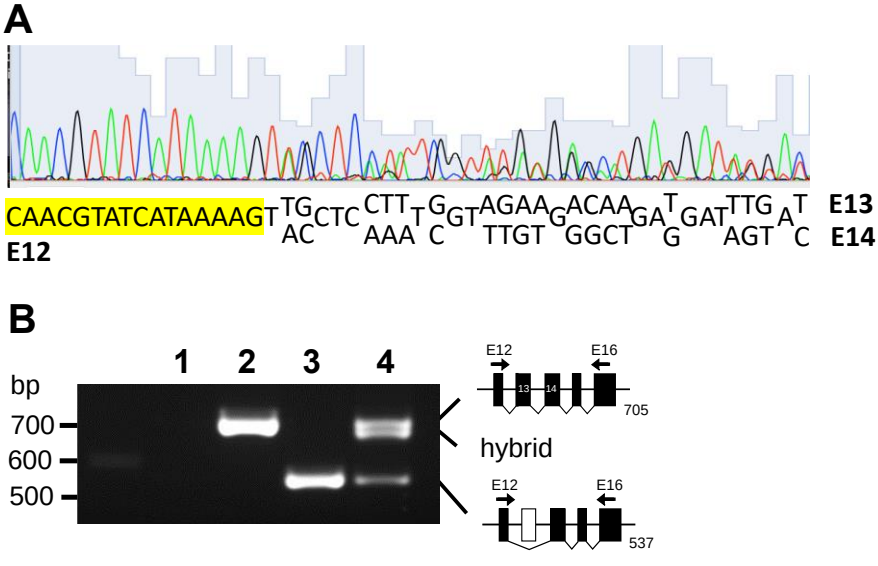

Figure 3.11 Hybridisation of PCR products of reaction targeting E13 and E14 variants. (A) Fragment of the sequencing reaction chromatogram of a hybrid product (intermediate band) of the PCR reaction with primer pair E12-E16 (Figure 3.10D). The hybrid band was purified from an agarose gel and sequenced with E12 forward primer. The 3' end of E12 is highlighted in yellow. It is followed by mixed sequences compatible with E13 and E14, confirming that the band is a hybrid of E13in and E13out DNA fragments. **(B)** Hybridisation of E13in and E13out amplicons in a PCR reaction using plasmid DNA as template. Lane 1, negative control (no template); lane 2, plasmid containing full length MYPT1 cDNA as template; lane 3, plasmid containing an MYPT1 cDNA fragment lacking E13 as template; lane 4, mix of both plasmids as template (Figure S6 from (Saldanha et al., 2022)).

Finally, Figure 3.10 E shows the result of the PCR reaction targeting alternative splicing of E22 and E24. The single band slightly above 300 bp was confirmed by sequencing to correspond to an E22in/E24out transcript.

3.3.1. Low abundance *PPP1R12A* variants in HUVEC

The approached used in the previous section may have missed low abundance variants that would yield too small amounts of PCR product to be visualised in agarose gels. In order to capture very rare variants of *PPP1R12A* a second set of primer pairs were designed where one of the primers annealed either to one exon-exon boundary (to target exon-out variants) or to an exon normally not spliced in (to target exon-in variants) and increased the number of cycles (Table 2.14, section 2.1.3). PCR reactions using a reverse primer spanning the E5-E7 boundary yielded a relatively faint band of the expected size, confirming the presence of ΔE6 (Figure 3.12A). In contrast, PCR reactions using a reverse primer annealing on $E9^{+}$ were negative, supporting the absence of an $E9^{+}$ variant (Figure 3.12B). Splicing of the E13b variant of exon 13 was addressed with a reverse primer spanning the E13b-E12 boundary and the PCR reactions yielded a faint band of the expected size, confirming expression of this variant (Figure 3.12 C). To explore expression of ΔE22 a reverse primer spanning the E23-E21 boundary was used. This resulted in an amplicon of 300 bp, which was significantly larger than the expected 210 bp (Figure 3.12 D). Inspection of the amplicon sequence revealed that the 3' end of the reverse primer had annealed to and amplified through E22 and was therefore considered inconclusive. Finally, expression of LZ^{-} variants was addressed with a forward primer spanning the E23-E24 boundary that should reveal any of both variants of this exon (Figure 3.12 E). PCR reactions yielded an unexpected 900 bp product that contains intronic sequences and may correspond to the retained intron transcript PPP1R12A-210.

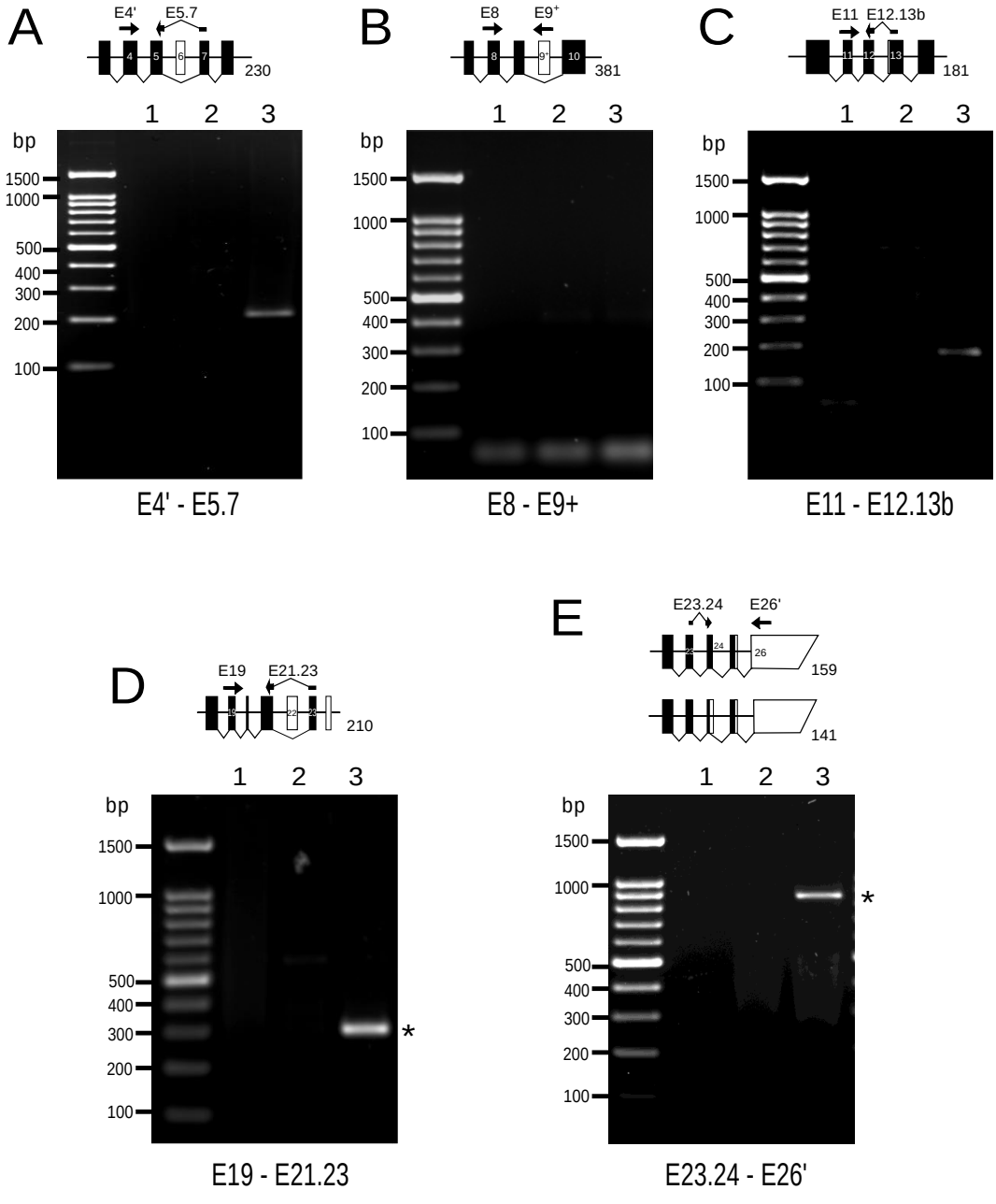

Figure 3.12 Rare *PPP1R12A* transcripts in HUVEC detected by RT-PCR. The diagrams accompanying each panel depict the expected size of PCR products corresponding the rare alternatively spliced variants if present. White and black boxes represent untranslated and translated exons, respectively. Exons are depicted at scale. Position of primer pairs is indicated schematically. **(A)** PCR reaction targeting the ΔE6 splicing variant. **(B)** PCR reaction targeting the $E9^{+}$ splicing variant. **(C)** PCR reaction targeting the E13b splicing variant. **(D)** PCR reaction targeting the ΔE22 splicing variant. **(E)** PCR reaction targeting LZ^{-} splicing variants. Asterisks indicate unexpected PCR products. PCR reactions were run using no template (lane 1), negative control for reverse transcriptase (lane 2) or cDNA (lane 3) as templates. Primer sequences and PCR conditions are shown in Table 2.14. 40% of each 25 µl reaction was loaded on 1.5% agarose gels (Figure 6 from (Saldanha et al., 2022)).

3.3.2. Transcription variants of *PPP1R12A* in HSVSMCs

Similar RT-PCR analysis as used in HUVECs was performed in HSVSMC to determine the pattern of *PPP1R12A* transcription variants in these cells. HSVSMCs were isolated and cultivated by Olapeju Bolanle of Professor Tim Palmer's laboratory at the centre for Biomedicine, HYMS. PCR reactions addressing the three transcription initiation sites indicated that, like in HUVECs, the transcription start on E1 is the only one used by HSVSMCs (Figure 3.13 A). Like in HUVECs too, the PCR reaction targeting alternative splicing of E6 only yielded the band corresponding to E6in variants (Figure 3.13 B), whereas the PCR reaction targeting alternative splicing of $E9^{+}$ only yielded the band corresponding to $E9^{+}$out variants (Figure 3.13 C).

The PCR reaction targeting splicing variants of E13 and E14 yielded the same pattern of three bands observed in HUVECs (Figure 3.13 D), with the difference that the uppermost band was clearly more intense than the others. The top approximately 700 bp band was verified by sequencing to correspond the more abundant variants including E13 and E14 whereas the bottom, slightly above 500 bp, band was confirmed to correspond to ΔE13. The middle, approximately 650 bp, was confirmed to correspond to a hybrid of E13in and E13out PCR products.

Figure 3.13 D shows the result of the PCR reaction targeting alternative splicing of E22 and E24. The single band slightly above 300 bp was confirmed by sequencing to correspond to an E22in/E24out transcript.

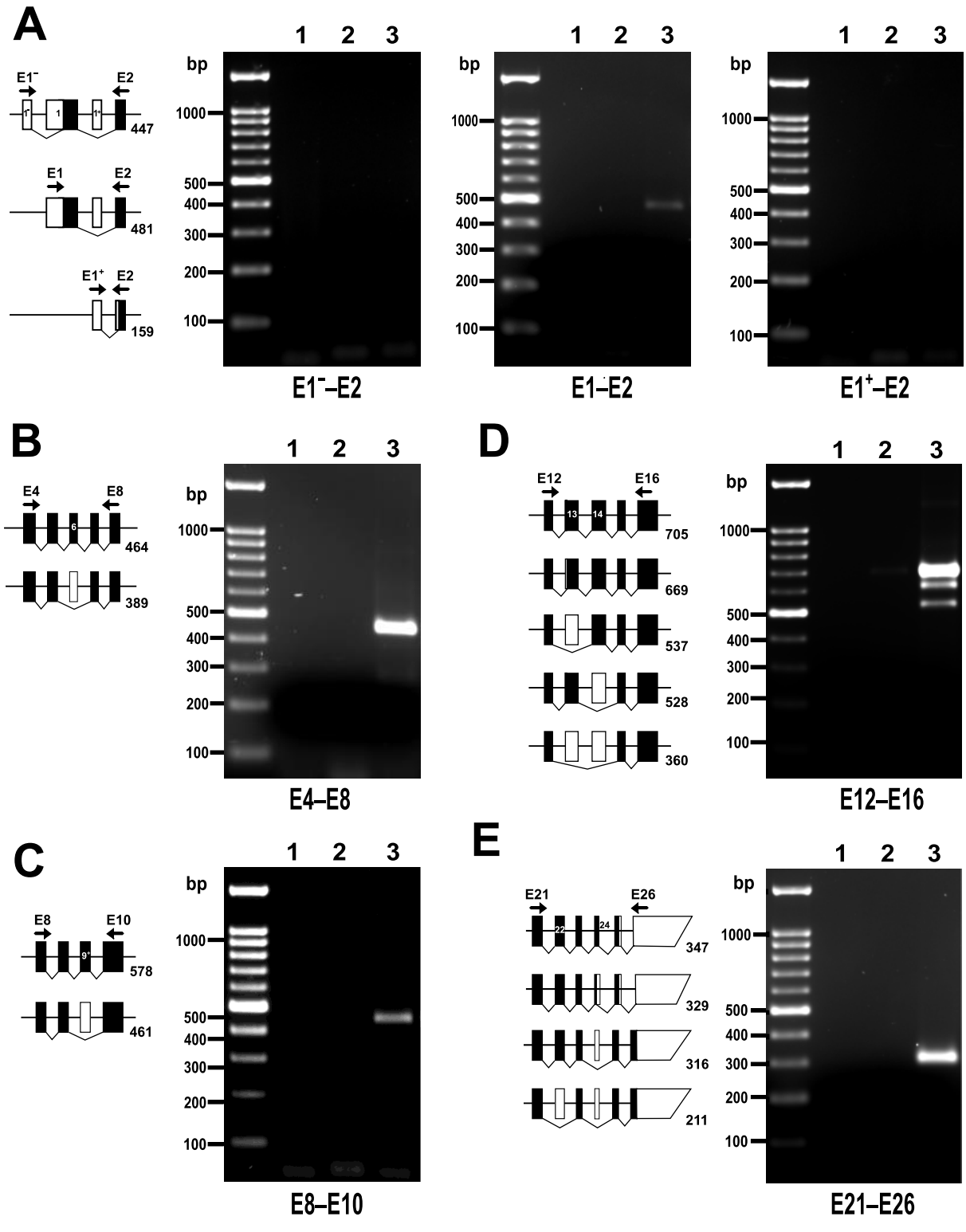

Figure 3.13 Figure Legend on the following page

Figure 3.13 *PPP1R12A* transcripts in human saphenous vein smooth muscle cells as determined by RT-PCR. The diagrams accompanying each panel depict the expected size of PCR products corresponding to all possible alternatively spliced variants sorted by size. White and black boxes represent untranslated and translated exons, respectively. Exons are depicted at scale. Position of primer pairs is indicated schematically. **(A)** PCR reactions targeting alternative transcription start sites. A transcription start on E1 is the only site used by HSVSMCs. PCR reactions targeting **(B)** E6, **(C)** $E9^{+}$, **(D)** E13 and E14, **(E)** E22 and E24 splicing variants. PCR reactions were run using no template (lane 1), negative control for reverse transcriptase (lane 2) or cDNA (lane 3) as templates. Primer sequences and PCR conditions are shown in Table 2.14 (Figure S7 from (Saldanha et al., 2022)).

3.3.3. Low abundance *PPP1R12A* variants in HSVSMCs

The same approach used in HUVECs was employed to identify low abundance *PPP1R12A* variants in HSVSMCs. PCR reactions using a reverse primer spanning the E5-E7 boundary yielded a 200 bp product that confirmed the presence of the ΔE6 variant (Figure 3.14 A). In contrast, PCR reactions using a reverse primer annealing on $E9^{+}$ were negative, supporting the absence of an $E9^{+}$ variant (Figure 3.14 B).

Splicing of the E13b variant of exon 13 was addressed with a reverse primer spanning the E13b-E12 boundary and the PCR reactions yielded a faint band of the expected size, confirming expression of this variant (Figure 3.14 C). Reactions for the ΔE22 variant produced an inconclusive result as in HUVECs (Figure 3.14 D).

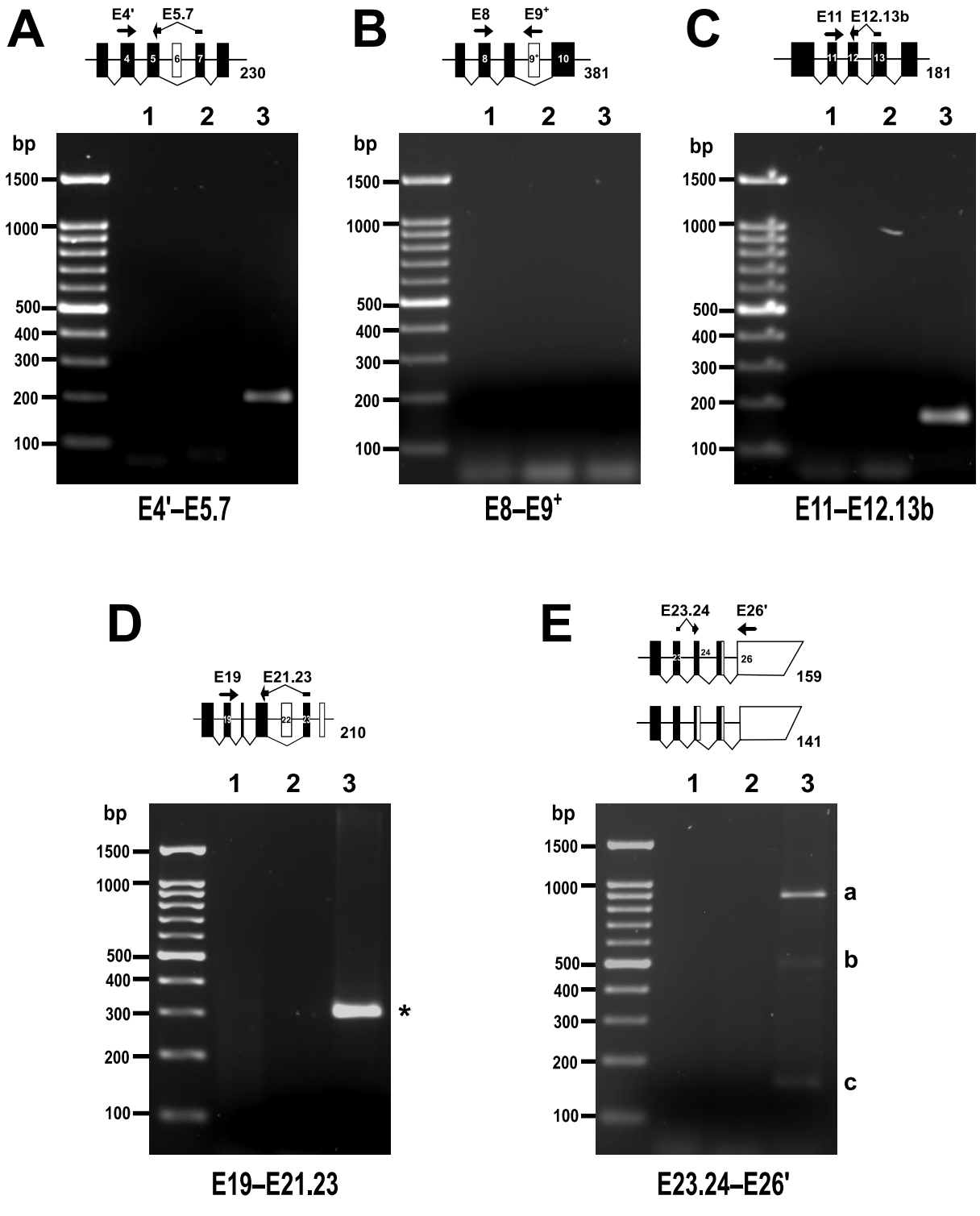

Figure 3.14 Figure Legend on the following page

Figure 3.14 Rare *PPP1R12A* transcripts in human saphenous vein smooth muscle cells as determined by RT-PCR. The diagrams accompanying each panel depict the expected size of PCR products corresponding to the rare alternatively spliced variants. White and black boxes represent untranslated and translated exons, respectively. Exons are depicted at scale. Position of primer pairs is indicated schematically. PCR reactions targeting the **(A)** ΔE6, **(B)** $E9^{+}$, **(C)** E13b and **(D)** ΔE22 splicing variants. The asterisk indicates an unexpected PCR product. **(E)** PCR reaction targeting LZ^{-} splicing variants. Bands a and b are unexpected amplicons, band c corresponds to the 159 bp product. PCR reactions were run using no template (lane 1), negative control for reverse transcriptase (lane 2) or cDNA (lane 3) as templates. Primer sequences and PCR conditions are shown in Table 2.14 (Figure S8 from (Saldanha et al., 2022)).

PCR reactions for LZ^{-} variants yielded three products: a 900 bp long product, an intermediate >500 bp product and a very faint band slightly above 150 bp (Figure 3.14 E). The 900 bp product was found to contain intronic sequence and may correspond to the retained intron transcript PPP1R12A-210 as found in HUVECs. The >150 bp amplicon was confirmed to correspond to the LZ^{-}a variant. Sequencing of the >500 bp amplicon returned a chromatogram compatible with a mix of the 900 bp and >150 bp PCR products (Figure 3.15 A), suggesting that it resulted from hybridisation of the top and bottom PCR products, as confirmed by PCR reactions using the >500 bp amplicon as template (Figure 3.15 B).

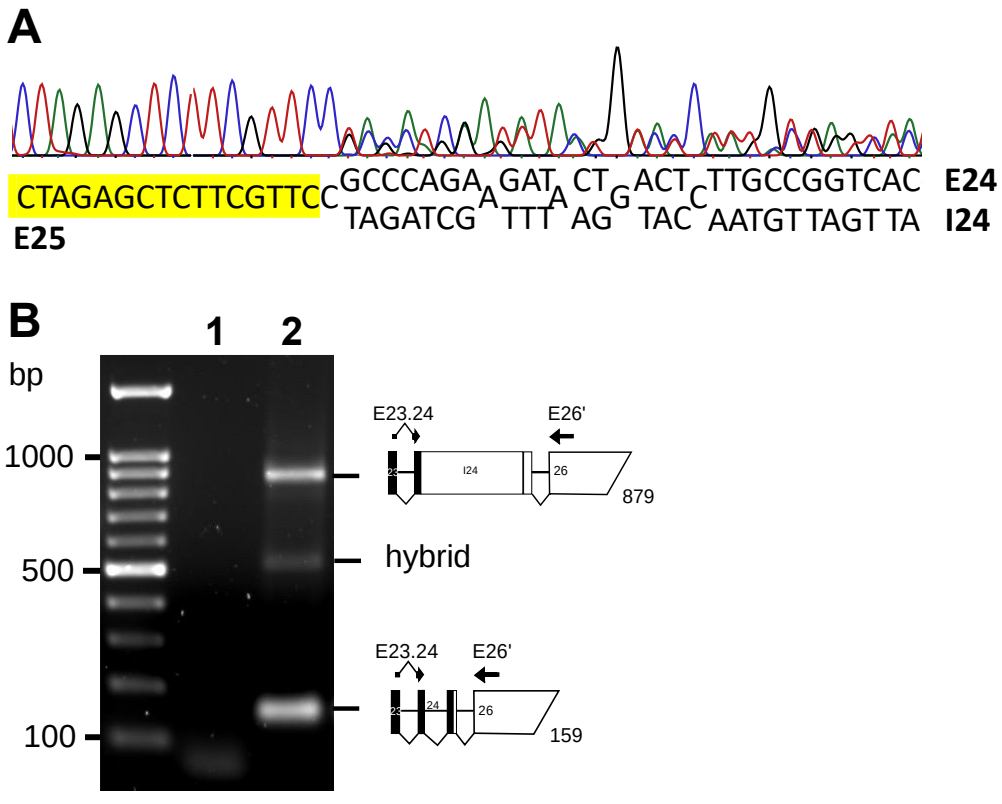

Figure 3.15 - Hybridisation of PCR products of the reaction targeting E24. (A) Fragment of the sequencing reaction chromatogram of a hybrid product (intermediate band) of the PCR reaction with primer pair E23.24-E26' (Figure 3.14 E). The hybrid band was purified from an agarose gel and sequenced with 26' reverse primer. The 5' end of E25 is highlighted in yellow. It is followed by mixed sequences compatible with E24 and I24, confirming that the band is a hybrid of E24in and retained intron DNA fragments. **(B)** Hybridisation of E24in (159 bp) and a retained intron (879 bp) DNA in a PCR reaction using the hybrid band as template (lane 2). Lane 1 is a negative control (no template). This reaction yielded the 159 bp and the 879 bp along with a small amount of hybrid product (Figure S9 from (Saldanha et al., 2022)).

In conclusion, this RT-PCR analysis revealed that in both HUVECs and HSVSMCs the main *PPP1R12A* variants are FL and ΔE13. The ΔE6 and the E13b variants are less abundant but can be detected in both cell types, whereas E9+ and ΔE22 variants were not. LZ^- variants were not detected in HUVECs but were found as low abundant variants in HSVSMCs.

3.4. Knockdown of *PPP1R12A* transcripts in HUVECs

The results of the RT-PCR and in silico analyses of the previous sections indicate that the most abundant MYPT1 isoforms in HUVEC are the FL and the CI variant lacking E13. They most likely correspond, respectively, to the upper and lower band of the MYPT1 doublet described in the 140 kDa region of western blots of HUVEC lysates (Yuen et al., 2011, Xia et al., 2005) and (Kim et al., 2012) (see also Figure 4.2). Based on this information, the approach was sought to set up a gene silencing using small interfering RNA (siRNA) with the aim of targeting individual isoforms in future functional studies.

3.4.1. Design of silencing oligonucleotides for *PPP1R12A*

Three silencing oligonucleotides were designed, two to target specifically the FL and ΔE13 isoforms and one to target all isoforms. Figure 3.16 illustrates how the siRNA oligonucleotides were designed. siRNA E13 was designed to target all transcripts that express E13, therefore predominantly the FL isoform. The sequence was determined by Dharmacon™ (siDESIGN Center) (Horizon Discovery Group, United Kingdom). siRNA E12.14 spans the E12-E14 boundary and was designed to target transcripts that do not express E13. siRNA E22.23 was designed as a control siRNA for all *PPP1R12A* transcripts.

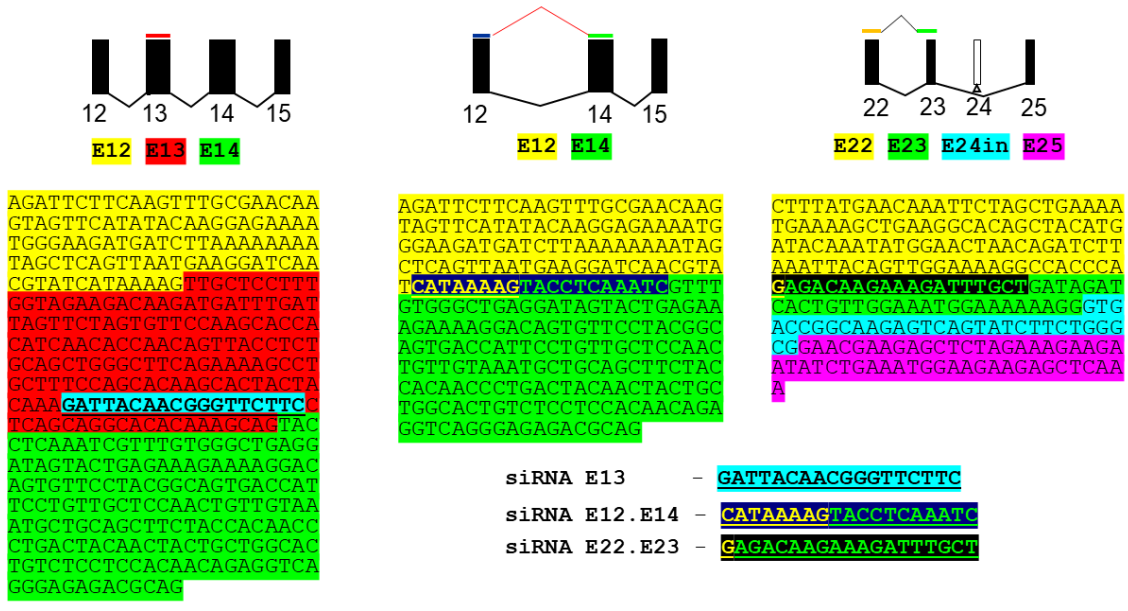

Figure 3.16 Design of oligonucleotides for knockdown of *PPP1R12A* transcripts in HUVECs. Exons are colour coded as indicated. The oligo siRNA E13 (left) will target specifically the transcripts that have exon 13. The oligo siRNA E12.E14 (middle) will target the ΔE13 transcript. The oligo siRNA E22.E23 (right) was designed to target all transcripts.

3.4.2. Knockdown of *PPP1R12A* transcripts in HUVEC

A pilot silencing experiment using HUVECs was performed following the protocol detailed in section 2.5.3. Subconfluent cells were employed to enhance the uptake of siRNA by the dividing cells. Given that multiple siRNA complexes may enter each dividing cell, this will lead to an increased number of cells not expressing the protein of interest. Ensuring that all cells take up siRNA is critical. The experiment included siRNA oligonucleotides targeting GAPDH as a positive a control for the siRNA experimental protocol, as well as non-targeting (NT) oligonucleotides as negative control and a mock transfection (without oligonucleotides) to rule out any artifacts and/or toxicity that might come from the transfection reagent (Oligofectamine™) and was conducted on one experiment with three technical repeats. To assess the efficacy of the siRNA technique, protein expression levels were analysed using western blotting. Alternatively, if optimised, qPCR could serve as another method to confirm mRNA downregulation.

As shown in Figure 3.17A-C and the quantifications in Figure 3.17 D, E, there is a trend towards both MYPT1 bands having less intensity relative to the NT samples when siRNA E22.23 was used. The other siRNA oligos, including GAPDH, did not appear to cause any noticeable alteration in the intensity of the MYPT1 bands. The siRNA for GAPDH, utilised as a positive control for silencing, cannot be deemed successful due to an overall silencing percentage of less than 20% The results were complemented by immunostaining of transfected cells with an anti-MYPT1 antibody (Figure 3.17 G). DAPI was used to stain cell nuclei, while TRITC-phalloidin was employed to stain F-actin (Appendix Figure 8.1-3). Before drawing into conclusions from the immunofluorescence results obtained after silencing, it is essential to perform consistent and reproducible titrations of the MYPT1 antibody for immunofluorescence. In summary, although this preliminary experiment demonstrated moderate silencing with siRNA targeting all MYPT1 protein isoforms, no distinct effect is observed with the siRNA targeting specific isoforms. Additional investigation is required to refine MYPT1 silencing in HUVECs for subsequent functional studies as the positive control to confirm siRNA effectiveness did not yield the desired results.

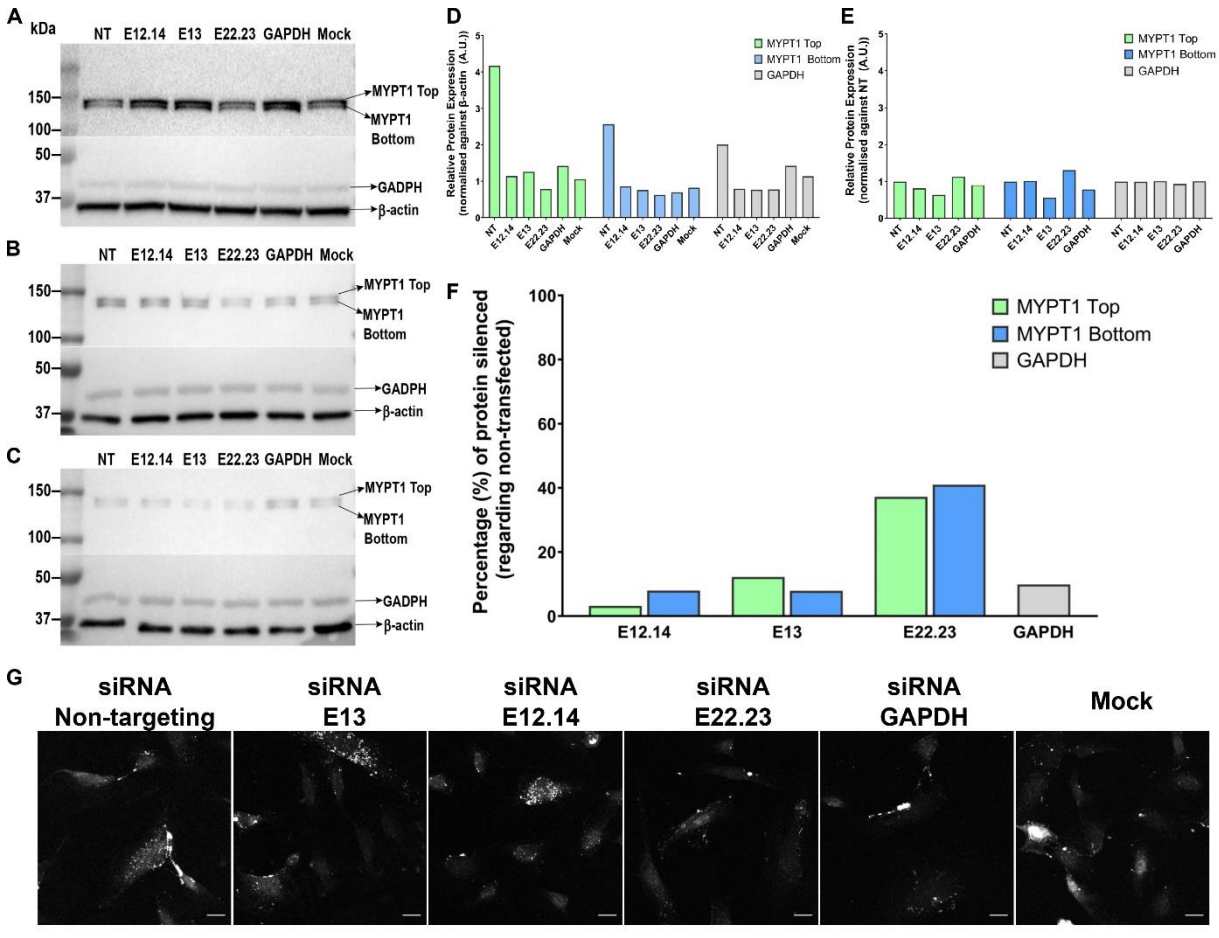

Figure 3.17 Knockdown of MYPT1 in HUVECs. (A-C) MYPT1 knockdown experiments in HUVECs performed with the three siRNA (50 nM) oligonucleotides described in section 3.4.1 Figure 3.16. Cells silencing was performed twice, at 24 and 48 hours after seeding. Cells were harvested after 72 hours of first silencing. Samples were electrophoresed on 7% SDS-PAGE gels and blotted onto PVDF membrane. GAPDH was used as a positive a control, non-targeting (NT) oligonucleotides were used as negative control, Mock is vehicle control (Opti-MEM™ and Oligofectamine™). Triplicates of one independent experiment is shown. 20 µg of lysates were loaded in each well. **(D)** Quantification and relative expression of proteins upon normalisation against ß-actin. **(E)** Quantification and relative expression knockdown proteins normalised against NT. **(F)** Knockdown percentage of MYPT1 and GAPDH from experiments A, B and C. siRNA E13 – targets all MYPT1 isoforms with E13. siRNAE12.14 targets all MYPT1 isoforms that do not have E13. siRNA22.23 targets all MYPT1 isoforms. **(G)** Representative of immunostainings of siRNA experiments in HUVECs (scale bar 50 µm). Staining was performed using a rabbit anti-MYPT1 antibody. GAPDH (glyceraldehyde 3-phosphate dehydrogenase); ß-actin, beta actin.

3.5. Discussion

The presence of alternative splicing variants of the gene encoding MYPT1 was recognised in early studies and the functional relevance of a small number of variants has been investigated extensively (Dippold and Fisher, 2014a, Dirksen et al., 2000, Khatri et al., 2001, Htet et al., 2021, Payne et al., 2004). However, previous studies have been restricted to few organs and tissues and do not reflect the complexity of the transcriptional capabilities of *PPP1R12A*, which is important to understand the specific cellular roles of MYPT1 isoforms. To begin filling these knowledge gaps, a comprehensive examination of the transcriptional landscape of the *PPP1R12A* gene, with a focus on protein-coding transcripts, was undertaken. These results have revealed a previously unrecognised complex transcriptional repertoire for the human *PPP1R12A* gene. A total of 32 exons were established, 29 of which are capable of encoding a minimum of 11 predicted protein variants expressed in different proportions across pure cell types and organs. Three exons are present only in nonsense-mediated decay transcripts. Additional analysis of RNAseq data has allowed to generate transcript profiles of *PPP1R12A* in HUVECs, HSVSMCs and platelets with up to 10 transcripts expressed with unique patterns of frequencies (Saldanha et al., 2022). These findings have provided valuable information for the design of functional studies targeting MYPT1 isoforms. In fact, the knowledge gained in this chapter has been put to good use in the design of siRNA oligonucleotides to knockdown specific *PPP1R12A* transcripts.

RT-PCR, both conventional and quantitative, has been commonly used to determine the presence and relative abundance of the LZ^- variant of *PPP1R12A* (Oslin et al., 2022, Khatri et al., 2001, Dordea et al., 2013, Lartey et al., 2016), and less frequently CI variants (Kim et al., 2012, Dirksen et al., 2000, Twomey et al., 2010, Payne et al., 2004). While still widely used, such approaches do not capture the complexity of the transcriptional status of *PPP1R12A*, particularly when investigating the function of MYPT1 in a particular cell type. The conventional RT-PCR approach used reveals some caveats if one intends to apply it for a comprehensive analysis of *PPP1R12A* variants. These include the need to design and test primers and optimise

reaction conditions for a number of primer sets, as well as the risk of missing variants that are expressed at very low levels. It is proposed to take into consideration an approach based on RNAseq data as a tool for gaining a comprehensive quantitative picture of *PPP1R12A* variants in a tissue or cell type of interest if suitable public data is available or can be generated.

MYPT1 plays important roles in the circulatory system. Its role as a key modulator of smooth muscle contractility is well established (Eto and Kitazawa, 2017). In the endothelium MYPT1 is important for maintenance of the barrier function (Kim et al., 2012, Kolozsvari et al., 2012, Batori et al., 2019, Aslam et al., 2010, Kovacs-Kasa et al., 2016), whereas in platelets it regulates shape change, spreading and thrombus stability (Aburima et al., 2017, Aburima et al., 2013). The profiles of *PPP1R12A* transcripts in HUVECs and HSVSMCs are very similar, with a predominance of the FL variant followed by the ΔE13 variant. Curiously, HSVSMCs express unexpectedly low levels of LZ$^-$ variants. However, studies on MYPT1 LZ$^-$ variants in venous smooth muscle, where these variants have reported to be very abundant, have been carried out in rat tissue (Payne et al., 2006, Khatri et al., 2001, Payne et al., 2004, Zhang and Fisher, 2007) rather than in cultivated smooth muscle cells. In platelets, LZ$^-$ variants account for 5.4% of transcripts (Saldanha et al., 2022), suggesting that, similar to what has been described for smooth muscle, sensitivity to nitric oxide signalling might play an important modulatory role in platelets too.

According to the analyses reported in Saldanha et al. (2022), MYPT1 isoforms lacking the CI region are ubiquitous and relatively common (Saldanha et al., 2022). In most tissues and cell types, CI variants are found at various proportions, ΔE13 being usually the predominant CI variant. Notably, in hematopoietic cells (including platelets) and organs the ΔE14 variant is not only the main CI variant, but the most frequent of all variants, clearly suggesting specific roles for ΔE14 in those cells. In spite of their relative abundance, CI variants have received little attention. ΔE13 and ΔE14 along with a E13b equivalent and an even shorter version of E13 have been reported in the rat (Dirksen et al., 2000, Payne et al., 2004). Dirksen et al. (2000) used a PCR approach to determine the relative proportions of FL and CI variants in various rat

organs (Dirksen et al., 2000) that are in good agreement with results using human RNAseq data (Saldanha et al., 2022). E13 and/or E14 variants are annotated in various vertebrates, indicating they are phylogenetically conserved. Very little is known about the consequences of CI deletions for MYPT1 function. In HeLa cells, where FL and ΔE13 are the main variants, silencing of individual variants showed that both are important for dephosphorylation of MLC and regulation of the actin cytoskeleton architecture, with only subtle differences between variants (Xia et al., 2005). One obvious consequence would be the removal of binding sites for interacting proteins, as is the case of the ΔE13 reportedly showing low binding affinity for radixin (Kim et al., 2012). Another possible consequence is an alteration in the susceptibility to regulation of MLCP activity by phosphorylation of critical residues situated in the vicinity of the CI. Although not fully comparable to mammalian CI variants, a lower rate, but not extent, of PKG-mediated phosphorylation *in vitro* has been reported in the ΔE12 chicken variant (Machida et al., 2001).

LZ^- isoforms of MYPT1 have been extensively studied predominantly using avian and rodent models, and more recently this knowledge has been transposed to human, where E24 is not annotated in GenBank. (Dordea et al., 2013) and (Lartey et al., 2016) used quantitative RT-PCR to demonstrate the LZ^- variant in placental and myometrial arteries and in uterine smooth muscle, respectively. In a recent extensive study Oslin *et al*. (2022) (Oslin et al., 2022) used a combination of genetic mouse models, human tissues, and public RNAseq data (including GTEx) to characterise the expression of the LZ^- variant. In the mouse this variant is abundant in smooth muscle isolated from various organs, broadly matching the RNAseq pattern reported in human tissues (Saldanha et al., 2022). However, ratios of LZ^-/LZ^+ variants in isolated murine smooth muscle cannot be compared directly to ratios calculated from RNAseq data of human tissues and organs because these are a mix of cell types (smooth muscle, endothelial, fibroblast, platelets, whole blood, epithelial cells, adipocytes, immune cells) each with its own pattern of *PPP1R12A* variants. It is interesting to note that the existence of a LZ^- variant with a 13 bp version of E24 has not been previously detected. This shorter LZ^-b variant is less frequent than the

longer LZ$^-$a variant but is expected to be functionally equivalent (Saldanha et al., 2022).

As well as refining the knowledge about CI and LZ variants, this work has consolidated the existence of a ΔE22 variant and uncovered two more, ΔE6 and ΔE9$^+$. These three variants bring about the deletion or addition of short stretches of amino acids (25-35 residues) and are infrequent, although a higher relative abundance and a clear functional relevance in specific cell populations cannot be ruled out. Out of these three rare variants, E9$^+$ seems to be phylogenetically conserved in some vertebrates and the exon is annotated and supported by rat RNAseq data (GenBank).

It is noteworthy that the majority of previous studies on MYPT1 transcripts have been conducted in other species such as chicken (Dirksen et al., 2000), rat (Dippold and Fisher, 2014b) and mice (Htet et al., 2021). Dippold reported that the mammalian MYPT1 gene consists of 26 exons, being three of them alternatively spliced (E13, E14 and E24) (Dippold and Fisher, 2014a). The insights gathered in this chapter have provided clarity on which exons might undergo splicing and represent the first study to characterise all potential coding protein transcripts expressed in human cells.

In this chapter the knowledge about the *PPP1R12A* promoter region was extended by identifying a total of four predicted transcription initiation sites, each with an Sp1 binding site, one of them in a novel P1$^-$ promoter region shortly upstream of the most frequently used P1 promoter region. The three transcription initiation sites in the P1 region appear to be used equally frequently, but it remains to be established why the site in the P1$^-$ region is rarely used. Very little is known about transcriptional regulation of *PPP1R12A*, but it is noteworthy that *PPP1R12A-AS1*, the gene that overlaps with the 5' region of *PPP1R12A*, encodes an antisense transcript that functions as a translation up-regulator (Schein et al., 2016). The novel ΔN variant of MYPT1 seems to arise from a transcription start located within I1 of *PPP1R12A* that reads into exon E1$^+$. Although this variant is globally very rare, it accounts for about one fourth of *PPP1R12A* transcripts in testis, the only organ where it is expressed (Saldanha et al., 2022). What cell type(s) within the testis express(es) the ΔN variant and what role it plays will require investigation. A ΔN variant is not documented in

rodents (GenBank), where MYPT1 has been widely researched. However, in *C. elegans* a potential splice variant that lacks the first 37 residues of the MYPT1 ortholog functions normally in the spermatheca but not in the embryonic epidermis (Wissmann et al., 1999). One potential consequence of the N-terminal deletion is the ablation of the ability of MYPT1 to bind PP1c, as three PP1c-binding regions would be missing: the K35VKF38 motif that appears to be essential for the interaction, the MyPhoNE motif and the first ankyrin repeat (Toth et al., 2000, Terrak et al., 2004). In addition to that, nuclear localisation signals identified in the N-terminal region are lost (Terrak et al., 2004, Wu et al., 2005), likely resulting in a protein that is unable to translocate to the nucleus, where MYPT1 is known to regulate gene expression (Kiss et al., 2019).

MYPT1, initially known for its role in regulating cytoskeletal elements and contractility, has been found in both the nuclear and microsomal fractions of various cell types, extending its role beyond cytoskeletal regulation (Kiss et al., 2019). One of its unconventional nuclear substrates is histone deacetylase 7 (HDAC7), which acts as a repressor of genes involved in T-lymphocyte differentiation, such as Nur77. Through its interaction with HDAC7, MYPT1 regulates the survival of thymocytes by attenuating Nur77 expression (Parra et al., 2005). Additionally, MYPT1 influences the subcellular localisation of the Nkx2.5 transcription factor, a crucial marker for cardiomyogenic differentiation. MYPT1's interaction with Nkx2.5 leads to its exclusion from the nucleus, inhibiting its transcriptional activity (Jamali et al., 2001, Savage et al., 2009, Ryan et al., 2013, Kiss et al., 2019). Moreover, MYPT1 interacts with various other proteins involved in transcriptional regulation, including RNA helicase and protein phosphatase 1B. These interactions suggest a role for MYPT1 in modulating gene expression and cellular processes. Furthermore, MYPT1-mediated dephosphorylation inhibits the activity of protein arginine methyltransferase 5 (PRMT5), altering the expression of genes involved in cell cycle, tumour morphology and metabolism (Sipos et al., 2017, Kiss et al., 2019). Thyroid hormone stimulation leading to the phosphorylation of MYPT1 at the Thr853 inhibitory phosphorylation site via the ROCK signalling pathway, resulting in decreased osteocalcin expression

in osteoblasts, further underscores the diverse nuclear functions of MYPT1 (Kondo et al., 2013, Kiss et al., 2019).

The utilisation of HUVECs and HSVSMC is pivotal, owing to their accessibility and distinct characteristics. HUVECs, obtained non-invasively, offer advantages in research due to their expression of endothelial cell morphology, including features like Weibel-Palade bodies, smooth muscle actomyosins, and von Willebrand Factor (Jaffe et al., 1973b, Jaffe et al., 1973a, Weibel, 2012). They are documented to display essential endothelial markers and signalling molecules linked to vascular homeostasis (Boerma et al., 2006, Caniuguir et al., 2016, Kocherova et al., 2019). HUVECs also exhibit responsiveness to stimuli like high glucose and can be differentiated into 3D spheroids for advanced research models (Kocherova et al., 2019). However, limitations such as loss of endothelial characteristics over time and heterogeneity among donor populations can affect experimental reliability and reproducibility (Kocherova et al., 2019, Staton et al., 2009).

HSVSMC, as venous smooth muscle cells, contribute to venous tone and compliance due to their arrangement in thinner layers within the tunica media of veins, making veins less muscular than arteries (Schwartz et al., 1990, Aalkjaer and Nilsson, 2005, Intengan and Schiffrin, 2001). Their greater distensibility and compliance allow them to accommodate changes in blood volume without significant pressure alterations. In contrast, arterial smooth muscle cells (ASMCs) in arteries, arranged in thick layers within the tunica media and interspersed with elastic fibres, provide strength and elasticity to withstand pulsatile pressure (Schwartz et al., 1990, Aalkjaer and Nilsson, 2005, Intengan and Schiffrin, 2001). ASMCs exhibit high contractility and relaxation in response to various stimuli, regulating blood flow and systemic blood pressure (Schwartz et al., 1990, Aalkjaer and Nilsson, 2005, Intengan and Schiffrin, 2001). Comparing venous versus arterial smooth muscle cells could provide valuable insights, particularly regarding the expression of LZ transcripts and variants that have demonstrated high expression in mice and rat SMC arteries (Dippold and Fisher, 2014b, Payne et al., 2006, Payne et al., 2004, Htet et al., 2021).

In summary, the results of this chapter extend the knowledge about the complex patterns of transcription of *PPP1R12A* in cells of the circulatory system and across tissues. It is expected that this information will contribute to guide future studies on the specific roles of understudied MYPT1 isoforms in health and disease.

Chapter 4. Interaction of MYPT1 with the regulatory subunits of PKA

4.1. Introduction

The regulation of actomyosin-driven contraction is essential for various cellular functions within the cardiovascular system. These functions include maintaining smooth muscle tone, modulating the permeability of endothelial cell monolayers, and facilitating platelet shape change and spreading. The principal regulatory mechanism underlying these processes involves the phosphorylation and dephosphorylation of the 20-kDa myosin II regulatory light chains (MLC). MLC acts as a critical node that integrates and directs both activatory and inhibitory signals towards the modulation of myosin II function. MLCP is composed of a 38-kDa protein phosphatase catalytic subunit (PP1c; specifically, the ß isoform), a 130-kDa myosin-phosphatase targeting subunit 1 (MYPT1) and, in smooth muscle, a 20-kDa subunit of unknown physiological function (Hartshorne et al., 2004, Kiss et al., 2019, Dippold and Fisher, 2014b), but the data so far suggest that it increases Rho-A. Rho-associated protein kinase (ROCK) dependent inhibitory phosphorylation of MYPT2 (the heart-specific MYPT isoform) in cardiomyocytes resulting in suppression of MP activity (Shichi et al., 2010). Data has also shown that M20/21 is involved in regulating microtubule dynamics (Takizawa et al., 2003, Kiss et al., 2019).

MYPT1 functions as a scaffold that facilitates the proximity of PP1c to its substrates. The precise activity, protein-protein interactions, and subcellular localisation of myosin light chain phosphatase (MLCP) are finely regulated by the phosphorylation status of MYPT1, which serves as a target for multiple protein kinases. Although more than 30 phosphorylation sites have been identified, the most extensively studied ones include S^{695}, T^{696}, S^{852}, and T^{853} (MacDonald and Walsh, 2018). The phosphorylation of these sites, mediated by the activities of Rho kinase (ROCK) and cAMP/cGMP-dependent protein kinases (PKA and PKG), critically determines the

activity of MLCP (MacDonald and Walsh, 2018). Upon activation of G protein-coupled receptors by various agents, MYPT1 undergoes ROCK-dependent phosphorylation at T^{696} and T^{853}, leading to an autoinhibitory mechanism that diminishes the phosphatase activity of MLCP (Khromov et al., 2009, Muranyi et al., 2005). Conversely, phosphorylation at the S^{695} and S^{852} sites by PKA and PKG is believed to counteract or prevent the inhibitory effect elicited by ROCK phosphorylation, often referred to as a disinhibition mechanism (Wooldridge et al., 2004).

cAMP signalling promotes endothelial cell monolayer barrier integrity, and it is the most potent endogenous mechanism for the control of platelet function and is also an important mediator of smooth muscle relaxation (Wooldridge et al., 2004, Aburima et al., 2013, Aslam et al., 2010, Batori et al., 2019). The most important effector of cAMP is PKA. This enzyme is a heterotetramer composed of two regulatory (PKA-R) and two catalytic (PKA Cat) subunits. Four PKA-R variants exist (RIα, RIß, RIIα or RIIß) that are differentially expressed and give rise to PKA isoforms with distinct biochemical properties and subcellular localisation, possibly playing non-redundant roles in the regulation of cell functions (Gold, 2019).

PKA isoforms are tethered to different subcellular regions and brought to the vicinity of PKA substrates by binding to A kinase anchoring proteins (AKAPs) that define distinct signalling compartments and assemble complex signalosomes (Torres-Quesada et al., 2017). AKAPs typically possess an amphipathic helix that mediates the interaction with the dimerisation and docking (DD) domain at the N-terminus of PKA-R subunits (Pidoux and Taskén, 2010). Previous study by Raslan et al. (2015), has shown evidence for cAMP signalling compartmentalisation in platelets, where moesin functions as an AKAP to target type I PKA to lipid rafts (Raslan et al., 2015). It has been hypothesised previously (Khalil, 2018) that, similarly, MYPT1 might function as an AKAP to target PKA to the MLCP signalling node, where the kinase phosphorylates MYPT1 and potentially other proteins in complex with MYPT1.

In the work of Khalil Khalil (2018), HeliQuest software was utilised to analyse the MYPT1 amino acid sequence for the presence of potential amphipathic helices, characterised by specific structural features. Five candidate sequences with

potential for amphipathic helix formation were identified and further evaluated based on various criteria. After excluding certain residues, two regions (aa267-285 and aa986-1004) are identified selected as potential amphipathic helix sites (Khalil, 2018). Furthermore, the physicochemical properties of these regions exhibit a strong amphipathic character akin to known AKAP disruptor peptides used as reference models. These findings provide evidence to support the notion that MYPT1 may function as an AKAP with hypothetical amphipathic helices. The research sheds light on the potential role of MYPT1 in mediating cAMP/PKA signalling and its impact on actin regulation (Khalil, 2018). With this information Khalil (2018) performed affinity pull downs to confirm the interaction between MYPT1 and PKA and showed that GST fused recombinant PKA-R subunits would interact with Myc-MYPT1 (full length and C-terminal) proteins from transfected HEK 293T cells. No interaction was observed between Myc-MYPT1 (N-terminal) and PKA-R subunits. To further understand the interaction, 4 fragments of the C-terminus labelled C1, C2, C3, and C4 were transfected to HEK 293T cells. Subsequent analysis has shown that the C2 fragment presented higher intensity bands upon incubation with recombinant PKA-R subunits than other fragments (Appendix Figure 8.2-1) (Khalil, 2018). This study also included immunoprecipitation, affinity pull down and affinity cAMP pull-down, all performed with platelets lysates.

There is a need to confirm the results of previous studies and extend them to the additional cells of the vascular system (in this particular case endothelial cells) using robust quantitative approaches. To do so it was hypothesised that:

MYPT1 and PKA subunits directly interact in endothelial cells.

Aims of this chapter:

1. To verify the existence of protein complexes of MYPT1 and PKA subunits in vivo
2. To determine the co-localisation of MYPT1 with PKA subunits.
3. To determine the interaction of MYPT1 with PKA subunits using an *in situ* proximity ligation assay.

To address these aims, a combination of immunoprecipitation, affinity pulldown, immunofluorescence, and in situ proximity ligation assay techniques were used.

4.2. Expression of MYPT1 and PKA subunits in ECs and platelets.

4.2.1. Characterisation of antibodies used in this study.

In previous work by Khalil (Khalil, 2018) the MYPT1-PKA interaction was analysed by immunoprecipitation (IP) in platelets. The goal was to adapt the same IP protocol to HUVEC lysates. Due to the previously used antibody being discontinued, the need arose to identify and test another suitable MYPT1 antibody. As shown in Appendix B Fig. 8.2-4 A and B, the IP of MYPT1 using the anti-MYPT1 antibodies ABS1495 and 07-0672-I (Sigma-Aldrich, Merck Millipore) was not successful. A further antibody, the rabbit monoclonal antibody D6C1 (Cell Signalling Technology, Netherlands), was identified that is compatible with immunoprecipitation and immunoblotting, according to the company provider. The rabbit (DA1E) monoclonal antibody IgG was used as isotype matching control for the MYPT1 antibody, to ensure specificity in IP as well as immunofluorescence studies.

The integrity and concentration of the MYPT1 and PKA subunit antibodies and their isotype-matching controls were examined by SDS-PAGE and, where possible, protein concentration determination (Figure 4.1; see also Appendix Figure 8.2-2 and Table 2.8 and Table 2.9). MYPT1 and PKA subunit antibodies and their corresponding isotype-matching controls were observed at comparable concentrations. As shown in Figure 4.1A and B, an intense band of about 72 kDa size is apparent in almost all antibodies This band could be due to bovine serum albumin (BSA) as its size is around 72 kDa. In panel A it can also be observed a band around 150 kDa on the MYPT1 antibody which is not visible on the IgG and again shown in panel B on PKA antibodies. This molecular size is compatible with full antibody; therefore, this band could be an incomplete reduction of MYPT1 antibody (Liu et al., 2007), but it could also correspond to the stabilisers added by the manufacturer to the antibody solutions.

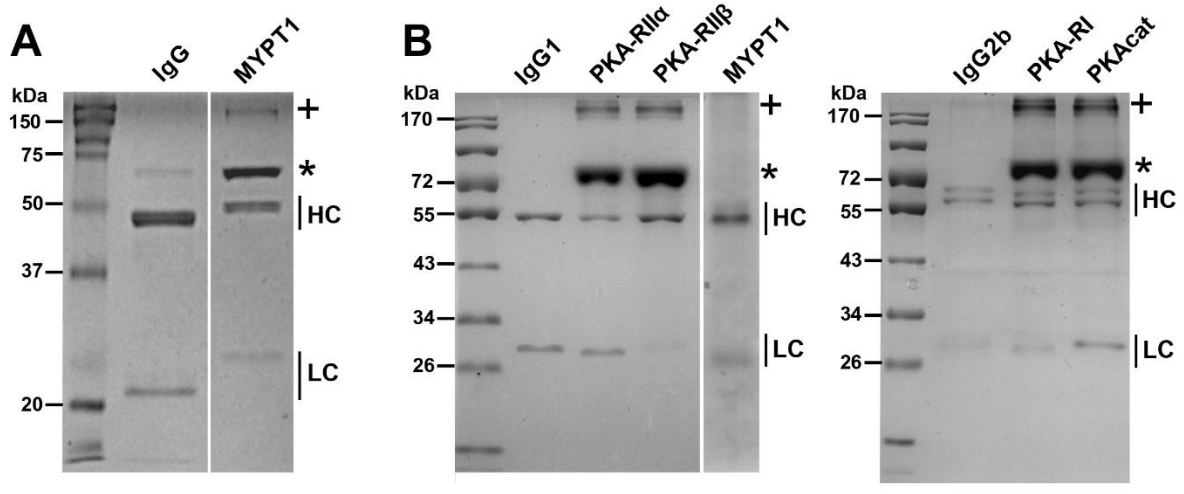

Figure 4.1 Characterisation of antibodies used in this study. Monoclonal antibodies against MYPT1 and PKA subunits and their matching immunoglobulin isotype controls. Antibodies were resolved by SDS-PAGE and gels were stained with Coomassie brilliant blue. **(A)** MYPT1 antibody raised in rabbit against MYPT1 and its matching immunoglobulin control. 0.5 µg of each were loaded. **(B)** Antibodies raised in mouse against MYPT1 and PKA subunits and their matching immunoglobulin isotype controls. 1 µg of each were loaded. The bands marked with ***** around 72 kDa match in size to BSA. The bands marked with **+** are probably high molecular weight stabilisers. HC, heavy chain; LC, light chain.

4.2.2. Expression of MYPT1 and PKA subunits in endothelial cells and platelets

After the successful characterisation of antibodies, the next goal was to investigate the expression of MYPT1 and PKA subunits in endothelial cells and platelet lysates. Lysates were resolved by SDS-PAGE and the presence of the proteins of interest was determined by western blotting using the antibodies characterised in the previous section. β-Actin and GAPDH were used as loading controls (Figure 4.2). Endogenous expression of MYPT1 and all PKA subunits were observed in both platelets and HUVECs. In endothelial cell lysates, both HUVECs (Figure 4.2 A) and HDBECs (Figure 4.2 B), MYPT1 is present as a double band of approximately ~140 kDa that corresponds to two main isoforms. Two bands are also present in platelet lysates (overexposed blot in (Figure 4.2 A), with the lower of the two MYPT1 bands having much higher intensity than the upper one. As stated in the previous chapter, the lower band corresponds to isoforms lacking E14 in platelets or E13 in HUVECs and

HDBECs and the upper band corresponds to the full-length) isoform. All PKA-R subunits are expressed at the expected size in the 50 kDa region but their relative amounts in HUVECs and platelets appear to be variable. PKA-RIα/ß as well as PKA-RIIß present higher expression in platelets than in HUVECs, while on the other hand the expression of PKA-RIIα was higher in HUVECs than in platelets. The antibody raised against the PKAcat α subunit (40 kDa) also recognises the 93% identical slightly larger ß subunit in both HUVEC and platelet lysates.

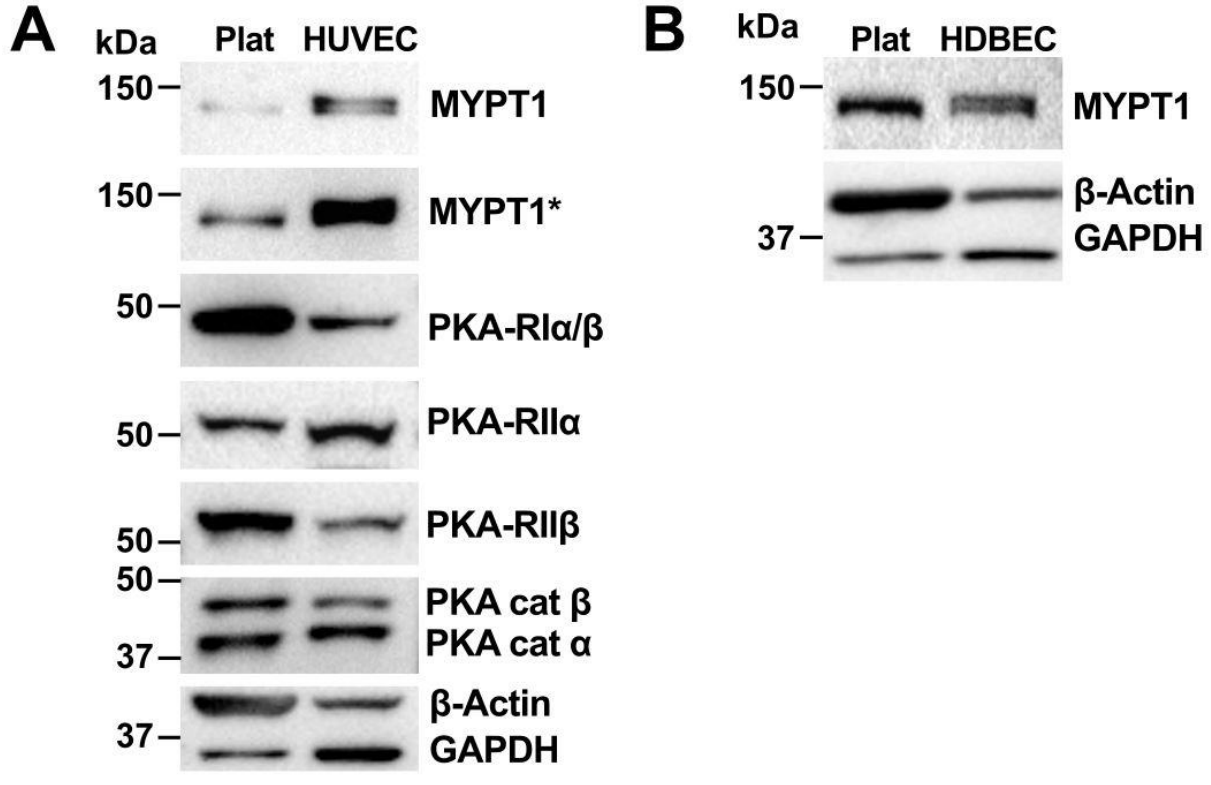

Figure 4.2 Expression of MYPT1 and PKA subunits in ECs and washed human platelets. **(A)** Expression of MYPT1 and PKA-RIα/ß, PKA-RIIα, PKA-RIIß and PKA catalytic subunits in HUVECs and human platelets. Lysates (10 µg) of platelets lysate and (20 µg) of HUVECs lysate were resolved by SDS-PAGE, transferred to PVDF membrane, and probed with the indicated antibodies. A rabbit antibody was used for MYPT1. PKAcat α band was identified previously by Khalil (2018) as the lower band and top band was identified as PKAcat ß, as shown in Figure 4.1D (Khalil, 2018). **(B)** Expression of MYPT1 in HDBECs (20 µg) and human platelets (10µg). Lysates were processed as in A and probed for MYPT1 with a mouse antibody. ß-Actin and GAPDH were used as loading controls. *Long exposure. Uncropped blots are shown in Appendix Figure 8.2-3.

4.3. Immunoprecipitation of MYPT1 and co-immunoprecipitation of PKA subunits

Previous attempts to reproduce an IP protocol, used on platelet lysates, performed by Khalil (2018) were unconclusive. These attempts were made using HUVEC lysates and neither MYPT1 was immunoprecipitated nor the PKA subunits were able to co-IP due to the control IgG IP presenting unspecific binding and a very high background. (Appendix Figure 8.2-4). Therefore, it was decided to set up a new IP protocol in order to ensure specificity of the immunoprecipitated proteins to subsequently investigate the presence of PKA subunits in the immune complexes as described in section 2.4.4. In view of these results, a protocol to performed immunoprecipitation of MYPT1 was devised as described in section 2.4.4.

As show in Figure 4.3, the anti-MYPT1 monoclonal antibody D6C1 (#8574, Cell Signalling Technologies, Netherlands) raised in rabbit was used to immunoprecipitate MYPT1 in HUVECs. MYPT1 protein from HUVEC lysates could not be detected after incubation of the lysate with MYPT1 antibody and removal of beads, whereas the protein was recovered in the immunoprecipitate. In the control reaction with IgG IP there was no detectable presence of MYPT1. Upon immunoblotting with IgG rabbit light chain specific antibody, a higher band intensity of the antibody light chain was observed in the IP with IgG compared to MYPT1 antibody. The antibody heavy chain showed the same intensity with both antibodies.

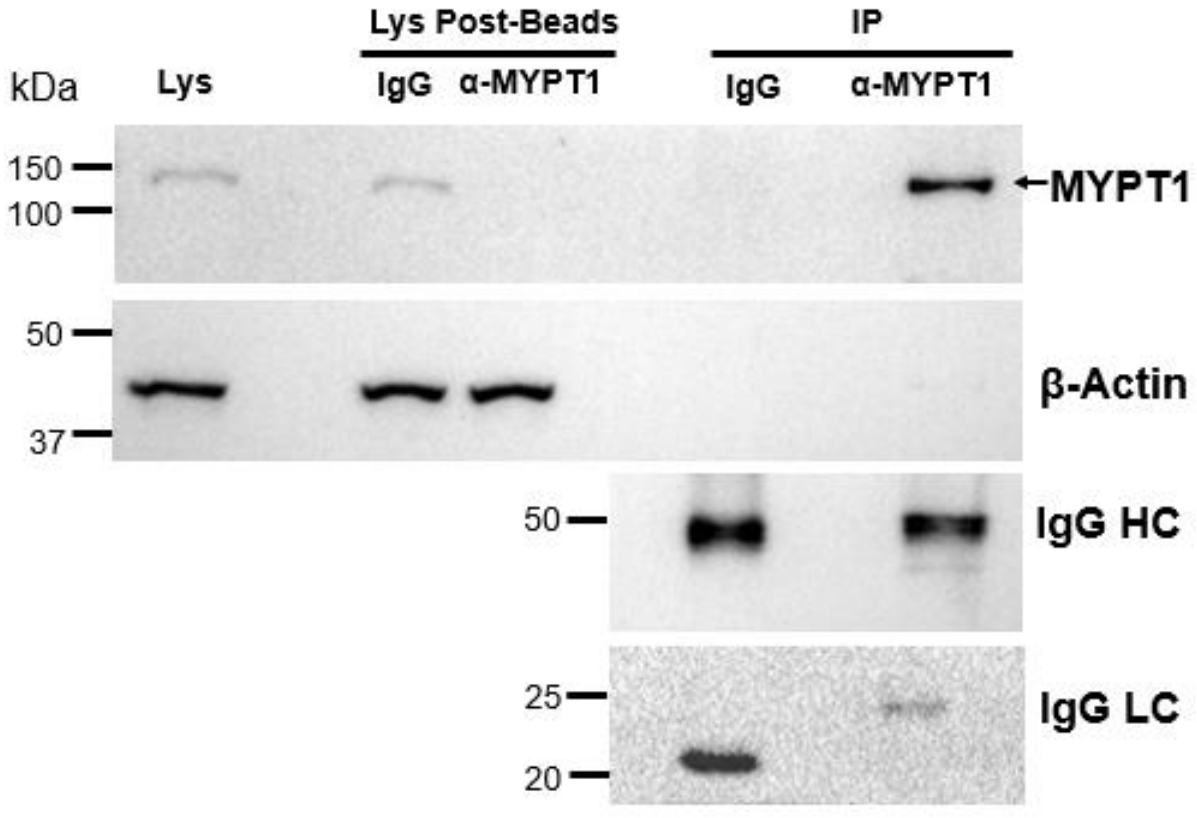

Figure 4.3 Representative immunoprecipitation of MYPT1 from HUVEC lysate. HUVEC lysate was subject to immunoprecipitation with anti-MYPT1 ((D6C1), #8574, Cell Signalling Technologies, Netherlands) monoclonal rabbit -specific antibody or isotype-specific immunoglobulin G ((IgG) (DA1E), #3900, Cell Signalling Technologies, Netherlands) as a control. Immune complexes were examined by Western blot for the presence of MYPT1 and for the immunoglobulin heavy chain (HC) and light chains (LC). ß-Actin was used as loading control for lysates. Lys, lysate.

Having successfully immunoprecipitated MYPT1 in HUVECs, the next step was to investigate whether PKA subunits were present in the immune complexes. As shown in Figure 4.4 A, all PKA subunits with the exception of the PKA-RI co-immunoprecipitated with MYPT1. ß-actin was used as loading control for the lysates whereas the IgG light and heavy chains were used as normalisation control for the immunoprecipitation. The depletion ratios of MYPT1 and PKA subunits were calculated (Figure 4.4 B and Appendix Table 8.2-2). MYPT1 depletion was significant ($p=5.46x10^{-7}$, Kruskall Wallis test, overall group comparison) in comparison to PKAcat and PKA-R. There was no statistical significance difference when comparing

depletion between PKA-R and PKAcat. The quantification of IP and co-IP is shown in Figure 4.4 C. IP of MYPT1 was statistically significant ($p = 7.28x10^{-14}$, paired T-test). It was also found that co-IP of PKA-RIIα ($p= 1.75x10^{-4}$); PKA-RIIß ($p= 1.03x10^{-3}$), and PKAcat ($p= 5.89x10^{-3}$) were also statistically significant (Appendix Table 8.2-3). In conclusion, under these experimental conditions PKA-RII (although not RI) and PKAcat were recovered significantly in immune complexes with MYPT1 in HUVECs.

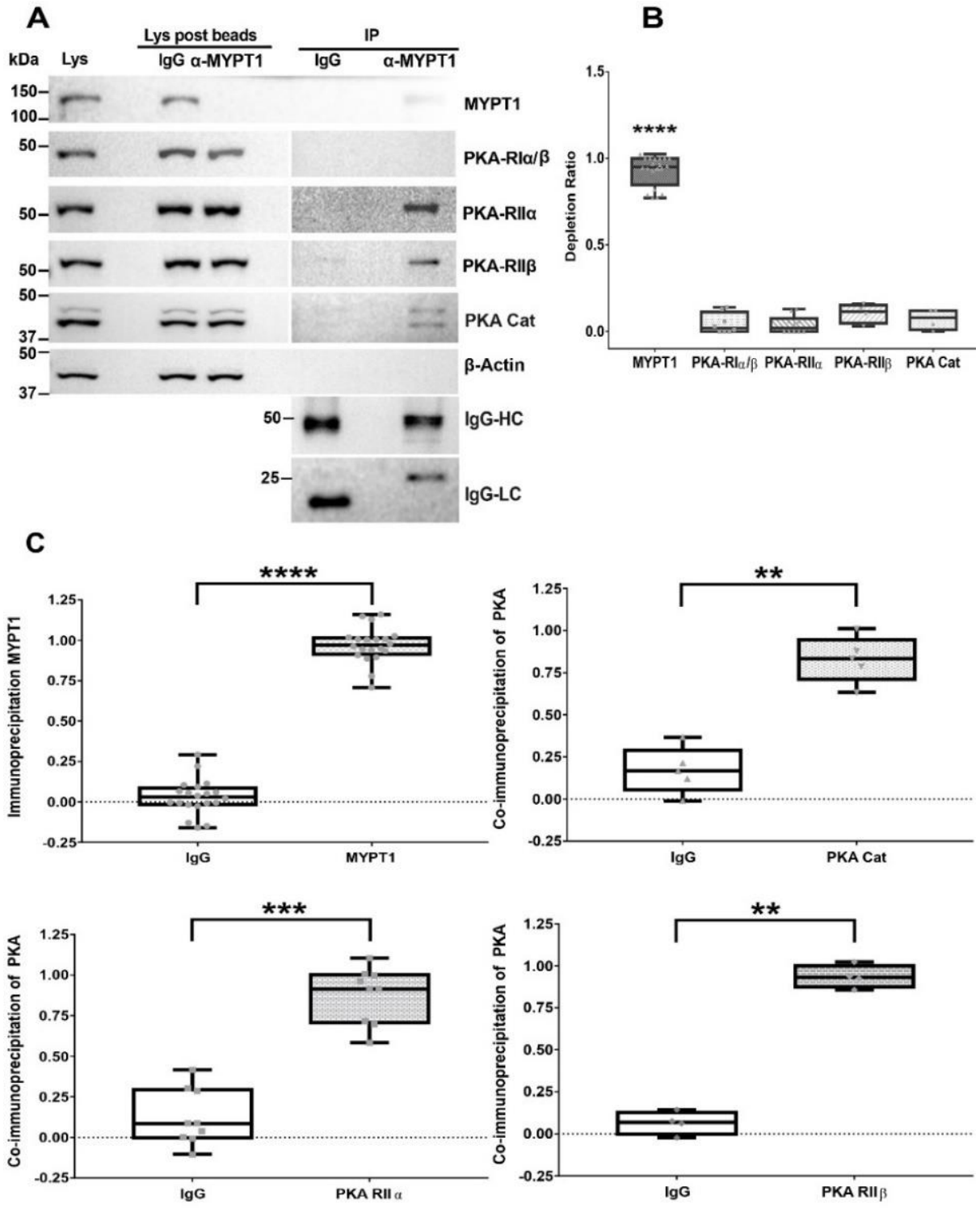

Figure 4.4 Legend on the following page

Figure 4.4 Immunoprecipitation of MYPT1 from HUVEC lysate. (A) MYPT1 co-immunoprecipitate PKA subunits. HUVEC lysates were subject to immunoprecipitation with rabbit MYPT1-specific antibody or isotype-specific immunoglobulin G (IgG) as a control. Protein complexes were examined by western blot for the presence of PKA-R subunits, the PKAcat subunit and for the immunoglobulin heavy chain (HC) and light chains (LC). ß-Actin was used as a loading control for lysates. Lys, total cell lysate. Note that the immunoprecipitation (IP) blots for PKA subunits required longer exposures than the lysates **(B)** Quantification of protein depletion. The boxplots depict the median with the first and third quartile of the distribution. Whiskers extend to 1.5 times the interquartile range; no outliers beyond this point were found ($p= 5.47x10^{-7}$, Kruskal-Wallis test). **(C)** Quantifications of MYPT1 immunoprecipitation and co-immunoprecipitation of PKA subunits. The boxplots depict the median with the first and third quartile of the distribution. Whiskers extend to 1.5 times the interquartile range; no outliers beyond this point were found. Immunoprecipitation of MYPT1 (n=20); co-IPs of PKA cat (n=4), PKA-RIIα (n=9), PKA-RIIß (n=4). Paired t-test, ** $p<0.01$; ****$p<0.001$. PKA RI (n=3) was not co-immunoprecipitated. Depletion and co-immunoprecipitation ratios were calculated as described in section 2.4.14. Results of all individual experiments are presented in Appendix Figure 8.2-5.

To confirm that MYPT1 and PKA subunits form part of a complex, a reverse immunoprecipitation, in which the PKA-R subunits are immunoprecipitated and MYPT1 is detected in the immune complexes, was attempted. As showed in Appendix Figure 8.2-6, immunoprecipitations using antibodies against PKA-R subunits did not prove efficient at immunodepleting any of the PKA-RI subunits from the lysates. Only PKA-RII was recovered in the immune complexes, but the proteins were visible only after long exposures and no MYPT1 was detected. Immunoprecipitation with PKAcat antibodies was similarly inefficient at immunodepleting PKAcat and no protein was visible in the immune complexes. In view of these results, it was decided not to pursue the reverse immunoprecipitation approach.

4.3.1. Immunoprecipitation of MYPT1 and co-immunoprecipitation of PKA subunits in platelets

It has previously been shown (using an immunoprecipitation approach) that PKA-R subunits can be identified in immunocomplexes with MYPT1 in platelets (Khalil, 2018). In this study it was aimed to reproduce those results using the MYPT1 monoclonal antibody D6C1 raised in rabbit (#8574, Cell Signalling Technologies, Netherlands) and protein A coated magnetic beads as opposed to a rabbit polyclonal antibody H-130 (sc-25618, Santa Cruz Biotechnologies) and conventional protein G-Sepharose beads used in the previous study. Applying the same conditions and systematic approach used in HUVEC lysates, immunodepletion of MYPT1 from the platelet lysate and enrichment in the immunoprecipitate were observed, although some unspecific MYPT1 was recovered with the control IgG (Figure 4.5). Unspecific binding to the control IgG was observed with all PKA subunits. Regarding the PKAcat subunit, only the α isoform is observed in the immunoprecipitate. Notably, ß-actin, used for lysate control, was also present in the immunoprecipitates.

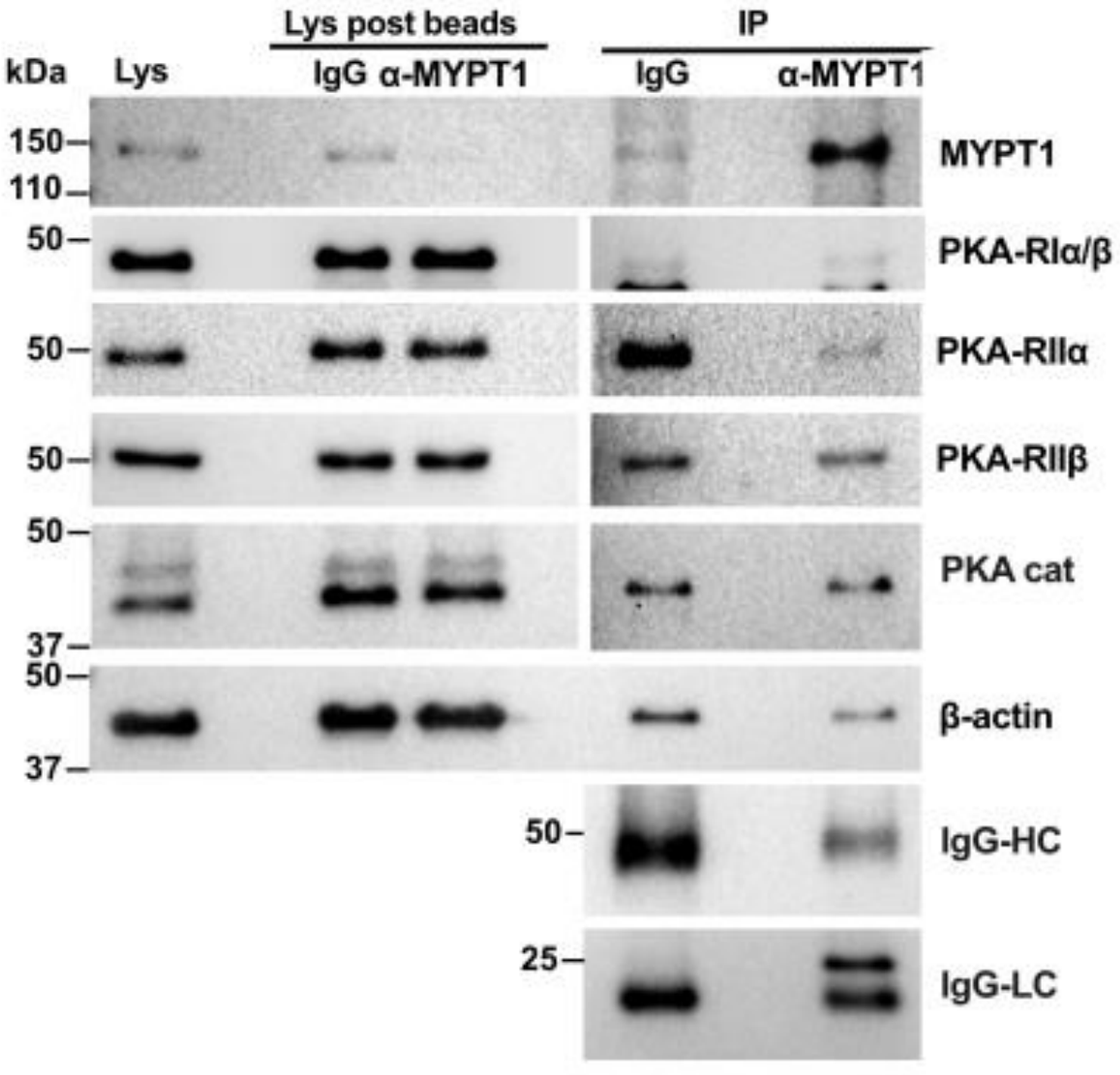

Figure 4.5 Immunoprecipitation of MYPT1 from platelet lysates. Human washed platelet lysates were subject to immunoprecipitation with MYPT1-specific rabbit antibodies or isotype-specific immunoglobulin G (IgG) as a control. Protein complexes were examined by Western blot for the presence of PKA-R subunits as well as for the PKAcat subunit and for the immunoglobulin heavy chain (HC) and light chains (LC). ß-Actin was used as a loading control for lysates. Lys, total cell lysate. IP, immunoprecipitation.

4.4. cAMP affinity pull-down of PKA subunits

Upon binding to cAMP, the PKA-R subunits change conformation and release the PKAcat subunits (Gold, 2019). To investigate whether the interaction of PKA with MYPT1 is conformation-dependent, an affinity pulldown with agarose beads functionalised with cAMP (8-(6-aminohexylamino) adenosine-3',5'-cyclic monophosphate (8-AHA-cAMP)) was chosen. This approach was used both in HUVEC and platelet lysates.

4.4.1. cAMP affinity pull-down of PKA subunits in HUVECs

In HUVECs the cAMP affinity pulldown depleted most of all PKA-R variants and, as expected, very little PKA cat was found attached to the beads, where PKA-R subunits were significantly recovered. No MYPT1 was recovered with the beads, suggesting that the PKA-MYPT1 complex occurs when PKA-R subunits are not bound to cAMP (Figure 4.6 A). More than 85% of PKA-RIα/ß, PKA RIIα and PKA RIIß was depleted from the lysates with cAMP beads in comparison to control (EtOHN) beads and these depletions were highly significant ($p<0.0001$) (Figure 4.6 B). cAMP affinity pulled down PKA-RIα/ß ($p = 4.82x10^{-4}$), PKA-RIIα ($p= 4.65x10^{-3}$), PKA-RIIß ($p= 3.06x10^{-3}$) and PKAcatß ($p= 2.13x10^{-2}$), all statistically significant in comparison to control (EtOHN) beads. MYPT1 and the α isoform of PKAcat were not pulled down indirectly by cAMP beads (Figure 4.6.C). All statistical analyses are presented in Appendix Table 8.2-4 to Appendix Table 8.2-7.

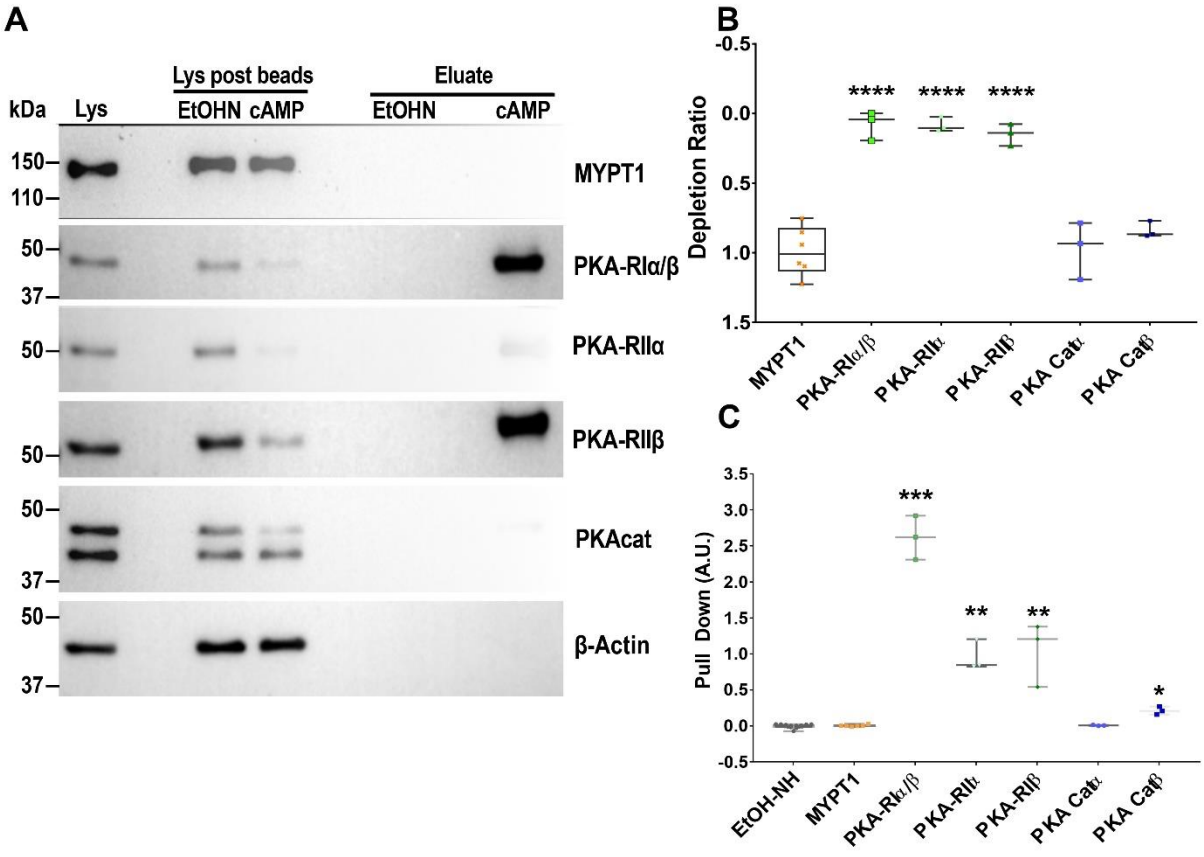

Figure 4.6 Affinity pull-down with cAMP beads in HUVECs. (A) cAMP pull-down on HUVECs. Lysates were incubated with 8-AHA-cAMP (cAMP) or control ethanolamine (EtOHN) agarose beads. Complexes were examined by western immunoblot for the presence of MYPT1 and PKA subunits. Beta-actin (ß-actin) was used as a loading control for lysates. Lys, cell lysate. Eluate – Samples eluted directly from the beads. **(B)** Quantification of protein depletion ratios. The boxplots depict the median with the first and third quartile of the distribution. Whiskers extend to 1.5 times the interquartile range; no outliers beyond this point were observed. P-values obtained by ANOVA with adjusted Tukey's test. **** = $p<0.0001$. Depletions were normalised to ß-actin. Statistical analysis is presented in Appendix B Tables 8.2-4 and 8.2-5. **(C)** Quantification of affinity pull-down of PKAs. Boxplots as in panel B. P-values obtained by Kruskal Wallis with Dunn's post-hoc test. * = $p<0.05$; ** = $p<0.01$; *** = $p<0.001$; Blots are representative of 3-6 independent experiments. Statistical analysis is shown in Appendix Table 8.2-6 Normality of cAMP affinity in HUVECs. Appendix Table 8.2-6 and Appendix Table 8.2-7. Depletion ratios and pulldown amounts were calculated as described in Materials and Methods Quantification of pulldown 2.4.13.

4.4.2. cAMP affinity pull-down of PKA subunits in platelets

In platelet lysates, the cAMP affinity pulldown visibly depleted PKA-R variants and, as expected, very little PKAcat. It also yielded a significant amount of MYPT1 bound to the beads, but also of ß-actin (Figure 4.7 A), in contrast to HUVEC lysates (Figure 4.7 A). To rule out that the interaction of MYPT1 with PKA in platelets is mediated by the actin cytoskeleton, latrunculin B, was used to disrupt the actin cytoskeleton prior to the cAMP pulldown. Riley et al. (2020) reported that 20 µM of latrunculin B has shown the depolymerisation of F-actin in human platelets (Riley et al., 2020). However, under those conditions, significant amounts of MYPT1 and actin were still recovered with the beads (Figure 4.7 B and Appendix Figure 8.2-8). The different behaviour of MYPT1 between HUVECs and platelets in immunoprecipitation and cAMP pulldown assays might be explained by differences in their relative amounts of actin, which are considerably higher in platelets (Figure 4.2).

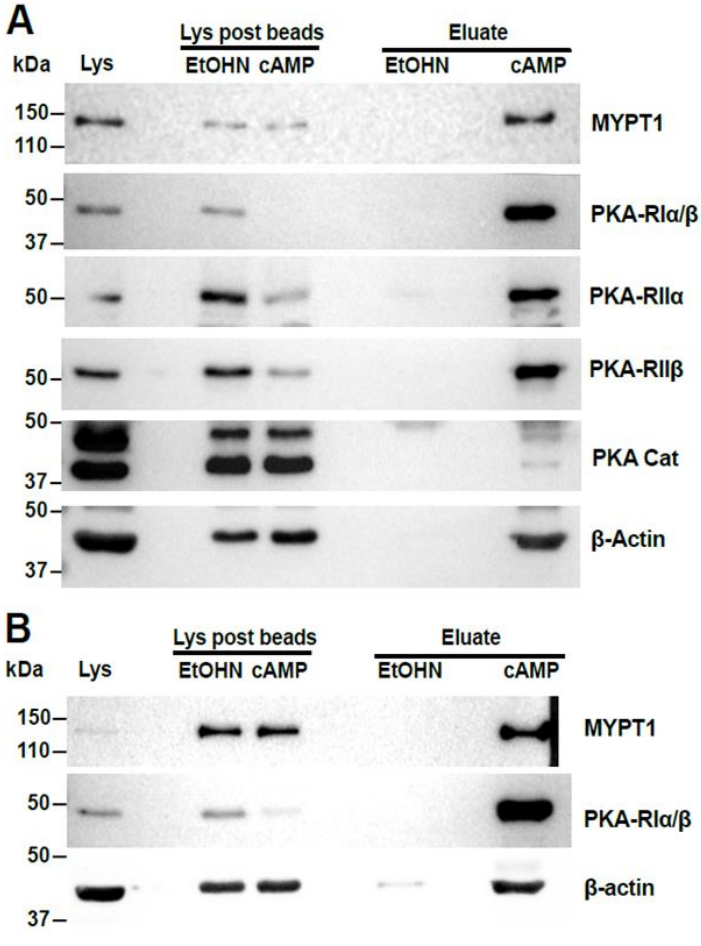

Figure 4.7 cAMP affinity pulldown of MYPT1 in platelets. (A) cAMP affinity pull-down. Platelet lysates (500 µg) were incubated with 25 µl of 8-AHA-cAMP (cAMP) agarose beads or control ethanolamine (EtOHN) agarose beads. Attached complexes were examined by western immunoblot for the presence of MYPT1 and PKA subunits. **(B)** cAMP affinity pull-down in the presence of latrunculin B. Washed platelets were incubated with 20 µM latrunculin B for 30 min at 37°C, lysed and processed as in B. Beta-actin (ß-actin) was used as a loading control for lysates in A and B. Immunoblots are representative of at least three independent experiments. immunoblots are representative of at least three independent experiments. Lys, cell lysate. Eluate – Samples eluted directly from the beads.

4.5. Subcellular localisation of MYPT1 and PKA subunits in HUVECs

MYPT1 has been shown to form complexes with PKA-R subunits (section 4.3.1) therefore it was important to investigate whether they can be colocalised in HUVECs as it has been shown in platelets by Khalil (Khalil, 2018). To test the subcellular location of MYPT1 and PKA subunits in HUVECs and their possible co-localisation, an immunofluorescence approach was undertaken. Preliminary experiments were conducted to determine optimal fixation and permeabilisation methods as well as antibody concentrations.

4.5.1. Determination of optimal fixation method for immunofluorescence of HUVECs

It was important to identify a suitable method for fixation of HUVECs for immunofluorescence. Paraformaldehyde (PFA) and acetone-methanol fixation were compared. The MYPT1 and PKA antibodies characterised in Figure 4.1. were tested.

As shown in Figure 4.8 A, with PFA fixation MYPT1 staining is distributed throughout the cell, with some cortical enrichment. PKA-RI, PKA-RIIα and PKA-RIIß also showed clear staining with PFA fixation. Only PKAcat staining displayed a very low intensity compared to other PKA subunits. When acetone-methanol was used (Figure 4.8 B), the only antibody that showed improved staining compared to PFA fixation was anti-PKAcat. The PKA-R subunits produced lower staining intensity compared with PFA fixation. Isotype specific controls did not show unspecific signals with any of the fixation methods. The fixation method, 4% PFA, has proven to be the best fixation method and was therefore selected for subsequent experiments.

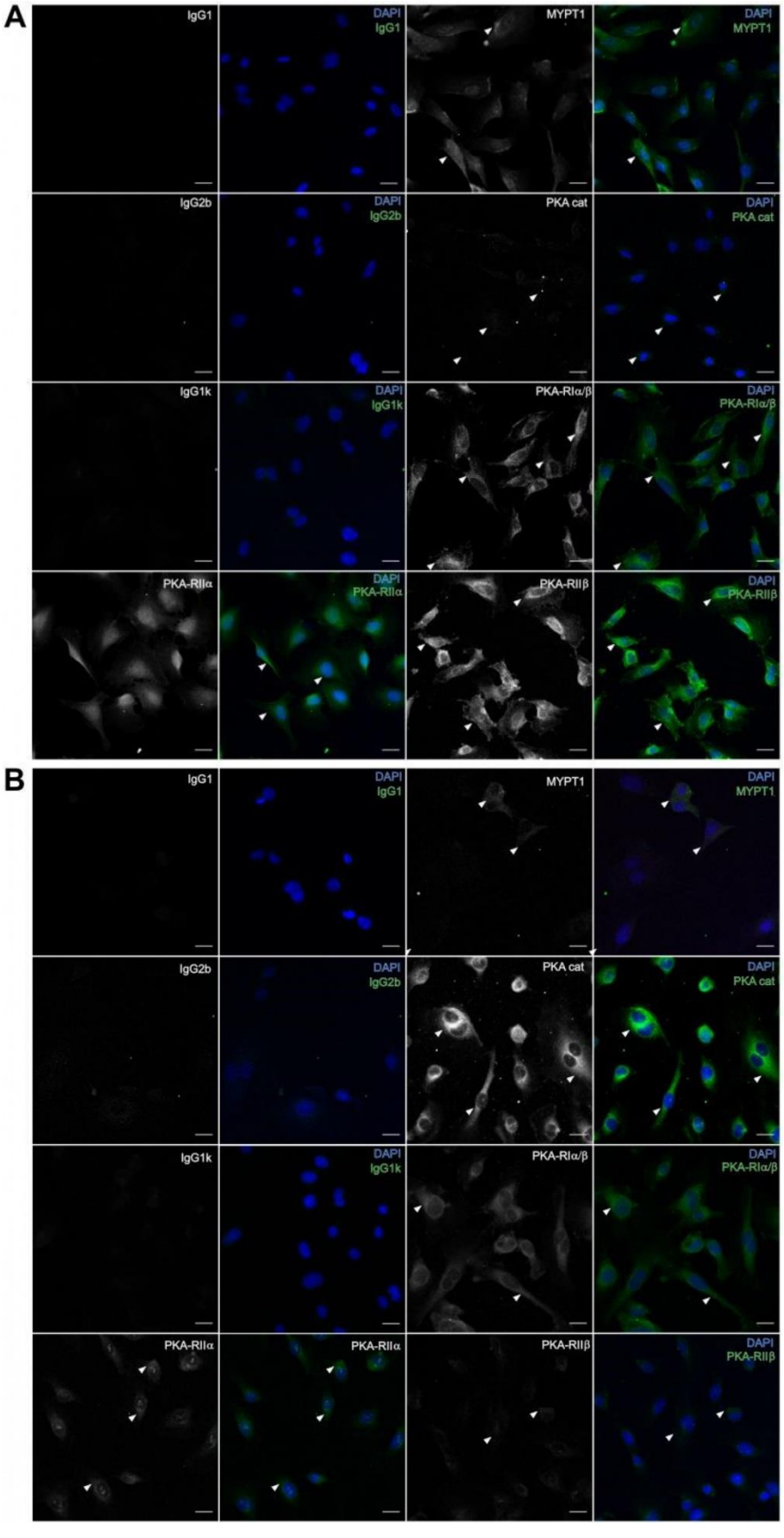

Figure 4.8 Expression of MYPT1 and PKA subunits in HUVECs determined by immunofluorescence. Cells were fixed with 4% PFA **(A),** or with an acetone methanol solution **(B).** In both fixation methods cells were permeabilised and incubated with rabbit MYPT1 specific antibody and the indicated mouse PKA-R and catalytic subunit antibodies followed by species-specific fluorescently labelled Alexa fluor488® (green) conjugated secondary antibody. Nuclei were counterstained with DAPI. All antibodies were used with their respective immunoglobulin G (IgG) isotype matching control. (IgG1k is the isotype matching control for the PKA RIIα and RIIß; IgG2b is the isotype matching control for PKAcat and PKA-RIα/ß. Images were acquired with a ZEISS LSM 710 confocal laser scanning microscope equipped with a 20× objective. Scale bar represents 20 µm. White arrowheads show examples of protein recognition by its specific antibody.

Double staining of MYPT1 with PKA-R and PKAcat are the next step to be achieved. Prior to this it was essential to test Alexa® 568 (red) for MYPT1 and try to improve the signal on PKA antibodies. This secondary antibody gave comparable results as shown in the Appendix Figure 8.2-9.

For double staining, Alexa®488 (green) was selected as secondary labelling for mouse antibodies (PKA-R and PKAcat) and Alexa®568 (red) as secondary labelling for rabbit antibodies (MYPT1). To allow for the visualisation of the cell perimeter on single staining, fluorescently labelled phalloidin was tested to stain F-actin.

As previously shown, PKA antibodies labelled with conjugated fluorescent ones have similar intensity and need, therefore, to be optimised for acquiring high quality images in HUVECs. This test was restricted to PKA-RIIα. To increase the intensity of the staining without compromising the specificity, additional amount of antibody was added from this point forward. This increase is first observed in Fig. 4.9, increasing PKA-R antibody concentration as well its isotype matching control did not result in unspecific binding of IgG.

Figure 4.9 shows that staining MYPT1 with Alexa Fluor 568(red) conjugated secondary along with FITC-phalloidin provided good signals. Comparable results were obtained when staining PKA-RIIα with Alexa Fluor 488(green) conjugated secondary along with TRITC-phalloidin. This idea was conceived to help visualising all the dots that proximity ligation assay experiments might bring. In a similar experiment MYPT1, non-smooth muscle myosin IIa and F-actin, staining with a far-red tagged phalloidin, were tested. Both non-smooth muscle myosin IIa and actin appear to co-localise, the same seems to happen with myosin and MYPT1 (Appendix Figure 8.2-10).

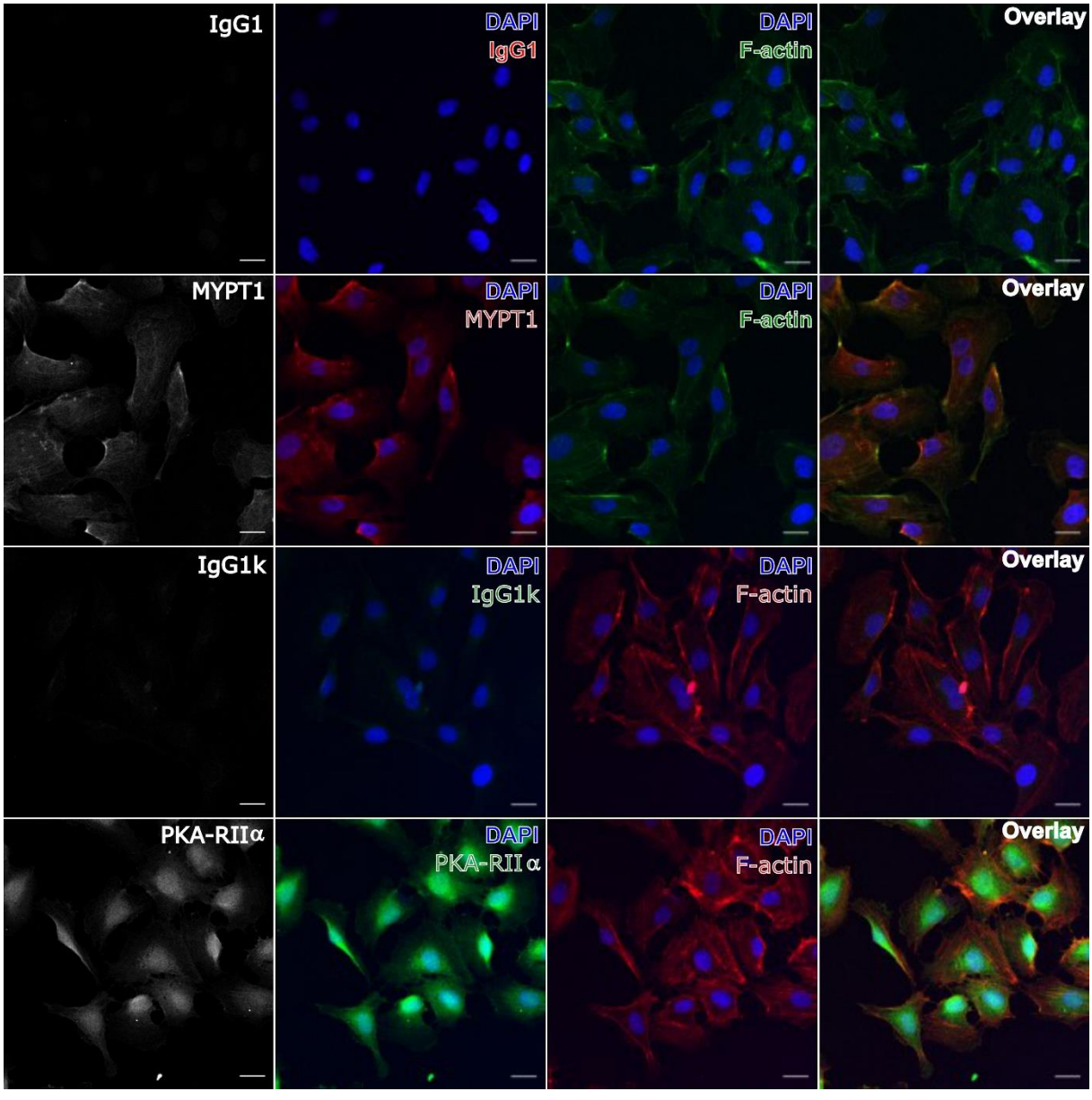

Figure 4.9 MYPT1 and PKA expression in HUVECs with cytoskeleton F-actin fibres staining. Cells were fixed (4%PFA), permeabilised and incubated with MYPT1 (IgG1 as its isotype matching control) and PKA-RIIα (IgG1k as its isotype matching control) followed by species specific Alexa® Fluor 488 (green) or Alexa® Fluor 568 (red) conjugated secondary antibodies. On the two upper rows rabbit anti MYPT1 antibody and its isotype matching control IgG1 were used same concentration. F-actin staining in green (FITC-phalloidin) Images were acquired with ZEISS LSM 710 confocal laser scanning microscope with a 20x objective. On the two lower rows PKA-RIIα was labelled with secondary antibody Alexa Fluor 488. F-actin staining in red (TRITC-phalloidin) Images were acquired with ZEISS LSM 710 confocal microscope with 20X objective. Scale bar represents 20 μm.

4.6. Co-localisation of MYPT1 with PKA-R subunits

Having shown that MYPT1 forms complexes with PKA-R subunits in HUVECs and established optimal conditions for immunofluorescence studies of MYPT1 and PKA subunits, it was proposed to investigate whether PKA subunits colocalise in HUVECs. HUVECs were fixed and double immunostained with antibodies against MYPT1 and either PKA-RIα/ß, PKA-RIIα or PKA-RIIß (Figure 4.10). MYPT1 displayed a dispersed distribution with accumulation in the nucleus and enrichment in discrete cortical regions (Figure 4.10 A), as reported by others (van Nieuw Amerongen et al., 2007). The anti-PKA-RI antibody yielded a predominantly cytoplasmic pattern with very little signal in the nucleus and, in some cells, enrichment in perinuclear and cortical regions. PKA-RIIα staining was diffuse across the cytoplasm and nucleus, with a weak accumulation in cortical regions. PKA-RIIß was also diffuse across the cell, with a higher accumulation in a perinuclear region that resembles the Golgi and, in some cells, cortical enrichment. Due to the predominantly diffuse distribution of these proteins and the variety of patterns of subcellular distribution, a noticeable co-localisation of MYPT1 and PKA-R subunits was only apparent in restricted regions, predominantly at the cell cortex (Figure 4.10 A). Correlation analysis showed Pearson's correlation coefficients (mean ± SEM) significantly above the control (0.018 ± 0.020) for PKA-RI (0.667 ± 0.011), PKA-RIIα (0.833 ± 0.012) and PKA-RIIß (0.640 ± 0.017). All PKA-R showed similar statistically significant values ($p < 2.11 \times 10^{-15}$) (ANOVA followed by Tukey test). The Pearson's correlation coefficient for PKA-RIIα in comparison with the other two PKA-R subunits was significantly higher; PKA-RI (p-value = 2.59×10^{-11}) and PKA-RIIß (p-value = 6.72×10^{-14}), this may likely be a result of the more uniform distribution of this subunit. Statistical analysis is shown in Appendix Table 8.2-8 and Appendix Table 8.2-9.

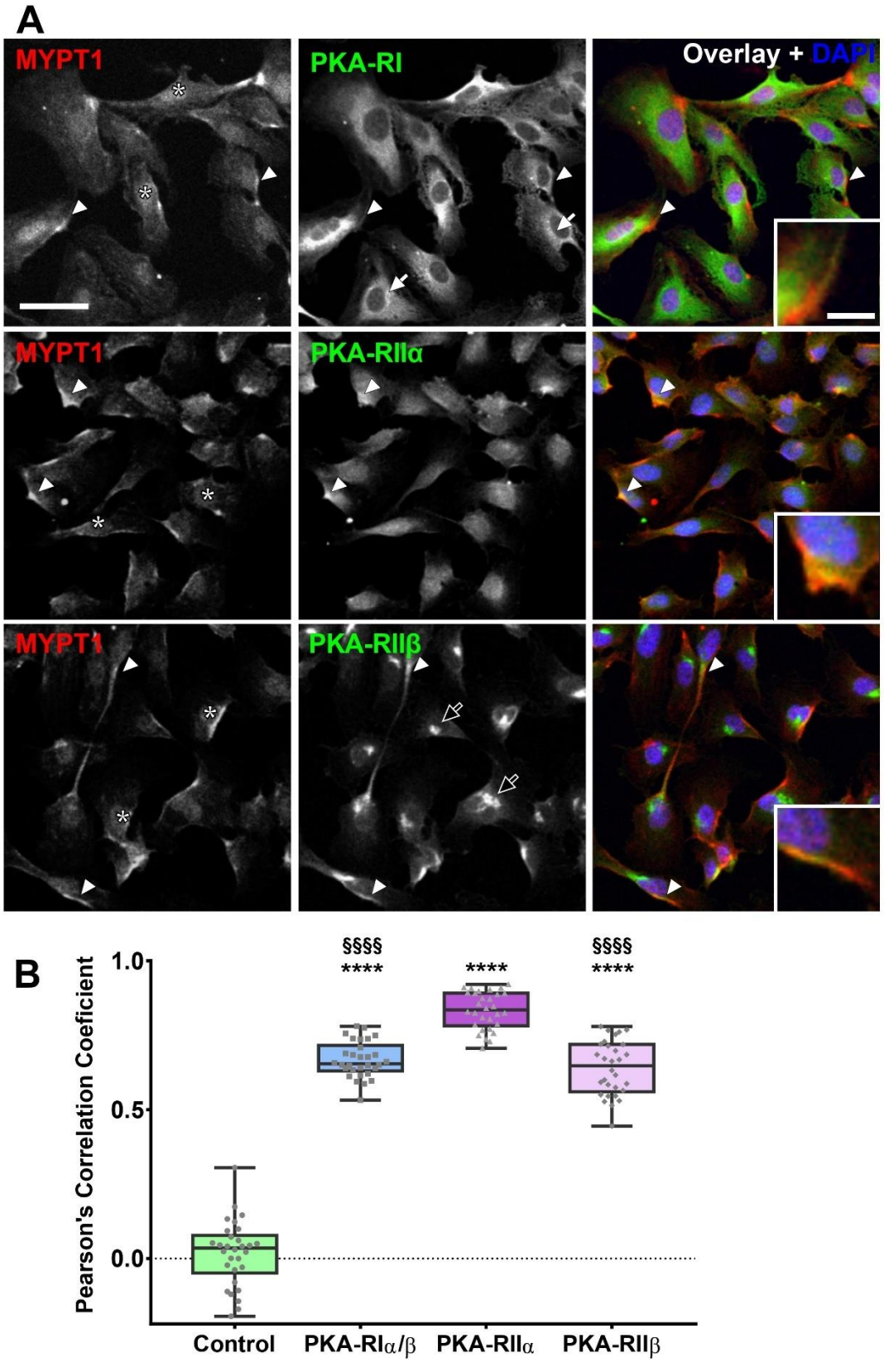

Figure 4.10 Figure Legend on the following page

Figure 4.10 Double immunofluorescence staining of MYPT1 and PKA-R subunits in HUVECs. (A) Cells were fixed, permeabilised and incubated with rabbit MYPT1-specific antibody and the indicated mouse PKA-R subunit antibody followed by species-specific fluorescently labelled Alexa fluor® 568 (red) or Alexa fluor® 488 (green) conjugated secondary antibodies. Nuclei were counterstained with DAPI. White arrowheads indicate examples of possible co-localisation by overlapping of two fluorescent signals; for each image, one is zoomed in the insets. Images were acquired with a ZEISS LSM 710 confocal microscope equipped with a 20× objective. Representative images are central slices from Z stacks taken at 1.80 µm intervals. Scale bar represents 50 µm. and applies to all panels. **(B)** Pearson's correlation coefficients for MYPT1 and PKA-R subunit double staining. For each condition the boxplots depict the median with the first and third quartile of the distribution. Whiskers extend to 1.5 times the interquartile range; no outliers beyond this point. Each boxplot contains the data of 30 regions of interest from 30 cells across 3 independent experiments. Images were analysed as described in the Materials and Methods section. **** $p<0.0001$ relative to the control (C); §§§§ $p<0.0001$ relative to PKA-RIIα (One Way ANOVA test followed by Tukey's post hoc test).

Previous work by (Khalil, 2018) using an affinity pulldown approach with recombinantly expressed proteins demonstrated that a central region of MYPT1 encompassing amino acids 501-706 is able to pull down PKA-R subunits (Khalil, 2018). To confirm the interaction of MYPT1 and PKA-R *in situ,* the DuoLink® - Proximity Ligation assay (PLA) technique was used in HUVECs. As part of the setup of the procedure, a positive and a negative control were tested. As positive control a combination of rabbit and mouse anti-MYPT1 antibodies was used, each raised against a different part of the protein. The anti-MYPT1 mouse monoclonal was raised against amino acids 711-840 whereas the anti-MYPT1 rabbit monoclonal antibody was raised against a region centred on E195, providing an opportunity of a strong positive control. As negative controls, MYPT1 and PKA subunit antibodies in combination with the respective isotype-specific mouse and rabbit immunoglobulins showed residual signal. Under those conditions, the positive control produced numerous dots, whereas negative controls showed very reduced signal (Figure 4.11). For another positive control, it would be intriguing to observe the outcomes of MYPT1 antibody combined with PP1c antibody.

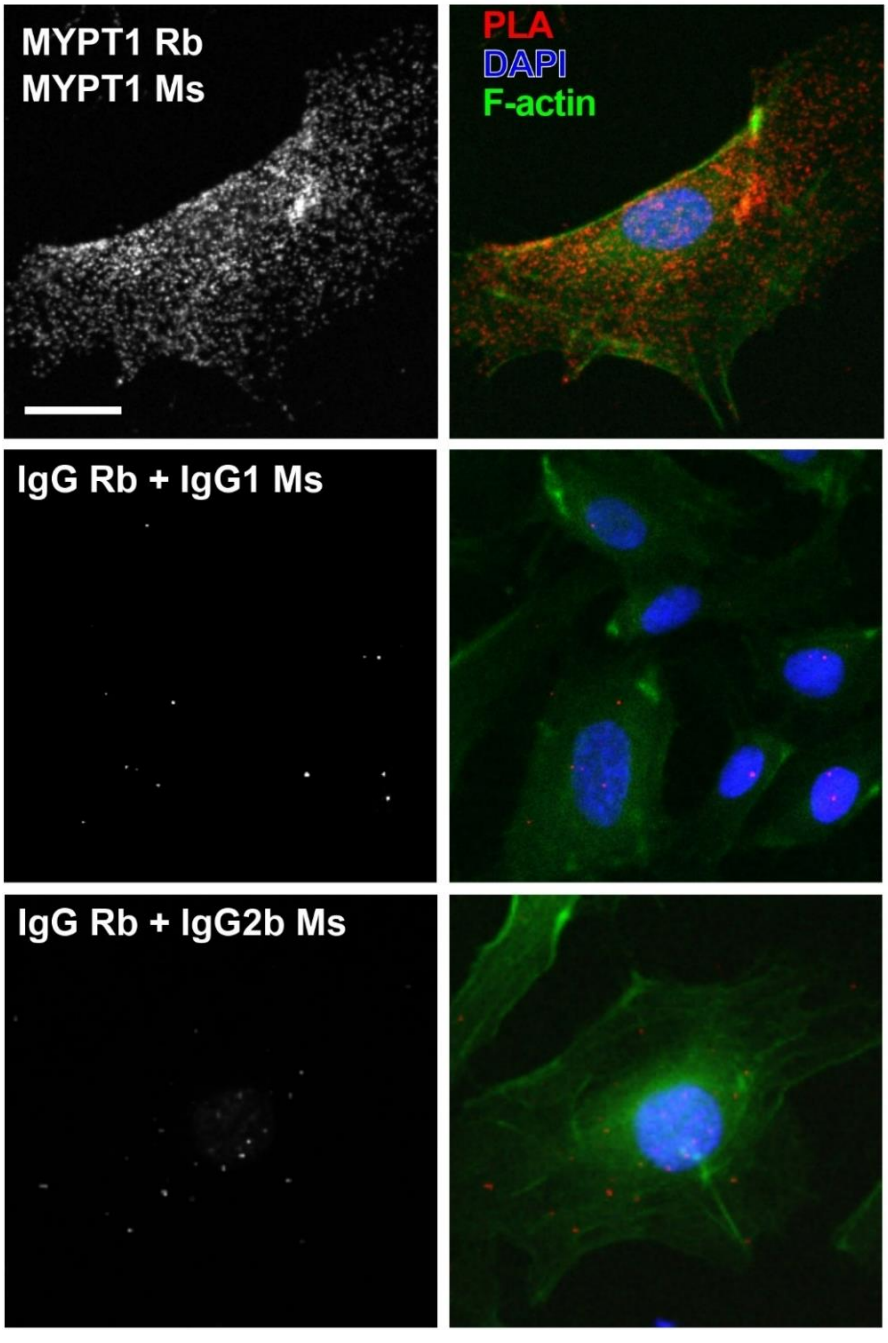

Figure 4.11 Proximity ligation assay controls for MYPT1 and PKA-R interaction. HUVECs were fixed, permeabilised and incubated with the indicated antibody pairs, followed by PLA reaction (white dots in grey scale and red dots in overlay panels). The top panel is a positive control using mouse and rabbit anti-MYPT1 antibodies that recognise different epitopes. The lower panels are isotype-specific immunoglobulin negative controls with rabbit IgG (to be used for MYPT1) and mouse IgG2b or IgG1 to be used with PKA subunits (see legend to Figure 4.12). Matching antibody concentrations were used. F-actin was stained with FITC-phalloidin (green) and nuclei with DAPI (blue). Images were acquired with a Zeiss laser scanning microscope equipped with a 20× objective. Representative images are central slices from Z stacks taken at 1.80 µm intervals comprising the complete cell thickness. Scale bar, 25 µm.

PLA reactions using anti-MYPT1 rabbit antibody in combination with subunit-specific anti-PKA-R mouse antibodies showed numerous dots, whereas the reaction with PKAcat antibody clearly yielded a weaker signal (Figure 4.12 A). For the results of PLA assay, data may be presented as number of PLA spots observed/number of cells in the field or, in case of ~~strong~~ interaction, observed PLA signal per field (Hegazy et al., 2020). Due to the intensity and proximity of the signals, counting individual dots was impractical, therefore the corrected fluorescence signal of individual cells was the methodology used for quantification. This approach not only quantifies the intensity of signal inside each delimited cell but also takes into account the quantified background and measured area as described in Materials and Methods (2.5.2.4).

As show in Figure 4.12 B, the reactions of MYPT1 with PKA-RI ($p= 1.51x10^{-10}$) PKA-RIIα ($p= 3.55x10^{-10}$) and PKA-RIIß ($p= 1.72x10^{-8}$) produced high intensity signals, which proved to be statistically significant relative to their respective controls, whereas the reaction of MYPT1 with PKAcat was modestly significant ($p= 0.01722$) (Kruskal-Wallis rank sum test followed by Dunn post-hoc test.

Notably, the signal obtained with anti-PKA-RI antibody was well above that obtained with each anti-PKA-RII antibody, probably reflecting the fact that the anti-PKA-RI antibody recognises both PKA-RIα and RIß variants. These results suggest that a significant number of PKA-R subunits exist in a complex with MYPT1 in HUVECs.

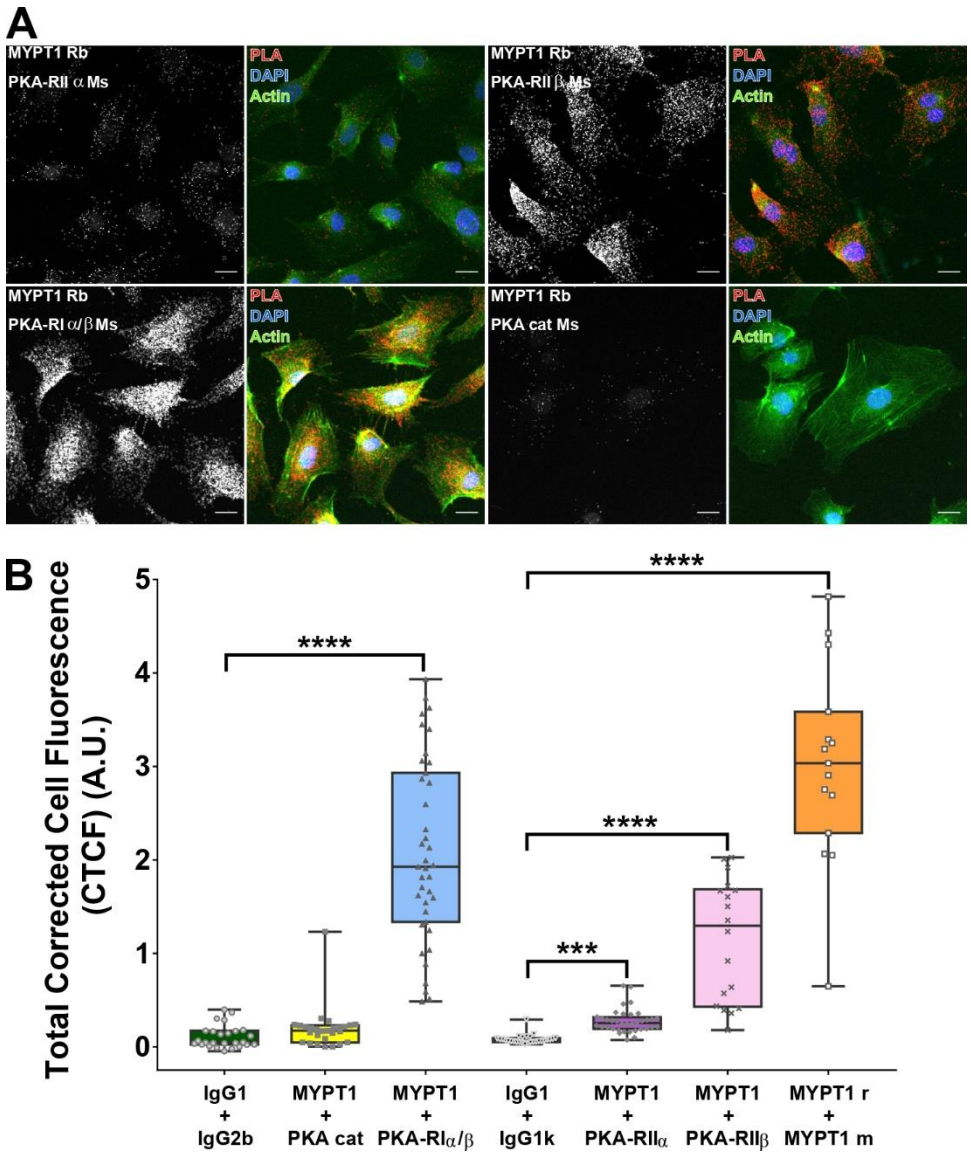

Figure 4.12 MYPT1 and PKA-R interact directly. (A) Interaction of MYPT1 with PKA-R demonstrated by proximity ligation assay (PLA) in HUVEC. Cells were fixed, permeabilised and incubated with the indicated antibody pairs, followed by PLA reaction (grey scale panels and red dots inn overlay panels). Matching antibody concentrations were used. F-actin was stained with FITC-phalloidin (green) and nuclei with DAPI (blue). Images were acquired with a Zeiss laser scanning microscope equipped with a 20× objective. Representative images are central slices from Z stacks taken at 1.80 µm intervals comprising the complete cell thickness. Scale bars, 25 µm. **(B)** Quantification of the *in situ* PLA. Total corrected cell fluorescence intensity was calculated from 14-39 cells from at least 3 independent images as described in the Materials and Methods chapter. Quantification of control images (Figure 4.11 is also included). The boxplots depict the median with the first and third quartile of the distribution. Whiskers extend to 1.5 times the interquartile range; no outliers beyond this point were found. Statistical significance was calculated relative to the respective control (IgG2b for PKA cat and PKA-RI; IgG1k for PKA-RIIα and ß and MYPT1 mouse (positive control). The boxplots depict the median with the first and third quartile of the distribution. Whiskers extend to 1.5 times the interquartile range; no outliers beyond this point were exhibited. *** p <0.001; **** p<0.0001, Kruskal-Wallis rank sum test followed by Dunn post-hoc test.

4.7. Discussion

In this chapter the hypothesis that MYPT1 interacts directly with PKA subunits in endothelial cells was addressed. Using western blot, it was first verified that MYPT1 and all PKA subunits are expressed in endothelial cells, using as a control platelet lysate where previous studies have confirmed expression of both MYPT1 and PKA subunits (Aburima et al., 2013, Raslan et al., 2015, Khalil, 2018). In HUVECs, MYPT1 exhibits a double band when using western blot. This might be due to the existence of more than one *PPP1R12A* transcript, resulting in more than one protein isoform. The presence of these two variants has been reported in HeLa (Hirano et al., 1999), HEK293 (Xia et al., 2005), endothelial cells (Kim et al., 2012), and in intestinal epithelial cells (Zha et al., 2016). Here it was reported that another endothelial cell type, HDBEC, presents a similar pattern of two variants. Results obtained by RT-PCR and analysis of publicly available RNAseq data showed that these two variants correspond to the one considered full length (also called canonical) and the one lacking exon 13 (ΔE13) (Chapter 3). Two bands are also visible in platelet lysates. (Saldanha et al., 2022) postulates that the most abundant band may correspond to the isoform lacking E14 followed by the one lacking E13. Unlike endothelial cells, where the full-length variant is abundant, in platelets it accounts only for a very faint band (Saldanha et al., 2022). These different frequencies of isoforms expressed in these two cell types of the human vasculature emphasise the importance of understanding the function of each isoform. An attempt to determine the function of this variants was made by using siRNA (section 3.4) by knocking down each variant individually.

In previous work in Dr Rivero's laboratory, Khalil (Khalil, 2018) showed co-immunoprecipitation of MYPT1 with all subunits of the PKA holoenzyme in platelet lysates. The first aim addressed in this chapter was to verify the existence of protein complexes containing MYPT1 and PKA subunits *in vivo* in another cell type of the vasculature, namely endothelial cells. Protein-protein interactions are important for understanding the molecular mechanisms of various biological processes and for developing new drugs and therapies. Amongst the *in vivo*, *in silico* and *in vitro*

techniques that are used to study PPIs, in this study a co-immunoprecipitation approach was chosen. This technique explores interactions using a whole cell lysate where proteins are present in their native form in a complex mixture of cellular components (Rao et al., 2014).

In addition to molecular biology techniques like the yeast two-hybrid system (Fields and Song, 1989), fluorescence resonance energy transfer (FRET), bimolecular fluorescence complementation (BiFC) (Hu et al., 2002, Walter et al., 2004), and similar methods, biochemical approaches such as co-immunoprecipitations (co-IPs) and pull-down experiments (PDs) are highly useful and complementary methodologies for identifying and characterising the interacting partners of a protein. These techniques provide valuable insights into the protein-protein interactions and contribute to a comprehensive understanding of a protein's functional associations (Isono and Schwechheimer, 2010). In this chapter, the approaches chosen were co-IP and affinity pull downs, two powerful techniques for studying protein interactions as they offer several advantages: they can be performed in vivo or in vitro; they can provide unbiased approach, enabling the discovery of novel interacting partners that can offer new insights into protein function; and they can reveal the complexity of protein interaction networks (Isono and Schwechheimer, 2010). As reported in section 4.3.1 the co-IP in platelets did not produce the same results obtained in HUVECs. (Khalil, 2018) reported co-IP of PKA subunits while immunoprecipitating MYPT1. In his work the experiment was performed with a different MYPT1 antibody (now discontinued). Without the possibility of reproducing the protocol, it was important to identify and characterise a new MYPT1 antibody capable of immunoprecipitating native MYPT1.The immunoprecipitation (IP) performed in platelets indicated that this protocol is not well-suited for such cells. During the IP in platelets (Section 4.3.1), it was observed that even the isotype-specific IgG antibody showed some bands, and non-specific proteins were also present in the purified fractions. This might be due to the co-immunoprecipitation of large structures, such as lipid rafts or cytoskeletal fragments that carry numerous proteins. To achieve results similar to those obtained with

HUVECs, a different buffer should be tested. In this chapter it is shown that MYPT1 interacts *in vitro* with PKA-RIIα and -RIIß but not PKA-RI, even though the antibody used in this study recognised both PKA-RI α and PKA-RIß. RIα and RIIα are ubiquitously expressed (Clegg et al., 1988, Lee et al., 1983, Scott et al., 1987), RIß is primarily found in brain (Cadd and McKnight, 1989), and RIIß is expressed in endocrine tissues, brain, fat and reproductive organs (Taskén et al., 1997, Jahnsen et al., 1986, Cadd and McKnight, 1989). One possible explanation for the absence of PKA-RI on the co-IP could be its distribution in cells/tissues. A recent study has demonstrated that the stoichiometric relation between RI and RII is 0.6 µM to 1.5 µM, revealing a 2.5-fold excess of RII in any given tissue (Walker-Gray et al., 2017, Søberg and Skålhegg, 2018). The sensitivity of the co-IP technique could be missing the detection for RI while capturing RII subunits. The protein-protein interaction between MYPT1 and PKA-RI might be transient or weak and lie under the detection range for this technique (Perkins et al., 2010). If low-affinity or transient interactions are not being detected, co-IP often requires further optimisation, such as crosslinking, to be successful. Another recognised high-throughput (protein-protein interaction (PPI)detection method is tandem affinity purification combined with mass spectroscopy (TAP-MS) (Collins and Choudhary, 2008). Traditionally, this method struggles to detect transient interactions, which are often lost during washing steps to remove nonspecific binding. However, chemical crosslinking can freeze these transient complexes by inducing covalent bonds between interacting partners *in vivo* (Worthington et al., 2006, Perkins et al., 2010).

In this chapter It was also explored whether the interaction of MYPT1 with PKA-R subunits is conformation-dependent. Upon binding to cAMP, the PKA-R subunits change conformation and release the PKAcat subunits (Gold, 2019). Affinity cAMP pull-down assay in HUVEC lysates showed that all PKA-R subunits bind to the cAMP functionalised beads, efficiently depleting the lysates. The absence of MYPT1 upon cAMP-PKA-R complex formation in HUVECs indicates that the MYPT1-PKA interaction occurs when the PKA-R subunits are not bound to cAMP. In seems that in resting conditions PKA-R subunits are bound to MYPT1 but, upon the first cAMP molecule

binding and the subsequent conformational change allowing the second cAMP molecule to bind, this interaction might disappear. The mechanism for restraining PKAcat subunits after their release is still unclear, as well as the PKA-R – PKAcat complexes which lack D/D domain, cannot explain how the holoenzymes are targeted to specific sites by docking to AKAPs, and they do not tell us whether there are interactions between the two R:C heterodimers (Ilouz et al., 2012).The postulated mechanism of two cAMP molecules binding PKA-R leading to dissociation of PKAcat, suggests that when PKA holoenzymes are bound to MYPT1, cAMP would cause the complex to dissociate, releasing PKAcat that could now access MYPT1 and phosphorylate it. When PKA undergoes a conformational change, the catalytic subunit (PKAcat) dissociates from the regulatory subunit (PKA-R). This dissociation is critical, as it allows PKAcat to phosphorylate nearby proteins. The precise localisation of PKA is essential for targeting specific substrates, ensuring that PKAcat can efficiently phosphorylate proteins in its immediate vicinity once it is released from PKA-R. Ultimately, this mirrors the role of AKAPs in facilitating PKA signalling. AKAPs enhance the specificity and efficiency of PKA signalling by compartmentalising PKA to specific intracellular regions (Carnegie et al., 2009, Manni et al., 2008). This compartmentalisation underscores the critical role of AKAPs in optimising complex network performance through the coordination of spatial and temporal signalling of proteins and enzymes regulated by the cAMP second messenger (Rababa'h et al., 2014). PKAcat can only phosphorylate proteins in its immediate vicinity. Upon cAMP binding to PKA-R, the interaction between MYPT1 and PKA-R is disrupted, allowing PKAcat to phosphorylate local proteins.

A very different result arose when conducting the cAMP pulldown in platelet lysates. MYPT1 and ß-actin (possibly unpolymerised actin monomers) were found bound to cAMP beads. To investigate whether the interaction between MYPT1 and PKA in platelets is influenced by the actin cytoskeleton, latrunculin B was used to disrupt the actin cytoskeleton prior to the cAMP pulldown. Surprisingly, even under these conditions, significant levels of MYPT1 and actin were still recovered with the beads, suggesting that the interaction is not solely dependent filamentous actin. This duality

of results might be explained by differences in the amounts of actin monomers in HUVECs and platelets, which are higher in platelets. MYPT1 is recognised for its interaction with actin and various actin-binding proteins (Alvarez-Santos et al., 2020). Furthermore, there is evidence suggesting a direct interaction between PKA-RIIα and actin (Rivard et al., 2009). Thus, it is speculated that in platelets the abundant actin might be bridging the interaction between MYPT1 and at least some of the PKA-R subunits independently of any conformation changes in PKA-R upon cAMP binding.

The cAMP pull-down assay requires additional support experiments. While cAMP is immobilised on 8-AHA-cAMP agarose beads, phosphodiesterases (PDEs) might degrade cAMP. It is crucial to use beads such as 8-(2-aminoethylamino) adenosine 3', 5'-cyclic monophosphorothioate, Sp-isomer, immobilised on agarose gel (Sp-8-AEA-cAMPS-Agarose) that resist PDE hydrolysis. Additionally, conducting further experiments using AMP as a control can provide further insight compared to the control used in these experiments (ethanolamine). Previously *in vitro* work showed that MYPT1 and PKA interacted (Khalil, 2018). Here upon the IP results in HUVECs shown that MYPT1 and PKA possibly interact *in situ* co-localisation would be helpful to strengthen this interaction claim.

Even acknowledging the limitations of co-localisation, it was important to perform this technique. In HUVECs, quantification of co-localisation revealed that all PKA subunits are co-localised with MYPT1. However, while PLA analysis indicated that all PKA-R subunits interact with MYPT1, PKAcat appears not to significantly. This finding was supported by quantification of both co-localisation and PLA images. To fully understand the co-localisation and PLA results obtain in this study, it will be crucial to test co-localisation and perform PLA with adenylyl cyclase stimulators. The current results suggest a possible interaction, but these stimulators are essential to validate the findings from both techniques in addition to antibody titration as stated before.

While co-immunoprecipitation and co-localisation studies inform about two proteins being part of a complex, these techniques do not provide any information on the

nature of the interaction, more specifically whether the interaction is regulated. The third aim of this chapter was to demonstrate the interaction of MYPT1 with PKA-R subunits in HUVECs *in situ* using the proximity ligation assay technique (Söderberg et al., 2006). Proximity ligation assay provides an advantage over immunofluorescence co-localisation and, immunoprecipitation, as it pairs with the ability to observe subcellular localisation.

Alternative biotechnological fluorescence methods, such as biomolecular fluorescence complementation, fluorescence resonance energy transfer (FRET), or optogenetics, can provide insights into subcellular localisation. However, the utilisation of these approaches necessitates the expression of exogenously introduced proteins, and the design of the protein constructs involved can be riddled with challenges and complexities (Duwé and Dedecker, 2019). Also, FRET technique requires specialised microscopy setups.

The data from this study combined with (Khalil, 2018) leads to the postulation that MYPT1 might function as a non-canonical AKAP because both studies have shown direct interaction of MYPT1 and PKA. (Khalil, 2018) pulldowns have shown also that the D/D domain is not required for this interaction. In summary, in this chapter it has been shown that the interaction of MYPT1 with PKA occurs in a PKA non-stimulated state. PKA stimulators should be used in follow-up experiments to support these claims. Complementary techniques such as Surface Plasmon Resonance (SPR) or cryogenic transmission electron microscopy (cryo-EM) would strengthen this hypothesis and would help to obtain deeper understanding of this interaction. The activation of PKA using cAMP beads has shown that MYPT1 is not bound to PKA in HUVECs. This pull-down experiment would need a supplementary study by using Sp-8-AEA-cAMPS-Agarose beads allowing to understand if hydrolysis of cAMP by PDEs occur. Co-localisation studies have shown that MYPT1 and PKA-R colocalise. Stimulatory experiments are necessary to confirm both co-localisation and PLA experiments and lend support to the specificity of these findings.

Chapter 5. Biochemical interaction sites of MYPT1 with PKA regulatory subunits

5.1. Introduction

The identification of key players and their interactions is fundamental for understanding biochemical mechanisms at the molecular level. Protein-protein interactions (PPIs) are the physical contacts established between two or more protein molecules that are essential for various biological processes and the ability to study these interactions is crucial for advancing our understanding of cellular function (Xing et al., 2016). PPIs play a crucial role in the regulation of cellular functions, including signal transduction, gene expression, and metabolic pathways. PPIs are based on noncovalent contacts between the residue side chains, which induce a variety of interactions and associations among the proteins (Rao et al., 2014). Several techniques can be used to detect PPIs such as Bioluminescence Resonance Energy Transfer (BRET), Fluorescence Resonance Energy Transfer (FRET), Surface Plasmon Resonance (SPR), Co-immunoprecipitation (Co-IP), peptide array, Pull-down Assay/Affinity Chromatography, etc.

Previous work utilised pull-down assay/affinity chromatography to determine that MYPT1 interacts directly with PKA-R variants and narrowed down the interaction region to a C-terminal fragment encompassing residues I501-E706 (MYPT1-C2) as it is shown on Figure 5.1 (Khalil, 2018).

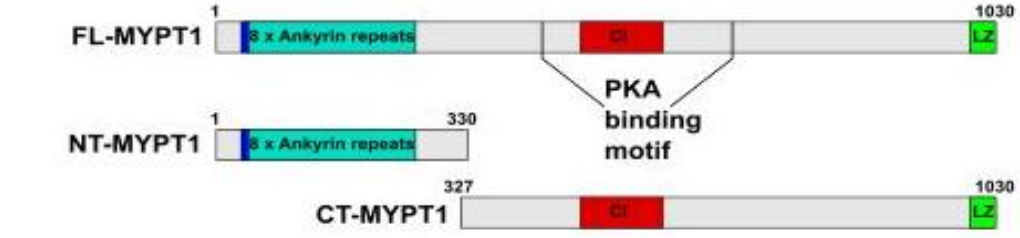

Structure	Amino acids	Association with PKA
1 8 x Ankyrin repeats CI LZ 1030	1 - 1030	***
1 8 x Ankyrin repeats 330	1 - 330	
327 CI LZ 1030	331 - 1030	***
C1 327 531	327 - 531	*
C2 501 706	501 - 706	***
C3 676 881	676 - 881	
C4 825 LZ 1030	825 - 1030	

n

Figure 5.1 Summary of MYPT1 association with PKA-R subunits. MYPT1 is 1030 amino acids long. GST pull-down experiments have shown that the region comprising amino acids 501-706 is responsible for the interaction with all four PKA-R subunits. Weak interaction of PKA-R was shown with amino acids 327-531. Taken from (Khalil, 2018).

It was sought to map the sites of the MYPT1-PKA-R interaction using a peptide array overlay approach to narrow down the I501-E706 peptide to short motif(s). This approach was selected due to its cost effectiveness and reproducibility. Spot synthesis is an easy technique in molecular biology and chemical synthesis that have allowed for the exploration of the immense diversity of molecular structures accessible to oligo- and polymeric biomolecules such as proteins and nucleic acids. (Frank, 1992). This focuses on the systematic screening of extensive series of short peptide sequences in biological assay systems, which has become a powerful approach for investigating protein-protein interactions (Frank, 1992).

Peptide arrays enable the identification of interaction sites between two proteins and screening for peptides that bind the target protein for therapeutic purposes. This technique has several limitations, one of them is linear peptides may not properly represent the 3D structure of the binding site in the protein, which can lead to false negative results. Another limitation is that false positive results can be caused by binding of the antibody to the array, which can be detected by performing a control experiment. Additionally, false negative results can also be obtained if the protein epitope that is recognised by the antibody becomes unexposed upon binding to the peptide array (Amartely et al., 2014).

Having demonstrated that MYPT1 and PKA-R interact directly and having knowledge from previous studies about the region of MYPT1 involved in the interaction (Khalil, 2018), the hypothesis proposed is that a limited number of MYPT1 residues are key for the binding of PKA-R subunits to MYPT1.
The **aims** for this chapter are:

1. To narrow down the interaction site of PKA-R subunits on MYPT1 by identifying peptides by peptide array technique.

2. To discover which residues are important for the interaction by alanine replacement.

3. To investigate the effects of the phosphorylation status of MYPT1 on the interaction with PKA-R.

5.2. Epitope mapping of MYPT1 binding sites to GST-tagged PKA-RIß and RIIß

In order to narrow down the mapping of the interaction sites of PKA-R with the MYPT1-C2 region, a peptide overlay approach that involves the probing of an array of overlapping peptides spanning the MYPT1 segment between residues I501 and E706 with epitope tagged recombinant PKA-R was chosen. Because all PKA-R subunits interact with MYPT1 (Khalil, 2018), in this study PKA-RIß and PKA-RIIß were used as representative of the two types PKA-R subunits. GST-tagged PKA-R subunits that had been used successfully in previous pull-down assays performed in Dr Rivero's laboratory (Khalil, 2018) was chosen. Plasmids for expression of recombinant PKA-RIß and RIIß proteins subcloned in pGEX-4T-2 vector were transformed in XL-1blue *E. coli* strain as described in section 2.1.4., Table 2.15. Expression and purification of recombinant GST-tagged protein from 1 litre culture was conducted as described in section 2.4.1 and the process monitored by SDS-PAGE followed by Coomassie blue staining of the gels as describe in section 2.4.7. Throughout these procedures, all solutions underwent filtration and were maintained on ice. To prevent protein degradation, protein inhibitor cocktails, DTT, and PMSF were supplemented into the lysis buffer.

A successful expression of GST-PKA-RIß was observed at about 72 kDa after induction (Figure 5.2 A, top panel, black arrow, lane I). The bacterial lysate was centrifuged (17000x*g*, at 4°C, for 30 minutes) to separate the soluble supernatant (lane S1) from the insoluble pellet (lane P) fraction. It was observed that the pellet fraction contained a relatively large amount of GST-PKA-RIß in comparison to the supernatant. Nonetheless, a significant amount of recombinant protein was captured by glutathione-Sepharose beads (lane B1) and the supernatant after such incubation was found depleted of GST-PKA-RIß (lane S2). A small proportion of recombinant protein bound to the beads was found degraded (Figure 5.2 A, blue arow). Expression and purification of GST-PKA-RIIß was similar to GST-PKA-RIIß. The fusion protein is apparent above 72 kDa after induction (Figure 5.2 B, top panel, black arrow, lane I). GST-PKA-RIIß is comparatively more abundant in the soluble fraction and was

successfully captured by glutathione-Sepharose beads but a higher proportion was found degraded (Figure 5.2 B, blue arrow).

Both recombinant proteins were successfully eluted from the glutathione-Sepharose beads (Figure 5.2 A and B, middle panels, E1 to E4 or E6 lanes) but the yield of GST-PKA-RIß was higher, probably due to higher degradation of GST-PKA-RIIß. Some recombinant protein was still bound to the beads after the last elution step (B2 lanes). For dialysis it was decided to combine eluates to maintain high concentration of recombinant protein (Figure 5.2 A middle panel and Figure 5.2 B lower panel). Eluate E1 of GST-PKA-RIß was kept separate in the expectation that this fraction would show the highest concentration of recombinant protein, which did not prove correct. After dialysis the dialysates were centrifuged to separate insoluble protein (500x*g*, at 4°C, for 5 minutes). It was observed that a substantial amount of recombinant protein, both intact and degraded, became insoluble (Figure 5.2 A middle panel and Figure 5.2 B lower panel, P fractions), more notably in the case of GST-PKA-RIIß, however sufficient soluble protein was recovered (E fractions).

Although GST-tagged PKA RI and PKA RII were successfully expressed and eluted, additional bands around 43 kDa were observed, which could potentially represent proteolytic products of the desired protein. Protein determination was achieved as described in section 2.4.7.1. Details of quantification of the eluates and the proportion of intact protein are shown in Figure 2.3 and Appendix Table 8.3-1 Determination of GST-tagged PKA RIß and RIIß total and intact protein concentration (Appendix Table 8.3-1).

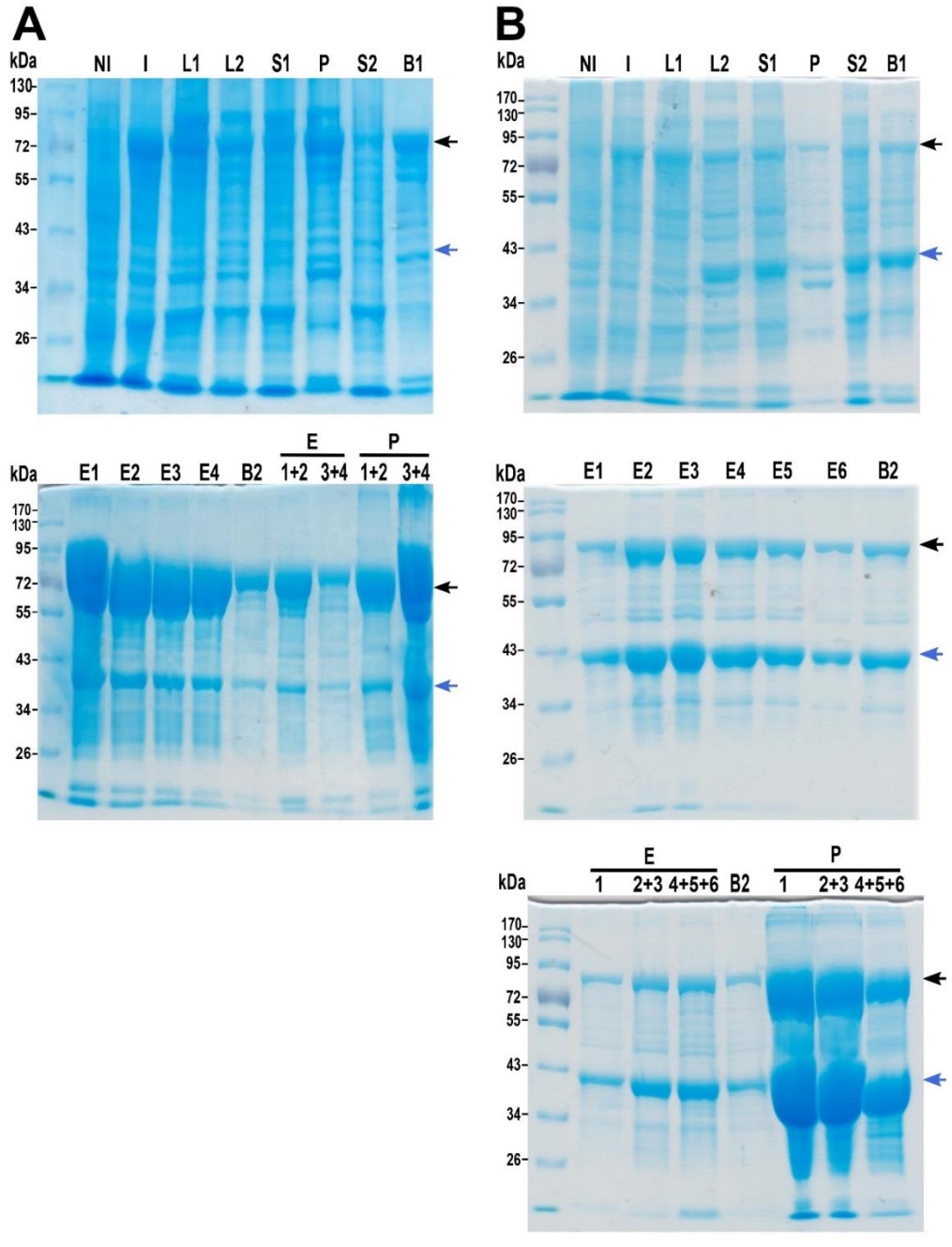

Figure 5.2 Purification of GST-tagged PKA RIß and IIß. (A) Expression and purification of GST-tagged PKA-RIß. **(B)** Expression and purification of GST-tagged PKA RIIß. NI, non-Induced; I, induced; L1, total cell lysate before French press lysis; L2, lysate after French press lysis; S1, supernatant after lysis; P, pellet after lysis; S2, supernatant after incubation with glutathione-Sepharose beads; B1, beads before elution; B2, beads after elution, E, eluates; E and P on top of the bars means eluates and pellets, respectively, after dialysis. Black arrows indicate the target fusion protein; blue arrows indicate major protein degradation products. 10 µL of each sample in Laemmli buffer were electrophoresed in 10% SDS-PAGE. Gels were stained with Fast Blue staining.

Having expressed and partially purified GST-tagged PKA-RIß and RIIß, the proteins were shipped to the laboratory of collaborator Professor George Baillie (University of Glasgow) for probing of peptide arrays. Peptide arrays covering MYPT1-C2 (I501-E706) were overlaid with GST-tagged PKA-RIß and IIß (Figure 5.3). The results showed high intensity spots upon incubation with PKA-RIß for peptides 4, 14-16, 20, 31, 35 and 36. Upon quantification, it was shown that PKA-RIIß displayed higher binding than PKA-RIß. However, in both cases, the controls with GST antibody produced high level of background signal and therefore those peptides should be removed. This background signal was attributed to unspecific binding of the GST moiety to the peptides. Consequently, it was decided to probe the peptide arrays with his-tagged recombinant PKA-R subunits.

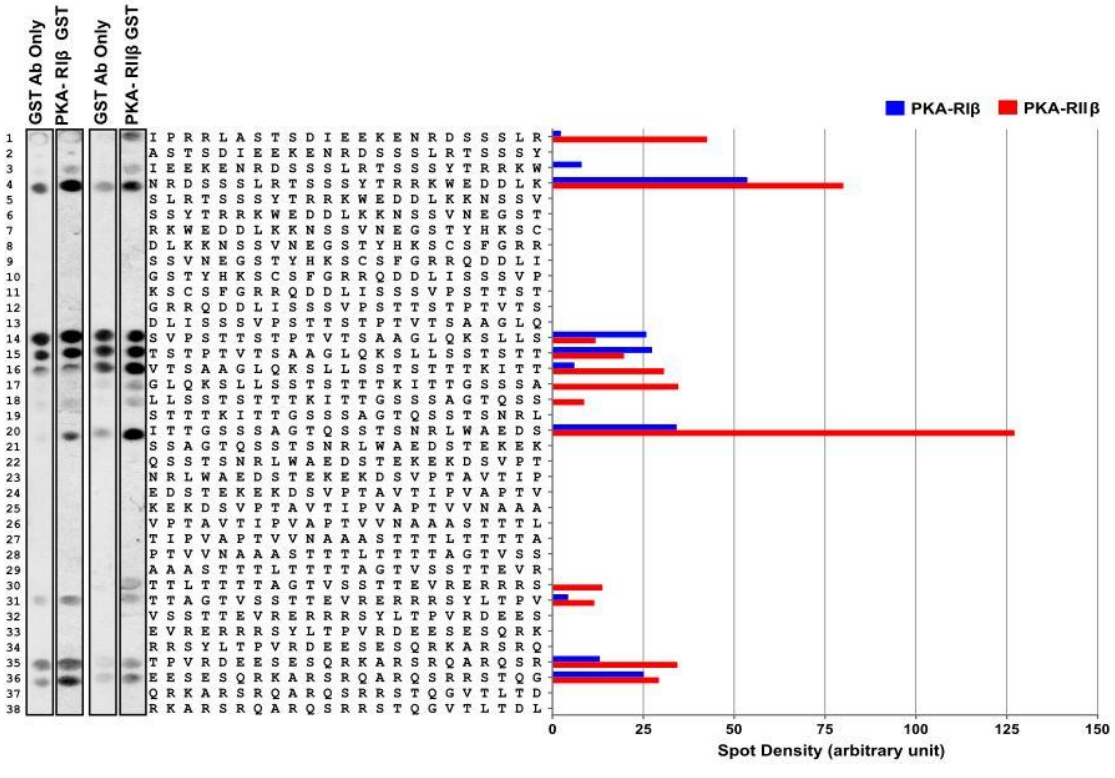

Figure 5.3 Peptide array epitope mapping of recombinant GST proteins PKA-RIß and RIIß subunits on MYPT1. An array of 25mers, sequentially shifted by 5 amino acids, spanning MYPT1-C2 protein segment (I501-E706) was overlaid with GST PKA-RIß or RIIß, probed with HRP-conjugated anti-GST antibody and visualised by enhanced chemiluminescence. For antibody only (Ab only) control, PKA-R was omitted. Blue and red bars indicate interaction of PKA-RIß and PKA-RIIß, respectively, with MYPT1 peptides; spot densities were normalised to the density of the corresponding GST antibody-only spot. (Peptide array synthesis and probing were carried out in Professor George Baillie's laboratory).

5.3. Epitope mapping of MYPT1 binding sites to his-tagged PKA-RIß and RIIß

Plasmids for expression of recombinant PKA-RIß and RIIß proteins subcloned in pQE30 vector were transformed in XL-1blue *E. coli* strain as described in section 2.4.1, Table 2.15. Expression and purification of recombinant his-tagged protein from 500 ml culture was conducted as described in section 2.4.2 and the process monitored by SDS-PAGE followed by Coomassie blue staining of the gels as described in section 2.4.7 (Figure 5.4).

Successful expression of his-PKA-RIß at approximately 51 kDa was observed after induction (Figure 5.4 A, top panel, black arrow, lane I), although significant expression was also observed in the absence of IPTG (NI lane), suggesting leaky expression. The bacterial lysate was centrifuged (17000x*g*, at 4°C, for 30 minutes) to separate the soluble supernatant (lane S1) from the insoluble pellet (lane P) fraction. It was observed that the pellet fraction contained similar amounts of his-PKA-RIß in comparison to the supernatant. Nonetheless, a significant amount of recombinant protein was captured by NiNTA agarose beads (lane B1) and the supernatant after such incubation was found almost depleted of his-PKA-RIß (lane S2). Expression and purification of his-PKA-RIIß was similar to GST-PKA-RIIß. The fusion protein is apparent above 55 kDa after induction (Figure 5.4 B, top panel, black arrow, lane I). His-PKA-RIIß is comparatively more abundant in the insoluble fraction and was successfully captured by NiNTA agarose beads.

Both recombinant proteins were successfully eluted from the NiNTA agarose beads in 6 fractions (Figure 5.4Figure 5.4 A and B, middle panels, E1 to E6 lanes) but the yield of his-PKA-RIß was considerably higher. Some residual recombinant protein was still bound to the beads after the last elution step (B2 lanes). For dialysis, fractions 2+3 and 4+5+6 were combined (Figure 5.4 A and B, middle panels). After dialysis, the dialysates were centrifuged (17000x*g*, at 4°C, for 30 minutes) to separate insoluble protein. It was observed that a substantial amount of recombinant protein became insoluble (Figure 5.4 A lower panels, P fractions), however sufficient soluble protein was recovered (E fractions), particularly his-PKA-RIß. Protein determination

was achieved as described in sections 2.4.7.1 and Figure 2.3. Details of quantification of the eluates and the proportion of intact protein are shown in (Appendix Figure 8.3-2. And Appendix Table 8.3-2).

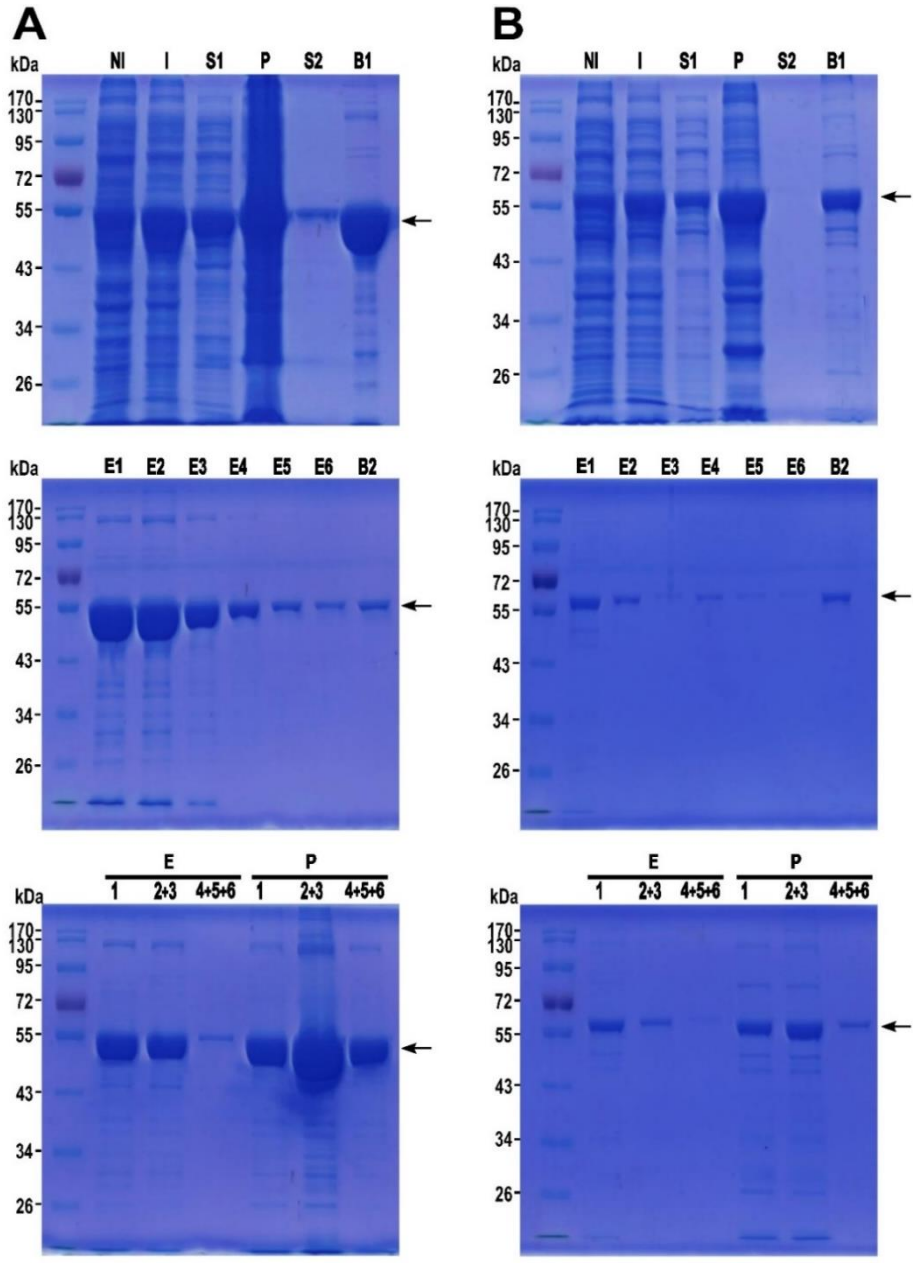

Figure 5.4 Purification of His tagged PKA Iß and RIIß. (A) Expression and purification of His tagged PKA RIß. **(B)** Expression and purification of His tagged PKA RIIß. NI, Non-Induced; I, Induced; S1, Supernatant after French Press; P, Pellet; S2, Supernatant after incubation with NiNTA Beads; B1, Beads before elution; B2, Beads after elution; E, elutes; E and P on the top of the bars means eluates and pellets, respectively, after dialysis The black arrow indicates the target protein. 10 µL of each sample in 1x Laemmli buffer was run in a 10% SDS-PAGE. Gels were stained with Coomassie Blue.

Having successfully expressed and purified His-tagged PKA-RIß and RIIß, the proteins were shipped to the laboratory of Professor George Baillie (University of Glasgow) for probing of the MYPT1-C2 peptide arrays. It was observed that the antibody control in this experiment showed considerably less unspecific binding compared to the experiment with GST fusion proteins (Figure 5.2).

As shown in Figure 5.5, both PKA-R variants demonstrated a similar pattern of binding to three regions of MYPT1-C2, with high intensity spots on the peptide array. Peptides 13-18 and 29-37 demonstrate high spot intensity suggesting high affinity binding, therefore they may represent primary binding sites. On the other the peptides 1-6 have low spot density, suggesting lower affinity binding and therefore might represent an accessory binding site. Peptides 1-6 localise in the portion of MYPT1-C2 that overlaps with MYPT1-C1 (Figure 5.1), which explains the relatively weak binding of MYPT1-C1 fragment to PKA-R variants found in a previous study (Khalil, 2018). Peptides 15 and 35 appeared to be the peptides of interest within each binding region. On the light of these results all three regions were selected for follow up substitution analysis to uncover which amino acid or short peptide is responsible for the interaction.

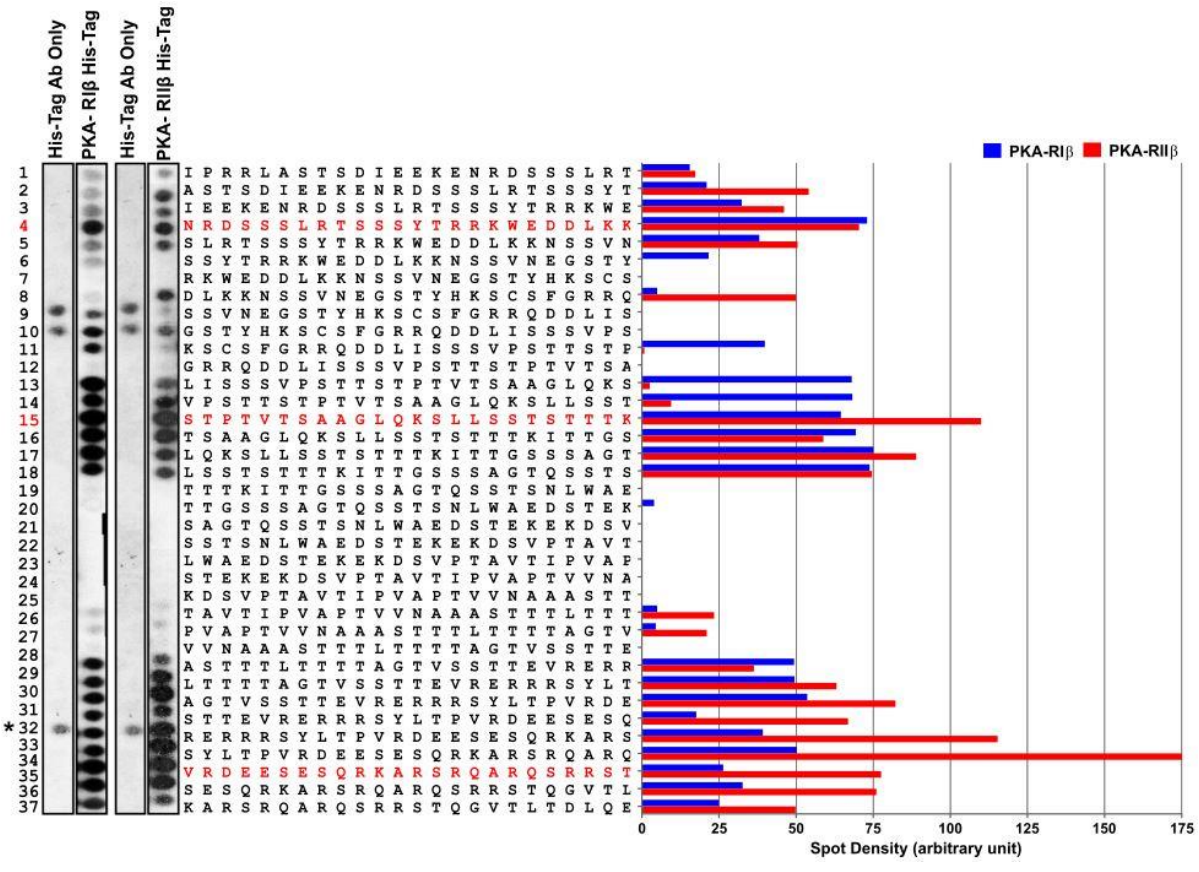

Figure 5.5 Peptide array epitope mapping of recombinant His-Tag PKA-RI RIß and RIIß subunits on MYPT1. An array of overlapping 25mers, sequentially shifted by 5 amino acids, spanning MYPT1-C2 protein segment (I501 – E706) was overlaid with recombinant His-tagged PKA-RIß or RIIß, probed with HRP conjugated anti-polyHis antibody and visualised by enhanced chemiluminescence. For the antibody only (Ab only) control, PKA-R was omitted. Binding peptides selected for follow up analysis are indicated in red. The asterisk next to peptide 32 indicates antibody-associated non-specific binding. Blue and red bars indicate interaction of PKA-RIß and PKA-RIIß, respectively, with MYPT1 peptides; spot densities were normalised to the density of the corresponding His-tag antibody-only spot. (Peptide array synthesis and probing were carried out in Professor George Baillie's laboratory).

In the light of these results, it was proposed to further study the peptides 4, 15 and 35 using amino acid substitute to uncover furthermore, which amino acid or short peptide binding sequence that was responsible for this interaction.

5.4. Substitution analysis of peptide array epitope mapping

Peptides 15 and 35 presented high intensity spots in the peptide arrays that might indicate higher binding affinity between MTYPT1-C2 and PKA-RIß and RIIß (Figure 5.5). Comprehensive alanine substitutions of these two peptides showed abolished binding when K595 was replaced by alanine, suggesting that this is a major residue involved in the interaction with PKA-R (Figure 5.6 A). In peptide 35, E676 is part of an acidic patch, and almost abolished binding was observed with both PKA-R subunits studied when E676 was substituted by alanine, and a trend towards reduced binding was also seen when the adjacent D675 and E677 were replaced by alanine. However, the binding was not affected when these acidic residues were replaced by lysine (Figure 5.6 B). Substitution analysis of residues 693-696 revealed a 50% binding reduction when R693, R694 and S695 were replaced by alanine, and abolished binding when T696 was replaced. Furthermore, substitution of R693 and R694 by residues of the opposite charge abolished binding (Figure 5.6 B). These results indicate that residues involved in the substrate motif for Ser/Thr protein kinases are important for the interaction of MYPT1 with PKA-R. Substitution analysis was also conducted on peptide 4, which presented lower binding to PKA-R but the results were less conclusive (Appendix Figure 8.3-3).

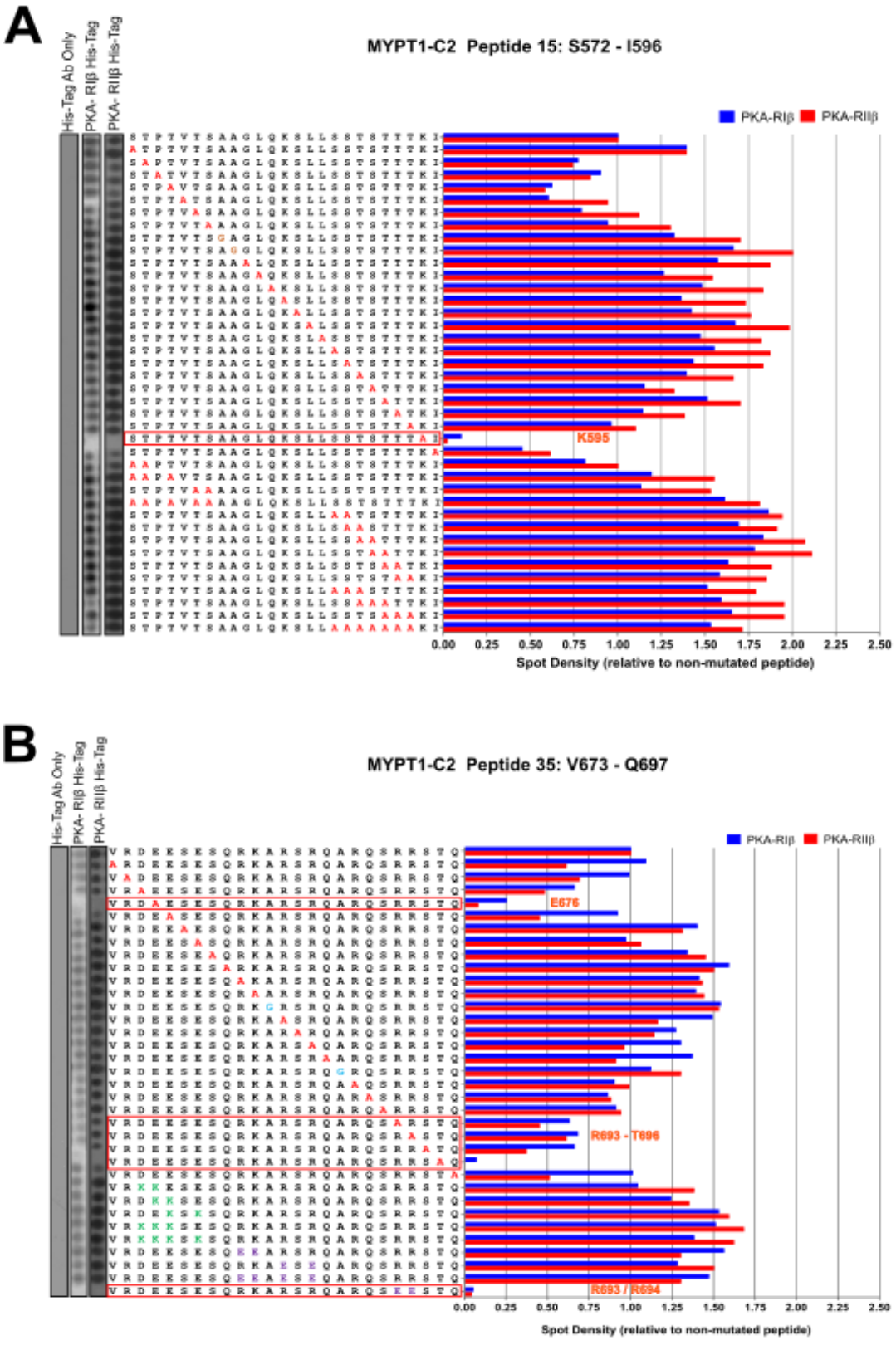

Figure 5.6 Legend presented on the following page.

Figure 5.6. Peptide array substitution analysis of MYPT1-C2 peptides. (A) Peptide array substitution analysis of MYPT1-C2 peptide 15. Key MYPT1-C2 hot spots were identified by single, dual or multiple alanine substitutions. Arrays were processed as in fig. 5.4. The red box highlights a peptide where a substitution resulted in complete loss of binding. Spot densities are shown relative to the non-mutated peptide after subtraction of the antibody only control. **(B)** Peptide array substitution analysis of MYPT1-C2 peptide 35. Key MYPT1-C2 hot spots were identified by single alanine substitutions or by opposite charge residue substitutions. Arrays were processed as in Appendix Figure 8.3-3. The red boxes highlight peptides where substitutions resulted in consistent reduction or complete loss of binding. Spot densities are shown relative to the non-mutated peptide after subtraction of the antibody only control. (Peptide array synthesis and probing were carried out in Professor George Baillie's laboratory).

5.5. Substitution analysis of phosphorylation sites S695 and T696

Next it was investigated whether the phosphorylation status of S695 and T696 would affect the interaction with PKA-R. Having established that PKA-RIß and RIIß behave similarly, this experiment was restricted to PKA-RIIß. A peptide array was synthesised in which S695 and T696 were substituted, either individually or in combination, by either alanine, the phosphomimetic aspartic acid or the corresponding phosphorylated residue. Peptide 37 was used for this purpose, to provide additional structural environment to the S695 and T696 residues (Fig. 5.7 A and B). Under these conditions, substitution of S695 by alanine resulted in weaker binding of PKA-RIIß, whereas substitution of T696 or both did not significantly alter binding. In contrast, substitution of S695 and T696, alone or in combination, by aspartic acid or a phosphorylated residue completely abolished binding. This indicates that the phosphorylation status of S695 and T696 might modulate the interaction of MYPT1 with PKA-R.

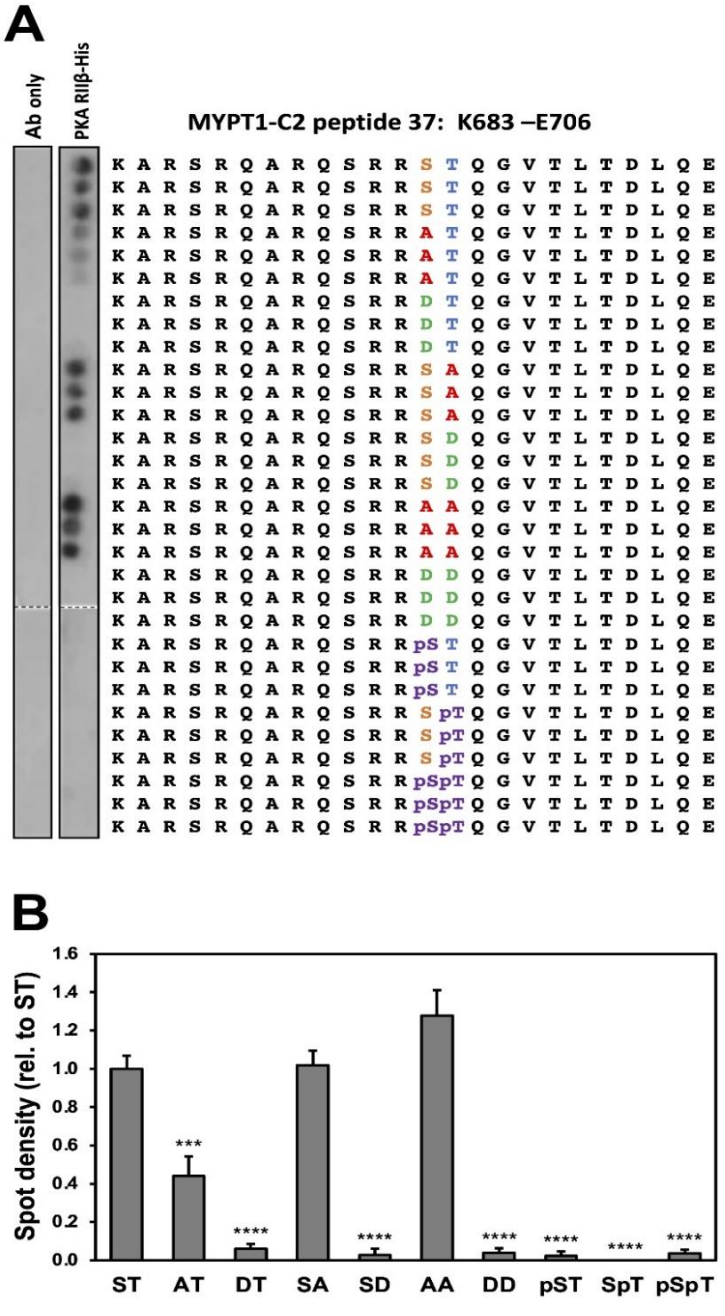

Figure 5.7 Peptide array substitution analysis of phosphorylation targets S^{695} and T^{696}. **(A)** An array of overlapping 24mers, sequentially shifted by 5 amino acids, spanning MYPT1-C2 peptide 37 was used for single and double alanine, aspartate, or phosphorylated residue substitutions. The array was processed as in figure 5.6 but was probed only for PKA-RIIß. Each substitution was tested in triplicate. **(B)** Spot densities of panel D were analysed with Image J. For each spot the intensity of the corresponding antibody only background spot was subtracted and calculated relative to the non-mutated (ST) peptide. Data are mean ± SEM. *** $p<0.001$, **** $p<0.0001$ relative to the ST peptide, ANOVA followed by Tukey test. (Peptide array synthesis and probing were carried out in Professor George Baillie's laboratory).

5.6. Epitope mapping of PKA-R binding sites to his-tagged MYPT1-C2Ext (Y496-T779)

Having mapped the interaction sites of PKA-R on MYPT1, the same approach was designed to investigate the interaction sites of MYPT1-C2 on PKA-R. This would involve probing a peptide array spanning one PKA-R subunit with recombinantly expressed His-tagged MYPT1-C2 (I501-E706). Because PKA-RIß and RIIß displayed a similar behaviour in the MYPT1-C2 arrays, it was decided to probe a PKA-RIß array only. Upon production of this recombinant protein, it was observed that either no expression or excessive degradation of the protein was present on every attempt of protein production. As a result of this, the plan was to produce a new recombinant protein extending the construct to include additional amino acids (Y496-T779). With a larger peptide the goal was to reduce protein degradation upon expression in bacteria. To do so, the oligos specified in section 2.1.3, Table 2.11 were used to amplify a corresponding DNA fragment from an MYPT1 cDNA. The PCR product was inserted in a pET-40b(+) plasmid. The plasmid was verified by sequencing (Eurofins, Wolverhampton, UK) using a T7 primer and transformed in BL21 *E. coli* strain. BL-21 strain was used for recombinant protein expression as they have high-level expression capability, protein production capacity and tolerance to high expression levels (Studier and Moffatt, 1986). In comparison, XL-1 blue are characterised by stable genotype and reduced recombination rate, making it particularly suitable for cloning and library construction and are preferred to achieve hight transformation efficiency (Georgiou and Valax, 1996).

His-tagged MYPT1-C2Ext was expressed and purified in *E.coli* as described in section 2.4.2. and the process monitored by SDS-PAGE followed by Coomassie blue staining of the gels (Figure 5.8). Following induction, noticeable expression of his-MYPT1-C2Ext at the expected size (33 kDa) was not observed (Fig. 5.8, lane I). The bacterial lysate was centrifuged (17000x*g*, at 4°C, for 30 minutes) to separate the soluble supernatant (lane S1) from the insoluble pellet (lane P) fraction and the supernatant was incubated with NiNTA agarose beads. A noticeable amount of a 40 kDa protein was captured by NiNTA agarose beads (lane B1, arrow), indicating that the

recombinant protein migrates with a higher apparent molecular weight. The elution steps were set up to uncouple the protein from the beads, where the first eluate (E1 lane) showed the highest amount of protein in comparison with subsequent eluates. A substantial amount of recombinant protein was still bound to the beads upon elution (B2 lane). Only the two first eluates were subjected to dialysis. After dialysis, the dialysates were centrifuged (500x*g*, at 4°C, for 5 minutes) to remove insoluble protein. It was observed that a substantial amount of recombinant protein became insoluble (P fractions), however sufficient soluble protein was recovered (E fractions). Protein determination was achieved as described in sections 2.4.7.1 and Figure 2.3. Fractions quantified for this experiment are represented on Appendix Figure 8.3-4. Details of quantification of the eluates and the proportion of intact protein are shown in Appendix Table 8.3-3.

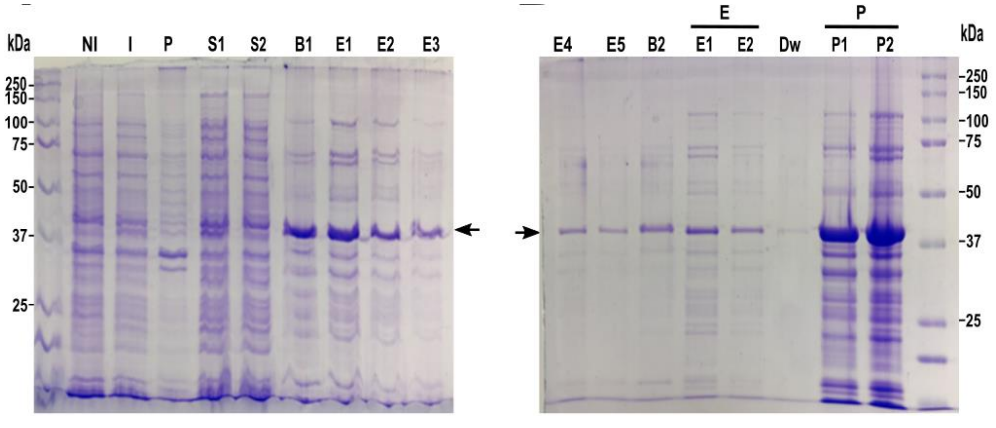

Figure 5.8 Purification of His tagged MYPT1-C2Ext. Expression and Purification of His-tagged extended MYPT1-C2. NI, Non-Induced; I, induced; P, pellet; S1, Supernatant after sonication; S2, Supernatant after incubation with NiNTA Beads; B1, Beads before elution; B2, Beads after elution; Dw – dialysis solution; E, eluates; E and P on the top of the bars means eluates and pellets, respectively, after dialysis and centrifugation. The black arrow indicates the target protein. 10 µL of each sample in 1x Laemmli Buffer was run in a 10% SDS-PAGE. Gels were stained with Coomassie Blue. The calculated molecular weight for MYPT1-C2Ext 33kDa.

Having successfully expressed and purified His-tagged MYPT1-C2Ext (expected molecular weight 33 kDa, apparent molecular weight 40 kDa), 100 µl of the protein eluate (E4-E6 with 1.32 µg/µl) was shipped to the laboratory of Professor George Baillie (University of Glasgow) for probing of a PKA-RIß peptide array. Several

interactions between these two proteins were observed (Figure 5.9 A-D, peptides highlighted in red). Nonetheless, it was observed that peptides 80-82 appears to represent interesting binding regions therefore it could be a region of interest for future studies. It is also evident that these findings require validation, given that the negative control exhibits more significant background noise compared to, for instance, Figure 5.5.

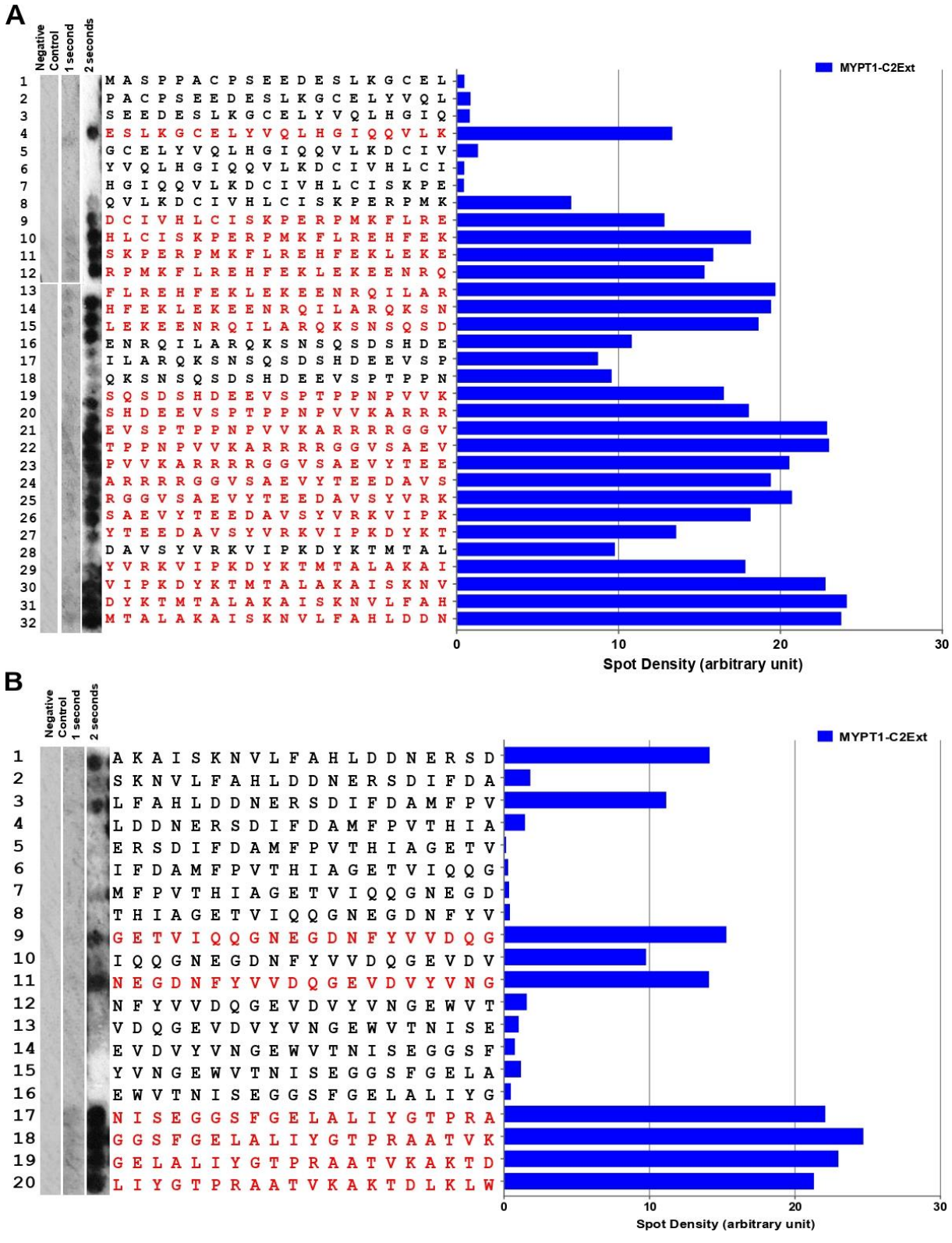

Figure 5.9 Legend on the following page.

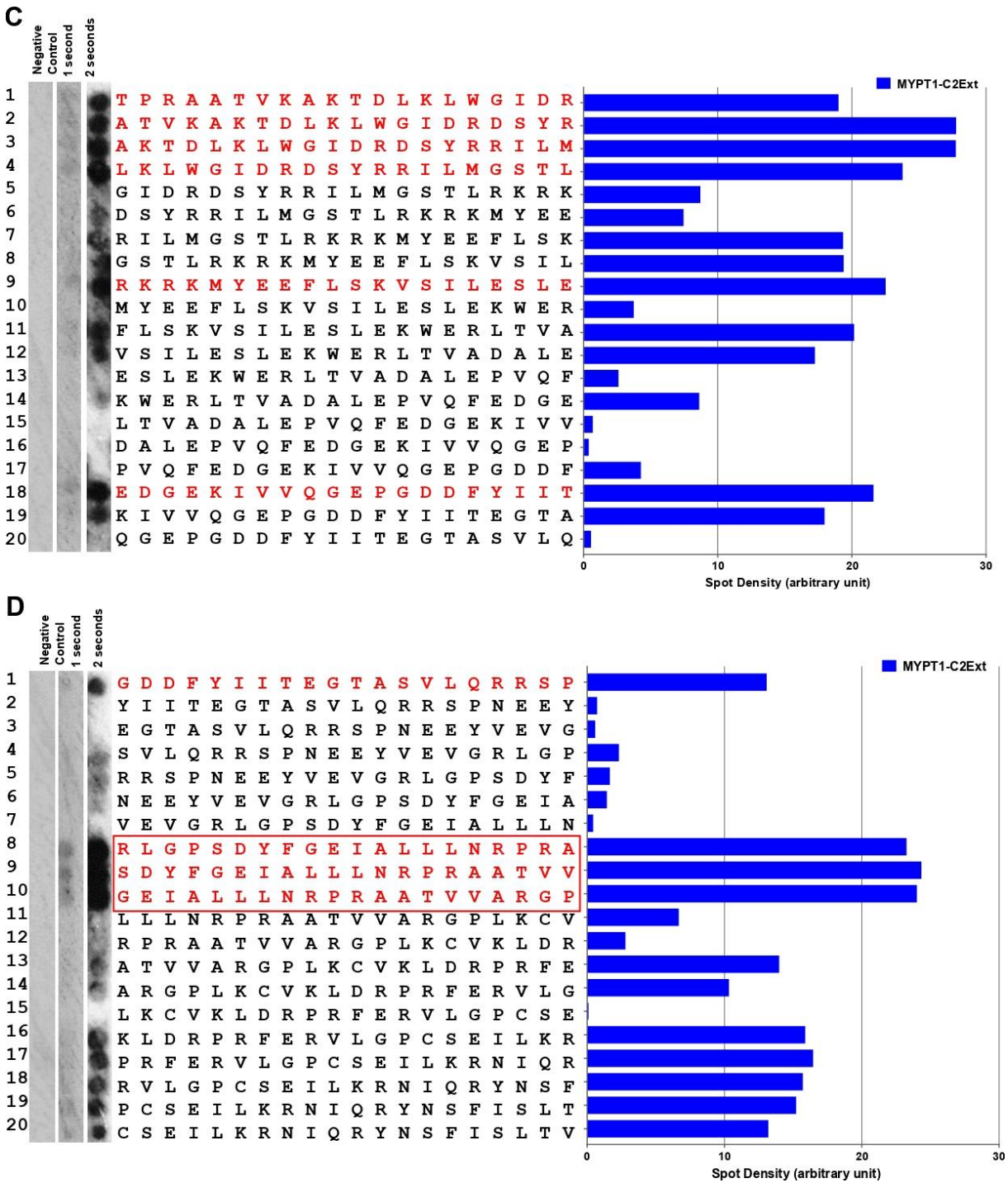

Figure 5.9 Peptide array epitope mapping of his-tagged MYPT1-C2Ext (Y496-T779) protein on PKA-RI. An array of 25mers, sequentially shifted by 5 amino acids, spanning PKA-RIß was overlaid with His-tagged MYPT1-C2Ext (Y496-T779), probed with HRP conjugated anti-polyHis antibody and visualised by enhanced chemiluminescence. For antibody only (Ab only) control, PKA-R was omitted. Blue bars indicate spot densities normalised to the density of the corresponding anti-polyHis antibody-only spot. (Peptide array synthesis and probing were carried out in Professor George Baillie's laboratory).

Further analyses could include alanine substitutions to identify critical residues for the interaction. It would also be necessary to determine whether PKA-RIIß binds to the same MYPT1-C2Ext peptides like PKA-RIß.

Peptide array experiments are commonly conducted and reported with a population size n=1 for several reasons. Firstly, the synthesis and spotting of peptide arrays are performed using automated robots, minimising the possibility of human error, and streamlining the process of peptide array design, thereby reducing potential errors. Secondly, the synthesis of peptides is both costly and time-consuming, making it Impractical to replicate experiments multiple times. Thirdly, similar to western blots, conducting far-western experiments on peptide arrays to evaluate potential PPI binding motifs allows for only semi-quantitative analysis at best. Fourthly, each control spot on the peptide array serves as a control that can be compared with every other variation of that peptide, such as alanine substitutions. Therefore, an n=1 approach, used on all the peptide arrays presented before on this chapter, is often deemed appropriate, especially when positive and negative controls have been successfully validated, as evident from visual or qualitative analysis. This approach ensures efficiency in experimental design and execution, maximising the utility of peptide arrays while minimising resource expenditure and experimental variability. Due to these factors, the findings outlined in this chapter were carried out as single experiments. It is worth noting that peptide arrays using both GST and His-tagged proteins yielded comparable results, although GST exhibited some background noise in the negative control.

5.7. Discussion

In the previous chapter it has been shown that MYPT1 and PKA-R might interact. As outlined in 4.7, additional experiments are required to validate these findings. Making use of knowledge from previous studies that mapped the region of MYPT1 involved in the interaction to I501-E706 (Khalil, 2018), the goal was to narrow down the interaction site to short stretches of amino acids using peptide array technique. The results in this chapter have narrowed down the interaction of PKA-R to three MYPT1 regions. Peptides 13-18 (L562 – S610) and 29-37 (A643 – E706) may represent primary binding sites due to higher intensity spot areas, whereas peptides 1-6 (I501 – Y549) may represent an accessory binding site. Both PKA-Rs subunit types appear to rely upon the same residues for effective binding to MYPT1, indicating they may compete for the same binding sites.

A comprehensive substitution analysis of peptides 15 (S572 – I596) and 35 (V673 – Q697) has helped identify residues K595, E676 as well as the stretch R693-T696 as critical for the interaction (Figure 5.10). Note that the stretch R693-T696, that will be called RRST in what follows, corresponds to the recognition site for PKA and other Ser/Thr kinases and is also targeted by the PP1c subunit of the myosin light chain phosphatase complex (Konya et al., 2023).

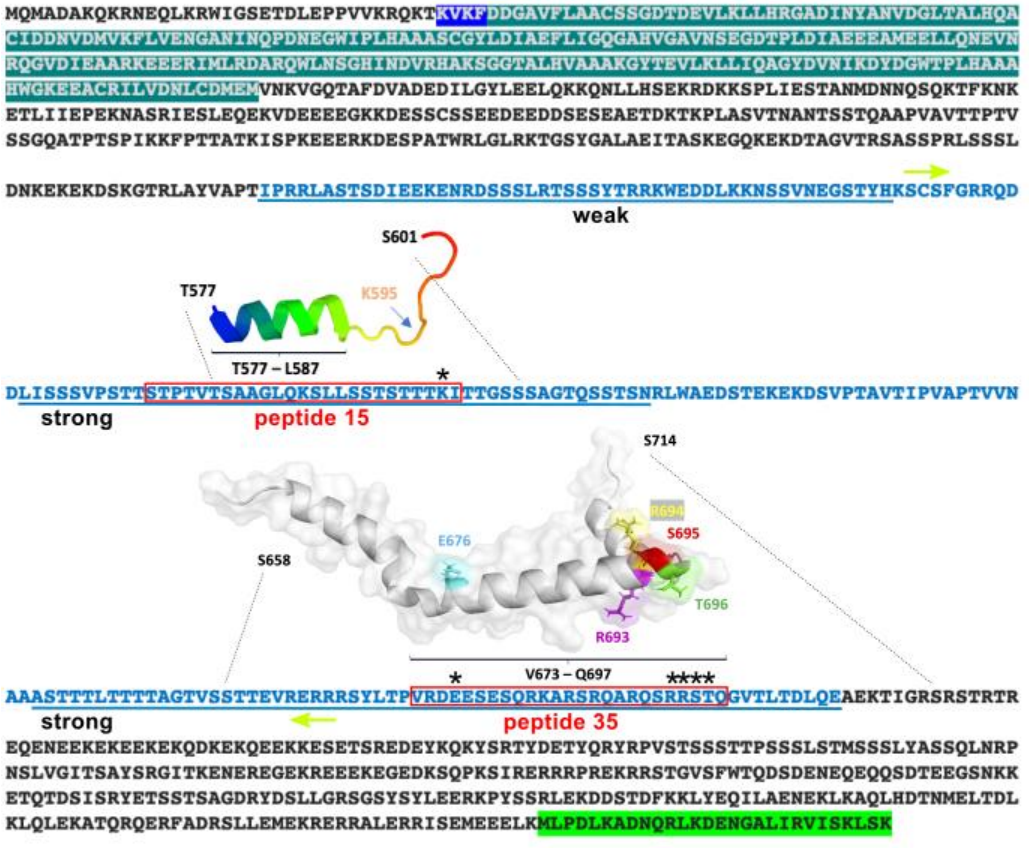

Figure 5.10 Summary of the interaction between MYPT1 and PKA-R. MYPT1-FL domains are highlighted: PP1c binding site (dark blue), ankyrin repeats (teal) and leucine zipper motif (green). The central insert region spans between the lime colour arrows. The stretch encompassing the MYPT1-C2 region identified in GST pulldown assays (figure 4.8 from (Khalil, 2018)) is shown in blue characters. The three binding regions identified in the peptide array overlay (Figure 5.5) are underlined. Red boxes contain peptides 15 and 35 used for substitution analysis. Asterisks indicate critical residues involved in the interaction with PKA-R identified in peptide array screening analyses (Figure 5.6). Structures of peptides 16 and 35 are shown. For peptide 16, PEP-FOLD3.5 predictive software indicates structure to be in part (T577-L587) helical based on 200 simulations (Connor Blair from Professor Baillie's laboratory). Note that peptide 16 was used instead of 15 in order to provide more structural context to K595. Peptide 35 is part of an amphipathic α-helix of the T658-S714 peptide resolved by nuclear magnetic resonance (PDB accession number 2KJY)(Mori et al., 2009). Critical residues are coloured in the structures.

The peptide array overlay technique has the advantage of being consistent and therefore its repeats are precise but, on the other hand does not allow us to study the protein on their 3D structure (Kramer and Schneider-Mergener, 1998).

PPIs and ligand-protein interactions play crucial roles in various biological processes, and studying these interactions is essential for understanding cellular function. Several mass spectrometry (MS)-based methods have been developed to investigate protein interaction affinity and immobilised ligand-protein interactions. One such method is native MS, which allows for the analysis of noncovalent complexes directly from solution. It offers advantages such as the ability to study protein-protein and protein-ligand interactions in real-time, dynamic conditions, and the capacity to analyse large protein complexes. However, native MS cannot determine high-resolution 3D protein structures (Titeca et al., 2019, Kool et al., 2011).

Another technique is the single-molecule pull-down assay (SiMPull). It is based on interaction proteomics, which involves immobilising the protein or ligand of interest to create an affinity column. This method enables the identification of multiprotein complexes but is not suitable for studying dynamic binding events. It is valuable for characterising cellular protein complexes involved in signalling events (Titeca et al., 2019).

Chemical proteomics is another approach that utilises MS to screen ligand selectivity profiles for drug targets and off-targets. It allows for the analysis of multiple interactions simultaneously and provides insights into the selectivity of ligands. However, it requires the availability of suitable chemical probes for specific targets (Pfleger and Eidne, 2006).

Surface plasmon resonance (SPR) coupled with MS is a powerful technique for studying protein binding events. SPR enables real-time monitoring of biomolecular interactions, and when combined with MS, it allows for protein affinity analysis, quantification, and identification. This integrated approach provides complementary information and can reveal structural modifications not detected by SPR alone (Berggård et al., 2007).

Each of these MS-based techniques offers unique advantages for studying PPIs, such as real-time analysis, high sensitivity, and the ability to analyse complex mixtures. However, they also have limitations. For example, native MS cannot provide high-

resolution structural information, and pull-down-based proteomics is not suitable for dynamic binding studies. Additionally, chemical proteomics requires appropriate chemical probes, and SPR coupled with MS requires specialised instrumentation (Berggård et al., 2007, Kool et al., 2011).

In summary, MS-based methods provide valuable tools for investigating protein-protein affinity and immobilised ligand-protein interactions. The choice of technique depends on the specific research objectives, allowing researchers to gain insights into protein interaction networks, identify novel interacting partners, and elucidate the functional significance of these interactions (Kool et al., 2011).

PEP FOLD 3.5 software (Lamiable et al., 2016)) was used by Connor Blair from the collaborator Professor Baillie's research group to predict the structure of peptide 15 (S572 – I596). For this prediction, it was opted to extend the sequence and provide more structural context to K595, therefore peptide 16 (T577 – T597) was used. The predictive software indicated, based in 200 simulations, a structure to be in part helical between T577 and L587. The other structure of interest (peptide 35 – V673 – Q697) is part of an α-helix of the T658-S714 peptide that has been resolved by magnetic resonance (PDB accession number 2KJY) (Figure 5.10) (Mori et al., 2009).

Both PKA RIß and RIIß subunits were unable to bind to MYPT1 following dual substitution for R693 and R694 by glutamic acid, which flipped the electric charges. This suggests the existence of a direct point of contact between PKA-R and MYPT where salt bridges are established between oppositely charged residues. The phosphorylation status of S^{695} and T^{696} is also critical for the interaction of MYPT1 with PKA-R and may help explain the observation that phosphorylation of T696 by ROCK prevents the subsequent phosphorylation of S^{695} (Grassie et al., 2012).

Further studies, such as visualisation of structure by cryogenic transmission electron microscopy (cryo-EM) or analysis of the interaction by surface plasmon resonance, will be necessary to define the interfaces between PKA-R and MYPT1, outside the phosphorylation sites. These interfaces are expected to determine the specificity of recognition of PKA-R as opposed to ROCK and other kinases that target the same

phosphorylation site. A recent study using GST pulldowns and synthetic peptides has identified short MYPT1 regions (called docking motifs) close to T^{696} and T^{853} that are important for interaction with ROCK (Amano et al., 2022). One docking motif encompasses residues 682-690 (RKARSRQAR) and is therefore part of peptide 35 (V673 – Q697). This suggests overlapping between ROCK and PKA-R interaction sites, but the requirements for each kinase appear to be different: replacing basic amino acids of the 682-690 docking motif by alanine negatively affects the interaction with ROCK (Amano et al., 2022) but does not affect the interaction with PKA-R. In contrast, the acidic patch around E676 might be critical for interaction with PKA-R. It is also important to note that the RRST region is also recognised by the MLCP catalytic subunit (Muranyi et al., 2005) and this has implications when it comes to understand the complex molecular interactions in the signalling node assembled by MYPT1.

Further work will be needed to identify the interfaces on PKA-R that interact with MYPT1. Here it is envisioned an extensive substitution analysis to identify critical residues of PKA-R. In addition, the critical residues identified in MYPT1 will need to be subject to validation *in vivo*, for example by repeating pulldowns using a set of mutagenised MYPT1 proteins and by designing functional assays that were outside of the scope of this thesis.

Chapter 6. General Discussion

MLCP has established its role in regulating actomyosin contractility by antagonising the effect of MLCK. MLCP is a holoenzyme comprised by the 110-133 kDa protein phosphatase 1 regulatory subunit 12, known as myosin light chain phosphatase target subunit 1 (MYPT1), protein phosphatase 1c (PP1c) and the M20/21 subunit. MYPT1 exerts crucial functions within smooth muscle cells, endothelial cells, platelets, amongst many others. Its gene, *PPP1R12A*, has been considered a housekeeping gene due to it being expressed in many tissues, including epithelial, muscle, and nervous tissues (Xia et al., 2005). Its well-established role as a key modulator of smooth muscle contractility has been extensively documented (Eto and Kitazawa, 2017). In endothelial cells, MYPT1 plays a vital role in maintaining barrier function (Kim et al., 2012, Kolozsvari et al., 2012, Batori et al., 2019, Aslam et al., 2010, Kovacs-Kasa et al., 2016), while in platelets, it regulates critical processes such as shape change, spreading, and thrombus stability (Aburima et al., 2017, Aburima et al., 2013).

6.1. Complexity of transcription patterns of the *PPP1R12A* gene in cells of the circulatory system

Previous investigations have revealed the existence of alternative splicing variants within the *PPP1R12A* gene. Subsequently, a few of these variants, in particular the LZ$^-$ variant, were subjected to comprehensive investigations to elucidate their functional significance (Dippold and Fisher, 2014a, Dirksen et al., 2000, Khatri et al., 2001, Htet et al., 2021, Payne et al., 2004). However, prior investigations have been limited in scope, focusing on only a few organs and tissues. As a result, they fail to capture the full extent of the transcriptional capabilities of *PPP1R12A*, which is crucial for comprehending the precise cellular functions of MYPT1 isoforms (Saldanha et al., 2022).

A thorough examination of the transcriptional landscape of the human *PPP1R12A* gene was undertaken to fill this knowledge gap, with a focus on protein-coding transcripts. This study, along with additional data, establishes that the *PPP1R12A* gene accounts for a total of 32 exons, 29 of which are capable of encoding 11 protein variants expressed in different proportions across pure cell types and organs. Three exons are exclusively present in specific transcripts subject to nonsense-mediated decay. Through analysis of RNA sequencing (RNA-seq) data, quantitative transcript profiles of *PPP1R12A* in HUVECs, HSVSMCs and platelets were constructed. This analysis revealed the expression of up to ten distinct transcripts, each exhibiting unique frequency patterns in the various cell types (Saldanha et al., 2022).

The findings in this work have led to a better understanding of the existing transcripts and their frequency and therefore put us in a much better position to design functional studies targeting MYPT1 isoforms. RT-PCR, encompassing both conventional and quantitative approaches, has emerged as a widely employed methodology for assessing the presence and relative abundance of the LZ$^-$ variant (Oslin et al., 2022, Khatri et al., 2001, Dordea et al., 2013, Lartey et al., 2016) and less frequently central insert (CI) variants (Kim et al., 2012, Dirksen et al., 2000, Twomey et al., 2010, Payne et al., 2004). The conventional RT-PCR approach used in this study has revealed some limitations when using PCR for an extensive analysis

of *PPP1R12A* variants. This approach requires design, testing and optimisation of PCR conditions for an extensive set of primers, and bears the risk of overlooking variants that are expressed at exceedingly low levels, thereby posing a challenge to comprehensive variant detection.

The transcript profiles of *PPP1R12A* in HUVECs and HSVSMCs exhibit striking similarities, characterised by a prevalent expression of the FL variant, closely followed by the ΔE13 variant. Surprisingly, HSVSMCs demonstrate notably low levels of LZ^- variants. Previous investigations into MYPT1 LZ^- variants, which are reported to be highly abundant in venous smooth muscle, have primarily focused on rat tissue rather than cultivated smooth muscle cells (Payne et al., 2006, Khatri et al., 2001, Payne et al., 2004, Zhang and Fisher, 2007). During cultivation, smooth muscle cells undergo a process called dedifferentiation, which might be the reason why the levels of LZ^- transcripts are lower than expected from the literature. In platelets, LZ^- variants constitute approximately 5.4% of transcripts, indicating that, akin to smooth muscle, sensitivity to nitric oxide (NO) signalling may also exert a crucial modulatory role in platelet function. The LZ domain of MYPT1 has been shown to be important for PKGIα-mediated activation of MLC phosphatase activity, and changes in LZ^- MYPT1 isoform expression result in changes in the sensitivity of smooth muscle. LZ^+ isoforms are rapidly phosphorylated by PKGIα whereas LZ^- isoforms are poor PKGIα substrates (Yuen et al., 2011, Yuen et al., 2014). NO activates the soluble guanylyl cyclase and the cGMP produced activates PKG. NO is important in platelet aggregation (Naseem and Riba, 2008), therefore different responses to NO action may be expected in the different isoforms. An NO donor sodium nitroprusside can be used in order to test NO sensitivity in platelets (Priora et al., 2011) and other cell types that express both LZ transcripts.

The comprehensive analysis done in this study reveals that MYPT1 isoforms lacking the CI region are widely distributed and relatively common. Across various tissues and cell types, CI variants are present in varying proportions, with ΔE13 typically being the predominant CI variant. Notably, in haematopoietic cells (including platelets) and organs, the ΔE14 variant not only represents the primary CI variant

but also emerges as the most prevalent among all variants, implying distinct roles for ΔE14 in these specific cells. Despite their relative abundance, CI variants have received limited attention. Previous reports in rats have identified ΔE13 and ΔE14 variants, along with an equivalent of E13b and a shorter version of E13 (Dirksen et al., 2000, Payne et al., 2004). CI variants are important to study. The knockdown of isoforms by RNA interference inhibited RLC dephosphorylation, cell migration, and adhesion, resulting in a significant increase in RLC phosphorylation, in HeLa cells. The knockdown leads to robust stress fibre formation and prominent focal adhesions, correlating with RLC phosphorylation and indicating a role in stress fibre and focal adhesion assembly (Xia et al., 2005). The full-length MYPT1 isoform is crucial for maintaining actomyosin-based cellular functions, such as adhesion and migration (Xia et al., 2005).

Dirksen et al. (2000) employed a PCR-based approach to assess the relative proportions of FL and CI variants in various rat organs (Dirksen et al., 2000). These findings align well with the results obtained from human RNAseq data, lending support to the consistency of variant distribution across species. Annotation of E13 and/or E14 variants in diverse vertebrates indicates their evolutionary conservation. However, the understanding of the functional consequences associated with CI deletions in MYPT1 remains limited. In HeLa cells, where FL and ΔE13 are the predominant variants, silencing experiments demonstrated the significance of both variants in MLC dephosphorylation and the regulation of the actin cytoskeleton architecture, albeit with subtle differences (Xia et al., 2005). The removal of binding sites for interacting proteins, such as the lower binding affinity of ΔE13 for radixin, represents a potential consequence of CI deletions (Kim et al., 2012). Another possible consequence is the alteration of susceptibility to MLCP activity regulation through phosphorylation of critical residues near the CI region. While not directly comparable to mammalian CI variants, a study reported a lower rate of PKG-mediated phosphorylation in vitro for the ΔE12 variant in chickens, without affecting the extent of phosphorylation (Yuen et al., 2011).

The LZ$^-$ isoforms of MYPT1 have been extensively investigated, primarily in avian and rodent models. Recently, efforts have been made to translate this knowledge to humans; however, in this work it was found out that the E24 variant is not annotated in GenBank. Lartey et al. (2016) employed quantitative RT-PCR to identify the LZ$^-$ variant in placental and myometrial arteries, as well as uterine smooth muscle (Lartey et al., 2016). In a comprehensive study by Oslin et al. (2022) (Oslin et al., 2022), the expression of the LZ$^-$ variant was characterised using a combination of genetic mouse models, human tissues, and publicly available RNAseq data, including the GTEx dataset. In mice, the LZ$^-$ variant was found to be abundant in smooth muscle derived from various organs, which broadly corresponds to the observed RNAseq pattern in human tissues. However, the ratios of LZ$^-$/LZ$^+$ variants in isolated murine smooth muscle cannot be compared directly to the ratios calculated from the RNAseq data of human tissues and organs because these contain a mix of cell types (from follicular cells in the thyroid gland to endometrium, blood vessels including fibroblast, endothelial cells, smooth muscle cells, nerve cells and intestinal epithelial cells), each with its own pattern of *PPP1R12A* variants (Saldanha et al., 2022).

This limitation is clearly demonstrated in the GTEx dataset for the oesophagus, where the muscularis expresses more than 50% LZ$^-$ variants while the mucosa expresses just over 10% (Saldanha et al., 2022). This discrepancy has also been acknowledged by other researchers (Oslin et al., 2022). Additionally, it is worth noting that a shorter LZ$^-$b variant with a 13-bp version of E24 has not been previously identified, although it is less common than the longer LZ$^-$a variant and is expected to be functionally equivalent.

The *in silico* analysis in this study has not only yielded a better understanding of CI and LZ variants but has also revealed the presence of three rare variants: ΔE22, ΔE6, and E9$^+$. These variants involve the deletion or addition of short stretches of amino acids, typically 25-35 residues. Although these variants are uncommon, it is possible that they may have a higher relative abundance and possess specific functional relevance in certain cell populations. Among these rare variants, E9$^+$ appears to be

phylogenetically conserved in some vertebrates, and the exon is supported by rat RNAseq data (GenBank annotation).

In addition to elucidating the diversity of MYPT1 isoforms, this investigation expanded the knowledge of the *PPP1R12A* promoter region. Four predicted transcription initiation sites have been identified, each harbouring an Sp1 binding site. Notably, one of these initiation sites resides in a novel P1^{-} promoter region located upstream P1 promoter region that is more frequently used. The three transcription initiation sites within the P1 region appear to be utilised with similar frequency, but the reason for the infrequent utilisation of the site in the P1^{-} region remains to be determined. Currently, limited information is available regarding the transcriptional regulation of *PPP1R12A*. However, it is worth mentioning that *PPP1R12A-AS1*, an antisense transcript overlapping with the 5' region of *PPP1R12A*, has been shown to function as a translation upregulator (Schein et al., 2016).

A novel ΔN variant of MYPT1 was identified in this study, which seems to originate from a transcription start site located within intron 1 (I1) of *PPP1R12A*, extending into exon E1+. Although this variant is rare overall, it constitutes approximately one-fourth of *PPP1R12A* transcripts in the testis, the only organ where its expression was observed (Saldanha et al., 2022). Investigating the specific cell type(s) within the testis that express(es) the ΔN variant and exploring its functional role will be crucial. It is important to note that no ΔN variant has been documented in rodents (GenBank annotation), which have been extensively studied regarding MYPT1. However, in *C. elegans*, a potential splice variant lacking the first 37 residues of the MYPT1 ortholog functions normally in the spermatheca but not in the embryonic epidermis (Wissmann et al., 1999). The deletion of the N-terminal region in the ΔN variant may result in the loss of three PP1c-binding regions: the K35VKF38 motif, which appears to be essential for the interaction, the MyPhoNE motif, and the first ankyrin repeat (Toth et al., 2000, Terrak et al., 2004). Additionally, nuclear localisation signals identified in the N-terminal region may be lost (Eto et al., 2005, Wu et al., 2005), potentially resulting in a protein incapable of translocating to the nucleus, where MYPT1 is known to regulate gene expression (Kiss et al., 2019).

In conclusion, this part of the study expands the understanding of the intricate transcriptional patterns of *PPP1R12A* in cells and various tissues in the circulatory system. It is believed that this valuable information will serve as a guide for future research on the specific functions of less explored MYPT1 isoforms in both normal physiological processes and pathological conditions.

6.2. Direct interaction of MYPT1 with PKA-R *in vitro* and *in situ*: from cell lysates to proximity ligation assay

Understanding intricate mechanisms at the molecular level requires the identification and characterisation of key players and their interactions. PPIs play a fundamental role in numerous biological processes, and the ability to investigate these interactions is paramount in advancing our comprehension of cellular function (Xing et al., 2016). The production of recombinant proteins is widely used in laboratory research for biophysical and structural studies, diagnostic and therapeutic purposes (Oliveira and Domingues, 2018). Various methodologies are available for the detection of PPIs, including Bioluminescence Resonance Energy Transfer (BRET), Fluorescence Resonance Energy Transfer (FRET), Surface Plasmon Resonance (SPR), co-immunoprecipitation (Co-IP), peptide array, pull-down assay/affinity chromatography, and other techniques. These diverse approaches enable researchers to explore and unravel the complex network of interactions between proteins in biological systems.

In this study, several techniques were utilised to demonstrate the possible interaction of MYPT1 with PKA-R. Co-immunoprecipitation, cAMP affinity pull-down, co-localisation, and Duolink® -proximity ligation assay techniques were used to prove that MYPT1 and PKA interact both in HUVEC lysates and *in vitro*. Previous research investigated the potential role of MYPT1 as a PKA anchor through its interaction with PKA-R subunits using an affinity pulldown approach in platelet lysates with GST-tagged PKA-R subunits. Notably, all four PKA-R variants demonstrated a significant capacity to associate with MYPT1, as well as with the PKAcat subunit (Khalil, 2018). To address the hypothesis formulated in this study that MYPT1 plays a role in compartmentalising PKA signalling by acting as an AKAP that would target PKA to the MLCP at the signalling node, the aim was to confirm the existence of MYPT1-PKA immune complexes by using a rigorous immunoprecipitation approach in both HUVECs and platelets. In combination, these findings provided the first evidence that MYPT1 might form complexes with the PKA holoenzyme, supporting the hypothesis that it functions as a PKA anchor by

facilitating interactions with PKA-R subunits. Further studies are suggested on section 6.4 to strengthen this hypothesis.

Upon binding to cAMP, the PKA-R subunits change conformation and release the PKAcat subunits (Gold, 2019). To investigate whether the interaction of PKA with MYPT1 is also conformation-dependent, affinity pulldowns in HUVEC and platelet lysates with agarose beads functionalised with cAMP were performed. In HUVECs a higher quantity of PKA-Rs subunits were found attached to the beads in comparison with PKAcat, where very little was observed. MYPT1 though, was not recovered with beads, suggesting that PKA-MYPT1 complex occurs when PKA-R subunits are not bound to cAMP.

Significantly, in the cAMP affinity pulldown performed on platelet lysates substantial binding of MYPT1 to the beads, along with the presence of ß-actin was observed. This contrasted with the results obtained from HUVEC lysates. To investigate whether the interaction between MYPT1 and PKA in platelets is dependent on the actin cytoskeleton, latrunculin B was employed to disrupt the actin cytoskeleton prior to the cAMP pulldown. Surprisingly, even under these conditions, significant amounts of MYPT1 were still detected, and actin associated with the beads. The distinct behaviour of MYPT1 observed in immunoprecipitation and cAMP pulldown assays between HUVECs and platelets could potentially be attributed to differences in the relative levels of actin monomers, which are considerably higher in platelets. It is known that MYPT1 interacts with actin and various actin-binding proteins (Kiss et al., 2019), and it has been demonstrated that at least PKA-RIIα directly interacts with actin as well (Rivard et al., 2009).

After establishing the formation of complexes between MYPT1 and PKA-R subunits, the goal was to investigate their co-localisation in HUVECs. Considering the predominantly diffuse distribution of all these proteins and their diverse patterns of subcellular distribution, noticeable colocalisation between MYPT1 and PKA-R subunits was only evident in restricted regions, primarily at the cell cortex. Further studies to confirm this technique are specified in section 6.4. To confirm the interaction of MYPT1 and PKA-R in their native cellular environment, the proximity

ligation assay technique was used in HUVECs (Fredriksson et al., 2002). PLA reactions using a rabbit anti-MYPT1 antibody in combination with subunit-specific mouse anti-PKA subunit antibodies exhibited significantly numerous dots with PKA-R but not with PKAcat. The results suggest that a significant number of PKA-R subunits exist in a complex with MYPT1in HUVECs. It is suggested that PKA-R does not bind to PKAcat due to the low signal observed with MYPT1 and PKAcat in PLA (Figure 4.12). This could be because PKA-R subunits are collectively more abundant than PKAcat, Experimental measurements indicate that the cellular concentrations of PKA subunits show a significant molar excess of PKA regulatory (PKA-R) subunits relative to PKA catalytic (PKAcat) subunits, approximately 10-15 times more PKA-R than PKAcat (Walker-Gray et al., 2017, Aye et al., 2010), the PKA-R subunits associating with MYPT1might contribute for the capture of PKAcat, maintaining PKAcat nearby MYPT1. Another possibility is that the PKAcat antibody cannot bind PKAcat when it is associated with PKA-R, possibly because the antigenic region is obscured by the PKA-R – PKAcat interaction. Technically, PKAcat may not be detected by PLA due to its proximity to MYPT1 being lower than the minimal detection distance of 40 nm, as PLA can only detect proteins within this range (Fredriksson et al., 2002, Söderberg et al., 2006, Jarvius et al., 2007).

6.3. MYPT1 as a non-canonical AKAP: Towards a model of the MYPT1-PKA interaction

In this work the hypothesis that MYPT1 might function as an AKAP was explored. Typically, AKAPs are characterised by the presence of an amphipathic helix that facilitates their interaction with the dimerisation and docking (D/D) domain of PKA-R (Pidoux and Taskén, 2010). Previous work by Khalil (2018), using HeliQuest (Gautier et al., 2008) software has shown that MYPT1 presents two regions of 267-285 and 986-1004 amino acids, exhibited a pronounced amphipathic character akin to known AKAP disruptor peptides like Ht31 and RIAD. Interestingly, neither of these regions' co-sediments with PKA-R subunits, suggesting that MYPT1 does not function as a canonical AKAP.

Most AKAPS possess unique targeting domains, which direct the AKAP-PKA complex to defined cellular compartments including membranes, cytoskeletal components or other structures (Langeberg and Scott, 2015, Skroblin et al., 2010, Szaszak et al., 2008, Troger et al., 2012, Dema et al., 2016); however, some AKAPs lack canonical targeting domains (Duwé and Dedecker, 2019). Furthermore, the interaction between MYPT1 and PKA-R does not rely on the D/D domain, indicating that MYPT1 does not function as a canonical AKAP (Khalil, 2018). While the majority of AKAPs recruit PKA-R subunits through a specific amphipathic helix that interacts with the D/D domain, in non-canonical AKAPs, such as pericentrin, RSK1, neurochondrin, tubulin, and actin, the interaction with PKA-R does not involve the D/D domain, except for neurochondrin (Dema et al., 2015). Hence, it can be postulated that MYPT1 can be categorised as a non-canonical AKAP with dual specificity, although the specific affinities for each PKA-R subunit have yet to be determined.

Previous work showed that MYPT1 interacts with all four PKA-R subunits and this interaction was narrowed down to the residues I501-E706 of MYPT1 (Khalil, 2018). One aim of this study was to identify the residue(s) responsible for this interaction. A peptide array approach helped narrow the interaction sites to three potentials regions of MYPT1. The effective binding of both PKA-RI and RII subunits to MYPT1 is dependent on the same set of residues, suggesting a potential competition for the

shared binding sites. Additionally, the substitution analysis has revealed the critical involvement of specific residues, namely K595 and E676, along with the PKA phosphorylation site, in this binding interaction.

The peptide encompassing K595 exhibits predicted partial helical structure (T577-L587). Additionally, NMR studies have revealed that peptide 35, comprising E676 and the PKA recognition site, is situated within an α-helix of the T658-S714 peptide (Mori et al., 2009). The dual substitution of R693 and R694 with E, altering the electric charges, resulted in the inability of both PKA-RI and RII subunits to bind. This suggests the presence of a direct point of contact between PKA-R and MYPT1, where salt bridges may form between oppositely charged residues. The phosphorylation status of S695 and T696 also plays a critical role in the interaction between MYPT1 and PKA-R, and this observation may help explain the effects of antagonistic kinases (PKA/PKG and ROCK) on MYPT1. Further investigations are required to elucidate the specific interfaces between PKA-R and MYPT1 that exist beyond the phosphorylation sites, as these interfaces contribute to the selective recognition of PKA-R compared to ROCK and other kinases that utilise the same phosphorylation site.

A recent study utilising GST pulldowns and synthetic peptides has identified short regions of MYPT1, referred to as docking motifs, located near the phosphorylation sites T696 and T853, which are crucial for the interaction with ROCK (Amano et al., 2022). Peptide 35 contains a docking motif composed of residues 682-690 (RKARSRQAR) that overlaps with the ROCK interaction site, indicating a potential shared region. However, the requirements for binding differ between the two interactions: substituting the basic amino acids in the 682-690 motif with alanine negatively impacts the ROCK interaction (Amano et al., 2022), but it does not affect the interaction with PKA-R. Conversely, the acidic cluster located upstream, particularly E676, seems to play a critical role in the interaction with PKA-R.

Collectively, these findings support a model in which the recognition of the RRST motif of MYPT1 by PKA primarily occurs through the PKA-R subunits (Fig 6.1). In this highly speculative model, the presence of the RRST motif may displace the inhibitor site of PKA-R, allowing it to interact with PKAc. Unfortunately, there is currently no

available structural data on the conformation of the N-terminal region of cAMP-free PKA-R subunits to investigate this hypothesis. Once PKA-R subunits are bound to MYPT1, they can recruit catalytic subunits, causing the substrate or pseudosubstrate motifs within the inhibitor site of PKA-R subunits to occupy the catalytic cleft of PKAcat. Upon an increase in cAMP levels, binding of this second messenger to PKA-R induces a conformational change that leads to the dissociation of PKAcat. This conformational change may also contribute to the dissociation of PKA-R from MYPT1. In support of this, the cAMP pulldown data demonstrate that PKA-R bound to 8-AHA-cAMP-functionalised beads is unable to co-sediment with MYPT1. Consequently, PKAcat gains access to the RRST motif and phosphorylates the S695 residue, thereby protecting MYPT1 from ROCK-mediated phosphorylation. It has been previously reported that pre-phosphorylation of S695 by PKA in vitro prevents phosphorylation of T696 without affecting the activity of PP1c (Wooldridge et al., 2004, Grassie et al., 2012). Although the current PLA results do not conclusively support this model, it would be possible to test the effect of cAMP binding to PKA-R, leading to PKAcat dissociation from PKA-R and subsequent phosphorylation of MYPT1 on RSST. For this, a stimulus would be required, for example using the adenylyl cyclase activator forskolin.

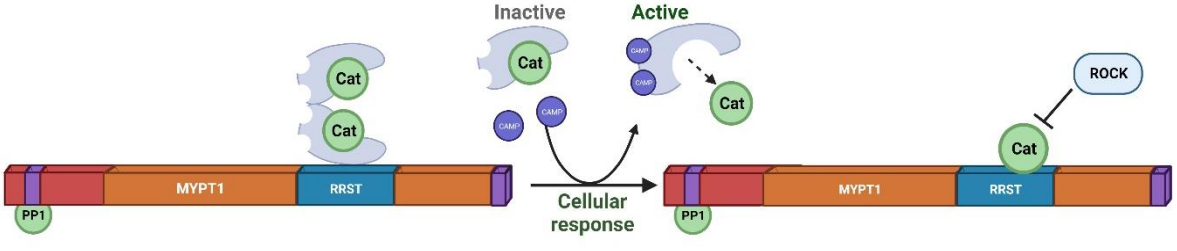

Figure 6.1 Working model of the interaction between MYPT1 and PKA-R. For simplicity, PKA subunits are shown as monomers. In resting conditions PKA-R binds to MYPT1 at the RRST motif *and recruits* PKAcat (Cat*)* but prevents it from phosphorylating S695. Upon binding of cAMP, PKA-R changes conformation, unmasks S695 and allows phosphorylation of this residue by activated and released PKAcat. The phosphorylated RRST motif is protected from ROCK and other kinases, but PP1c activity is not affected and subsequently would dephosphorylate S695. MYPT1 would then become available for association with the PKA holoenzyme. The domain architecture of MYPT1 is indicated by colours: PP1c binding motif (teal), ankyrin repeats (red), central insert (blue) and leucine zipper motif (purple).

The proposed model (Figure 6.1) provides insights into the dynamic phosphorylation of MYPT1 by antagonistic signalling pathways. It is suggested the existence of two distinct pools of MLCP that may be dictated by different MYPT1 isoforms in platelets and possibly endothelial cells too. One pool is associated with PKA-R, acting as a non-canonical AKAP, and can be phosphorylated by PKAc at the S695 residue. It has been reported that MYPT1 undergoes basal phosphorylation at S695 and other residues in various cell types (Wooldridge et al., 2004, Grassie et al., 2012, Kitazawa et al., 2003). In circulating platelets, endothelial PGI2 (and also NO) likely plays a role in maintaining a certain level of pMYPT1-S695 (Khalil, 2018). This effect is balanced by the phosphatase activity of PP1c, which remains unaffected by the phosphorylation of MYPT1 at S695. Within this pool, PKA-R keeps MLCP disinhibited and protected against ROCK-mediated phosphorylation. This is supported by the observation that levels of pMYPT1-S695 remain constant upon stimulation by thrombin (Khalil, 2018).

The other pool of MLCP is not associated with PKA-R and is susceptible to phosphorylation by ROCK and other kinases (Kiss et al., 2002). However, under resting conditions, the activity of PP1c keeps pMYPT1-T696 levels very low. Agonists that activate RhoA would trigger an increase in pMYPT1-T696 above a certain threshold, resulting in an increase of phosphorylation that is further enhanced by the inhibition of MLCP activity associated with T696 phosphorylation (Khromov et al., 2009). As the stimulus fades, PP1c activity is restored, leading to a return of pMYPT1-T696 to basal levels (Kaneko-Kawano et al., 2012, Kiss et al., 2008).

In summary, the findings of this part of the study suggest a novel mechanism of regulation of MYPT1 phosphorylation by PKA. This mechanism involves the direct interaction of PKA-R with a central MYPT1 region that includes the kinase substrate motif of PKAcat but also ROCK. It is proposed that MYPT1 could function as a non-canonical AKAP to target the PKA holoenzyme to the MLCP signalling node, where it would modulate the crosstalk between PKA and ROCK and MLCP activity. Future studies should address the functional relevance of the novel mechanism uncovered in this study.

6.4. Future Perspectives

MYPT1, a crucial component in cells with higher importance for the ones that are part of the circulatory system, plays significant roles in various aspects. Its well-established function as a key regulator of smooth muscle contractility has been extensively studied (Eto and Kitazawa, 2017). Additionally, MYPT1 is involved in maintaining the integrity of the endothelial barrier, contributing to the proper functioning of the endothelium (Kim et al., 2012, Kolozsvari et al., 2012, Batori et al., 2019, Aslam et al., 2010, Kovacs-Kasa et al., 2016). Furthermore, in platelets, MYPT1 governs essential processes such as shape change, spreading, and the stability of thrombus formation (Aburima et al., 2017, Aburima et al., 2013, Saldanha et al., 2022). These multifaceted roles of MYPT1 highlight its significance in maintaining proper circulatory system function and provide a foundation for further investigations into its specific contributions to health and disease.

While this thesis has contributed valuable information to the advancement of the knowledge on MYPT1, many more questions are raised. The following points should be considered when performing future research into the MYPT1 role within of the vasculature:

- MYPT1 transcripts were successfully identified in HUVECs and HSVSMC and confirmed by RT-PCR, however these transcripts were not confirmed in platelets using the same approach. Future studies should attempt to confirm the presence of MYPT1 transcripts within platelets, to allow for comparison between cells of the vascular system. Although platelets contain mRNA (Rowley et al., 2012), the protocol that was used in this study for the collection of platelets is not completely free of leukocytes contamination, therefore the use of other techniques to isolate pure platelets would be required. Isolation of mRNA could be done by removing contaminating white blood cells with magnetic beads functionalised with antibodies to leukocyte markers to ensure that the only cells remining are platelets (Amisten, 2012). The findings of transcripts in platelets could then be compared to the findings on the transcripts within HUVECs and HSVSMC.

- To understand the function of specific MYPT1 variants, a gene silencing approach could be implemented. Successful silencing of individual transcripts could provide information about the roles of each variant in cell signalling pathways. A silencing approach for *PPP1R12A* variants in HUVECs was designed. Although preliminary trials were not conclusive, additional work is warranted to establish optimal conditions for future studies. A CRISPR (clustered regularly interspaced short palindromic repeats) approach is likely not to be successful, as it has been demonstrated that the knockout of the *Ppp1r12a* gene in mice is lethal (Okamoto et al., 2005). Upon successful silencing, the effects of PGI2 and thrombin on cell permeability could be evaluated by measuring transendothelial electrical resistance in HUVECs. This experimental approach will provide valuable insights into the influence of MYPT1-PKA interaction on the regulation of cellular responses. In principle it should be possible to address individual isoforms of MYPT1 by tailoring the siRNA approach with primers that target specific transcriptional variants.
- To strengthen the results on the interaction between MYPT1 and PKA, three different techniques could be used in future experiments. Two of them would add similar information to the one obtained with peptide arrays. Using kinetic bioluminescence resonance energy transfer) (BRET) and surface plasmon resonance (SPR) in support of the peptide array technique would confirm previous results and provide quantitative information. The third technique, cryogenic transmission electron microscopy (Cryo-TEM), would support results obtained with the PLA technique. In this technique protein structure is preserved by embedding the sample in an environment of vitreous ice.
- Repetition of cAMP pull downs using other agarose beads: Sp-8-AHA-cAMPS agarose beads that are resistant to PDEs activity. Also, the use of other controls such as AMP should be considered. Beads from BioLog – Life Science Institute are also prepared with other ligands. One type of beads that could be used in future studies are Rp-8-AHA-cAMPS agarose beads where PKCat does not dissociate from the PKA-R upon cAMP binding to PKA-R, allowing to

verify whether the binding of PKA-R to MYPT1 depends on the conformation of PKA-R.

- PLA should be performed using different stimuli (cAMP, thrombin, ROCK inhibitors). This is important to investigate the interaction of MYPT1 and PKA under various physiologic conditions.
- Experiments to determine MYPT1-PKA dissociation constant to determine the strength of the interaction using for example surface plasmon resonance.

Chapter 7. Bibliography

AAGAARD, L. & ROSSI, J. J. 2007. RNAi therapeutics: principles, prospects and challenges. *Adv Drug Deliv Rev,* 59**,** 75-86.

AALKJAER, C. & NILSSON, H. 2005. Vasomotion: cellular background for the oscillator and for the synchronization of smooth muscle cells. *Br J Pharmacol,* 144**,** 605-16.

ABOUHAMED, M., GROBE, K., SAN, I. V., THELEN, S., HONNERT, U., BALDA, M. S., MATTER, K. & BAHLER, M. 2009. Myosin IXa regulates epithelial differentiation and its deficiency results in hydrocephalus. *Mol Biol Cell,* 20**,** 5074-85.

ABURIMA, A., WALLADBEGI, K., WAKE, J. D. & NASEEM, K. M. 2017. cGMP signaling inhibits platelet shape change through regulation of the RhoA-Rho Kinase-MLC phosphatase signaling pathway. *J Thromb Haemost,* 15**,** 1668-1678.

ABURIMA, A., WRAITH, K. S., RASLAN, Z., LAW, R., MAGWENZI, S. & NASEEM, K. M. 2013. cAMP signaling regulates platelet myosin light chain (MLC) phosphorylation and shape change through targeting the RhoA-Rho kinase-MLC phosphatase signaling pathway. *Blood,* 122**,** 3533-45.

AGRAWAL, N., DASARADHI, P. V., MOHMMED, A., MALHOTRA, P., BHATNAGAR, R. K. & MUKHERJEE, S. K. 2003. RNA interference: biology, mechanism, and applications. *Microbiol Mol Biol Rev,* 67**,** 657-85.

ALARCON-MARTINEZ, L., YEMISCI, M. & DALKARA, T. 2021. Pericyte morphology and function. *Histol Histopathol,* 36**,** 633-643.

ALBERTS, B. H., REBECCA; JOHNSON, ALEXANDER; MORGAN, DAVID; RAFF, MARTIN; ROBERTS, KEITH; WALTER, PETER; WILSON, JOHN; HUNTER, TIM; 2022. *Molecular biology of the cell,* New York, W. W. Norton & Company.

ALESSI, D., MACDOUGALL, L. K., SOLA, M. M., IKEBE, M. & COHEN, P. 1992. The control of protein phosphatase-1 by targetting subunits. The major myosin phosphatase in avian smooth muscle is a novel form of protein phosphatase-1. *Eur J Biochem,* 210**,** 1023-35.

ALVAREZ-SANTOS, M. D., ALVAREZ-GONZALEZ, M., ESTRADA-SOTO, S. & BAZAN-PERKINS, B. 2020. Regulation of Myosin Light-Chain Phosphatase Activity to Generate Airway Smooth Muscle Hypercontractility. *Front Physiol,* 11**,** 701.

AMANO, M., ITO, M., KIMURA, K., FUKATA, Y., CHIHARA, K., NAKANO, T., MATSUURA, Y. & KAIBUCHI, K. 1996. Phosphorylation and activation of myosin by Rho-associated kinase (Rho-kinase). *J Biol Chem,* 271**,** 20246-9.

AMANO, M., KANAZAWA, Y., KOZAWA, K. & KAIBUCHI, K. 2022. Identification of the Kinase-Substrate Recognition Interface between MYPT1 and Rho-Kinase. *Biomolecules,* 12**,** 159.

AMANO, M., NAKAYAMA, M. & KAIBUCHI, K. 2010. Rho-kinase/ROCK: A key regulator of the cytoskeleton and cell polarity. *Cytoskeleton (Hoboken),* 67**,** 545-54.

AMARTELY, H., IOSUB-AMIR, A. & FRIEDLER, A. 2014. Identifying protein-protein interaction sites using peptide arrays. *J Vis Exp***,** e52097.

AMISTEN, S. 2012. A Rapid and Efficient Platelet Purification Protocol for Platelet Gene Expression Studies. *In:* GIBBINS, J. M. & MAHAUT-SMITH, M. P. (eds.) *Platelets and Megakaryocytes: Volume 3, Additional Protocols and Perspectives*. New York, NY: Springer New York.

ANAND, G. S., HOTCHKO, M., BROWN, S. H., TEN EYCK, L. F., KOMIVES, E. A. & TAYLOR, S. S. 2007. R-subunit isoform specificity in protein kinase A: distinct features of protein interfaces in PKA types I and II by amide H/2H exchange mass spectrometry. *J Mol Biol,* 374**,** 487-99.

ASLAM, M., HARTEL, F. V., ARSHAD, M., GUNDUZ, D., ABDALLAH, Y., SAUER, H., PIPER, H. M. & NOLL, T. 2010. cAMP/PKA antagonizes thrombin-induced inactivation of endothelial myosin light chain phosphatase: role of CPI-17. *Cardiovasc Res,* 87**,** 375-84.

ASPELUND, A., ROBCIUC, M. R., KARAMAN, S., MAKINEN, T. & ALITALO, K. 2016. Lymphatic System in Cardiovascular Medicine. *Circ Res,* 118**,** 515-30.

AYE, T. T., SCHOLTEN, A., TAOUATAS, N., VARRO, A., VAN VEEN, T. A., VOS, M. A. & HECK, A. J. 2010. Proteome-wide protein concentrations in the human heart. *Mol Biosyst,* 6**,** 1917-27.

BAHLER, M., KROSCHEWSKI, R., STOFFLER, H. E. & BEHRMANN, T. 1994. Rat myr 4 defines a novel subclass of myosin I: identification, distribution, localization, and mapping of calmodulin-binding sites with differential calcium sensitivity. *J Cell Biol,* 126**,** 375-89.

BAILLIE, G. S., SCOTT, J. D. & HOUSLAY, M. D. 2005. Compartmentalisation of phosphodiesterases and protein kinase A: opposites attract. *FEBS Lett,* 579**,** 3264-70.

BANNERT, N., VOLLHARDT, K., ASOMUDDINOV, B., HAAG, M., KÖNIG, H., NORLEY, S. & KURTH, R. 2003. PDZ Domain-mediated Interaction of Interleukin-16 Precursor Proteins with Myosin Phosphatase Targeting Subunits*. *J Biol Chem,* 278**,** 42190-42199.

BARLAN, K. & GELFAND, V. I. 2017. Microtubule-Based Transport and the Distribution, Tethering, and Organization of Organelles. *Cold Spring Harb Perspect Biol,* 9.

BATORI, R., KUMAR, S., BORDAN, Z., CHERIAN-SHAW, M., KOVACS-KASA, A., MACDONALD, J. A., FULTON, D. J. R., ERDODI, F. & VERIN, A. D. 2019. Differential mechanisms of adenosine- and ATPgammaS-induced microvascular endothelial barrier strengthening. *J Cell Physiol,* 234**,** 5863-5879.

BAUMAN, A. L., SOUGHAYER, J., NGUYEN, B. T., WILLOUGHBY, D., CARNEGIE, G. K., WONG, W., HOSHI, N., LANGEBERG, L. K., COOPER, D. M., DESSAUER, C. W. & SCOTT, J. D. 2006. Dynamic regulation of cAMP synthesis through anchored PKA-adenylyl cyclase V/VI complexes. *Mol Cell,* 23**,** 925-31.

BAYS, J. L. & DEMALI, K. A. 2017. Vinculin in cell-cell and cell-matrix adhesions. *Cell Mol Life Sci,* 74**,** 2999-3009.

BEAVO, J. A., BECHTEL, P. J. & KREBS, E. G. 1974. Preparation of homogeneous cyclic AMP-dependent protein kinase(s) and its subunits from rabbit skeletal muscle. *Methods Enzymol,* 38**,** 299-308.

BEEBE, S. J., OYEN, O., SANDBERG, M., FROYSA, A., HANSSON, V. & JAHNSEN, T. 1990. Molecular cloning of a tissue-specific protein kinase (C gamma) from

human testis--representing a third isoform for the catalytic subunit of cAMP-dependent protein kinase. *Mol Endocrinol,* 4**,** 465-75.

BELENGUER, P. & PELLEGRINI, L. 2013. The dynamin GTPase OPA1: more than mitochondria? *Biochim Biophys Acta,* 1833**,** 176-83.

BENZ, P. M., DING, Y., STINGL, H., LOOT, A. E., ZINK, J., WITTIG, I., POPP, R. & FLEMING, I. 2020. AKAP12 deficiency impairs VEGF-induced endothelial cell migration and sprouting. *Acta Physiol (Oxf),* 228**,** e13325.

BERG, J. S., POWELL, B. C. & CHENEY, R. E. 2001. A millennial myosin census. *Mol Biol Cell,* 12**,** 780-94.

BERGGÅRD, T., LINSE, S. & JAMES, P. 2007. Methods for the detection and analysis of protein–protein interactions. *PROTEOMICS,* 7**,** 2833-2842.

BERRERA, M., DODONI, G., MONTERISI, S., PERTEGATO, V., ZAMPARO, I. & ZACCOLO, M. 2008. A toolkit for real-time detection of cAMP: insights into compartmentalized signaling. *Handb Exp Pharmacol***,** 285-98.

BIELING, P., HANSEN, S. D., AKIN, O., LI, T. D., HAYDEN, C. C., FLETCHER, D. A. & MULLINS, R. D. 2018. WH2 and proline-rich domains of WASP-family proteins collaborate to accelerate actin filament elongation. *EMBO J,* 37**,** 102-121.

BIERHANSL, L., CONRADI, L. C., TREPS, L., DEWERCHIN, M. & CARMELIET, P. 2017. Central Role of Metabolism in Endothelial Cell Function and Vascular Disease. *Physiology (Bethesda),* 32**,** 126-140.

BIRD, J. E., TAKAGI, Y., BILLINGTON, N., STRUB, M. P., SELLERS, J. R. & FRIEDMAN, T. B. 2014. Chaperone-enhanced purification of unconventional myosin 15, a molecular motor specialized for stereocilia protein trafficking. *Proc Natl Acad Sci U S A,* 111**,** 12390-5.

BLOEMINK, M. J. & GEEVES, M. A. 2011. Shaking the myosin family tree: biochemical kinetics defines four types of myosin motor. *Semin Cell Dev Biol,* 22**,** 961-7.

BOERMA, M., BURTON, G. R., WANG, J., FINK, L. M., MCGEHEE, R. E., JR. & HAUER-JENSEN, M. 2006. Comparative expression profiling in primary and immortalized endothelial cells: changes in gene expression in response to hydroxy methylglutaryl-coenzyme A reductase inhibition. *Blood Coagul Fibrinolysis,* 17**,** 173-80.

BOLTE, S. & CORDELIERES, F. P. 2006. A guided tour into subcellular colocalization analysis in light microscopy. *J Microsc,* 224**,** 213-32.

BORNSCHLOGL, T. 2013. How filopodia pull: what we know about the mechanics and dynamics of filopodia. *Cytoskeleton (Hoboken),* 70**,** 590-603.

BOSSIS, I. & STRATAKIS, C. A. 2004. Minireview: PRKAR1A: normal and abnormal functions. *Endocrinology,* 145**,** 5452-8.

BRANDON, E. P., LOGUE, S. F., ADAMS, M. R., QI, M., SULLIVAN, S. P., MATSUMOTO, A. M., DORSA, D. M., WEHNER, J. M., MCKNIGHT, G. S. & IDZERDA, R. L. 1998. Defective motor behavior and neural gene expression in RIIbeta-protein kinase A mutant mice. *J Neurosci,* 18**,** 3639-49.

BRITO, C. & SOUSA, S. 2020. Non-Muscle Myosin 2A (NM2A): Structure, Regulation and Function. *Cells,* 9.

BROWN, K. M., DAY, J. P., HUSTON, E., ZIMMERMANN, B., HAMPEL, K., CHRISTIAN, F., ROMANO, D., TERHZAZ, S., LEE, L. C., WILLIS, M. J., MORTON, D. B., BEAVO, J. A., SHIMIZU-ALBERGINE, M., DAVIES, S. A., KOLCH, W., HOUSLAY, M. D. & BAILLIE, G. S. 2013. Phosphodiesterase-8A binds to and regulates Raf-1 kinase. *Proc Natl Acad Sci U S A,* 110**,** E1533-42.

BUCKO, P. J. & SCOTT, J. D. 2021. Drugs That Regulate Local Cell Signaling: AKAP Targeting as a Therapeutic Option. *Annu Rev Pharmacol Toxicol,* 61**,** 361-379.

BUSS, F., KENDRICK-JONES, J., LIONNE, C., KNIGHT, A. E., COTE, G. P. & PAUL LUZIO, J. 1998. The localization of myosin VI at the golgi complex and leading edge of fibroblasts and its phosphorylation and recruitment into membrane ruffles of A431 cells after growth factor stimulation. *J Cell Biol,* 143**,** 1535-45.

BUTLER, T., PAUL, J., EUROPE-FINNER, N., SMITH, R. & CHAN, E. C. 2013. Role of serine-threonine phosphoprotein phosphatases in smooth muscle contractility. *Am J Physiol Cell Physiol,* 304**,** C485-504.

BUXTON, I. L. & BRUNTON, L. L. 1983. Compartments of cyclic AMP and protein kinase in mammalian cardiomyocytes. *J Biol Chem,* 258**,** 10233-9.

BYRNE, K. M., MONSEFI, N., DAWSON, J. C., DEGASPERI, A., BUKOWSKI-WILLS, J. C., VOLINSKY, N., DOBRZYNSKI, M., BIRTWISTLE, M. R., TSYGANOV, M. A.,

KIYATKIN, A., KIDA, K., FINCH, A. J., CARRAGHER, N. O., KOLCH, W., NGUYEN, L. K., VON KRIEGSHEIM, A. & KHOLODENKO, B. N. 2016. Bistability in the Rac1, PAK, and RhoA Signaling Network Drives Actin Cytoskeleton Dynamics and Cell Motility Switches. *Cell Syst,* 2**,** 38-48.

CADD, G. & MCKNIGHT, G. S. 1989. Distinct patterns of cAMP-dependent protein kinase gene expression in mouse brain. *Neuron,* 3**,** 71-79.

CAMERON, R. S., LIU, C. & PIHKALA, J. P. 2013. Myosin 16 levels fluctuate during the cell cycle and are downregulated in response to DNA replication stress. *Cytoskeleton (Hoboken),* 70**,** 328-48.

CANIUGUIR, A., KRAUSE, B. J., HERNANDEZ, C., UAUY, R. & CASANELLO, P. 2016. Markers of early endothelial dysfunction in intrauterine growth restriction-derived human umbilical vein endothelial cells revealed by 2D-DIGE and mass spectrometry analyses. *Placenta,* 41**,** 14-26.

CAO, W., MATTAGAJASINGH, S. N., XU, H., KIM, K., FIERLBECK, W., DENG, J., LOWENSTEIN, C. J. & BALLERMANN, B. J. 2002. TIMAP, a novel CAAX box protein regulated by TGF-beta1 and expressed in endothelial cells. *Am J Physiol Cell Physiol,* 283**,** C327-37.

CAPETANAKI, Y., BLOCH, R. J., KOULOUMENTA, A., MAVROIDIS, M. & PSARRAS, S. 2007. Muscle intermediate filaments and their links to membranes and membranous organelles. *Exp Cell Res,* 313**,** 2063-76.

CARLSON, C. R., RUPPELT, A. & TASKEN, K. 2003. A kinase anchoring protein (AKAP) interaction and dimerization of the RIalpha and RIbeta regulatory subunits of protein kinase a in vivo by the yeast two hybrid system. *J Mol Biol,* 327**,** 609-18.

CARMELIET, P., LAMPUGNANI, M. G., MOONS, L., BREVIARIO, F., COMPERNOLLE, V., BONO, F., BALCONI, G., SPAGNUOLO, R., OOSTHUYSE, B., DEWERCHIN, M., ZANETTI, A., ANGELLILO, A., MATTOT, V., NUYENS, D., LUTGENS, E., CLOTMAN, F., DE RUITER, M. C., GITTENBERGER-DE GROOT, A., POELMANN, R., LUPU, F., HERBERT, J. M., COLLEN, D. & DEJANA, E. 1999. Targeted deficiency or cytosolic truncation of the VE-cadherin gene in mice impairs VEGF-mediated endothelial survival and angiogenesis. *Cell,* 98**,** 147-57.

CARNEGIE, G. K., MEANS, C. K. & SCOTT, J. D. 2009. A-kinase anchoring proteins: from protein complexes to physiology and disease. *IUBMB Life,* 61**,** 394-406.

CARVALHO, R. L., JONKER, L., GOUMANS, M. J., LARSSON, J., BOUWMAN, P., KARLSSON, S., DIJKE, P. T., ARTHUR, H. M. & MUMMERY, C. L. 2004. Defective paracrine signalling by TGFbeta in yolk sac vasculature of endoglin mutant mice: a paradigm for hereditary haemorrhagic telangiectasia. *Development,* 131**,** 6237-47.

CEULEMANS, H., STALMANS, W. & BOLLEN, M. 2002. Regulator-driven functional diversification of protein phosphatase-1 in eukaryotic evolution. *Bioessays,* 24**,** 371-81.

CHANG, L. & GOLDMAN, R. D. 2004. Intermediate filaments mediate cytoskeletal crosstalk. *Nat Rev Mol Cell Biol,* 5**,** 601-13.

CHARRAS, G. & PALUCH, E. 2008. Blebs lead the way: how to migrate without lamellipodia. *Nat Rev Mol Cell Biol,* 9**,** 730-6.

CHARRAS, G. T., YARROW, J. C., HORTON, M. A., MAHADEVAN, L. & MITCHISON, T. J. 2005. Non-equilibration of hydrostatic pressure in blebbing cells. *Nature,* 435**,** 365-9.

CHATURVEDI, D., POPPLETON, H. M., STRINGFIELD, T., BARBIER, A. & PATEL, T. B. 2006. Subcellular localization and biological actions of activated RSK1 are determined by its interactions with subunits of cyclic AMP-dependent protein kinase. *Mol Cell Biol,* 26**,** 4586-600.

CHEN, C. S., ALONSO, J. L., OSTUNI, E., WHITESIDES, G. M. & INGBER, D. E. 2003. Cell shape provides global control of focal adhesion assembly. *Biochem Biophys Res Commun,* 307**,** 355-61.

CHEN, Y. Q., ZHANG, L., LV, X. Y. & WANG, H. Z. 2016. Lack of Association between MYO9B Gene Polymorphisms and Susceptibility to Coeliac Disease in Caucasians: Evidence from a Meta-Analysis. *Immunol Invest,* 45**,** 396-405.

CHENG, F. & ERIKSSON, J. E. 2017. Intermediate Filaments and the Regulation of Cell Motility during Regeneration and Wound Healing. *Cold Spring Harb Perspect Biol,* 9.

CHING, G. Y. & LIEM, R. K. 1998. Roles of head and tail domains in alpha-internexin's self-assembly and coassembly with the neurofilament triplet proteins. *J Cell Sci,* 111 (Pt 3), 321-33.

CHO-CHUNG, Y. S., PEPE, S., CLAIR, T., BUDILLON, A. & NESTEROVA, M. 1995. cAMP-dependent protein kinase: role in normal and malignant growth. *Crit Rev Oncol Hematol,* 21, 33-61.

CHOPRA, H., HUNG, M. K., KWONG, D. L., ZHANG, C. F. & POW, E. H. N. 2018. Insights into Endothelial Progenitor Cells: Origin, Classification, Potentials, and Prospects. *Stem Cells Int,* 2018, 9847015.

CHRZANOWSKA-WODNICKA, M. & BURRIDGE, K. 1996. Rho-stimulated contractility drives the formation of stress fibers and focal adhesions. *J Cell Biol,* 133, 1403-15.

CLEGG, C. H., CADD, G. G. & MCKNIGHT, G. S. 1988. Genetic characterization of a brain-specific form of the type I regulatory subunit of cAMP-dependent protein kinase. *Proc Natl Acad Sci U S A,* 85, 3703-3707.

COLE, W. C. & WELSH, D. G. 2011. Role of myosin light chain kinase and myosin light chain phosphatase in the resistance arterial myogenic response to intravascular pressure. *Arch Biochem Biophys,* 510, 160-173.

COLLINS, M. O. & CHOUDHARY, J. S. 2008. Mapping multiprotein complexes by affinity purification and mass spectrometry. *Curr Opin Biotechnol,* 19, 324-30.

COLSON, B. A., PATEL, J. R., CHEN, P. P., BEKYAROVA, T., ABDALLA, M. I., TONG, C. W., FITZSIMONS, D. P., IRVING, T. C. & MOSS, R. L. 2012. Myosin binding protein-C phosphorylation is the principal mediator of protein kinase A effects on thick filament structure in myocardium. *J Mol Cell Cardiol,* 53, 609-16.

COLUCCIO, L. M. 2018. Structure and Function of Mammalian Class I Myosins. *In:* BROADBENT, D. (ed.) *Myosin: Biosynthesis, Classes and Function.* Hauppauge, NY, USA: Nova Science.

COLUCCIO, L. M. 2020. Myosins and Disease. *In:* COLUCCIO, L. M. (ed.) *Myosins: A Superfamily of Molecular Motors.* Cham: Springer International Publishing.

CONSORTIUM, G. T. 2013. The Genotype-Tissue Expression (GTEx) project. *Nat Genet,* 45**,** 580-5.

CONTI, M. A., KAWAMOTO, S. & ADELSTEIN, R. S. 2008. Non-Muscle Myosin II. *In:* COLUCCIO, L. M. (ed.) *Myosins: A Superfamily of Molecular Motors*. Dordrecht: Springer Netherlands.

CORBIN, J. D., SUGDEN, P. H., WEST, L., FLOCKHART, D. A., LINCOLN, T. M. & MCCARTHY, D. 1978. Studies on the properties and mode of action of the purified regulatory subunit of bovine heart adenosine 3':5'-monophosphate-dependent protein kinase. *J Biol Chem,* 253**,** 3997-4003.

DAGDA, R. K. & DAS BANERJEE, T. 2015. Role of protein kinase A in regulating mitochondrial function and neuronal development: implications to neurodegenerative diseases. *Rev Neurosci,* 26**,** 359-70.

DECHAT, T., PFLEGHAAR, K., SENGUPTA, K., SHIMI, T., SHUMAKER, D. K., SOLIMANDO, L. & GOLDMAN, R. D. 2008. Nuclear lamins: major factors in the structural organization and function of the nucleus and chromatin. *Genes Dev,* 22**,** 832-53.

DELL'ACQUA, M. L., DODGE, K. L., TAVALIN, S. J. & SCOTT, J. D. 2002. Mapping the protein phosphatase-2B anchoring site on AKAP79. Binding and inhibition of phosphatase activity are mediated by residues 315-360. *J Biol Chem,* 277**,** 48796-802.

DELL'ACQUA, M. L., FAUX, M. C., THORBURN, J., THORBURN, A. & SCOTT, J. D. 1998. Membrane-targeting sequences on AKAP79 bind phosphatidylinositol-4, 5-bisphosphate. *EMBO J,* 17**,** 2246-60.

DELMAR, M. & MCKENNA, W. J. 2010. The cardiac desmosome and arrhythmogenic cardiomyopathies: from gene to disease. *Circ Res,* 107**,** 700-14.

DEMA, A., PERETS, E., SCHULZ, M. S., DEAK, V. A. & KLUSSMANN, E. 2015. Pharmacological targeting of AKAP-directed compartmentalized cAMP signalling. *Cell Signal,* 27**,** 2474-87.

DEMA, A., SCHROTER, M. F., PERETS, E., SKROBLIN, P., MOUTTY, M. C., DEAK, V. A., BIRCHMEIER, W. & KLUSSMANN, E. 2016. The A-Kinase Anchoring Protein (AKAP) Glycogen Synthase Kinase 3beta Interaction Protein (GSKIP) Regulates

beta-Catenin through Its Interactions with Both Protein Kinase A (PKA) and GSK3beta. *J Biol Chem,* 291**,** 19618-30.

DENG, J. T., SUTHERLAND, C., BRAUTIGAN, D. L., ETO, M. & WALSH, M. P. 2002. Phosphorylation of the myosin phosphatase inhibitors, CPI-17 and PHI-1, by integrin-linked kinase. *Biochem J,* 367**,** 517-24.

DESSAUER, C. W. 2009. Adenylyl cyclase--A-kinase anchoring protein complexes: the next dimension in cAMP signaling. *Mol Pharmacol,* 76**,** 935-41.

DI BENEDETTO, G., ZOCCARATO, A., LISSANDRON, V., TERRIN, A., LI, X., HOUSLAY, M. D., BAILLIE, G. S. & ZACCOLO, M. 2008. Protein kinase A type I and type II define distinct intracellular signaling compartments. *Circ Res,* 103**,** 836-44.

DILLS, W. L., JR., BEAVO, J. A., BECHTEL, P. J. & KREBS, E. G. 1975. Purification of rabbit skeletal muscle protein kinase regulatory subunit using cyclic adenosine-3':5'-monophosphate affinity chromatography. *Biochem Biophys Res Commun,* 62**,** 70-7.

DIPPOLD, R. P. & FISHER, S. A. 2014a. A bioinformatic and computational study of myosin phosphatase subunit diversity. *Am J Physiol Regul Integr Comp Physiol,* 307**,** R256-70.

DIPPOLD, R. P. & FISHER, S. A. 2014b. Myosin Phosphatase Isoforms as Determinants of Smooth Muscle Contractile Function and Calcium Sensitivity of Force Production. *Microcirculation,* 21**,** 239-248.

DIRKSEN, W. P., VLADIC, F. & FISHER, S. A. 2000. A myosin phosphatase targeting subunit isoform transition defines a smooth muscle developmental phenotypic switch. *Am J Physiol Cell Physiol,* 278**,** C589-600.

DIVIANI, D., ABUIN, L., COTECCHIA, S. & PANSIER, L. 2004. Anchoring of both PKA and 14-3-3 inhibits the Rho-GEF activity of the AKAP-Lbc signaling complex. *EMBO J,* 23**,** 2811-20.

DIVIANI, D., LANGEBERG, L. K., DOXSEY, S. J. & SCOTT, J. D. 2000. Pericentrin anchors protein kinase A at the centrosome through a newly identified RII-binding domain. *Curr Biol,* 10**,** 417-20.

DIVITO, M. M. & CHENEY, R. E. 2008. Myosin X. *In:* COLUCCIO, L. M. (ed.) *Myosins: A Superfamily of Molecular Motors.* Dordrecht: Springer Netherlands.

DIZ-MUÑOZ, A., KRIEG, M., BERGERT, M., IBARLUCEA-BENITEZ, I., MULLER, D. J., PALUCH, E. & HEISENBERG, C.-P. 2010. Control of directed cell migration in vivo by membrane-to-cortex attachment. *PLoS biology,* 8**,** e1000544.

DORDEA, A. C., SWEENEY, M., TAGGART, J., LARTEY, J., WESSEL, H., ROBSON, S. C. & TAGGART, M. J. 2013. Differential vasodilation of human placental and myometrial arteries related to myofilament Ca(2+)-desensitization and the expression of Hsp20 but not MYPT1. *Mol Hum Reprod,* 19**,** 727-36.

DOSE, A. C., HILLMAN, D. W., WONG, C., SOHLBERG, L., LIN-JONES, J. & BURNSIDE, B. 2003. Myo3A, one of two class III myosin genes expressed in vertebrate retina, is localized to the calycal processes of rod and cone photoreceptors and is expressed in the sacculus. *Mol Biol Cell,* 14**,** 1058-73.

DURBEEJ, M. 2010. Laminins. *Cell and Tissue Research,* 339**,** 259-268.

DUWÉ, S. & DEDECKER, P. 2019. Optimizing the fluorescent protein toolbox and its use. *Curr Opin Biotechnol,* 58**,** 183-191.

EDDINGER, T. J. & MEER, D. P. 2007. Myosin II isoforms in smooth muscle: heterogeneity and function. *Am J Physiol Cell Physiol,* 293**,** C493-508.

ERLICHMAN, J., HIRSCH, A. H. & ROSEN, O. M. 1971. Interconversion of cyclic nucleotide-activated and cyclic nucleotide-independent forms of a protein kinase from beef heart. *Proc Natl Acad Sci U S A,* 68**,** 731-5.

ETO, M., KIRKBRIDE, J. A. & BRAUTIGAN, D. L. 2005. Assembly of MYPT1 with protein phosphatase-1 in fibroblasts redirects localization and reorganizes the actin cytoskeleton. *Cell Motil Cytoskeleton,* 62**,** 100-9.

ETO, M. & KITAZAWA, T. 2017. Diversity and plasticity in signaling pathways that regulate smooth muscle responsiveness: Paradigms and paradoxes for the myosin phosphatase, the master regulator of smooth muscle contraction. *J Smooth Muscle Res,* 53**,** 1-19.

FAGHIHI, M. A., MODARRESI, F., KHALIL, A. M., WOOD, D. E., SAHAGAN, B. G., MORGAN, T. E., FINCH, C. E., ST LAURENT, G., 3RD, KENNY, P. J. & WAHLESTEDT, C. 2008. Expression of a noncoding RNA is elevated in Alzheimer's disease and drives rapid feed-forward regulation of beta-secretase. *Nat Med,* 14**,** 723-30.

FANG, Q., INDZHYKULIAN, A. A., MUSTAPHA, M., RIORDAN, G. P., DOLAN, D. F., FRIEDMAN, T. B., BELYANTSEVA, I. A., FROLENKOV, G. I., CAMPER, S. A. & BIRD, J. E. 2015. The 133-kDa N-terminal domain enables myosin 15 to maintain mechanotransducing stereocilia and is essential for hearing. *Elife,* 4.

FELICIELLO, A., GOTTESMAN, M. E. & AVVEDIMENTO, E. V. 2001. The biological functions of A-kinase anchor proteins. *Journal of Molecular Biology,* 308**,** 99-114.

FIELDS, S. & SONG, O.-K. 1989. A novel genetic system to detect protein–protein interactions. *Nature,* 340**,** 245-246.

FISCHER, R. S., LAM, P. Y., HUTTENLOCHER, A. & WATERMAN, C. M. 2019. Filopodia and focal adhesions: An integrated system driving branching morphogenesis in neuronal pathfinding and angiogenesis. *Dev Biol,* 451**,** 86-95.

FOTH, B. J., GOEDECKE, M. C. & SOLDATI, D. 2006. New insights into myosin evolution and classification. *Proc Natl Acad Sci U S A,* 103**,** 3681-6.

FRANCIS, S. H., HOUSLAY, M. D. & CONTI, M. 2011. Phosphodiesterase Inhibitors: Factors That Influence Potency, Selectivity, and Action. *In:* FRANCIS, S. H., CONTI, M. & HOUSLAY, M. D. (eds.) *Phosphodiesterases as Drug Targets.* Berlin, Heidelberg: Springer Berlin Heidelberg.

FRANK, R. 1992. Spot-synthesis: an easy technique for the positionally addressable, parallel chemical synthesis on a membrane support. *Tetrahedron,* 48**,** 9217-9232.

FRANTZ, C., STEWART, K. M. & WEAVER, V. M. 2010. The extracellular matrix at a glance. *J Cell Sci,* 123**,** 4195-200.

FREDRIKSSON, S., GULLBERG, M., JARVIUS, J., OLSSON, C., PIETRAS, K., GUSTAFSDOTTIR, S. M., OSTMAN, A. & LANDEGREN, U. 2002. Protein detection using proximity-dependent DNA ligation assays. *Nat Biotechnol,* 20**,** 473-7.

FREZZA, C., CIPOLAT, S., MARTINS DE BRITO, O., MICARONI, M., BEZNOUSSENKO, G. V., RUDKA, T., BARTOLI, D., POLISHUCK, R. S., DANIAL, N. N., DE STROOPER, B. & SCORRANO, L. 2006. OPA1 controls apoptotic cristae remodeling independently from mitochondrial fusion. *Cell,* 126**,** 177-89.

FRUGTNIET, B., JIANG, W. G. & MARTIN, T. A. 2015. Role of the WASP and WAVE family proteins in breast cancer invasion and metastasis. *Breast Cancer (Dove Med Press),* 7**,** 99-109.

FU, H. W. & CASEY, P. J. 1999. Enzymology and biology of CaaX protein prenylation. *Recent Prog Horm Res,* 54**,** 315-42; discussion 342-3.

FUJIOKA, M., TAKAHASHI, N., ODAI, H., ARAKI, S., ICHIKAWA, K., FENG, J., NAKAMURA, M., KAIBUCHI, K., HARTSHORNE, D. J., NAKANO, T. & ITO, M. 1998. A new isoform of human myosin phosphatase targeting/regulatory subunit (MYPT2): cDNA cloning, tissue expression, and chromosomal mapping. *Genomics,* 49**,** 59-68.

GABROVSEK, L., BUCKO, P., CARNEGIE, G. K. & SCOTT, J. D. 2018. A-Kinase Anchoring Protein (AKAP). *In:* CHOI, S. (ed.) *Encyclopedia of Signaling Molecules*. Cham: Springer International Publishing.

GAILLY, P., WU, X., HAYSTEAD, T. A., SOMLYO, A. P., COHEN, P. T., COHEN, P. & SOMLYO, A. V. 1996. Regions of the 110-kDa regulatory subunit M110 required for regulation of myosin-light-chain-phosphatase activity in smooth muscle. *Eur J Biochem,* 239**,** 326-32.

GAO, Y. 2022. Architecture of the Blood Vessels. *In:* GAO, Y. (ed.) *Biology of Vascular Smooth Muscle: Vasoconstriction and Dilatation*. Singapore: Springer Nature Singapore.

GARROD, D. & CHIDGEY, M. 2008. Desmosome structure, composition and function. *Biochim Biophys Acta,* 1778**,** 572-87.

GAUTIER, R., DOUGUET, D., ANTONNY, B. & DRIN, G. 2008. HELIQUEST: a web server to screen sequences with specific alpha-helical properties. *Bioinformatics,* 24**,** 2101-2.

GAUTREAU, A. M., FREGOSO, F. E., SIMANOV, G. & DOMINGUEZ, R. 2022. Nucleation, stabilization, and disassembly of branched actin networks. *Trends Cell Biol,* 32**,** 421-432.

GEORGIOU, G. & VALAX, P. 1996. Expression of correctly folded proteins in Escherichia coli. *Curr Opin Biotechnol,* 7**,** 190-7.

GESELLCHEN, F., STANGHERLIN, A., SURDO, N., TERRIN, A., ZOCCARATO, A. & ZACCOLO, M. 2011. Measuring spatiotemporal dynamics of cyclic AMP signaling in real-time using FRET-based biosensors. *Methods Mol Biol,* 746**,** 297-316.

GIBBS, C. S., KNIGHTON, D. R., SOWADSKI, J. M., TAYLOR, S. S. & ZOLLER, M. J. 1992. Systematic mutational analysis of cAMP-dependent protein kinase identifies unregulated catalytic subunits and defines regions important for the recognition of the regulatory subunit. *J Biol Chem,* 267**,** 4806-14.

GOLD, M. G. 2019. Swimming regulations for protein kinase A catalytic subunit. *Biochem Soc Trans,* 47**,** 1355-1366.

GOLD, M. G., LYGREN, B., DOKURNO, P., HOSHI, N., MCCONNACHIE, G., TASKEN, K., CARLSON, C. R., SCOTT, J. D. & BARFORD, D. 2006. Molecular basis of AKAP specificity for PKA regulatory subunits. *Mol Cell,* 24**,** 383-95.

GORELIK, R., YANG, C., KAMESWARAN, V., DOMINGUEZ, R. & SVITKINA, T. 2011. Mechanisms of plasma membrane targeting of formin mDia2 through its amino terminal domains. *Mol Biol Cell,* 22**,** 189-201.

GORY-FAURE, S., PRANDINI, M. H., POINTU, H., ROULLOT, V., PIGNOT-PAINTRAND, I., VERNET, M. & HUBER, P. 1999. Role of vascular endothelial-cadherin in vascular morphogenesis. *Development,* 126**,** 2093-102.

GRASSIE, M. E., MOFFAT, L. D., WALSH, M. P. & MACDONALD, J. A. 2011. The myosin phosphatase targeting protein (MYPT) family: a regulated mechanism for achieving substrate specificity of the catalytic subunit of protein phosphatase type 1delta. *Arch Biochem Biophys,* 510**,** 147-59.

GRASSIE, M. E., SUTHERLAND, C., ULKE-LEMÉE, A., CHAPPELLAZ, M., KISS, E., WALSH, M. P. & MACDONALD, J. A. 2012. Cross-talk between Rho-associated Kinase and Cyclic Nucleotide-dependent Kinase Signaling Pathways in the Regulation of Smooth Muscle Myosin Light Chain Phosphatase*. *Journal of Biological Chemistry,* 287**,** 36356-36369.

GRUENBAUM, Y., MARGALIT, A., GOLDMAN, R. D., SHUMAKER, D. K. & WILSON, K. L. 2005. The nuclear lamina comes of age. *Nat Rev Mol Cell Biol,* 6**,** 21-31.

GUMBINER, B. M. 2005. Regulation of cadherin-mediated adhesion in morphogenesis. *Nat Rev Mol Cell Biol,* 6**,** 622-34.

GUTHRIE, C. R., SKALHEGG, B. S. & MCKNIGHT, G. S. 1997. Two novel brain-specific splice variants of the murine Cbeta gene of cAMP-dependent protein kinase. *J Biol Chem,* 272**,** 29560-5.

HALL, A. & LALLI, G. 2010. Rho and Ras GTPases in axon growth, guidance, and branching. *Cold Spring Harb Perspect Biol,* 2**,** a001818.

HANLEY, P. J., XU, Y., KRONLAGE, M., GROBE, K., SCHON, P., SONG, J., SOROKIN, L., SCHWAB, A. & BAHLER, M. 2010. Motorized RhoGAP myosin IXb (Myo9b) controls cell shape and motility. *Proc Natl Acad Sci U S A,* 107**,** 12145-50.

HARTSHORNE, D. J. 1989. Biochemistry of the contractile process in smooth muscle. *Physiology of the gastrointestinal tract***,** 423-482.

HARTSHORNE, D. J., ITO, M. & ERDODI, F. 1998. Myosin light chain phosphatase: subunit composition, interactions and regulation. *J Muscle Res Cell Motil,* 19**,** 325-41.

HARTSHORNE, D. J., ITO, M. & ERDODI, F. 2004. Role of protein phosphatase type 1 in contractile functions: myosin phosphatase. *J Biol Chem,* 279**,** 37211-4.

HASSON, T., HEINTZELMAN, M. B., SANTOS-SACCHI, J., COREY, D. P. & MOOSEKER, M. S. 1995. Expression in cochlea and retina of myosin VIIa, the gene product defective in Usher syndrome type 1B. *Proc Natl Acad Sci U S A,* 92**,** 9815-9.

HAYES, J. S., BRUNTON, L. L., BROWN, J. H., REESE, J. B. & MAYER, S. E. 1979. Hormonally specific expression of cardiac protein kinase activity. *Proc Natl Acad Sci U S A,* 76**,** 1570-4.

HAYES, J. S., BRUNTON, L. L. & MAYER, S. E. 1980. Selective activation of particulate cAMP-dependent protein kinase by isoproterenol and prostaglandin E1. *J Biol Chem,* 255**,** 5113-9.

HEASMAN, S. J. & RIDLEY, A. J. 2008. Mammalian Rho GTPases: new insights into their functions from in vivo studies. *Nat Rev Mol Cell Biol,* 9**,** 690-701.

HEGAZY, M., COHEN-BARAK, E., KOETSIER, J. L., NAJOR, N. A., ARVANITIS, C., SPRECHER, E., GREEN, K. J. & GODSEL, L. M. 2020. Proximity Ligation Assay for Detecting Protein-Protein Interactions and Protein Modifications in Cells and Tissues in Situ. *Curr Protoc Cell Biol,* 89**,** e115.

HERMANN, J. S., SKROBLIN, P., BERTINETTI, D., HANOLD, L. E., VON DER HEIDE, E. K., WAGENER, E. M., ZENN, H. M., KLUSSMANN, E., KENNEDY, E. J. & HERBERG, F. W. 2015. Neurochondrin is an atypical RIIalpha-specific A-kinase anchoring protein. *Biochim Biophys Acta,* 1854**,** 1667-75.

HERRMANN, H. & AEBI, U. 2016. Intermediate Filaments: Structure and Assembly. *Cold Spring Harb Perspect Biol,* 8.

HIRANO, K., PHAN, B. C. & HARTSHORNE, D. J. 1997. Interactions of the subunits of smooth muscle myosin phosphatase. *J Biol Chem,* 272**,** 3683-8.

HIRANO, M., NIIRO, N., HIRANO, K., NISHIMURA, J., HARTSHORNE, D. J. & KANAIDE, H. 1999. Expression, subcellular localization, and cloning of the 130-kDa regulatory subunit of myosin phosphatase in porcine aortic endothelial cells. *Biochem Biophys Res Commun,* 254**,** 490-6.

HIRSCHI, K. K., BURT, J. M., HIRSCHI, K. D. & DAI, C. 2003. Gap junction communication mediates transforming growth factor-beta activation and endothelial-induced mural cell differentiation. *Circ Res,* 93**,** 429-37.

HOFMANN, F., BEAVO, J. A., BECHTEL, P. J. & KREBS, E. G. 1975. Comparison of adenosine 3':5'-monophosphate-dependent protein kinases from rabbit skeletal and bovine heart muscle. *J Biol Chem,* 250**,** 7795-801.

HOKANSON, D. E., LAAKSO, J. M., LIN, T., SEPT, D. & OSTAP, E. M. 2006. Myo1c binds phosphoinositides through a putative pleckstrin homology domain. *Mol Biol Cell,* 17**,** 4856-65.

HOLMES, K. C. 2008. Myosin Structure. *In:* COLUCCIO, L. M. (ed.) *Myosins: A Superfamily of Molecular Motors.* Dordrecht: Springer Netherlands.

HTET, M., URSITTI, J. A., CHEN, L. & FISHER, S. A. 2021. Editing of the myosin phosphatase regulatory subunit suppresses angiotensin II induced hypertension via sensitization to nitric oxide mediated vasodilation. *Pflugers Arch,* 473**,** 611-622.

HU, C. D., CHINENOV, Y. & KERPPOLA, T. K. 2002. Visualization of interactions among bZIP and Rel family proteins in living cells using bimolecular fluorescence complementation. *Mol Cell,* 9**,** 789-98.

HUDSON, C. A., HEESOM, K. J. & LOPEZ BERNAL, A. 2012. Phasic contractions of isolated human myometrium are associated with Rho-kinase (ROCK)-dependent phosphorylation of myosin phosphatase-targeting subunit (MYPT1). *Mol Hum Reprod,* 18**,** 265-79.

HULME, J. T., YAROV-YAROVOY, V., LIN, T. W., SCHEUER, T. & CATTERALL, W. A. 2006. Autoinhibitory control of the CaV1.2 channel by its proteolytically processed distal C-terminal domain. *J Physiol,* 576**,** 87-102.

HUXLEY, H. 1957. The double array of filaments in cross-striated muscle. *The Journal of Cell Biology,* 3**,** 631-648.

HYNES, R. O. 2002. Integrins: bidirectional, allosteric signaling machines. *Cell,* 110**,** 673-87.

HYNES, R. O. 2009. The extracellular matrix: not just pretty fibrils. *Science,* 326**,** 1216-9.

ICHIKAWA, K., ITO, M. & HARTSHORNE, D. J. 1996. Phosphorylation of the large subunit of myosin phosphatase and inhibition of phosphatase activity. *J Biol Chem,* 271**,** 4733-40.

ILOUZ, R., BUBIS, J., WU, J., YIM, Y. Y., DEAL, M. S., KORNEV, A. P., MA, Y., BLUMENTHAL, D. K. & TAYLOR, S. S. 2012. Localization and quaternary structure of the PKA RIbeta holoenzyme. *Proc Natl Acad Sci U S A,* 109**,** 12443-8.

INTENGAN, H. D. & SCHIFFRIN, E. L. 2001. Vascular remodeling in hypertension: roles of apoptosis, inflammation, and fibrosis. *Hypertension,* 38**,** 581-7.

IOZZO, R. V. & SCHAEFER, L. 2015. Proteoglycan form and function: A comprehensive nomenclature of proteoglycans. *Matrix Biol,* 42**,** 11-55.

ISENSEE, J., KAUFHOLZ, M., KNAPE, M. J., HASENAUER, J., HAMMERICH, H., GONCZAROWSKA-JORGE, H., ZAHEDI, R. P., SCHWEDE, F., HERBERG, F. W. & HUCHO, T. 2018. PKA-RII subunit phosphorylation precedes activation by cAMP and regulates activity termination. *J Cell Biol,* 217**,** 2167-2184.

ISEPPON, F., NAPOLITANO, L. M., TORRE, V. & COJOC, D. 2015. Cdc42 and RhoA reveal different spatio-temporal dynamics upon local stimulation with Semaphorin-3A. *Front Cell Neurosci,* 9**,** 333.

ISHIZAKI, T., MAEKAWA, M., FUJISAWA, K., OKAWA, K., IWAMATSU, A., FUJITA, A., WATANABE, N., SAITO, Y., KAKIZUKA, A., MORII, N. & NARUMIYA, S. 1996. The small GTP-binding protein Rho binds to and activates a 160 kDa Ser/Thr protein kinase homologous to myotonic dystrophy kinase. *EMBO J,* 15**,** 1885-93.

ISOGAI, T. & DANUSER, G. 2018. Discovery of functional interactions among actin regulators by analysis of image fluctuations in an unperturbed motile cell system. *Philos Trans R Soc Lond B Biol Sci,* 373.

ISOGAI, T., VAN DER KAMMEN, R., LEYTON-PUIG, D., KEDZIORA, K. M., JALINK, K. & INNOCENTI, M. 2015. Initiation of lamellipodia and ruffles involves cooperation between mDia1 and the Arp2/3 complex. *J Cell Sci,* 128**,** 3796-810.

ISONO, E. & SCHWECHHEIMER, C. 2010. Co-immunoprecipitation and Protein Blots. *In:* HENNIG, L. & KÖHLER, C. (eds.) *Plant Developmental Biology: Methods and Protocols*. Totowa, NJ: Humana Press.

ITO, M., FENG, J., TSUJINO, S., INAGAKI, N., INAGAKI, M., TANAKA, J., ICHIKAWA, K., HARTSHORNE, D. J. & NAKANO, T. 1997. Interaction of smooth muscle myosin phosphatase with phospholipids. *Biochemistry,* 36**,** 7607-14.

ITO, M., NAKANO, T., ERDODI, F. & HARTSHORNE, D. J. 2004. Myosin phosphatase: structure, regulation and function. *Mol Cell Biochem,* 259**,** 197-209.

JACQUEMET, G., HAMIDI, H. & IVASKA, J. 2015. Filopodia in cell adhesion, 3D migration and cancer cell invasion. *Curr Opin Cell Biol,* 36**,** 23-31.

JAFFE, E. A., HOYER, L. W. & NACHMAN, R. L. 1973a. Synthesis of antihemophilic factor antigen by cultured human endothelial cells. *J Clin Invest,* 52**,** 2757-64.

JAFFE, E. A., NACHMAN, R. L., BECKER, C. G. & MINICK, C. R. 1973b. Culture of human endothelial cells derived from umbilical veins. Identification by morphologic and immunologic criteria. *J Clin Invest,* 52**,** 2745-56.

JAHNSEN, T., HEDIN, L., KIDD, V., BEATTIE, W., LOHMANN, S., WALTER, U., DURICA, J., SCHULZ, T., SCHILTZ, E. & BROWNER, M. 1986. Molecular cloning, cDNA structure, and regulation of the regulatory subunit of type II cAMP-dependent

protein kinase from rat ovarian granulosa cells. *Journal of Biological Chemistry,* 261**,** 12352-12361.

JAMALI, M., ROGERSON, P. J., WILTON, S. & SKERJANC, I. S. 2001. Nkx2-5 activity is essential for cardiomyogenesis. *J Biol Chem,* 276**,** 42252-8.

JARVIUS, M., PAULSSON, J., WEIBRECHT, I., LEUCHOWIUS, K. J., ANDERSSON, A. C., WAHLBY, C., GULLBERG, M., BOTLING, J., SJOBLOM, T., MARKOVA, B., OSTMAN, A., LANDEGREN, U. & SODERBERG, O. 2007. In situ detection of phosphorylated platelet-derived growth factor receptor beta using a generalized proximity ligation method. *Mol Cell Proteomics,* 6**,** 1500-9.

JEGOU, A. & ROMET-LEMONNE, G. 2021. Mechanically tuning actin filaments to modulate the action of actin-binding proteins. *Curr Opin Cell Biol,* 68**,** 72-80.

JOHNSON, D., COHEN, P., CHEN, M. X., CHEN, Y. H. & COHEN, P. T. 1997. Identification of the regions on the M110 subunit of protein phosphatase 1M that interact with the M21 subunit and with myosin. *Eur J Biochem,* 244**,** 931-9.

JUANES-GARCÍA, A., LLORENTE-GONZÁLEZ, C. & VICENTE-MANZANARES, M. 2017. Nonmuscle Myosin II. *In:* CHOI, S. (ed.) *Encyclopedia of Signaling Molecules.* New York, NY: Springer New York.

KANEKO-KAWANO, T., TAKASU, F., NAOKI, H., SAKUMURA, Y., ISHII, S., UEBA, T., EIYAMA, A., OKADA, A., KAWANO, Y. & SUZUKI, K. 2012. Dynamic regulation of myosin light chain phosphorylation by Rho-kinase. *PLoS One,* 7**,** e39269.

KANG, R., TANG, D., YU, Y., WANG, Z., HU, T., WANG, H. & CAO, L. 2010. WAVE1 regulates Bcl-2 localization and phosphorylation in leukemia cells. *Leukemia,* 24**,** 177-86.

KELLER, R. 2002. Shaping the vertebrate body plan by polarized embryonic cell movements. *Science,* 298**,** 1950-4.

KENNELLY, P. J. & KREBS, E. G. 1991. Consensus sequences as substrate specificity determinants for protein kinases and protein phosphatases. *J Biol Chem,* 266**,** 15555-8.

KHALIL, J. S. 2018. *A novel interaction of the myosin light chain phosphatase with the regulatory subunits of protein kinase A in platelets.* Ph.D. Thesis.

KHASNIS, M., NAKATOMI, A., GUMPPER, K. & ETO, M. 2014. Reconstituted human myosin light chain phosphatase reveals distinct roles of two inhibitory phosphorylation sites of the regulatory subunit, MYPT1. *Biochemistry,* 53**,** 2701-9.

KHATRI, J. J., JOYCE, K. M., BROZOVICH, F. V. & FISHER, S. A. 2001. Role of myosin phosphatase isoforms in cGMP-mediated smooth muscle relaxation. *J Biol Chem,* 276**,** 37250-7.

KHROMOV, A., CHOUDHURY, N., STEVENSON, A. S., SOMLYO, A. V. & ETO, M. 2009. Phosphorylation-dependent autoinhibition of myosin light chain phosphatase accounts for Ca2+ sensitization force of smooth muscle contraction. *J Biol Chem,* 284**,** 21569-79.

KIM, K. M., CSORTOS, C., CZIKORA, I., FULTON, D., UMAPATHY, N. S., OLAH, G. & VERIN, A. D. 2012. Molecular characterization of myosin phosphatase in endothelium. *J Cell Physiol,* 227**,** 1701-8.

KIMURA, K., FUKATA, Y., MATSUOKA, Y., BENNETT, V., MATSUURA, Y., OKAWA, K., IWAMATSU, A. & KAIBUCHI, K. 1998. Regulation of the association of adducin with actin filaments by Rho-associated kinase (Rho-kinase) and myosin phosphatase. *J Biol Chem,* 273**,** 5542-8.

KIMURA, K., ITO, M., AMANO, M., CHIHARA, K., FUKATA, Y., NAKAFUKU, M., YAMAMORI, B., FENG, J., NAKANO, T., OKAWA, K., IWAMATSU, A. & KAIBUCHI, K. 1996. Regulation of Myosin Phosphatase by Rho and Rho-Associated Kinase (Rho-Kinase). *Science,* 273**,** 245-248.

KISS, A., ERDODI, F. & LONTAY, B. 2019. Myosin phosphatase: Unexpected functions of a long-known enzyme. *Biochim Biophys Acta Mol Cell Res,* 1866**,** 2-15.

KISS, A., LONTAY, B., BECSI, B., MARKASZ, L., OLAH, E., GERGELY, P. & ERDODI, F. 2008. Myosin phosphatase interacts with and dephosphorylates the retinoblastoma protein in THP-1 leukemic cells: its inhibition is involved in the attenuation of daunorubicin-induced cell death by calyculin-A. *Cell Signal,* 20**,** 2059-70.

KISS, E., MURÁNYI, A., CSORTOS, C., GERGELY, P., ITO, M., HARTSHORNE, D. J. & ERDÖDI, F. 2002. Integrin-linked kinase phosphorylates the myosin

phosphatase target subunit at the inhibitory site in platelet cytoskeleton. *Biochemical Journal,* 365**,** 79-87.

KITAZAWA, T., ETO, M., WOODSOME, T. P. & KHALEQUZZAMAN, M. 2003. Phosphorylation of the myosin phosphatase targeting subunit and CPI-17 during Ca2+ sensitization in rabbit smooth muscle. *J Physiol,* 546**,** 879-89.

KOCHEROVA, I., BRYJA, A., MOZDZIAK, P., ANGELOVA VOLPONI, A., DYSZKIEWICZ-KONWINSKA, M., PIOTROWSKA-KEMPISTY, H., ANTOSIK, P., BUKOWSKA, D., BRUSKA, M., IZYCKI, D., ZABEL, M., NOWICKI, M. & KEMPISTY, B. 2019. Human Umbilical Vein Endothelial Cells (HUVECs) Co-Culture with Osteogenic Cells: From Molecular Communication to Engineering Prevascularised Bone Grafts. *J Clin Med,* 8.

KOLOZSVARI, B., BAKO, E., BECSI, B., KISS, A., CZIKORA, A., TOTH, A., VAMOSI, G., GERGELY, P. & ERDODI, F. 2012. Calcineurin regulates endothelial barrier function by interaction with and dephosphorylation of myosin phosphatase. *Cardiovasc Res,* 96**,** 494-503.

KONDO, A., TOKUDA, H., KATO, K., MATSUSHIMA-NISHIWAKI, R., KUROYANAGI, G., MIZUTANI, J., KOZAWA, O. & OTSUKA, T. 2013. Rho-kinase negatively regulates thyroid hormone-stimulated osteocalcin synthesis in osteoblasts. *Biochimie,* 95**,** 719-24.

KONYA, Z., TAMAS, I., BECSI, B., LONTAY, B., RAICS, M., TIMARI, I., KOVER, K. E. & ERDODI, F. 2023. Phosphorylated Peptide Derived from the Myosin Phosphatase Target Subunit Is a Novel Inhibitor of Protein Phosphatase-1. *Int J Mol Sci,* 24.

KOOL, J., JONKER, N., IRTH, H. & NIESSEN, W. M. A. 2011. Studying protein–protein affinity and immobilized ligand–protein affinity interactions using MS-based methods. *Analytical and Bioanalytical Chemistry,* 401**,** 1109-1125.

KOTTKE, M. D., DELVA, E. & KOWALCZYK, A. P. 2006. The desmosome: cell science lessons from human diseases. *J Cell Sci,* 119**,** 797-806.

KOVACS-KASA, A., GORSHKOV, B. A., KIM, K. M., KUMAR, S., BLACK, S. M., FULTON, D. J., DIMITROPOULOU, C., CATRAVAS, J. D. & VERIN, A. D. 2016. The

protective role of MLCP-mediated ERM dephosphorylation in endotoxin-induced lung injury in vitro and in vivo. *Sci Rep,* 6**,** 39018.

KOVAR, D. R. & POLLARD, T. D. 2004. Insertional assembly of actin filament barbed ends in association with formins produces piconewton forces. *Proc Natl Acad Sci U S A,* 101**,** 14725-30.

KRAMER, A. & SCHNEIDER-MERGENER, J. 1998. Synthesis and Screening of Peptide Libraries on Continuous Cellulose Membrane Supports. *In:* CABILLY, S. (ed.) *Combinatorial Peptide Library Protocols*. Totowa, NJ: Humana Press.

KRISHNAMURTHY, S., MOORTHY, B. S., XIN XIANG, L., XIN SHAN, L., BHARATHAM, K., TULSIAN, N. K., MIHALEK, I. & ANAND, G. S. 2014. Active site coupling in PDE:PKA complexes promotes resetting of mammalian cAMP signaling. *Biophys J,* 107**,** 1426-40.

KRUGER, O., PLUM, A., KIM, J. S., WINTERHAGER, E., MAXEINER, S., HALLAS, G., KIRCHHOFF, S., TRAUB, O., LAMERS, W. H. & WILLECKE, K. 2000. Defective vascular development in connexin 45-deficient mice. *Development,* 127**,** 4179-93.

KÜHNE, W. 1864. *Untersuchungen über das Protoplasma und die Contractilität*, W. Engelmann.

KUMON, A., NISHIYAMA, K., YAMAMURA, H. & NISHIZUKA, Y. 1972. Multiplicity of adenosine 3',5'-monophosphate-dependent protein kinases from rat liver and mode of action of nucleoside 3',5'-monophosphate. *J Biol Chem,* 247**,** 3726-35.

KUROSU, T., HERNANDEZ, A. I., WOLK, J., LIU, J. & SCHWARTZ, J. H. 2009. Alpha/beta-tubulin are A kinase anchor proteins for type I PKA in neurons. *Brain Res,* 1251**,** 53-64.

LAEMMLI, U. K. 1970. Cleavage of structural proteins during the assembly of the head of bacteriophage T4. *Nature,* 227**,** 680-5.

LAFLAMME, A., YOUNG, K. E., LANG, I. & WEISER, D. C. 2018. Alternative splicing of (ppp1r12a/mypt1) in zebrafish produces a novel myosin phosphatase targeting subunit. *Gene,* 675**,** 15-26.

LAMIABLE, A., THEVENET, P., REY, J., VAVRUSA, M., DERREUMAUX, P. & TUFFERY, P. 2016. PEP-FOLD3: faster de novo structure prediction for linear peptides in solution and in complex. *Nucleic Acids Res,* 44**,** W449-54.

LANGEBERG, L. K. & SCOTT, J. D. 2015. Signalling scaffolds and local organization of cellular behaviour. *Nat Rev Mol Cell Biol,* 16**,** 232-44.

LAPPALAINEN, P., KOTILA, T., JEGOU, A. & ROMET-LEMONNE, G. 2022. Biochemical and mechanical regulation of actin dynamics. *Nat Rev Mol Cell Biol,* 23**,** 836-852.

LARTEY, J., TAGGART, J., ROBSON, S. & TAGGART, M. 2016. Altered Expression of Human Smooth Muscle Myosin Phosphatase Targeting (MYPT) Isovariants with Pregnancy and Labor. *PLoS One,* 11**,** e0164352.

LATOS, P. A., PAULER, F. M., KOERNER, M. V., SENERGIN, H. B., HUDSON, Q. J., STOCSITS, R. R., ALLHOFF, W., STRICKER, S. H., KLEMENT, R. M., WARCZOK, K. E., AUMAYR, K., PASIERBEK, P. & BARLOW, D. P. 2012. Airn transcriptional overlap, but not its lncRNA products, induces imprinted Igf2r silencing. *Science,* 338**,** 1469-72.

LEASK, A. & ABRAHAM, D. J. 2004. TGF-beta signaling and the fibrotic response. *FASEB J,* 18**,** 816-27.

LEE, D. C., CARMICHAEL, D. F., KREBS, E. G. & MCKNIGHT, G. S. 1983. Isolation of a cDNA clone for the type I regulatory subunit of bovine cAMP-dependent protein kinase. *Proc Natl Acad Sci U S A,* 80**,** 3608-3612.

LEFKIMMIATIS, K. & ZACCOLO, M. 2014. cAMP signaling in subcellular compartments. *Pharmacol Ther,* 143**,** 295-304.

LEUNG, T., MANSER, E., TAN, L. & LIM, L. 1995. A novel serine/threonine kinase binding the Ras-related RhoA GTPase which translocates the kinase to peripheral membranes. *J Biol Chem,* 270**,** 29051-4.

LI, J., HE, Y., LU, Q. & ZHANG, M. 2016. Mechanistic Basis of Organization of the Harmonin/USH1C-Mediated Brush Border Microvilli Tip-Link Complex. *Dev Cell,* 36**,** 179-89.

LIM, C. J., HAN, J., YOUSEFI, N., MA, Y., AMIEUX, P. S., MCKNIGHT, G. S., TAYLOR, S. S. & GINSBERG, M. H. 2007. Alpha4 integrins are type I cAMP-dependent protein kinase-anchoring proteins. *Nat Cell Biol,* 9**,** 415-21.

LINDAHL, P., JOHANSSON, B. R., LEVEEN, P. & BETSHOLTZ, C. 1997. Pericyte loss and microaneurysm formation in PDGF-B-deficient mice. *Science,* 277**,** 242-5.

LIU, H., GAZA-BULSECO, G., CHUMSAE, C. & NEWBY-KEW, A. 2007. Characterization of lower molecular weight artifact bands of recombinant monoclonal IgG1 antibodies on non-reducing SDS-PAGE. *Biotechnol Lett,* 29**,** 1611-1622.

LONDON, E., BLOYD, M. & STRATAKIS, C. A. 2020. PKA functions in metabolism and resistance to obesity: lessons from mouse and human studies. *J Endocrinol,* 246**,** R51-R64.

LOWRY, O. H., ROSEBROUGH, N. J., FARR, A. L. & RANDALL, R. J. 1951. Protein measurement with the Folin phenol reagent. *J Biol Chem,* 193**,** 265-75.

LUCENA-AGUILAR, G., SANCHEZ-LOPEZ, A. M., BARBERAN-ACEITUNO, C., CARRILLO-AVILA, J. A., LOPEZ-GUERRERO, J. A. & AGUILAR-QUESADA, R. 2016. DNA Source Selection for Downstream Applications Based on DNA Quality Indicators Analysis. *Biopreserv Biobank,* 14**,** 264-70.

MACDONALD, J. A. & WALSH, M. P. 2018. Regulation of Smooth Muscle Myosin Light Chain Phosphatase by Multisite Phosphorylation of the Myosin Targeting Subunit, MYPT1. *Cardiovasc Hematol Disord Drug Targets,* 18**,** 4-13.

MACHACEK, M., HODGSON, L., WELCH, C., ELLIOTT, H., PERTZ, O., NALBANT, P., ABELL, A., JOHNSON, G. L., HAHN, K. M. & DANUSER, G. 2009. Coordination of Rho GTPase activities during cell protrusion. *Nature,* 461**,** 99-103.

MACHESKY, L. M., MULLINS, R. D., HIGGS, H. N., KAISER, D. A., BLANCHOIN, L., MAY, R. C., HALL, M. E. & POLLARD, T. D. 1999. Scar, a WASp-related protein, activates nucleation of actin filaments by the Arp2/3 complex. *Proc Natl Acad Sci U S A,* 96**,** 3739-44.

MACHIDA, H., ITO, M., OKAMOTO, R., SHIRAKI, K., ISAKA, N., HARTSHORNE, D. J. & NAKANO, T. 2001. Molecular cloning and analysis of the 5'-flanking region of the human MYPT1 gene. *Biochim Biophys Acta,* 1517**,** 424-9.

MANNI, S., MAUBAN, J. H., WARD, C. W. & BOND, M. 2008. Phosphorylation of the cAMP-dependent protein kinase (PKA) regulatory subunit modulates PKA-AKAP interaction, substrate phosphorylation, and calcium signaling in cardiac cells. *J Biol Chem,* 283**,** 24145-54.

MARIGO, V., NIGRO, A., PECCI, A., MONTANARO, D., DI STAZIO, M., BALDUINI, C. L. & SAVOIA, A. 2004. Correlation between the clinical phenotype of MYH9-related disease and tissue distribution of class II nonmuscle myosin heavy chains. *Genomics,* 83**,** 1125-33.

MARTIN, K., REIMANN, A., FRITZ, R. D., RYU, H., JEON, N. L. & PERTZ, O. 2016. Spatio-temporal co-ordination of RhoA, Rac1 and Cdc42 activation during prototypical edge protrusion and retraction dynamics. *Sci Rep,* 6**,** 21901.

MASTERS, T. A., KENDRICK-JONES, J. & BUSS, F. 2017. Myosins: Domain Organisation, Motor Properties, Physiological Roles and Cellular Functions. *In:* JOCKUSCH, B. M. (ed.) *The Actin Cytoskeleton.* Cham: Springer International Publishing.

MATSUI, T., AMANO, M., YAMAMOTO, T., CHIHARA, K., NAKAFUKU, M., ITO, M., NAKANO, T., OKAWA, K., IWAMATSU, A. & KAIBUCHI, K. 1996. Rho-associated kinase, a novel serine/threonine kinase, as a putative target for small GTP binding protein Rho. *EMBO J,* 15**,** 2208-16.

MCCLOY, R. A., ROGERS, S., CALDON, C. E., LORCA, T., CASTRO, A. & BURGESS, A. 2014. Partial inhibition of Cdk1 in G2 phase overrides the SAC and decouples mitotic events. *Cell Cycle,* 13**,** 1400-1412.

MCINTOSH, J. R. 2016. Mitosis. *Cold Spring Harb Perspect Biol,* 8.

MERRITT, R. C., MANOR, U., SALLES, F. T., GRATI, M., DOSE, A. C., UNRATH, W. C., QUINTERO, O. A., YENGO, C. M. & KACHAR, B. 2012. Myosin IIIB uses an actin-binding motif in its espin-1 cargo to reach the tips of actin protrusions. *Curr Biol,* 22**,** 320-5.

MESSEGUER, X., ESCUDERO, R., FARRE, D., NUNEZ, O., MARTINEZ, J. & ALBA, M. M. 2002. PROMO: detection of known transcription regulatory elements using species-tailored searches. *Bioinformatics,* 18**,** 333-4.

MIZUNO, Y., ISOTANI, E., HUANG, J., DING, H., STULL, J. T. & KAMM, K. E. 2008. Myosin light chain kinase activation and calcium sensitization in smooth muscle in vivo. *Am J Physiol Cell Physiol,* 295**,** C358-64.

MOLL, D., PRINZ, A., GESELLCHEN, F., DREWIANKA, S., ZIMMERMANN, B. & HERBERG, F. W. 2006. Biomolecular interaction analysis in functional proteomics. *Journal of Neural Transmission,* 113**,** 1015-1032.

MORI, S., IWAOKA, R., ETO, M. & OHKI, S. Y. 2009. Solution structure of the inhibitory phosphorylation domain of myosin phosphatase targeting subunit 1. *Proteins,* 77**,** 732-5.

MURANYI, A., DERKACH, D., ERDODI, F., KISS, A., ITO, M. & HARTSHORNE, D. J. 2005. Phosphorylation of Thr695 and Thr850 on the myosin phosphatase target subunit: inhibitory effects and occurrence in A7r5 cells. *FEBS Lett,* 579**,** 6611-5.

MURPHY, P. J. 2005. The fetal circulation. *Continuing Education in Anaesthesia, Critical Care and Pain,* 5**,** 107-112.

NASEEM, K. M. & RIBA, R. 2008. Unresolved roles of platelet nitric oxide synthase. *J Thromb Haemost,* 6**,** 10-9.

NAUS, C. C. & LAIRD, D. W. 2010. Implications and challenges of connexin connections to cancer. *Nat Rev Cancer,* 10**,** 435-41.

NEWLON, M. G., ROY, M., MORIKIS, D., CARR, D. W., WESTPHAL, R., SCOTT, J. D. & JENNINGS, P. A. 2001. A novel mechanism of PKA anchoring revealed by solution structures of anchoring complexes. *EMBO J,* 20**,** 1651-62.

NEWLON, M. G., ROY, M., MORIKIS, D., HAUSKEN, Z. E., COGHLAN, V., SCOTT, J. D. & JENNINGS, P. A. 1999. The molecular basis for protein kinase A anchoring revealed by solution NMR. *Nat Struct Biol,* 6**,** 222-7.

NICHOLSON-DYKSTRA, S. M. & HIGGS, H. N. 2008. Arp2 depletion inhibits sheet-like protrusions but not linear protrusions of fibroblasts and lymphocytes. *Cell Motil Cytoskeleton,* 65**,** 904-22.

NIESSEN, C. M., LECKBAND, D. & YAP, A. S. 2011. Tissue organization by cadherin adhesion molecules: dynamic molecular and cellular mechanisms of morphogenetic regulation. *Physiol Rev,* 91**,** 691-731.

NIKITENKO, L. L., BLUCHER, N., FOX, S. B., BICKNELL, R., SMITH, D. M. & REES, M. C. 2006. Adrenomedullin and CGRP interact with endogenous calcitonin-receptor-like receptor in endothelial cells and induce its desensitisation by different mechanisms. *J Cell Sci,* 119**,** 910-22.

NIKOLAEV, V. O., BUNEMANN, M., HEIN, L., HANNAWACKER, A. & LOHSE, M. J. 2004. Novel single chain cAMP sensors for receptor-induced signal propagation. *J Biol Chem,* 279**,** 37215-8.

NIKOLAEV, V. O., BUNEMANN, M., SCHMITTECKERT, E., LOHSE, M. J. & ENGELHARDT, S. 2006. Cyclic AMP imaging in adult cardiac myocytes reveals far-reaching beta1-adrenergic but locally confined beta2-adrenergic receptor-mediated signaling. *Circ Res,* 99**,** 1084-91.

NORTON, J., BOLLINGER, R. R., CHANG, A. E. & LOWRY, S. F. 2012. *Surgery: basic science and clinical evidence*, Springer.

OAKES, P. W., BIDONE, T. C., BECKHAM, Y., SKEETERS, A. V., RAMIREZ-SAN JUAN, G. R., WINTER, S. P., VOTH, G. A. & GARDEL, M. L. 2018. Lamellipodium is a myosin-independent mechanosensor. *Proc Natl Acad Sci U S A,* 115**,** 2646-2651.

OGREID, D., EKANGER, R., SUVA, R. H., MILLER, J. P., STURM, P., CORBIN, J. D. & DOSKELAND, S. O. 1985. Activation of protein kinase isozymes by cyclic nucleotide analogs used singly or in combination. Principles for optimizing the isozyme specificity of analog combinations. *Eur J Biochem,* 150**,** 219-27.

OKAMOTO, R., ITO, M., SUZUKI, N., KONGO, M., MORIKI, N., SAITO, H., TSUMURA, H., IMANAKA-YOSHIDA, K., KIMURA, K., MIZOGUCHI, A., HARTSHORNE, D. J. & NAKANO, T. 2005. The targeted disruption of the MYPT1 gene results in embryonic lethality. *Transgenic Res,* 14**,** 337-40.

OLIVEIRA, C. & DOMINGUES, L. 2018. Guidelines to reach high-quality purified recombinant proteins. *Appl Microbiol Biotechnol,* 102**,** 81-92.

OMAR, M. H. & SCOTT, J. D. 2020. AKAP Signaling Islands: Venues for Precision Pharmacology. *Trends Pharmacol Sci,* 41**,** 933-946.

OSLIN, K., REHO, J. J., LU, Y., KHANAL, S., KENCHEGOWDA, D., PRIOR, S. J. & FISHER, S. A. 2022. Tissue-specific expression of myosin phosphatase subunits

and isoforms in smooth muscle of mice and humans. *Am J Physiol Regul Integr Comp Physiol,* 322, R281-R291.

PALUCH, E. K. & RAZ, E. 2013. The role and regulation of blebs in cell migration. *Curr Opin Cell Biol,* 25, 582-90.

PANKOV, R. & YAMADA, K. M. 2002. Fibronectin at a glance. *J Cell Sci,* 115, 3861-3.

PARRA, M., KASLER, H., MCKINSEY, T. A., OLSON, E. N. & VERDIN, E. 2005. Protein kinase D1 phosphorylates HDAC7 and induces its nuclear export after T-cell receptor activation. *J Biol Chem,* 280, 13762-70.

PAULIN, D. & LI, Z. 2004. Desmin: a major intermediate filament protein essential for the structural integrity and function of muscle. *Exp Cell Res,* 301, 1-7.

PAYNE, M. C., ZHANG, H. Y., PROSDOCIMO, T., JOYCE, K. M., KOGA, Y., IKEBE, M. & FISHER, S. A. 2006. Myosin phosphatase isoform switching in vascular smooth muscle development. *J Mol Cell Cardiol,* 40, 274-82.

PAYNE, M. C., ZHANG, H. Y., SHIRASAWA, Y., KOGA, Y., IKEBE, M., BENOIT, J. N. & FISHER, S. A. 2004. Dynamic changes in expression of myosin phosphatase in a model of portal hypertension. *Am J Physiol Heart Circ Physiol,* 286, H1801-10.

PEGORARO, A. F., JANMEY, P. & WEITZ, D. A. 2017. Mechanical Properties of the Cytoskeleton and Cells. *Cold Spring Harb Perspect Biol,* 9.

PELECHANO, V. & STEINMETZ, L. M. 2013. Gene regulation by antisense transcription. *Nat Rev Genet,* 14, 880-93.

PERKINS, J. R., DIBOUN, I., DESSAILLY, B. H., LEES, J. G. & ORENGO, C. 2010. Transient protein-protein interactions: structural, functional, and network properties. *Structure,* 18, 1233-43.

PERTZ, O., HODGSON, L., KLEMKE, R. L. & HAHN, K. M. 2006. Spatiotemporal dynamics of RhoA activity in migrating cells. *Nature,* 440, 1069-72.

PFLEGER, K. D. G. & EIDNE, K. A. 2006. Illuminating insights into protein-protein interactions using bioluminescence resonance energy transfer (BRET). *Nat Methods,* 3, 165-174.

PIDOUX, G. & TASKÉN, K. 2010. Specificity and spatial dynamics of protein kinase A signaling organized by A-kinase-anchoring proteins. *J Mol Endocrinol,* 44**,** 271-284.

PIDOUX, G., WITCZAK, O., JARNAESS, E., MYRVOLD, L., URLAUB, H., STOKKA, A. J., KUNTZIGER, T. & TASKEN, K. 2011. Optic atrophy 1 is an A-kinase anchoring protein on lipid droplets that mediates adrenergic control of lipolysis. *EMBO J,* 30**,** 4371-86.

PLEIN, A., FANTIN, A., DENTI, L., POLLARD, J. W. & RUHRBERG, C. 2018. Erythro-myeloid progenitors contribute endothelial cells to blood vessels. *Nature*.

POLLARD, T. D. 2020. Myosins in Cytokinesis. *In:* COLUCCIO, L. M. (ed.) *Myosins: A Superfamily of Molecular Motors*. Cham: Springer International Publishing.

POLLARD, T. D. & GOLDMAN, R. D. 2018. Overview of the Cytoskeleton from an Evolutionary Perspective. *Cold Spring Harb Perspect Biol,* 10.

PONSIOEN, B., ZHAO, J., RIEDL, J., ZWARTKRUIS, F., VAN DER KROGT, G., ZACCOLO, M., MOOLENAAR, W. H., BOS, J. L. & JALINK, K. 2004. Detecting cAMP-induced Epac activation by fluorescence resonance energy transfer: Epac as a novel cAMP indicator. *EMBO Rep,* 5**,** 1176-80.

POTENTE, M. & MAKINEN, T. 2017. Vascular heterogeneity and specialization in development and disease. *Nat Rev Mol Cell Biol,* 18**,** 477-494.

PRIORA, R., MARGARITIS, A., FROSALI, S., COPPO, L., SUMMA, D., DI GIUSEPPE, D., ALDINUCCI, C., PESSINA, G., DI STEFANO, A. & DI SIMPLICIO, P. 2011. In vitro inhibition of human and rat platelets by NO donors, nitrosoglutathione, sodium nitroprusside and SIN-1, through activation of cGMP-independent pathways. *Pharmacol Res,* 64**,** 289-97.

PROBST, F. J., FRIDELL, R. A., RAPHAEL, Y., SAUNDERS, T. L., WANG, A., LIANG, Y., MORELL, R. J., TOUCHMAN, J. W., LYONS, R. H., NOBEN-TRAUTH, K., FRIEDMAN, T. B. & CAMPER, S. A. 1998. Correction of deafness in shaker-2 mice by an unconventional myosin in a BAC transgene. *Science,* 280**,** 1444-7.

QIAO, J., HUANG, F. & LUM, H. 2003. PKA inhibits RhoA activation: a protection mechanism against endothelial barrier dysfunction. *Am J Physiol Lung Cell Mol Physiol,* 284**,** L972-80.

QIN, Z. & ZHANG, X. 2017. The identification of switch-like alternative splicing exons among multiple samples with RNA-Seq data. *PLoS One,* 12**,** e0178320.

QUINTERO, O. A., DIVITO, M. M., ADIKES, R. C., KORTAN, M. B., CASE, L. B., LIER, A. J., PANARETOS, N. S., SLATER, S. Q., RENGARAJAN, M., FELIU, M. & CHENEY, R. E. 2009. Human Myo19 is a novel myosin that associates with mitochondria. *Curr Biol,* 19**,** 2008-13.

RABABA'H, A., SINGH, S., SURYAVANSHI, S. V., ALTARABSHEH, S. E., DEO, S. V. & MCCONNELL, B. K. 2014. Compartmentalization role of A-kinase anchoring proteins (AKAPs) in mediating protein kinase A (PKA) signaling and cardiomyocyte hypertrophy. *Int J Mol Sci,* 16**,** 218-29.

RAMALINGAM, N., ZHAO, H., BREITSPRECHER, D., LAPPALAINEN, P., FAIX, J. & SCHLEICHER, M. 2010. Phospholipids regulate localization and activity of mDia1 formin. *Eur J Cell Biol,* 89**,** 723-32.

RAO, V. S., SRINIVAS, K., SUJINI, G. N. & KUMAR, G. N. 2014. Protein-protein interaction detection: methods and analysis. *Int J Proteomics,* 2014**,** 147648.

RASLAN, Z., MAGWENZI, S., ABURIMA, A., TASKÉN, K. & NASEEM, K. M. 2015. Targeting of type I protein kinase A to lipid rafts is required for platelet inhibition by the 3′,5′-cyclic adenosine monophosphate-signaling pathway. *J Thromb Haemost,* 13**,** 1721-1734.

REGGIANI, C. & BOTTINELLI, R. 2008. Myosin Ii: Sarcomeric Myosins, The Motors Of Contraction In Cardiac And Skeletal Muscles. *In:* COLUCCIO, L. M. (ed.) *Myosins: A Superfamily of Molecular Motors*. Dordrecht: Springer Netherlands.

REIMANN, E. M., BROSTROM, C. O., CORBIN, J. D., KING, C. A. & KREBS, E. G. 1971. Separation of regulatory and catalytic subunits of the cyclic 3',5'-adenosine monophosphate-dependent protein kinase(s) of rabbit skeletal muscle. *Biochem Biophys Res Commun,* 42**,** 187-94.

RILEY, D. R. J., KHALIL, J. S., NASEEM, K. M. & RIVERO, F. 2020. Biochemical and immunocytochemical characterization of coronins in platelets. *Platelets,* 31**,** 913-924.

RIVARD, R. L., BIRGER, M., GASTON, K. J. & HOWE, A. K. 2009. AKAP-independent localization of type-II protein kinase A to dynamic actin microspikes. *Cell Motil Cytoskeleton,* 66**,** 693-709.

RIVERO F., X., H.Y. 2017. Cytoskeleton in Encyclopedia of Cancer 4thEdition. *In:* SCHWAB, M. (ed.) *Encyclopedia of Cancer 4thEdition*

Berlin: Springer.

RODRIGUEZ, O. C. & CHENEY, R. E. 2002. Human myosin-Vc is a novel class V myosin expressed in epithelial cells. *J Cell Sci,* 115**,** 991-1004.

ROHN, J. L., PATEL, J. V., NEUMANN, B., BULKESCHER, J., MCHEDLISHVILI, N., MCMULLAN, R. C., QUINTERO, O. A., ELLENBERG, J. & BAUM, B. 2014. Myo19 ensures symmetric partitioning of mitochondria and coupling of mitochondrial segregation to cell division. *Curr Biol,* 24**,** 2598-605.

ROLAND, J. T., KENWORTHY, A. K., PERANEN, J., CAPLAN, S. & GOLDENRING, J. R. 2007. Myosin Vb interacts with Rab8a on a tubular network containing EHD1 and EHD3. *Mol Biol Cell,* 18**,** 2828-37.

ROMANO, R., DEL FIORE, V. S. & BUCCI, C. 2022. Role of the Intermediate Filament Protein Peripherin in Health and Disease. *Int J Mol Sci,* 23.

ROMERO, S., LE CLAINCHE, C., DIDRY, D., EGILE, C., PANTALONI, D. & CARLIER, M. F. 2004. Formin is a processive motor that requires profilin to accelerate actin assembly and associated ATP hydrolysis. *Cell,* 119**,** 419-29.

ROSSANT, J. & HOWARD, L. 2002. Signaling pathways in vascular development. *Annu Rev Cell Dev Biol,* 18**,** 541-73.

ROSSI, A. C., MAMMUCARI, C., ARGENTINI, C., REGGIANI, C. & SCHIAFFINO, S. 2010. Two novel/ancient myosins in mammalian skeletal muscles: MYH14/7b and MYH15 are expressed in extraocular muscles and muscle spindles. *J Physiol,* 588**,** 353-64.

ROTTNER, K., FAIX, J., BOGDAN, S., LINDER, S. & KERKHOFF, E. 2017. Actin assembly mechanisms at a glance. *J Cell Sci,* 130**,** 3427-3435.

ROTTNER, K. & SCHAKS, M. 2019. Assembling actin filaments for protrusion. *Curr Opin Cell Biol,* 56**,** 53-63.

ROWLEY, J. W., SCHWERTZ, H. & WEYRICH, A. S. 2012. Platelet mRNA: the meaning behind the message. *Curr Opin Hematol,* 19**,** 385-91.

RYAN, T., SHELTON, M., LAMBERT, J. P., MALECOVA, B., BOISVENUE, S., RUEL, M., FIGEYS, D., PURI, P. L. & SKERJANC, I. S. 2013. Myosin phosphatase modulates the cardiac cell fate by regulating the subcellular localization of Nkx2.5 in a Wnt/Rho-associated protein kinase-dependent pathway. *Circ Res,* 112**,** 257-66.

SAEZ, A. & GONZALEZ-GRANADO, J. M. 2022. Recent Advances in Intermediate Filaments-Volume 1. *Int J Mol Sci,* 23.

SAHLENDER, D. A., ROBERTS, R. C., ARDEN, S. D., SPUDICH, G., TAYLOR, M. J., LUZIO, J. P., KENDRICK-JONES, J. & BUSS, F. 2005. Optineurin links myosin VI to the Golgi complex and is involved in Golgi organization and exocytosis. *J Cell Biol,* 169**,** 285-95.

SALDANHA, P. A., BOLANLE, I. O., PALMER, T. M., NIKITENKO, L. L. & RIVERO, F. 2022. Complex Transcriptional Profiles of the PPP1R12A Gene in Cells of the Circulatory System as Revealed by In Silico Analysis and Reverse Transcription PCR. *Cells,* 11.

SALLES, F. T., MERRITT, R. C., JR., MANOR, U., DOUGHERTY, G. W., SOUSA, A. D., MOORE, J. E., YENGO, C. M., DOSE, A. C. & KACHAR, B. 2009. Myosin IIIa boosts elongation of stereocilia by transporting espin 1 to the plus ends of actin filaments. *Nat Cell Biol,* 11**,** 443-50.

SAMBROOK, J., FRITSCH, E. F. & MANIATIS, T. 1989. *Molecular Cloning: A Laboratory Manual*, Cold Spring Harbor Laboratory.

SARMA, G. N., KINDERMAN, F. S., KIM, C., VON DAAKE, S., CHEN, L., WANG, B. C. & TAYLOR, S. S. 2010. Structure of D-AKAP2:PKA RI complex: insights into AKAP specificity and selectivity. *Structure,* 18**,** 155-66.

SATO, T. N., TOZAWA, Y., DEUTSCH, U., WOLBURG-BUCHHOLZ, K., FUJIWARA, Y., GENDRON-MAGUIRE, M., GRIDLEY, T., WOLBURG, H., RISAU, W. & QIN, Y. 1995. Distinct roles of the receptor tyrosine kinases Tie-1 and Tie-2 in blood vessel formation. *Nature,* 376**,** 70-4.

SAVAGE, J., CONLEY, A. J., BLAIS, A. & SKERJANC, I. S. 2009. SOX15 and SOX7 differentially regulate the myogenic program in P19 cells. *Stem Cells,* 27**,** 1231-43.

SCHAKS, M., GIANNONE, G. & ROTTNER, K. 2019. Actin dynamics in cell migration. *Essays Biochem,* 63**,** 483-495.

SCHEIN, A., ZUCCHELLI, S., KAUPPINEN, S., GUSTINCICH, S. & CARNINCI, P. 2016. Identification of antisense long noncoding RNAs that function as SINEUPs in human cells. *Sci Rep,* 6**,** 33605.

SCHIAFFINO, S. & REGGIANI, C. 2011. Fiber types in mammalian skeletal muscles. *Physiol Rev,* 91**,** 1447-531.

SCHIAFFINO, S., ROSSI, A. C., SMERDU, V., LEINWAND, L. A. & REGGIANI, C. 2015. Developmental myosins: expression patterns and functional significance. *Skelet Muscle,* 5**,** 22.

SCHIMMEL, L. & GORDON, E. 2018. The precise molecular signals that control endothelial cell-cell adhesion within the vessel wall. *Biochem Soc Trans,* 46**,** 1673-1680.

SCHNEIDER, M. E., DOSE, A. C., SALLES, F. T., CHANG, W., ERICKSON, F. L., BURNSIDE, B. & KACHAR, B. 2006. A new compartment at stereocilia tips defined by spatial and temporal patterns of myosin IIIa expression. *J Neurosci,* 26**,** 10243-52.

SCHWARTZ, S. M., HEIMARK, R. L. & MAJESKY, M. W. 1990. Developmental mechanisms underlying pathology of arteries. *Physiol Rev,* 70**,** 1177-209.

SCOTT, J. D., GLACCUM, M. B., ZOLLER, M. J., UHLER, M. D., HELFMAN, D. M., MCKNIGHT, G. S. & KREBS, E. G. 1987. The molecular cloning of a type II regulatory subunit of the cAMP-dependent protein kinase from rat skeletal muscle and mouse brain. *Proceedings of the National Academy of Sciences,* 84**,** 5192-5196.

SCOTT, J. D. & SANTANA, L. F. 2010. A-kinase anchoring proteins: getting to the heart of the matter. *Circulation,* 121**,** 1264-71.

SCOTTO-LAVINO, E., GARCIA-DIAZ, M., DU, G. & FROHMAN, M. A. 2010. Basis for the isoform-specific interaction of myosin phosphatase subunits protein

phosphatase 1c beta and myosin phosphatase targeting subunit 1. *J Biol Chem,* 285**,** 6419-24.

SELLERS, J. R. 2000. Myosins: a diverse superfamily. *Biochimica et Biophysica Acta (BBA) - Molecular Cell Research,* 1496**,** 3-22.

SENA, C. M., PEREIRA, A. M. & SEICA, R. 2013. Endothelial dysfunction - a major mediator of diabetic vascular disease. *Biochim Biophys Acta,* 1832**,** 2216-31.

SHAPIRO, A. L., VINUELA, E. & MAIZEL, J. V., JR. 1967. Molecular weight estimation of polypeptide chains by electrophoresis in SDS-polyacrylamide gels. *Biochem Biophys Res Commun,* 28**,** 815-20.

SHARMA, R., SHAFER, M. E. R., BAREKE, E., TREMBLAY, M., MAJEWSKI, J. & BOUCHARD, M. 2017. Bmp signaling maintains a mesoderm progenitor cell state in the mouse tailbud. *Development,* 144**,** 2982-2993.

SHI, Q. & JACKOWSKI, G. 1998. One-dimensional polyacrylamide gel electrophoresis. *Gel electrophoresis of proteins: A practical approach,* 3**,** 1-52.

SHICHI, D., ARIMURA, T., ISHIKAWA, T. & KIMURA, A. 2010. Heart-specific small subunit of myosin light chain phosphatase activates rho-associated kinase and regulates phosphorylation of myosin phosphatase target subunit 1. *J Biol Chem,* 285**,** 33680-90.

SHIMIZU, H., ITO, M., MIYAHARA, M., ICHIKAWA, K., OKUBO, S., KONISHI, T., NAKA, M., TANAKA, T., HIRANO, K. & HARTSHORNE, D. J. 1994. Characterization of the myosin-binding subunit of smooth muscle myosin phosphatase. *J Biol Chem,* 269**,** 30407-11.

SHIRAZI, A., IIZUKA, K., FADDEN, P., MOSSE, C., SOMLYO, A. P., SOMLYO, A. V. & HAYSTEAD, T. A. 1994. Purification and characterization of the mammalian myosin light chain phosphatase holoenzyme. The differential effects of the holoenzyme and its subunits on smooth muscle. *J Biol Chem,* 269**,** 31598-606.

SHOULDERS, M. D. & RAINES, R. T. 2009. Collagen structure and stability. *Annu Rev Biochem,* 78**,** 929-58.

SIMONS, M., WANG, M., MCBRIDE, O. W., KAWAMOTO, S., YAMAKAWA, K., GDULA, D., ADELSTEIN, R. S. & WEIR, L. 1991. Human nonmuscle myosin heavy chains

are encoded by two genes located on different chromosomes. *Circ Res,* 69**,** 530-9.

SINGH, D. K., SARKAR, J., RAGHAVAN, A., REDDY, S. P. & RAJ, J. U. 2011. Hypoxia modulates the expression of leucine zipper-positive MYPT1 and its interaction with protein kinase G and Rho kinases in pulmonary arterial smooth muscle cells. *Pulm Circ,* 1**,** 487-98.

SIPOS, A., IVAN, J., BECSI, B., DARULA, Z., TAMAS, I., HORVATH, D., MEDZIHRADSZKY, K. F., ERDODI, F. & LONTAY, B. 2017. Myosin phosphatase and RhoA-activated kinase modulate arginine methylation by the regulation of protein arginine methyltransferase 5 in hepatocellular carcinoma cells. *Sci Rep,* 7**,** 40590.

SKALHEGG, B. S. & TASKEN, K. 2000. Specificity in the cAMP/PKA signaling pathway. Differential expression,regulation, and subcellular localization of subunits of PKA. *Front Biosci,* 5**,** D678-93.

SKINNER, J. A. & SALTIEL, A. R. 2001. Cloning and identification of MYPT3: a prenylatable myosin targetting subunit of protein phosphatase 1. *Biochem J,* 356**,** 257-67.

SKROBLIN, P., GROSSMANN, S., SCHAFER, G., ROSENTHAL, W. & KLUSSMANN, E. 2010. Mechanisms of protein kinase A anchoring. *Int Rev Cell Mol Biol,* 283**,** 235-330.

SKRUBER, K., READ, T. A. & VITRIOL, E. A. 2018. Reconsidering an active role for G-actin in cytoskeletal regulation. *J Cell Sci,* 131.

SMALL, J. V., STRADAL, T., VIGNAL, E. & ROTTNER, K. 2002. The lamellipodium: where motility begins. *Trends Cell Biol,* 12**,** 112-20.

SMITH, F. D., ESSELTINE, J. L., NYGREN, P. J., VEESLER, D., BYRNE, D. P., VONDERACH, M., STRASHNOV, I., EYERS, C. E., EYERS, P. A., LANGEBERG, L. K. & SCOTT, J. D. 2017. Local protein kinase A action proceeds through intact holoenzymes. *Science,* 356**,** 1288-1293.

SMITH, F. D., REICHOW, S. L., ESSELTINE, J. L., SHI, D., LANGEBERG, L. K., SCOTT, J. D. & GONEN, T. 2013. Intrinsic disorder within an AKAP-protein kinase A complex guides local substrate phosphorylation. *Elife,* 2**,** e01319.

SOBERG, K., MOEN, L. V., SKALHEGG, B. S. & LAERDAHL, J. K. 2017. Evolution of the cAMP-dependent protein kinase (PKA) catalytic subunit isoforms. *PLoS One,* 12, e0181091.

SØBERG, K. & SKÅLHEGG, B. S. 2018. The Molecular Basis for Specificity at the Level of the Protein Kinase a Catalytic Subunit. *Frontiers in Endocrinology,* 9.

SÖDERBERG, O., GULLBERG, M., JARVIUS, M., RIDDERSTRÅLE, K., LEUCHOWIUS, K.-J., JARVIUS, J., WESTER, K., HYDBRING, P., BAHRAM, F., LARSSON, L.-G. & LANDEGREN, U. 2006. Direct observation of individual endogenous protein complexes in situ by proximity ligation. *Nature Methods,* 3, 995-1000.

SODERLING, S. H., GUIRE, E. S., KAECH, S., WHITE, J., ZHANG, F., SCHUTZ, K., LANGEBERG, L. K., BANKER, G., RABER, J. & SCOTT, J. D. 2007. A WAVE-1 and WRP signaling complex regulates spine density, synaptic plasticity, and memory. *J Neurosci,* 27, 355-65.

SOMLYO, A. P. & SOMLYO, A. V. 2003. Ca2+ sensitivity of smooth muscle and nonmuscle myosin II: modulated by G proteins, kinases, and myosin phosphatase. *Physiol Rev,* 83, 1325-58.

SONG, Z., GHOCHANI, M., MCCAFFERY, J. M., FREY, T. G. & CHAN, D. C. 2009. Mitofusins and OPA1 mediate sequential steps in mitochondrial membrane fusion. *Mol Biol Cell,* 20, 3525-32.

STANGHERLIN, A., KOSCHINSKI, A., TERRIN, A., ZOCCARATO, A., JIANG, H., FIELDS, L. A. & ZACCOLO, M. 2014. Analysis of compartmentalized cAMP: a method to compare signals from differently targeted FRET reporters. *Methods Mol Biol,* 1071, 59-71.

STANGHERLIN, A. & ZACCOLO, M. 2012. Phosphodiesterases and subcellular compartmentalized cAMP signaling in the cardiovascular system. *Am J Physiol Heart Circ Physiol,* 302, H379-90.

STATON, C. A., REED, M. W. & BROWN, N. J. 2009. A critical analysis of current in vitro and in vivo angiogenesis assays. *Int J Exp Pathol,* 90, 195-221.

STEFFEN, A., FAIX, J., RESCH, G. P., LINKNER, J., WEHLAND, J., SMALL, J. V., ROTTNER, K. & STRADAL, T. E. 2006. Filopodia formation in the absence of functional WAVE- and Arp2/3-complexes. *Mol Biol Cell,* 17, 2581-91.

STRELKOV, S. V., HERRMANN, H. & AEBI, U. 2003. Molecular architecture of intermediate filaments. *Bioessays,* 25**,** 243-51.

STUDIER, F. W. & MOFFATT, B. A. 1986. Use of bacteriophage T7 RNA polymerase to direct selective high-level expression of cloned genes. *J Mol Biol,* 189**,** 113-30.

SUN, J., TAO, T., ZHAO, W., WEI, L., SHE, F., WANG, P., LI, Y., ZHENG, Y., CHEN, X., WANG, W., QIAO, Y., ZHANG, X. N. & ZHU, M. S. 2019. CPI-17-mediated contraction of vascular smooth muscle is essential for the development of hypertension in obese mice. *J Genet Genomics,* 46**,** 109-118.

SURANENI, P., FOGELSON, B., RUBINSTEIN, B., NOGUERA, P., VOLKMANN, N., HANEIN, D., MOGILNER, A. & LI, R. 2015. A mechanism of leading-edge protrusion in the absence of Arp2/3 complex. *Mol Biol Cell,* 26**,** 901-12.

SURESH, K. & SHIMODA, L. A. 2016. Lung Circulation. *Compr Physiol,* 6**,** 897-943.

SURI, C., JONES, P. F., PATAN, S., BARTUNKOVA, S., MAISONPIERRE, P. C., DAVIS, S., SATO, T. N. & YANCOPOULOS, G. D. 1996. Requisite role of angiopoietin-1, a ligand for the TIE2 receptor, during embryonic angiogenesis. *Cell,* 87**,** 1171-80.

SURKS, H. K., MOCHIZUKI, N., KASAI, Y., GEORGESCU, S. P., TANG, K. M., ITO, M., LINCOLN, T. M. & MENDELSOHN, M. E. 1999. Regulation of myosin phosphatase by a specific interaction with cGMP- dependent protein kinase Ialpha. *Science,* 286**,** 1583-7.

SURKS, H. K., RICHARDS, C. T. & MENDELSOHN, M. E. 2003. Myosin phosphatase-Rho interacting protein. A new member of the myosin phosphatase complex that directly binds RhoA. *J Biol Chem,* 278**,** 51484-93.

SZASZAK, M., CHRISTIAN, F., ROSENTHAL, W. & KLUSSMANN, E. 2008. Compartmentalized cAMP signalling in regulated exocytic processes in non-neuronal cells. *Cell Signal,* 20**,** 590-601.

TADA, M. & HEISENBERG, C.-P. 2012. Convergent extension: using collective cell migration and cell intercalation to shape embryos. *Development,* 139**,** 3897-3904.

TAKAHASHI, N., ITO, M., TANAKA, J., NAKANO, T., KAIBUCHI, K., ODAI, H. & TAKEMURA, K. 1997. Localization of the gene coding for myosin phosphatase, target subunit 1 (MYPT1) to human chromosome 12q15-q21. *Genomics,* 44**,** 150-2.

TAKIZAWA, N., SCHMIDT, D. J., MABUCHI, K., VILLA-MORUZZI, E., TUFT, R. A. & IKEBE, M. 2003. M20, the small subunit of PP1M, binds to microtubules. *Am J Physiol Cell Physiol,* 284**,** C250-62.

TAN, I., NG, C. H., LIM, L. & LEUNG, T. 2001. Phosphorylation of a novel myosin binding subunit of protein phosphatase 1 reveals a conserved mechanism in the regulation of actin cytoskeleton. *J Biol Chem,* 276**,** 21209-16.

TASKEN, K. & AANDAHL, E. M. 2004. Localized effects of cAMP mediated by distinct routes of protein kinase A. *Physiol Rev,* 84**,** 137-67.

TASKEN, K., SKALHEGG, B. S., SOLBERG, R., ANDERSSON, K. B., TAYLOR, S. S., LEA, T., BLOMHOFF, H. K., JAHNSEN, T. & HANSSON, V. 1993. Novel isozymes of cAMP-dependent protein kinase exist in human cells due to formation of RI alpha-RI beta heterodimeric complexes. *J Biol Chem,* 268**,** 21276-83.

TASKÉN, K., SKÅLHEGG, B. S., TASKÉN, K. A., SOLBERG, R., KNUTSEN, H. K., LEVY, F. O., SANDBERG, M., ORSTAVIK, S., LARSEN, T. & JOHANSEN, A. K. 1997. Structure, function, and regulation of human cAMP-dependent protein kinases. *Advances in second messenger and phosphoprotein research,* 31**,** 191-204.

TAYLOR, S. S., BUECHLER, J. A. & YONEMOTO, W. 1990. cAMP-dependent protein kinase: framework for a diverse family of regulatory enzymes. *Annu Rev Biochem,* 59**,** 971-1005.

TAYLOR, S. S., ILOUZ, R., ZHANG, P. & KORNEV, A. P. 2012. Assembly of allosteric macromolecular switches: lessons from PKA. *Nat Rev Mol Cell Biol,* 13**,** 646-58.

TERRAK, M., KERFF, F., LANGSETMO, K., TAO, T. & DOMINGUEZ, R. 2004. Structural basis of protein phosphatase 1 regulation. *Nature,* 429**,** 780-4.

THIERRY-MIEG, D. & THIERRY-MIEG, J. 2006. AceView: a comprehensive cDNA-supported gene and transcripts annotation. *Genome Biology,* 7**,** S12.

TILLO, S. E., XIONG, W. H., TAKAHASHI, M., MIAO, S., ANDRADE, A. L., FORTIN, D. A., YANG, G., QIN, M., SMOODY, B. F., STORK, P. J. S. & ZHONG, H. 2017. Liberated PKA Catalytic Subunits Associate with the Membrane via Myristoylation to Preferentially Phosphorylate Membrane Substrates. *Cell Rep,* 19**,** 617-629.

TITECA, K., LEMMENS, I., TAVERNIER, J. & EYCKERMAN, S. 2019. Discovering cellular protein-protein interactions: Technological strategies and opportunities. *Mass Spectrometry Reviews,* 38**,** 79-111.

TORRES-QUESADA, O., MAYRHOFER, J. E. & STEFAN, E. 2017. The many faces of compartmentalized PKA signalosomes. *Cell Signal,* 37**,** 1-11.

TOTH, A., KISS, E., HERBERG, F. W., GERGELY, P., HARTSHORNE, D. J. & ERDODI, F. 2000. Study of the subunit interactions in myosin phosphatase by surface plasmon resonance. *Eur J Biochem,* 267**,** 1687-97.

TROGER, J., MOUTTY, M. C., SKROBLIN, P. & KLUSSMANN, E. 2012. A-kinase anchoring proteins as potential drug targets. *Br J Pharmacol,* 166**,** 420-33.

TSUJI-TAMURA, K. & OGAWA, M. 2018. Morphology regulation in vascular endothelial cells. *Inflammation and Regeneration,* 38**,** 25.

TSUKITA, S., FURUSE, M. & ITOH, M. 2001. Multifunctional strands in tight junctions. *Nat Rev Mol Cell Biol,* 2**,** 285-93.

TUCKER, W. D., ARORA, Y. & MAHAJAN, K. 2024. Anatomy, Blood Vessels. *StatPearls*. Treasure Island (FL) ineligible companies. Disclosure: Yingyot Arora declares no relevant financial relationships with ineligible companies. Disclosure: Kunal Mahajan declares no relevant financial relationships with ineligible companies.

TUFARELLI, C., STANLEY, J. A., GARRICK, D., SHARPE, J. A., AYYUB, H., WOOD, W. G. & HIGGS, D. R. 2003. Transcription of antisense RNA leading to gene silencing and methylation as a novel cause of human genetic disease. *Nat Genet,* 34**,** 157-65.

TWOMEY, E., LI, Y., LEI, J., SODJA, C., RIBECCO-LUTKIEWICZ, M., SMITH, B., FANG, H., BANI-YAGHOUB, M., MCKINNELL, I. & SIKORSKA, M. 2010. Regulation of MYPT1 stability by the E3 ubiquitin ligase SIAH2. *Exp Cell Res,* 316**,** 68-77.

UDAN, R. S., CULVER, J. C. & DICKINSON, M. E. 2013. Understanding vascular development. *Wiley Interdiscip Rev Dev Biol,* 2**,** 327-46.

UHLER, M. D., CHRIVIA, J. C. & MCKNIGHT, G. S. 1986. Evidence for a second isoform of the catalytic subunit of cAMP-dependent protein kinase. *J Biol Chem,* 261**,** 15360-3.

VAN ANDEL, E., ROOSJEN, M., VAN DER ZANDEN, S., LANGE, S. C., WEIJERS, D., SMULDERS, M. M. J., SAVELKOUL, H. F. J., ZUILHOF, H. & TIJHAAR, E. J. 2022. Highly Specific Protein Identification by Immunoprecipitation–Mass Spectrometry Using Antifouling Microbeads. *ACS Applied Materials & Interfaces,* 14**,** 23102-23116.

VAN BODEGRAVEN, E. J. & ETIENNE-MANNEVILLE, S. 2020. Intermediate filaments against actomyosin: the david and goliath of cell migration. *Curr Opin Cell Biol,* 66**,** 79-88.

VAN NIEUW AMERONGEN, G. P., BECKERS, C. M., ACHEKAR, I. D., ZEEMAN, S., MUSTERS, R. J. & VAN HINSBERGH, V. W. 2007. Involvement of Rho kinase in endothelial barrier maintenance. *Arterioscler Thromb Vasc Biol,* 27**,** 2332-9.

VELASCO, G., ARMSTRONG, C., MORRICE, N., FRAME, S. & COHEN, P. 2002. Phosphorylation of the regulatory subunit of smooth muscle protein phosphatase 1M at Thr850 induces its dissociation from myosin. *FEBS Lett,* 527**,** 101-4.

VICENTE-MANZANARES, M., MA, X., ADELSTEIN, R. S. & HORWITZ, A. R. 2009. Non-muscle myosin II takes centre stage in cell adhesion and migration. *Nat Rev Mol Cell Biol,* 10**,** 778-90.

VIGIL, D., BLUMENTHAL, D. K., BROWN, S., TAYLOR, S. S. & TREWHELLA, J. 2004. Differential effects of substrate on type I and type II PKA holoenzyme dissociation. *Biochemistry,* 43**,** 5629-36.

VISWANADHA, R., SALE, W. S. & PORTER, M. E. 2017. Ciliary Motility: Regulation of Axonemal Dynein Motors. *Cold Spring Harb Perspect Biol,* 9.

VRHOVSKI, B. & WEISS, A. S. 1998. Biochemistry of tropoelastin. *Eur J Biochem,* 258**,** 1-18.

WALKER-GRAY, R., STENGEL, F. & GOLD, M. G. 2017. Mechanisms for restraining cAMP-dependent protein kinase revealed by subunit quantitation and cross-linking approaches. *Proc Natl Acad Sci U S A,* 114**,** 10414-10419.

WALTER, M., CHABAN, C., SCHUTZE, K., BATISTIC, O., WECKERMANN, K., NAKE, C., BLAZEVIC, D., GREFEN, C., SCHUMACHER, K., OECKING, C., HARTER, K. & KUDLA, J. 2004. Visualization of protein interactions in living plant cells using bimolecular fluorescence complementation. *Plant J,* 40**,** 428-38.

WANG, F. & SUN, Y. 2018. Overexpression of Myosin Phosphatase Target Subunit 1 (MYPT1) Inhibits Tumor Progression and Metastasis of Gastric Cancer. *Med Sci Monit,* 24**,** 2508-2517.

WANG, H., XU, J., LAZAROVICI, P., QUIRION, R. & ZHENG, W. 2018. cAMP Response Element-Binding Protein (CREB): A Possible Signaling Molecule Link in the Pathophysiology of Schizophrenia. *Front Mol Neurosci,* 11**,** 255.

WATANABE, N., KATO, T., FUJITA, A., ISHIZAKI, T. & NARUMIYA, S. 1999. Cooperation between mDia1 and ROCK in Rho-induced actin reorganization. *Nat Cell Biol,* 1**,** 136-43.

WEIBEL, E. R. 2012. Fifty years of Weibel-Palade bodies: the discovery and early history of an enigmatic organelle of endothelial cells. *J Thromb Haemost,* 10**,** 979-84.

WEISER, D. C., ROW, R. H. & KIMELMAN, D. 2009. Rho-regulated Myosin phosphatase establishes the level of protrusive activity required for cell movements during zebrafish gastrulation. *Development,* 136**,** 2375-2384.

WEIßENBRUCH, K., GREWE, J., HIPPLER, M., FLADUNG, M., TREMMEL, M., STRICKER, K., SCHWARZ, U. S. & BASTMEYER, M. 2021. Distinct roles of nonmuscle myosin II isoforms for establishing tension and elasticity during cell morphodynamics. *eLife,* 10**,** e71888.

WELLS, A. L., LIN, A. W., CHEN, L. Q., SAFER, D., CAIN, S. M., HASSON, T., CARRAGHER, B. O., MILLIGAN, R. A. & SWEENEY, H. L. 1999. Myosin VI is an actin-based motor that moves backwards. *Nature,* 401**,** 505-8.

WILLIAMS, D. A., BECKER, P. L. & FAY, F. S. 1987. Regional changes in calcium underlying contraction of single smooth muscle cells. *Science,* 235**,** 1644-8.

WISSMANN, A., INGLES, J. & MAINS, P. E. 1999. The Caenorhabditis elegans mel-11 myosin phosphatase regulatory subunit affects tissue contraction in the somatic gonad and the embryonic epidermis and genetically interacts with the Rac signaling pathway. *Dev Biol,* 209**,** 111-27.

WONG, B. W., MARSCH, E., TREPS, L., BAES, M. & CARMELIET, P. 2017. Endothelial cell metabolism in health and disease: impact of hypoxia. *EMBO J,* 36**,** 2187-2203.

WONG, W. & SCOTT, J. D. 2004. AKAP signalling complexes: focal points in space and time. *Nat Rev Mol Cell Biol,* 5**,** 959-70.

WOOLDRIDGE, A. A., MACDONALD, J. A., ERDODI, F., MA, C., BORMAN, M. A., HARTSHORNE, D. J. & HAYSTEAD, T. A. 2004. Smooth muscle phosphatase is regulated in vivo by exclusion of phosphorylation of threonine 696 of MYPT1 by phosphorylation of Serine 695 in response to cyclic nucleotides. *J Biol Chem,* 279**,** 34496-504.

WORTHINGTON, A. S., RIVERA, H., TORPEY, J. W., ALEXANDER, M. D. & BURKART, M. D. 2006. Mechanism-based protein cross-linking probes to investigate carrier protein-mediated biosynthesis. *ACS Chem Biol,* 1**,** 687-91.

WU, C., ASOKAN, S. B., BERGINSKI, M. E., HAYNES, E. M., SHARPLESS, N. E., GRIFFITH, J. D., GOMEZ, S. M. & BEAR, J. E. 2012. Arp2/3 is critical for lamellipodia and response to extracellular matrix cues but is dispensable for chemotaxis. *Cell,* 148**,** 973-87.

WU, G., XU, M., XU, K. & HU, Y. 2013. Benidipine protects kidney through inhibiting ROCK1 activity and reducing the epithelium-mesenchymal transdifferentiation in type 1 diabetic rats. *J Diabetes Res,* 2013**,** 174526.

WU, Y., MURÁNYI, A., ERDŐDI, F. & HARTSHORNE, D. J. 2005. Localization of Myosin Phosphatase Target Subunit and its Mutants. *Journal of Muscle Research & Cell Motility,* 26**,** 123-134.

XIA, D., STULL, J. T. & KAMM, K. E. 2005. Myosin phosphatase targeting subunit 1 affects cell migration by regulating myosin phosphorylation and actin assembly. *Exp Cell Res,* 304**,** 506-17.

XING, S., WALLMEROTH, N., BERENDZEN, K. W. & GREFEN, C. 2016. Techniques for the Analysis of Protein-Protein Interactions in Vivo. *Plant Physiology,* 171**,** 727-758.

YU, C., FENG, W., WEI, Z., MIYANOIRI, Y., WEN, W., ZHAO, Y. & ZHANG, M. 2009. Myosin VI undergoes cargo-mediated dimerization. *Cell,* 138**,** 537-48.

YUAN, A., RAO, M. V., SASAKI, T., CHEN, Y., KUMAR, A., VEERANNA, LIEM, R. K., EYER, J., PETERSON, A. C., JULIEN, J. P. & NIXON, R. A. 2006. Alpha-internexin is structurally and functionally associated with the neurofilament triplet proteins in the mature CNS. *J Neurosci,* 26**,** 10006-19.

YUAN, A., RAO, M. V., VEERANNA & NIXON, R. A. 2012. Neurofilaments at a glance. *J Cell Sci,* 125**,** 3257-63.

YUAN, S. Y. & RIGOR, R. R. 2010. Regulation of Endothelial Barrier Function. *Regulation of Endothelial Barrier Function*. San Rafael (CA).

YUEN, S., OGUT, O. & BROZOVICH, F. V. 2011. MYPT1 protein isoforms are differentially phosphorylated by protein kinase G. *J Biol Chem,* 286**,** 37274-9.

YUEN, S. L., OGUT, O. & BROZOVICH, F. V. 2014. Differential phosphorylation of LZ+/LZ- MYPT1 isoforms regulates MLC phosphatase activity. *Arch Biochem Biophys,* 562**,** 37-42.

ZACCOLO, M., DE GIORGI, F., CHO, C. Y., FENG, L., KNAPP, T., NEGULESCU, P. A., TAYLOR, S. S., TSIEN, R. Y. & POZZAN, T. 2000. A genetically encoded, fluorescent indicator for cyclic AMP in living cells. *Nat Cell Biol,* 2**,** 25-9.

ZACCOLO, M. & POZZAN, T. 2002. Discrete microdomains with high concentration of cAMP in stimulated rat neonatal cardiac myocytes. *Science,* 295**,** 1711-5.

ZHA, J. M., LI, H. S., WANG, Y. T., LIN, Q., TAO, M. & HE, W. Q. 2016. Characterization of isoform expression and subcellular distribution of MYPT1 in intestinal epithelial cells. *Gene,* 588**,** 1-6.

ZHANG, H., BERG, J. S., LI, Z., WANG, Y., LANG, P., SOUSA, A. D., BHASKAR, A., CHENEY, R. E. & STROMBLAD, S. 2004a. Myosin-X provides a motor-based link between integrins and the cytoskeleton. *Nat Cell Biol,* 6**,** 523-31.

ZHANG, H. & FISHER, S. A. 2007. Conditioning effect of blood flow on resistance artery smooth muscle myosin phosphatase. *Circ Res,* 100**,** 730-7.

ZHANG, W., MORRIS, G. Z. & BEEBE, S. J. 2004b. Characterization of the cAMP-dependent protein kinase catalytic subunit Cgamma expressed and purified from sf9 cells. *Protein Expr Purif,* 35**,** 156-69.

ZHANG, X., MA, D., CARUSO, M., LEWIS, M., QI, Y. & YI, Z. 2014. Quantitative phosphoproteomics reveals novel phosphorylation events in insulin signaling regulated by protein phosphatase 1 regulatory subunit 12A. *J Proteomics,* 109**,** 63-75.

ZIHNI, C., MILLS, C., MATTER, K. & BALDA, M. S. 2016. Tight junctions: from simple barriers to multifunctional molecular gates. *Nat Rev Mol Cell Biol,* 17**,** 564-80.

Chapter 8. Appendices

8.1. Appendix A

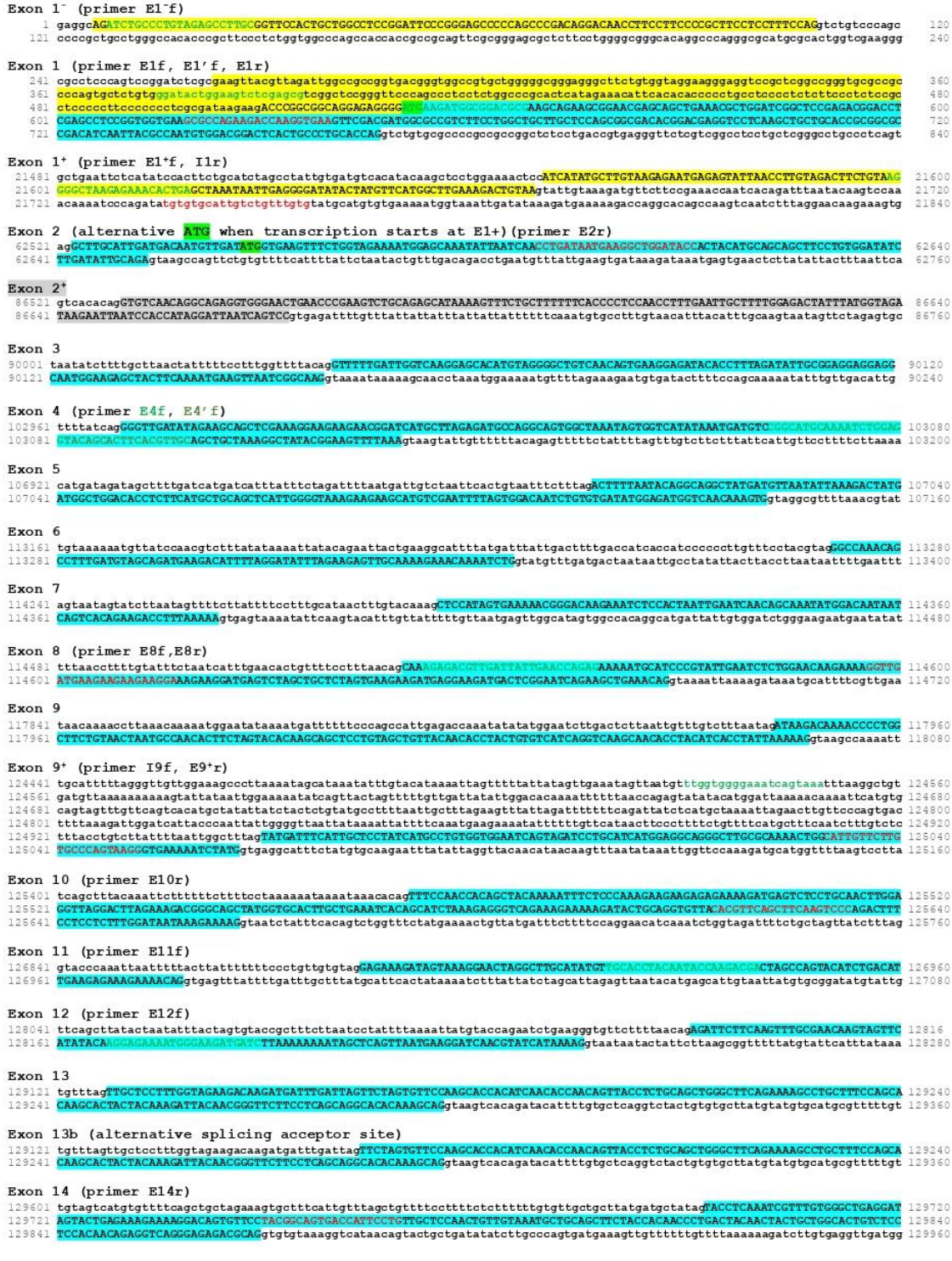

Appendix Figure 8.1-1 Legend on the following page.

Appendix Figure 8.1-1 Exon composition of *PPP1R12A* and location of PCR primers used in this study. Nucleotide numbering is as per Ensemble transcript PPP1R12A-202. Exons are in upper case except for the part of E1 that is spliced out when transcription starts at E1−. Introns are in lower case. Coding sequences are highlighted in turquoise except when E24 is spliced in, in which case the sequence after the alternative stop codon in E25 and E26 is non-coding. Non-coding sequences are highlighted in yellow. Exons of non-sense mediated decay transcripts are highlighted in grey. Translation start and stop codons are highlighted in green and red, respectively. Forward PCR primers are in green characters, reverse PCR primers in red characters except E26'r, that overlaps with E26r and is underlined. Primers spanning exon boundaries are not indicated. Note duplication of E13, E24, E25 and E26 to accommodate alternative splicing variants.

Appendix Table 8.1-1 Support for alternatively spliced variants of *PPP1R12A*. Accession numbers are EST clones, except the one marked with *, which is a direct submission.

Accession number	Tissue	Length (bp); observations
Start at E1-		
BM172316.1	Hippocampus	662
BG699041.1	Hippocampus	711
DB464112.1	Hippocampus	476
ΔN (start at E1$^+$)		
DC401921.1	Testis	551; start codon in E2
DC396310.1	Testis	555; start codon in E2
E2+		
BP279682.1	Glioma	582; frame shift → nonsense mediated decay mRNA?
ΔE6		
BI087523.1	Cervix	632
BQ320904.1	Colon	410
ΔE13		
CA445548.1	Chondrosarcoma	606
BM698400.1	Fetal eye	423
AW847768.1	Colon	740
CA424666.1	Chondrosarcoma	671
AA229965.1	Prostate cancer	346
BE731402.1	Choriocarcinoma	434
AI700011.1	Pool germ cell tumours	468
BE538099.1	Cervix	580
AA572791.1	Prostate epithelial cells	435
BI090128.1	Cervix	766
DB452394.1	Testis	488
AI949264.1	Clear cell kidney tumour	382
E13b		
BX109299.1	B cell	686
BG119754.1	Liver adenocarcinoma	959
AW968572.1	Colon tumour metastasis	482
AA91121.1	B cell	233
ΔE14		
AJ712781.1	Bone marrow	269
ΔE13+E14		
BX327398.2	T cells (Jurkat)	927
CT003136.1	T cells	895
BX327399.1	T cells (Jurkat)	991
AI868201.1	Stomach adenocarcinoma	256

E20+		
CR987322.1	T cells	953; frame shift → nonsense mediated decay mRNA?
BM969444.1	Primary lung epithelial cells	700; frame shift → nonsense mediated decay mRNA?
ΔE22		
*AF458589.1	Liver	4631
E22+		
BG180627.1	Prostate carcinoma	912; frame shift → nonsense mediated decay mRNA?
E24 in (31 bp variant)		
BM669210.1	Fetal eye	684
AI202675.1	Prostate	357
AA715976.1	Breast duct	323; 5'splicing unclear
E24 in (13 bp variant)		
CA390922.1	Retinal pigment epithelium/choroid	560
BF436241.1	Pooled	404
BF590153.1	Pooled	343

Appendix Table 8.1-2 EST, mRNA/cDNA and RNAseq data supporting *PPP1R12A* alternatively spliced variants. Data were collected from AceView, GenBank and GTEx as indicated in the Methods section. RNAseq data are spliced reads. See section 2.2.5 for details on the calculation of frequency of splicing and frequency of variant.

Junction	Variant	AceView ESTs + mRNAs	AceView RNA-Seq	GeneBank RNA-Seq	GTEx RNA-Seq	Sum			Average reads per exon boundary	Fraquency of splicing (%)	Frequency of variant (%)	Variant
E1$^-$-1		5	36	0	0	41				0.07		
E1-E2		162	46082	4521	1728	52493						
E1$^+$-E2	**ΔN**	4	0	70	6	80		**E1-E3 region**	61775	0.13	**0.13**	**ΔN**
E2-E3		122	59908	8888	2058	70976						
E3-E4		70	58081	11699	2157	72007						
E4-E5		32	51973	11528	1959	65492						
E5-E6		34	49362	10158	2014	61568						
E5-E7	**ΔE6**	2	1205	234	29	1470		**E4-E8 region**	71446	2.06	**2.01**	**ΔE6**
E6-E7		36	61749	12897	2697	77379						
E7-E8		37	62968	12781	2618	78404						
E8-E9		38	60873	10160	2680	73751						
E9-E9$^+$	**E9+**	0		315		315		**E8-E10 region**	10339	5.19	**5.06**	**E9$^+$**
E9$^+$-E10		0		443		443		**(only GeneBank data)**				
E9-E10		35	60505	9974	2412	72926						
E10-E11		39	47280	10489	2295	60103						
E11-E12		42	56848	11073	2786	70749						
E12-E13		25	33812	5934	1609	41380						
E12-E13b	**E13b**	4	2001	575	204	2784		**E11-E16 region**	67798	4.11	**4.00**	**E13b**
E12-E14	**ΔE13**	13	6676	2059	591	9339				13.77	**13.43**	**ΔE13**
E12-E15	**ΔE13-E14**	3	434	0	20	457				0.67	**0.66**	**ΔE13-E14**
E13/13b-E14		29	32892	5396	1808	40125						
E13-E15	**ΔE14**	2	9008	1062	274	10346				15.26	**14.87**	**ΔE14**
E14-E15		43	46056	11881	3128	61108						
E15-E16		44	57818	13169	3539	74570						
E16-E17		35	64720	12665	3856	81276						
E17-E18		38	77665	11185	4906	93794						
E18-E19		41	67343	14447	4141	85972						
E19-E20		39	43314	8680	3081	55114						
E20-E21		38	46407	9807	3026	59278						
E21-E22		46	63703	12554	3302	79605						
E21-E23	**ΔE22**	1	548	101	2	652	**E20-E25 region**		85519	0.7624	**0.74**	**ΔE22**
E22-E23		45	79926	14878	4785	99634						
E23-E24/24b		6	381	1140	864	2391						
E24b-E25	**LZ$^-$b**	3	103	289	171	566		**E22-E26 region**	102095	0.5544	**0.55**	**LZ$^-$b**
E24-E25	**LZ$^-$a**	2	254	1255	509	2020				1.9785	**1.98**	**LZ$^-$a**
E23-E25		43	83509	13116	3194	99862						
E25-E26		57	82364	15457	5516	103394						
Total		**1212**	**1415804**	**270880**	**73965**	**1761861**						
											56.58	**FL**

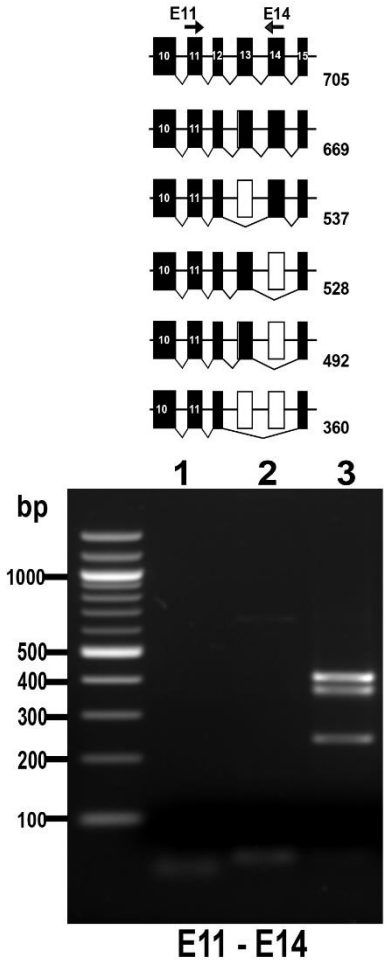

Appendix Figure 8.1-2 HUVEC expression of *PPP1R12A* transcripts. Represented here the RT-PCR to confirm that the transcript missing was the one not having exon13 (Δ13 – bottom band). The top band represents the full-length transcript. **1** negative control, no polymerase; **2** negative control, no retro transcriptase; **3** circular DNA.

Appendix Table 8.1-3 Collection of EST clones supporting terminator region T1 approximately 2100 bp downstream of the stop codon. Accession numbers are hyperlinked to the respective GenBank submission. Sequences at the end of each clone were taken directly from the GenBank submission, note that most are in antisense direction. Cleavage sites are highlighted in turquoise unless reliable identification was not possible. *Clones without a clear polyA stretch but with annotation that an oligo dT was used in the cDNA synthesis. §Clones without a clear polyA stretch and no annotation about an oligo dT being used in the cDNA synthesis.

Accession number	Tissue or cell type	Sequence at end of clone
BU620191.1	Chondrosarcoma cell line	ttttttttttttttttttaa tagttttatt cattttattt gtatatgtca
CA312676.1	Lung epithelial cells	ttttttttttttttttttca cacatttaaa atagttttat tcattttatt
CN278743.1	Embryonic stem cell line	aaatgtattt tgacatatac caataaaatg aataaaacta aaa
BU677557.1	Lung epithelial cells	ttttttttttttttttttag ttttattcat tttatttgta tatgtcaaaa tacatttttа
CA775922.1	Pancreatic islet	ttttttttagg tttattcatt ttatttgtat atgtcaaaat acatttttat
BQ477501.1	Insulinoma	ttttttttttttttttttagttt tattcatttt atttgtatat gtcaaaatat
CA310990.1	Lung epithelial cells	ttttttttttttttttttag ttttattcat tttatttgta tatgtcaaaa tacatttttа
BM993875.1	Subchondral bone	ttttttttttttttttttat agntttattc attttatttg tatatgtcaa
CN479410.1	Subchondral bone	ttttttttttttttttttat agntttattc attttatttg tatatgtcaa
BM968622.1	Lung epithelial cells	ttttttttttttttttttca cacatttaaa atagttttat tcattttatt
AW001851.1	Thymus	ttttttttttttcacatttaa aatagtttta ttcattttat ttgtatatgt
CA440121.1	Chondrosarcoma	ttttttttttttttttttaa aatagtttta ttcattttat ttgtatatgt
AI828759.1	Endometrial adenocarcinoma	ttttttttttaaaatagttt tattcatttt atttgtatat gtcaaaatac
BF197980.1*	Skin	aaaatagttt tattcatttt atttgtatat gtcaaaatac atttttattt
AI342381.1	Uterus	ttttttttttatagttttat tcattttatt tgtatatgtc aaaatacatt
CD678763.1	Eye trabecular meshwork	acatatacaa ataaaatgaa taaaactaaa aaaaaaaaaa gggcgg
CD677602.1	Eye trabecular meshwork	tgacatatac aaataaaatg aataaaacta aaaaaaaaaa aaaaaaaaag
BU608452.1	Lung epithelial cells	gacatataca aataaaatga ataaaactaa aaaaaaaaaa aaaaaaaaaa
BU070239.1	Insulinoma	ttttttttttttttttttagttt tattcatttt atttgtatat gtcaaaatac atttttattt
BQ272332.1	Insulinoma	ttttttttttttttttttagttt tattcatttt atttgtatat gtcaaaatac atttttattt
BM970383.1	Lung epithelial cells	ttttttttttttttttttag ttttattcat tttatttgta tatgtcaaaa tacatttttа
BM509287.1	Insulinoma	ttttttttttttttttttagttt tattcatttt atttgtatat gtcaaaatac
BI492551.1	Fetal cochlea	ttttttttttttttttttagttt tattcatttt atttgtatat gtcaaaatac
AW675588.1	Cervix	ttttttaatttttttttagttt tattcatttt atttgtatat gtcaaaatac
AW516268.1*	Endometrial adenocarcinoma	tagttttatt cattttattt gtatatgtca aaatacattt ttatttccaa

AW452563.1	B cells	ttttttttt ttttttagt tttattcatt ttatttgtat atgtcaaaat acatttttat
AW021595.1	Fetal cochlea	acatatacaa ataaaatgaa taaaactaaa aaaaaaaaaa aaa
AI439179.1*	Lymphoma	tagttttatt cattttattt gtatatgtca aaatacattt ttatttccaa
AI453664.1*	Stomach adenocarcinoma	tagttttatt cattttattt gtatatgtca aaatacattt ttatttccaa
AA830346.1	B-cell	ttttttttt tttagtttta ttcattttat ttgtatatgt caaaatacat
AI281137.1*	Colon adenocarcinoma	agttttattc attttatttg tatatgtcaa aatacatttt tatttccaaa
AI281011.1*	Colon adenocarcinoma	agttttattc attttatttg tatatgtcaa aatacatttt tatttccaaa
AA262664.1*	B-cell	agttttattc attttatttg tatatgtcaa aatacatttt tatttccaaa
AW968416.1§	Colon carcinoma	gttttattca ttttatttgt atatgtcaaa atacattttt atttccaaaa
AW967905.1§	Colon carcinoma	gttttattca ttttatttgt atatgtcaaa atacattttt atttccaaaa
AU310314.1§	Neuroblastomna	ttagttttat tcattttatt tgtatatgtc aaaatacatt tttatttcca
CK300902.1	Retina	ttttttttt tttttttag ttttattcat tttatttgta tatgtcaaaa
BQ189797.1	Fetal eye	gacatataca aataaaatga ataaaactaa aaaaaaaaaa aaaaaaggac
BE645430.1	Prostate	ttttagtttt attcatttta tttgtatatg tcaaaataca tttttatttc
AW316726.1*	Meningioma	tagttttatt cattttattt gtatatgtca aaatacattt ttatttccaa
AW264811.1*	Lung squamous cell carcinoma	tttaggttta ttcattttat ttgtatatgt caaaatacat ttttatttcc
AI678890.1	Stomach adenocarcinoma	ttttttttt tttttagttt tattcatttt atttggatat gtcaaaatac
AI082593.1§	Pooled	tagttttatt cattttattt gtatatgtca aaatacattt ttatttccaa
BM511639.1§	Insulinoma	tttattcatt ttatttgtat atgtcaaaat acatttttat ttccaaaata
DB507086.2	Testis	taaaaatgta ttttgacata tacaaataaa acgaataaaa ctaaaaaaac g
CK300002.1	Retina	ttttttttt agttttattc attttatttg aatatgtcaa aataaatttt
AI923578.1*	Endometrial adenocarcinoma	tagttttatt cattttattt gtatatgtca aaatacattt ttatttccaa
AI342464.1*	Uterus	tattcatttt atttgtatat gtcaaaatac atttttattt ccaaaatagt
AI926946.1*	Prostate	agttttattc attttatttg tatatgtcaa aatacatttt gtatttccaa
AI817061.1	Lung squamous adenocarcinoma	ttttagtttt attcatttta tttgtatatg tcaaaataca tttttatttc
BQ186919.1	Eye	aatttatttt gacatataca aataaaatga ataaaactaa aaaaaaaaaa atataaggac
BE965957.2	Leiomyosarcoma	ttttttttt tttttatag ttttattcat tttattggta tatgtcaaaa
AA282476.1*	B-cells	agttttattc attttatttg tatatgtcaa aatacatttt tatttccaaa
AI971777.1	Fibrothecoma	ttttttttt tagttttatt cattttattt gtatatgtca aaatacattt
AI284479.1*	Esophagus squamous cell carcinoma	aaaatagttt tattcatttt atttgtatat gtcaaaatac atttttattt
H89328.1	Cochlea	Taaaaatgta ttttgacata tacaaataaa atggaataaa actaaaaaaa aa

AW149875.1*	Endometrial adenocarcinoma	tagttttatt cattttattt gtatatgtca aaatacattt ttatttccaa
H89329.1*	Cochlea	catttattt gtatatgtca aaatacattt ttatttccaa aatagtgggt
DB345733.1§	Thymus	cacatttaaa atagttttat tcattttatt tgtatatgtc aaaatacatt
AW131950.1*	Kidney tumour	ttagttttat tcattttatt tgtatatgtc aaaatacatt tttatttcca
AI868665.1§	Pooled	tattcatttt atttgtatat gtcaaaatac atttttattt ccaaaatagt
BI492771.1*	Fetal cochlea	ttatttgtat atgtcaaaat acatccttat ttccaaaata gtgggttttg
Z40397.1*	Brain	attcatttta tttgtatatg tcaaaataca tttttatttc caaaatagtg
AI472433.1*	Colon adenocarcinoma	aaaatagttt tattcatttt atttgtatat gtcaaaatac atttttattt
N057465.1*	Breast carcinoma	ataaaaatgt attttgacat atacaaataa aatgaataaa actatttaa
FN057465.1*	Breast carcinoma	ataaaaatgt attttgacat atacaaataa aatgaataaa actatttaa
BU960397.1	Pool	aaaatgtatt ttgacatata caaataaaat gaataaaact aaaaaaaaaa
BG169053.1	Hypernephroma	ataaaaatgt attttgacat atacaaataa aatgaataaa actaaaaaaa
AA903120.1	Leiomyosarcoma	ttttttttt tcacacattt aaaatagttt tattcatttt atttgtatat
BI966891.1	Pancreas	ttttttttt catggcaaaa tacattttta tttccaaaat agtgggtttt
DW461699.1	Liver	tacaaataaa atgaataaaa ctattttaaa tgcgcaaaaa aaaaaaaaaa

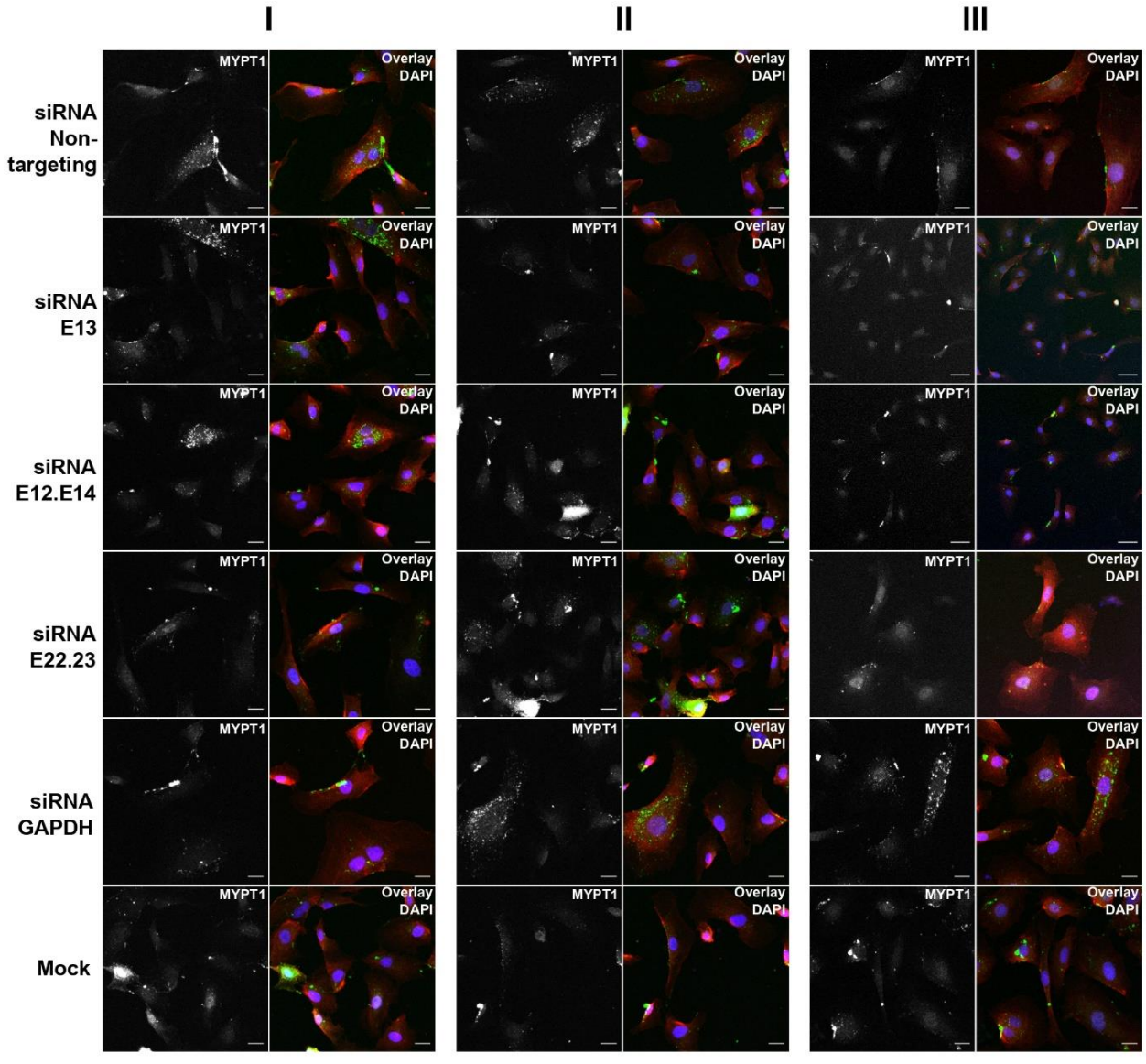

Appendix Figure 8.1-3 Overall imaging of MYPT1 knockdown trial experiment. I, II and III represents each trial. Represented is MYPT1 expression. Anti-MYPT1 rabbit antibody was used to target MYPT1 expression. TRITC phalloidin was used to stain cell cytoskeleton (scale bar 50 μm).

8.2. Appendix B

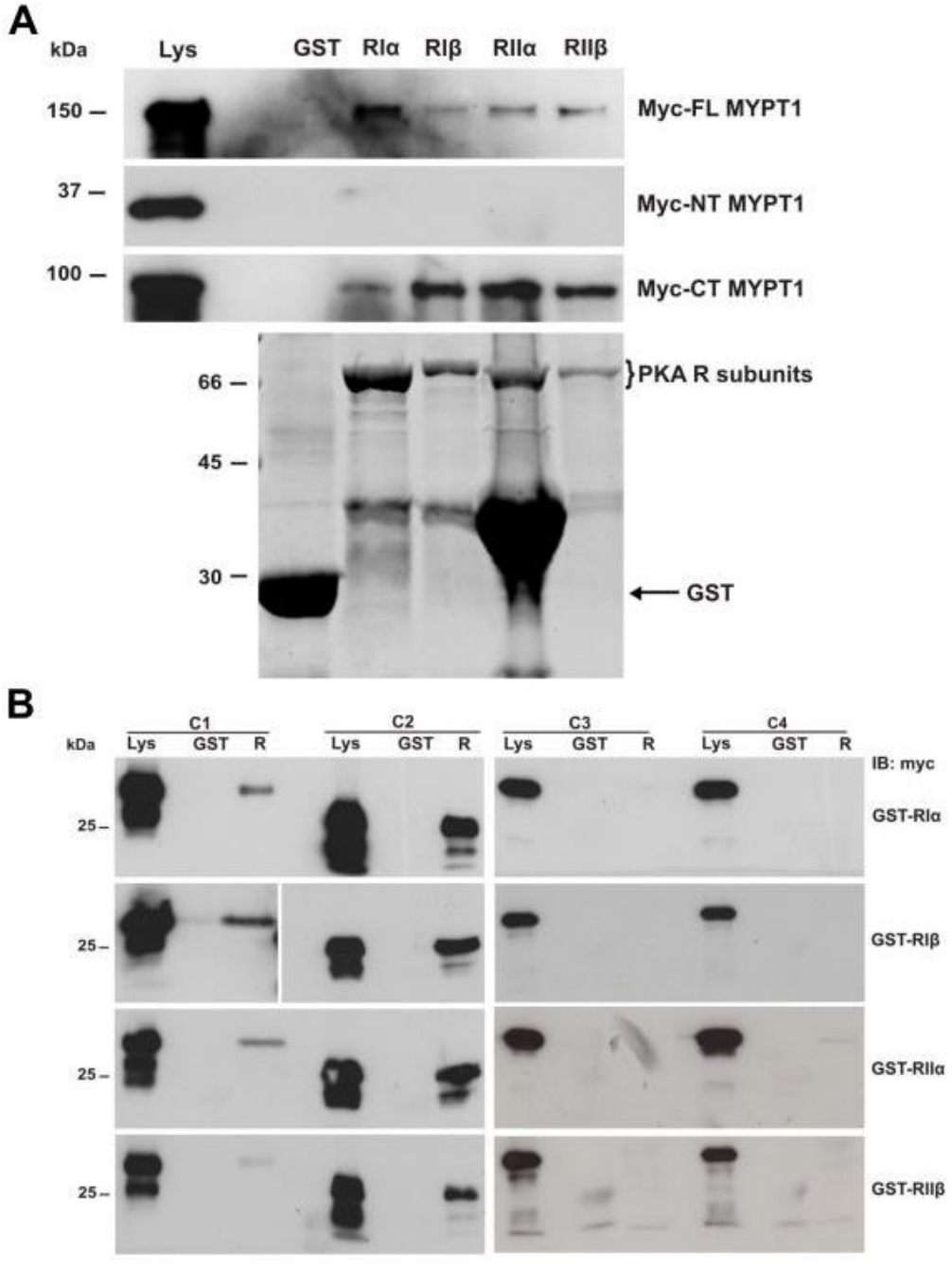

Appendix Figure 8.2-1 Mapping of the MYPT1-PKA interaction. (A) HEK293 T cells were transiently transfected with constructs allowing expression of Myc-MYPT1 (full length, N-terminal and C-terminal). PKA regulatory subunits (RIα, RIß, RIIα and RIIß) were expressed as a GST fusion. The bottom gel was stained with Coomassie-Brilliant-Blue as a control Figure 4.7, page 189 from (Khalil, 2018). **(B)** Binding motif of MYPT1 (C1, C2, C3, C4) fragments previously transfected to HEK 293T cells with recombinant GST PKA regulatory subunits GST. IB: immunoblot, Lys: lysate, R: regulatory subunit, Figure 4.8, page 191 from (Khalil, 2018). (Adapted from (Khalil, 2018)).

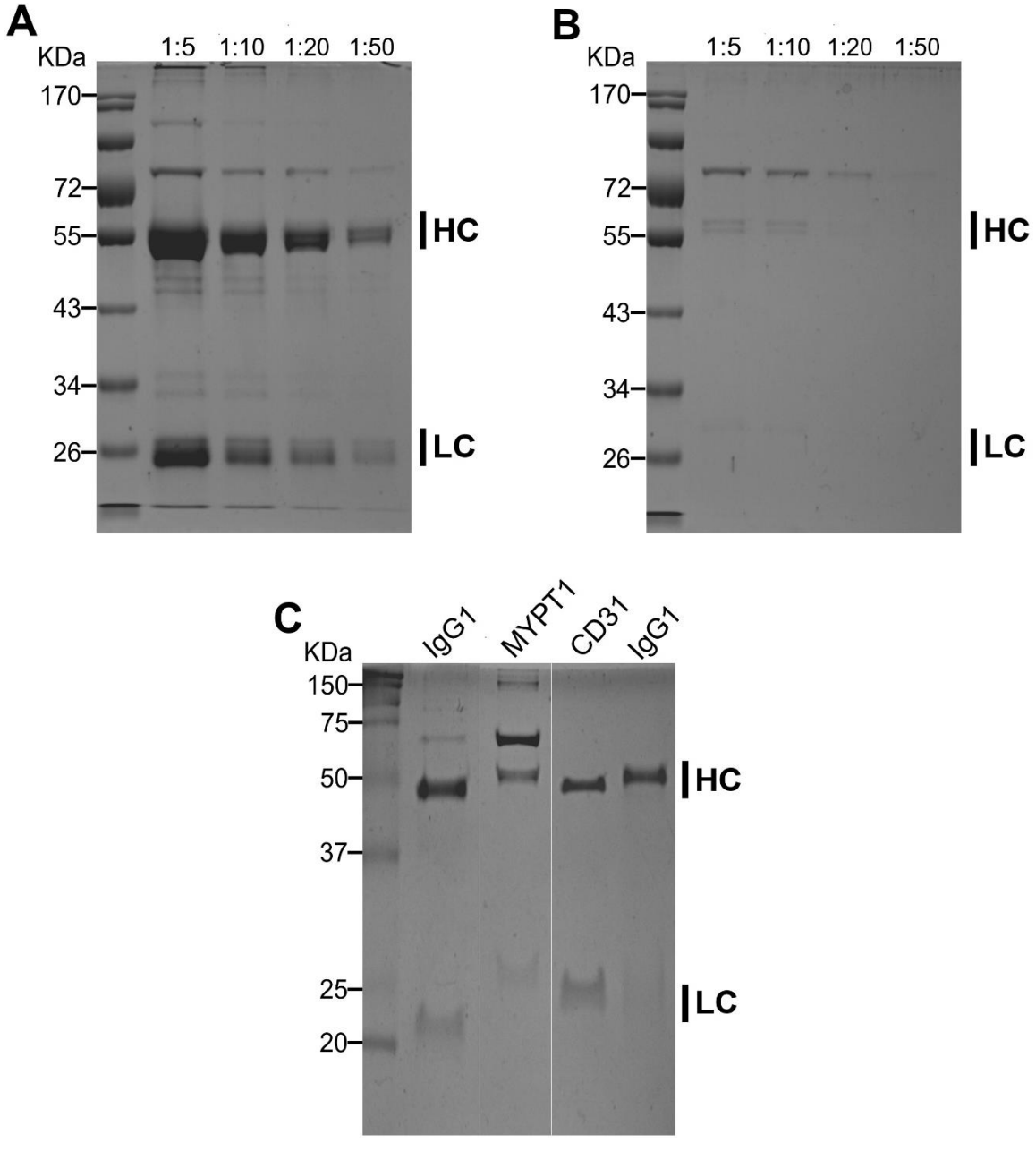

Appendix Figure 8.2-2 Characterisation of antibodies by SDS-PAGE. Antibodies were resolved by SDS-PAGE on 12% gels and gels were stained with Coomassie Brilliant Blue. **(A)** Rabbit immunoglobulin G and **(B)** MYPT1 rabbit antibody (MYPT1 (D6C1) Rabbit mAb #8574). A serial dilution of both MYPT1 and IgG1 antibodies were made from the respective commercial stocks. HC, heavy chain; LC, light chain. **(C)** Immunoglobulin G and MYPT1 raised in rabbit CD31 mouse and IgG1 rabbit polyclonal antibodies were used as control immunoglobulins for heavy chain (HC) and light chains (LC). HC in MYPT1 antibody presented less intensity that IgG1 and IgG1 LC appeared around 20 kDa whereas MYPT1 appeared around 25 kDa. 1 µg of each immunoglobulin were loaded. Rabbit IgG and MYPT1 antibody concentrations as determined using a Pierce™ BCA protein assay kit were:3.134 µg/µL and 0.083 µg/µL, respectively. It is observed that IgG antibody presents higher intensity bands around 50 kDa heavy chain (HC) and 25 kDa light chain (LC) in comparison with the panel B.

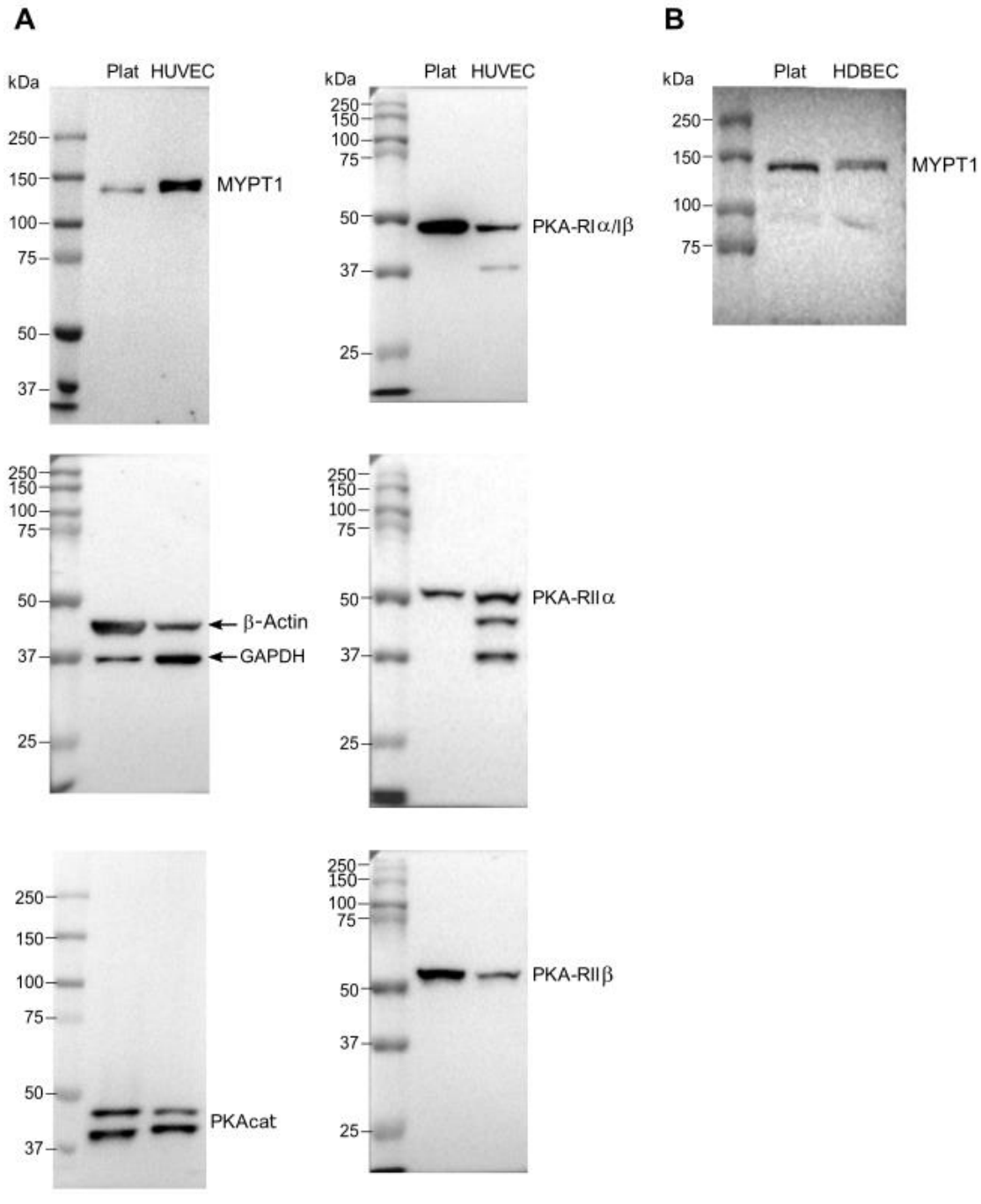

Appendix Figure 8.2-3 Specificity of antibodies used in this study. (A) Human washed platelets (20 µg) and HUVEC lysates (20 µg) were resolved by 10% SDS-PAGE and immunoblotted with antibodies against the indicated proteins. A rabbit anti-MYPT1 antibody (MYPT1 (D6C1) Rabbit mAb #8574, Cell Signalling Technologies, Netherlands) was used. The anti-PKA cat raised against the α subunit (40 kDa) also recognises the 93% identical slightly larger ß subunit. GAPDH and ß-actin were used as loading controls. **(B)** Human washed platelet (10 ug) and HDBEC lysates (10 ug) were resolved by 10% SDS-PAGE and immunoblotted with antibodies against anti-MYPT1 raised in mouse (MYPT1 (C-6): sc-514261, Santa Cruz Biotechnology, Germany).

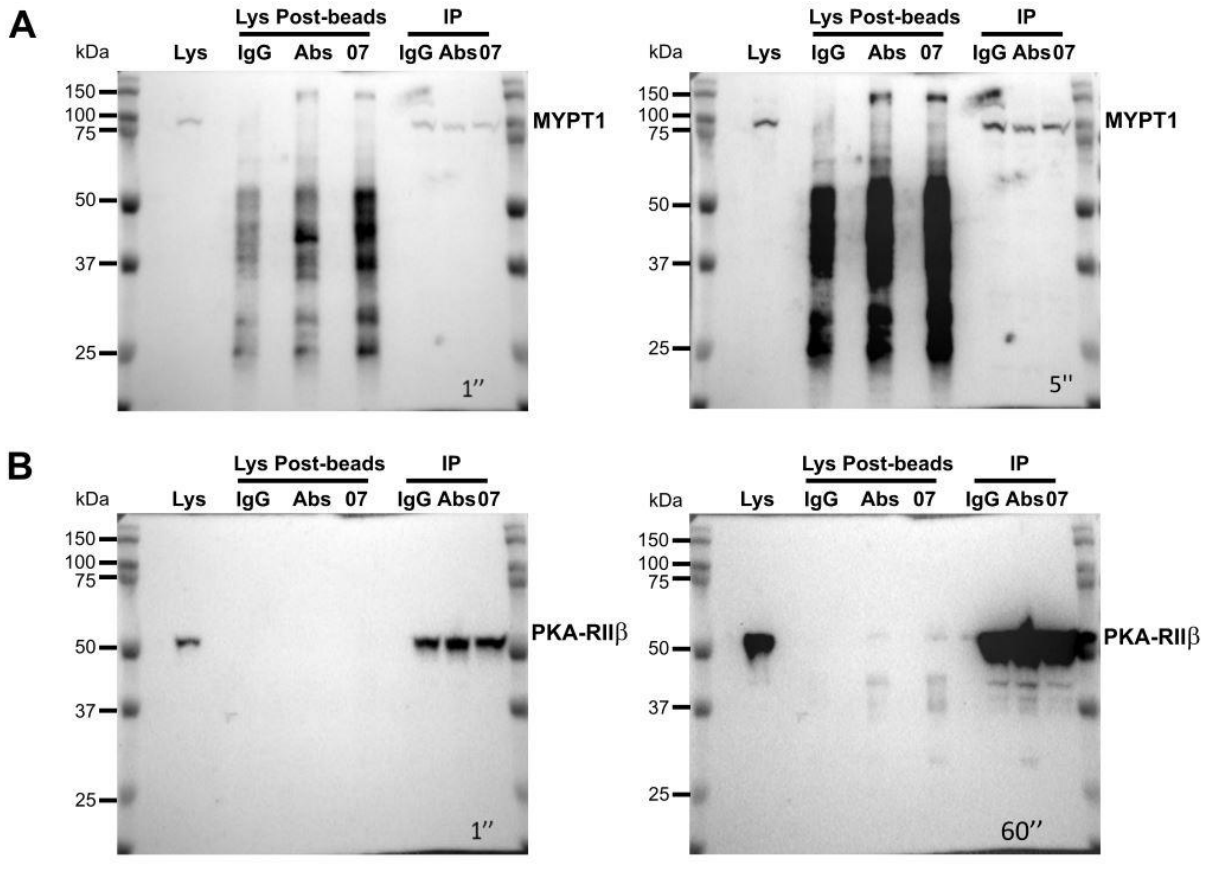

Appendix Figure 8.2-4 Immunoprecipitation of MYPT1 and co-immunoprecipitation of PKA-RIIß trial using agarose beads. (A) Immunoprecipitation of MYPT1 using two different polyclonal antibodies raised in rabbit, ABS1495 (Abs) and 07-672-I (07) (Sigma-Aldrich, Merck Millipore, UK). HUVECs lysate (500 µg) were incubated with agarose beads overnight. Lys (20µg), lysate was used to test protein expression. Membranes were immunoblotted with MYPT1 07-672-I (07). **(B)** Membranes used for IP were immunoblotted with PKA-RIIß antibody. Two exposure times (in seconds) of each blot are shown. Lys-lysate; IgG -immunoglobulin G; IP, immunoprecipitation lysate.

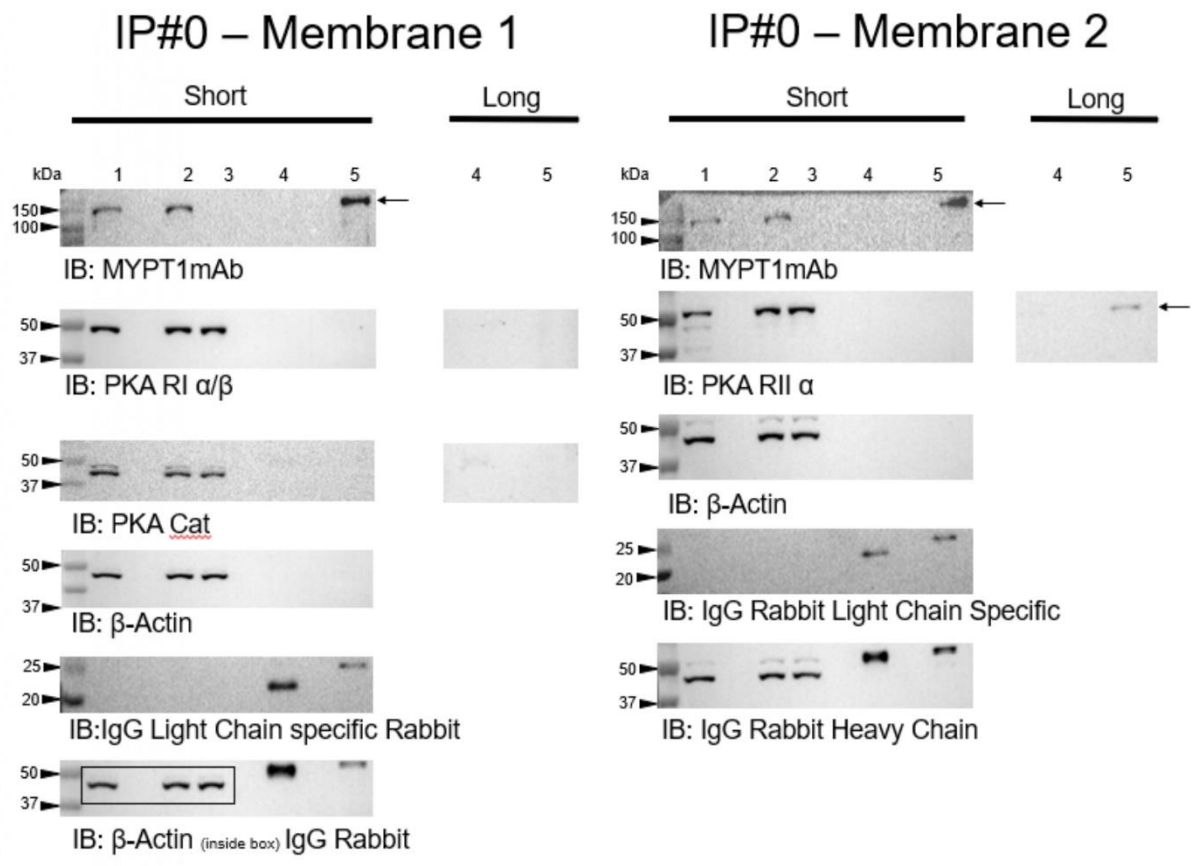
IP#0 – Membrane 1
Short
Long
kDa
1 2 3 4 5
4 5
150
100
IB: MYPT1mAb
50
37
IB: PKA RI α/β
IB: PKA Cat
IB: β-Actin
25
20
IB:IgG Light Chain specific Rabbit
IB: β-Actin (inside box) IgG Rabbit
IP#0 – Membrane 2
IB: MYPT1mAb
IB: PKA RII α
IB: β-Actin
IB: IgG Rabbit Light Chain Specific
IB: IgG Rabbit Heavy Chain

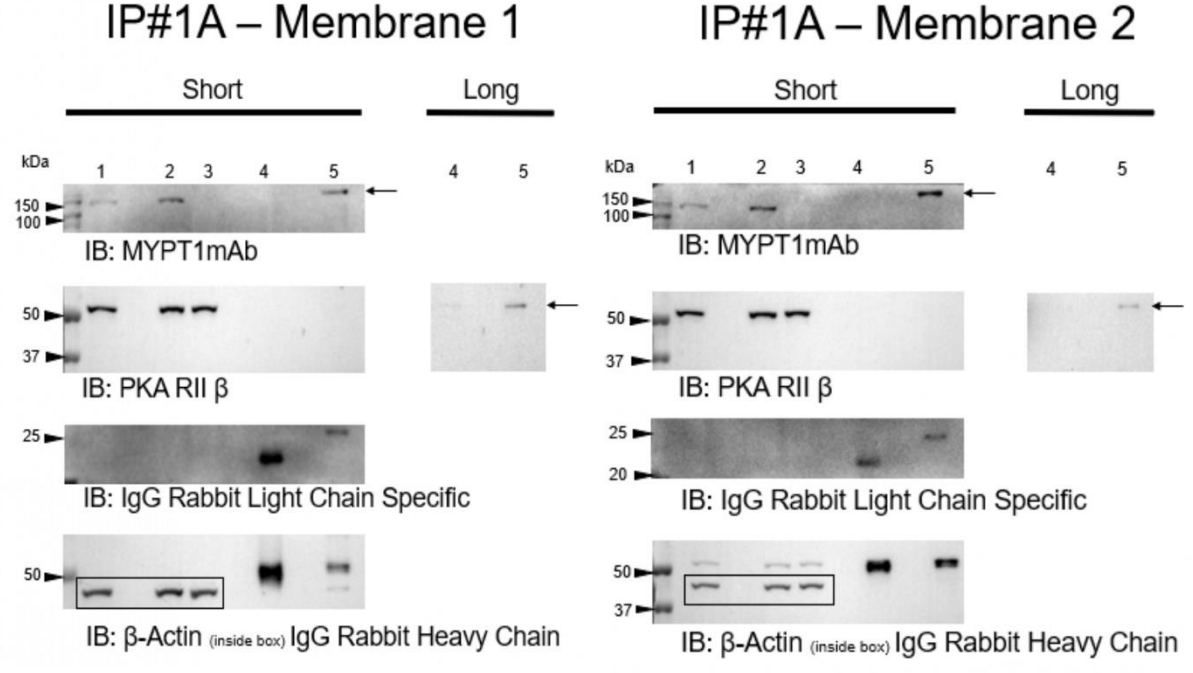
IP#1A – Membrane 1
Short
Long
kDa
1 2 3 4 5
4 5
150
100
IB: MYPT1mAb
50
37
IB: PKA RII β
25
IB: IgG Rabbit Light Chain Specific
IB: β-Actin (inside box) IgG Rabbit Heavy Chain
IP#1A – Membrane 2
IB: MYPT1mAb
IB: PKA RII β
20
IB: IgG Rabbit Light Chain Specific
IB: β-Actin (inside box) IgG Rabbit Heavy Chain

IP#1B – Membrane 1

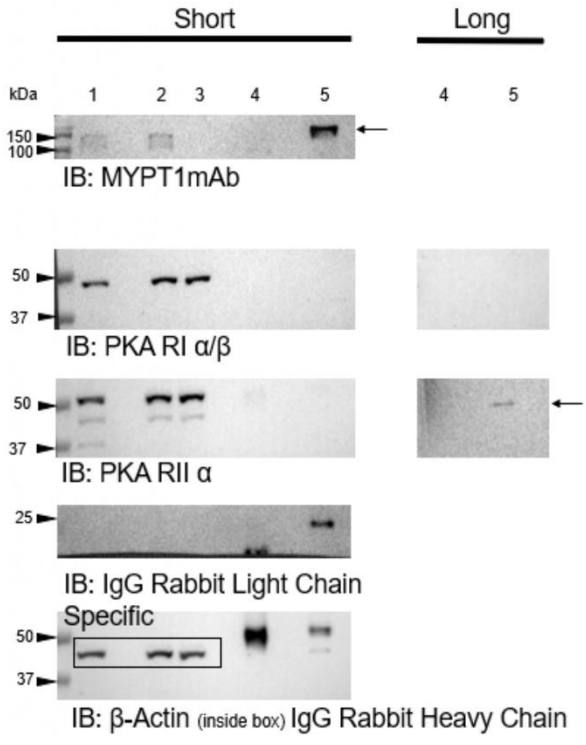

IP#1B – Membrane 2

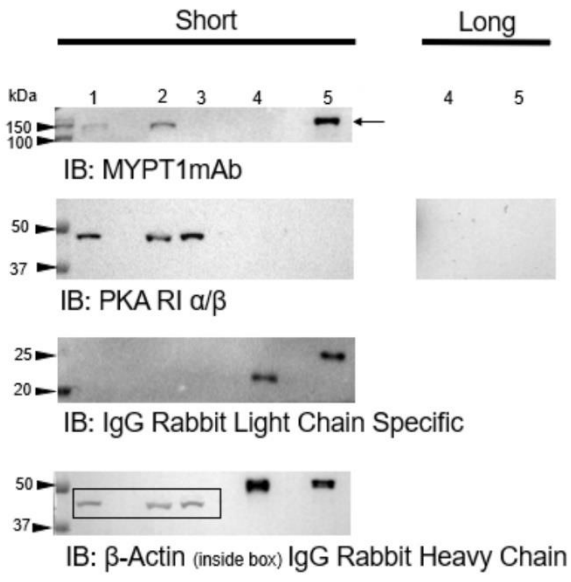

IP#1C – Membrane 1

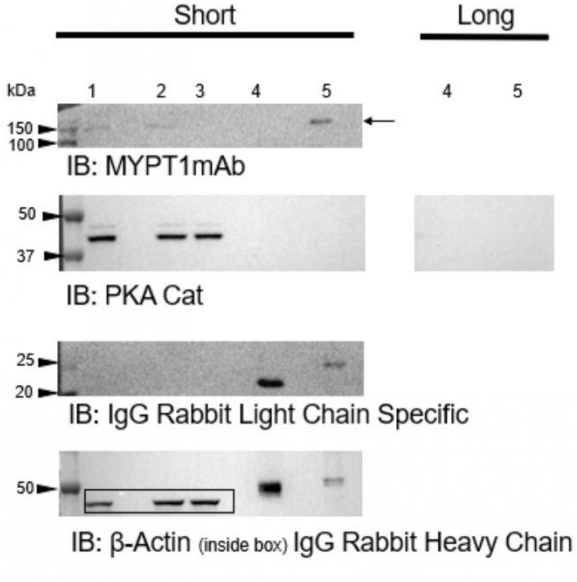

IP#1C – Membrane 2

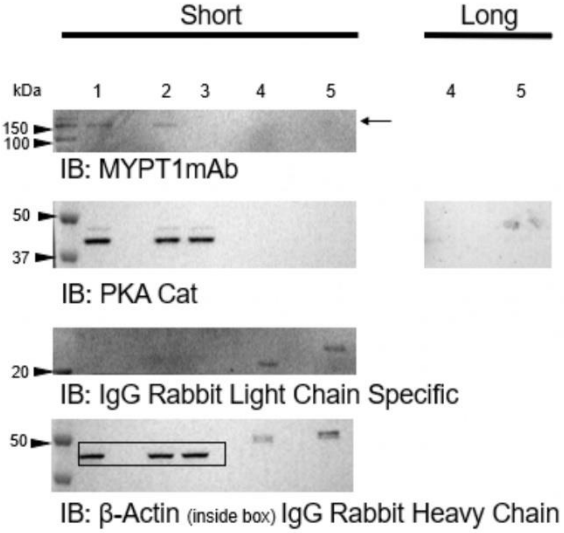

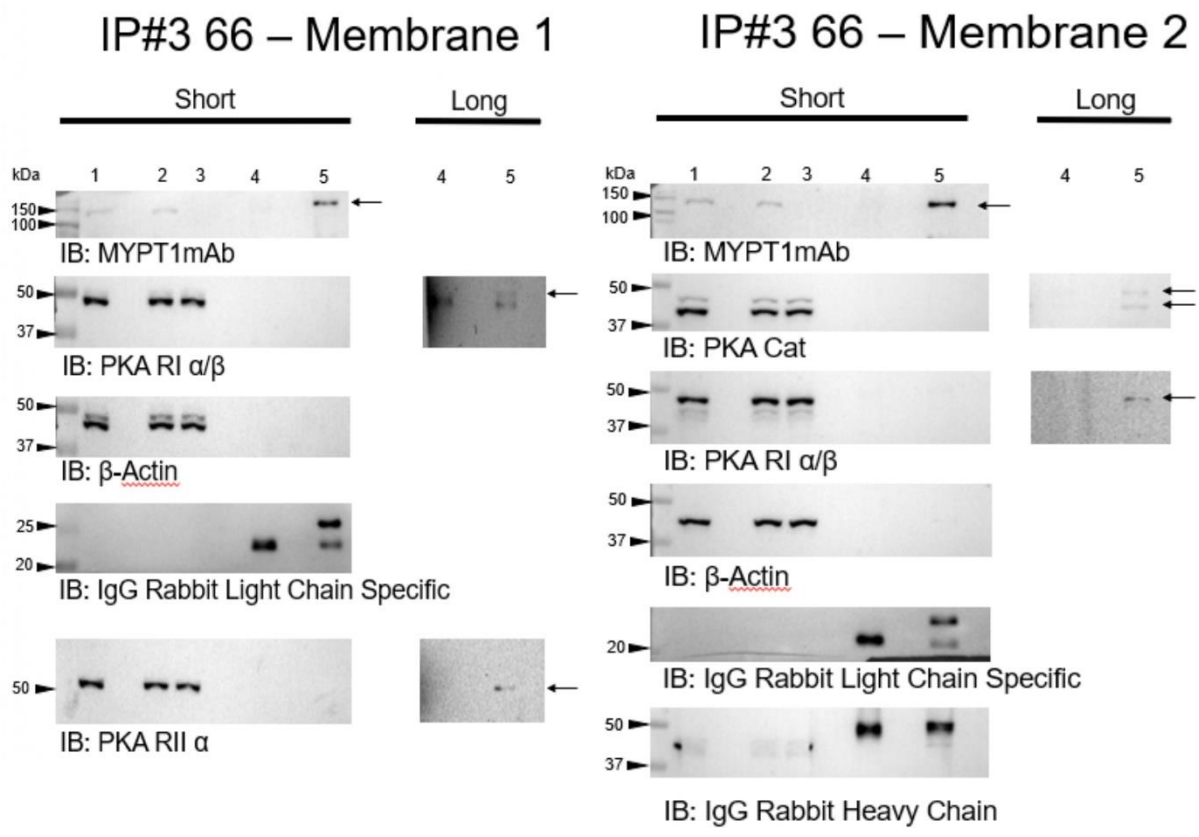
IP#3 66 – Membrane 1
Short
Long
kDa
1 2 3 4 5
4 5
150
100
IB: MYPT1mAb
50
37
IB: PKA RI α/β
IB: β-Actin
25
20
IB: IgG Rabbit Light Chain Specific
IB: PKA RII α
IP#3 66 – Membrane 2
IB: PKA Cat
IB: IgG Rabbit Heavy Chain

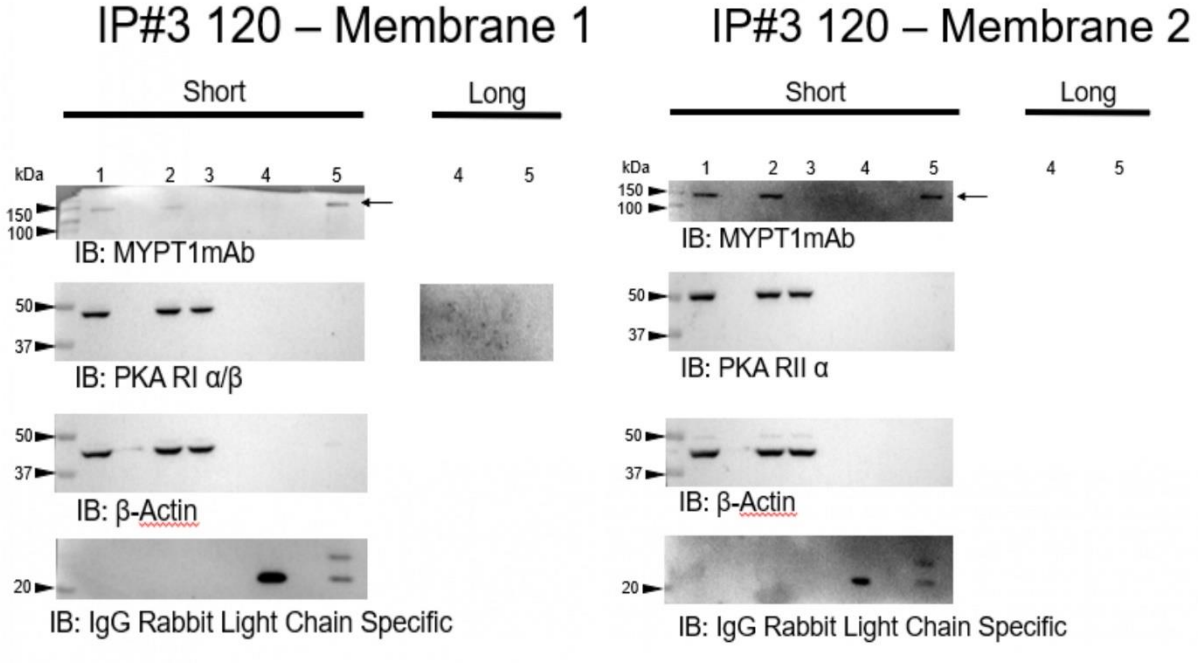
IP#3 120 – Membrane 1
Short
Long
kDa
1 2 3 4 5
4 5
150
100
IB: MYPT1mAb
50
37
IB: PKA RI α/β
IB: β-Actin
20
IB: IgG Rabbit Light Chain Specific
IP#3 120 – Membrane 2
IB: PKA RII α

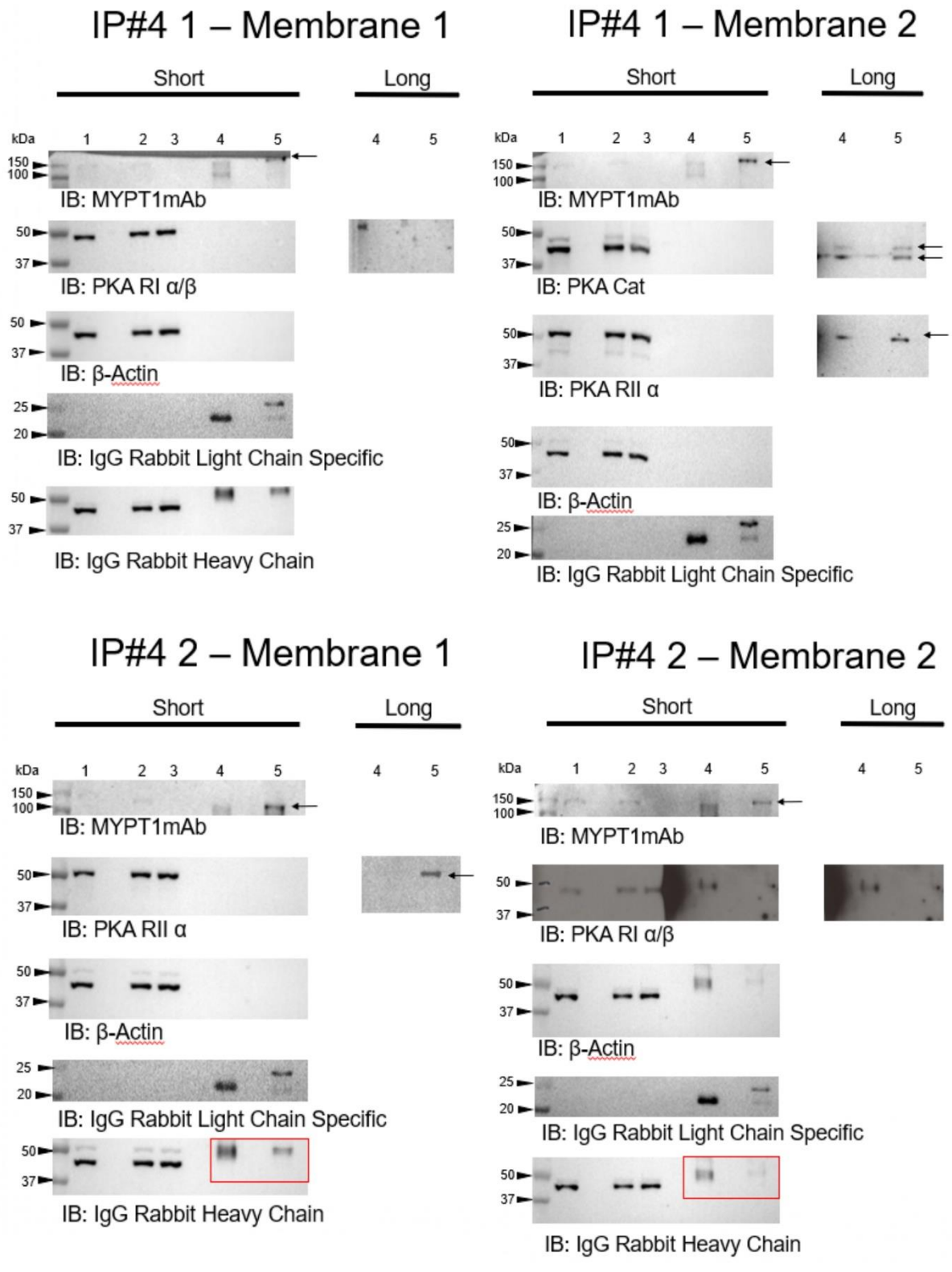
IP#4 1 – Membrane 1
Short
Long
kDa
1 2 3 4 5
4 5
150
100
IB: MYPT1mAb
50
37
IB: PKA RI α/β
IB: β-Actin
25
20
IB: IgG Rabbit Light Chain Specific
IB: IgG Rabbit Heavy Chain
IP#4 1 – Membrane 2
IB: PKA Cat
IB: PKA RII α
IP#4 2 – Membrane 1
IP#4 2 – Membrane 2

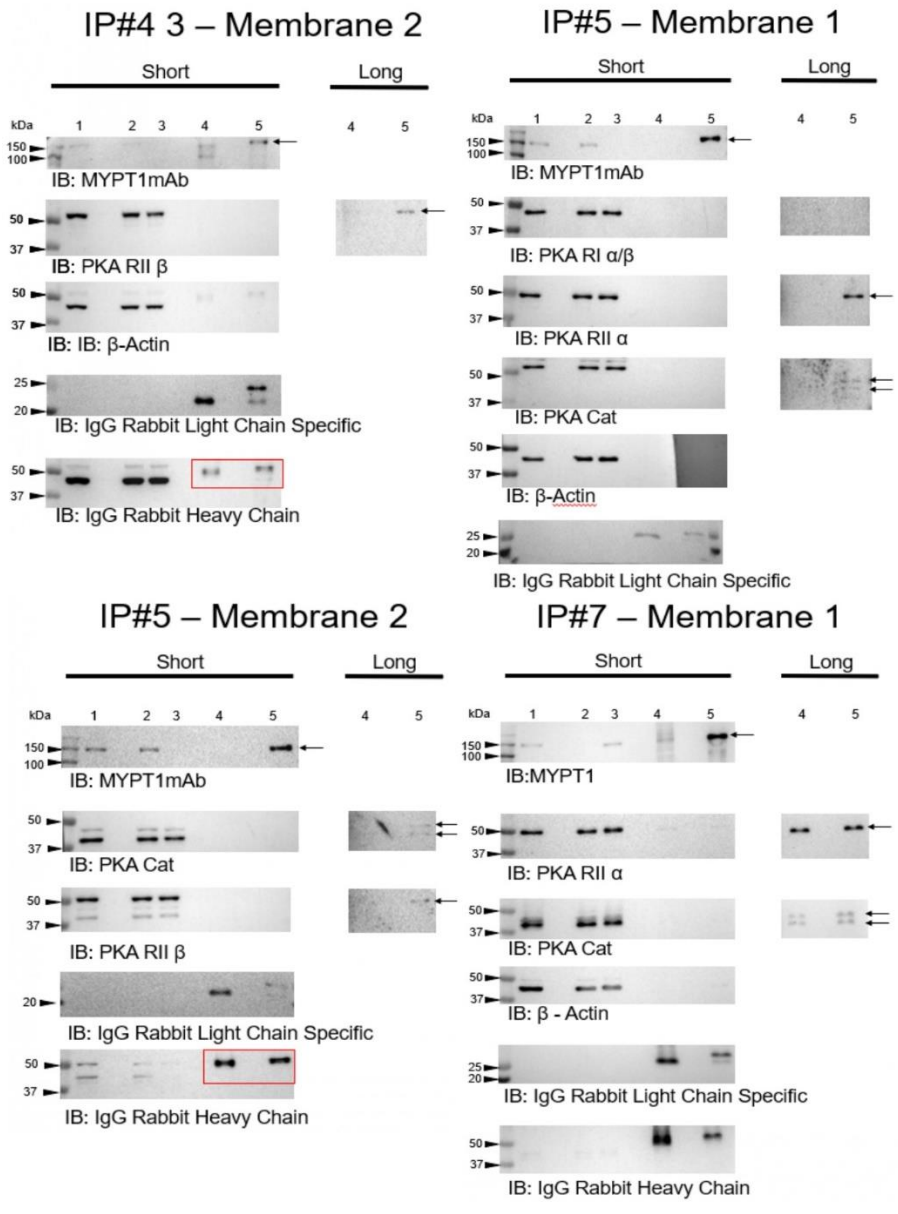

Appendix Figure 8.2-5 Individual experiments of immunoprecipitation of MYPT1 and co-immunoprecipitation of PKA subunits from HUVEC lysates. HUVEC lysates (500 µg) were subject to immunoprecipitation with rabbit MYPT1-(MYPT1 (D6C1) Rabbit mAb #8574, Cell Signalling Technologies, Netherlands) specific antibody or isotype-specific immunoglobulin G (IgG) (Rabbit (DA1E) mAb IgG XP ® Isotype Control#3900) as a control. Protein complexes were examined by Western blot for the presence of PKA regulatory subunits, the PKA catalytic subunit and for the immunoglobulin heavy chain (HC) and light chains (LC). ß-Actin was used as a loading control for lysates. Membranes were stripped and re-probed. Some membranes required long exposures, as indicated. 1-lysate; 2- IgG post beads incubation; 3- MYPT1 lysate post beads incubation; 4- IgG from immunoprecipitation; 5- MYPT1 from immunoprecipitation. Black arrows indicate protein immunoprecipitated or co-immunoprecipitated. Red square boxes indicate that those bands correspond to the protein that was immunoblotted for.

Appendix Table 8.2-1 Normality test for IP depletion in HUVECs.

Condition	Shapiro Wilks (Normality test)		Figure
	p Value	W	
MYPT1	0.00105	0.805	Figure 4.4 B
PKAcat	0.224	0.849	
PKA-RIα/β	0.0211	0.788	
PKA-RIIα	0.0119	0.793	
PKA-RIIβ	0.0759	0.957	

Appendix Table 8.2-2 Statistical test performed on IP depletion data for HUVECs.

Group Comparison	Kruskal-Wallis rank sum test				Figure
MYPT1, PKAcat, PKA-RIα/β, PKA-RIIα, PKA-RIIβ	df	Kruskal Wallis Chi-squared	*p-value*	Significance Level	Figure 4.4.B
	4	34.656	5.47E-07	**** p<0.0001	
Condition 1	Condition 2	Kruskal-Wallis multiple comparison			
		Z	P.unadjusted	Significance Level	
MYTP1	PKAcat	2.98873	1.8013610E-03	** p<0.01	
MYTP1	PKA-RIα/β	4.28213	1.8511500E-05	**** p<0.0001	
PKAcat	PKA-RIα/β	0.25205	8.0100630E-01		
MYTP1	PKA-RIIα	4.85951	1.1767870E-06	**** p<0.0001	
PKAcat	PKA-RIIα	0.41426	6.7868090E-01		
PKA-RIα/β	PKA-RIIα	0.19129	8.4829910E-01		
MYTP1	PKA-RIIβ	2.30559	2.1133290E-02	* p<0.05	
PKAcat	PKA-RIIβ	-0.5292	5.9669630E-01		
PKA-RIα/β	PKA-RIIβ	-0.8631	3.8810270E-01		
PKA-RIIα	PKA-RIIβ	-1.0467	2.9522510E-01		

Appendix Table 8.2-3 Statistical analysis for the IP and co-IP proteins analysed in this study in HUVECs.

Group	Condition 1	Condition 2	Shapiro Wilks (Normality test)		Statistic Test	Output			Significance Level	Figure
			p Value	W		p-value	t	df		
IgG vs MYPT1	IgG	MYPT1	0.2585	0.94173	Paired t-test	7.28 e-14	-19.109	19	**** p<0.0001	Figure 4.4C
IgG vs PKAcat	IgG	PKAcat	0.9647	0.98617	Paired t-test	0.005885	-5.3501	4	** p<0.01	
IgG vs PKA-RIIα	IgG	PKA-RIIα	0.3898	0.9197	Paired t-test	0.000175	-6.569	8	*** p<0.001	
IgG vs PKA-RIIß	IgG	PKA-RIIß	0.845	0.97057	Paired t-test	0.001027	-12.808	3	** p<0.01	

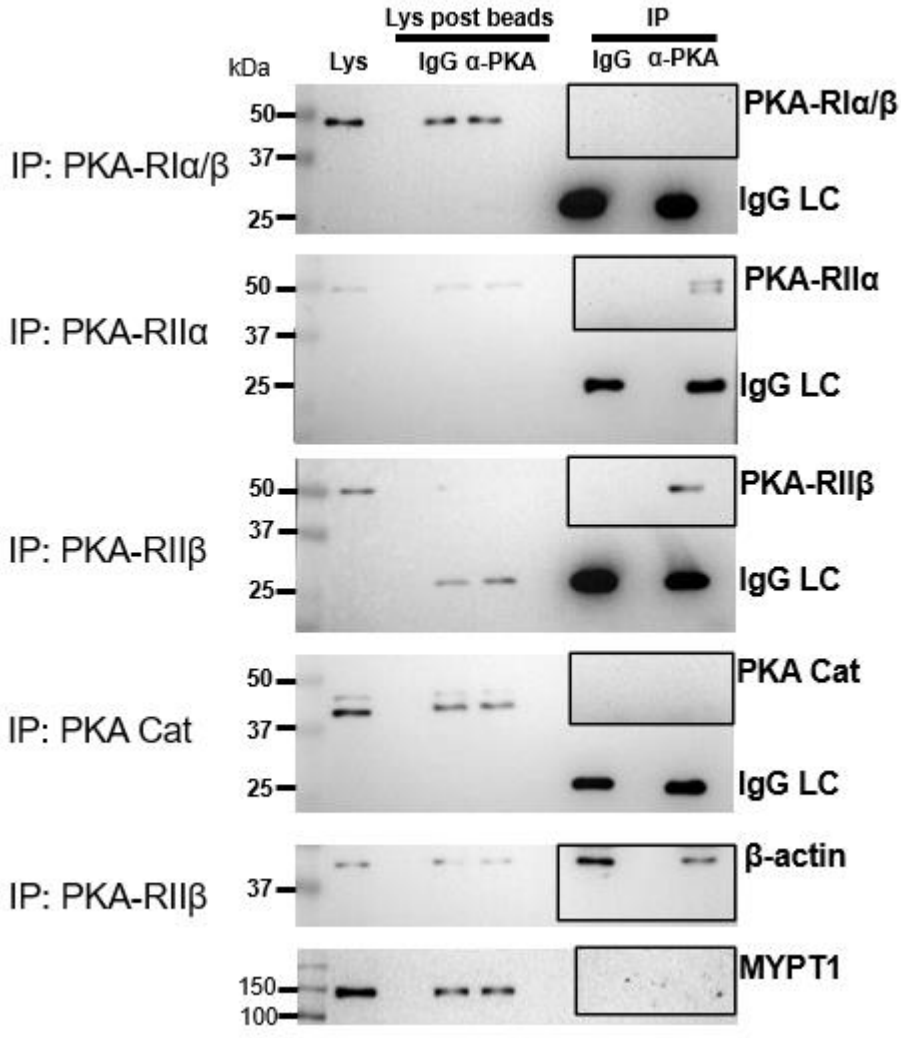

Appendix Figure 8.2-6 Immunoprecipitation of PKA subunits from HUVEC lysates. HUVEC lysates were subjected to immunoprecipitation with anti-PKA (RIα/β, RIIα, RIIß, Cat) mouse monoclonal antibodies. The immunoglobulin IgG1κ was used as control for PKA-RIIα and RIIß antibodies. The immunoglobulin IgG2b was used as control for PKA-RIα/β and cat antibodies. Protein complexes were examined by Western blotting for the presence of MYPT1, PKA-R subunits as well as PKAcat subunit and for the immunoglobulin of light chain. β-Actin was used as a loading control for lysates. Lys, lysate. Boxed images are inserted long exposure time images. MYPT1 represents all immunoblotting results acquired upon IP of PKA proteins.

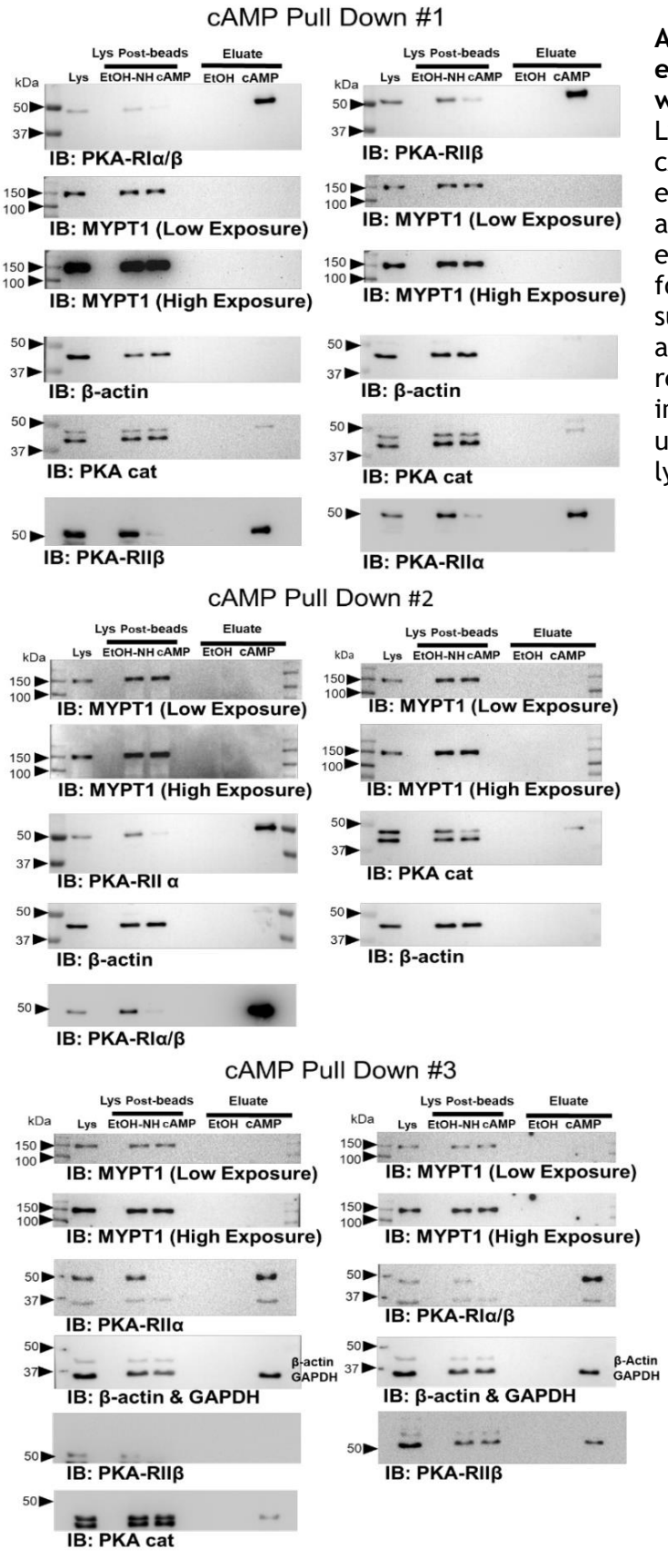

Appendix Figure 8.2-7 Individual experiments of affinity pull-down with cAMP beads in HUVECs. Lysates were incubated with 8-AHA-cAMP (cAMP) or control ethanolamine (EtOH-NH or EtOH) agarose beads. Complexes were examined by western immunoblot for the presence of MYPT1 and PKA subunits. Membranes were stripped and re-probed. Some membranes required long exposures, as indicated. Beta-actin (β-actin) was used as a loading control for lysates. Lys, lysate.

Appendix Table 8.2-4 Table of normality of depletion for cAMP affinity in HUVECs.

Condition	Shapiro Wilks (Normality test)		Figure
	p Value	W	
MYPT1	0.9178	0.97394	Fig. 4.6.B
PKAcatα	0.6986	0.9753	
PKA-RIα/ß	0.4176	0.90987	
PKA-RIIα	0.36	0.89184	
PKA-RIIß	0.7891	0.98785	
PKAcatß	0.1641	0.82037	

Appendix Table 8.2-5 Depletion of cAMP affinity HUVECs.

Group Comparison	Kruskal-Wallis rank sum test					Figure
MYPT1, PKAcatB, PKA-RIα/β, PKA-RIIα, PKA-RIIβ, PKAcatA	df	Kruskal Wallis Chi-squared		*p-value*	Significance Level	
	6	26.737		1.622E-04	*** p<0.0001	
Condition 1	Condition 2	One Way ANOVA with tukey post hoc test				Fig. 4.6B
		diff	lwr	upr	p.adjusted	Significance Level
PKA-RIIα	MYPT1	-0.90675	-1.2217016E+00	-5.92E-01	1.50E-06	**** p<0.0001
PKA-RIIβ	MYPT1	-8.41683333	-1.1566349E+00	-5.27E-01	3.90E-06	**** p<0.0001
PKA-RIα/β	MYPT1	-0.912166667	-1.2271182E+00	-5.97E-01	1.40E-06	**** p<0.0001
PKAcatA	MYPT1	-0.152385667	-4.6733720E-01	1.63E-01	6.27E-01	
PKAcatB	MYPT1	-0.019667	-3.3461860E-01	2.95E-01	1.00E+00	
PKA-RIIβ	PKA-RIIα	0.065066667	-2.9860810E-01	4.29E-01	9.91E-01	
PKA-RIα/β	PKA-RIIα	-0.005416667	-3.6909140E-01	3.58E-01	1.00E+00	
PKAcatA	PKA-RIIα	0.754364333	3.9068960E-01	1.12E+00	8.09E-05	**** p<0.0001
PKAcatB	PKA-RIIα	0.887083	5.2340820E-01	1.25E+00	1.21E-05	**** p<0.0001
PKA-RIα/β	PKA-RIIβ	-0.070483333	-4.3415810E-01	2.93E-01	9.87E-01	
PKAcatA	PKA-RIIβ	0.689297667	3.2562290E-01	1.05E+00	2.19E-04	*** p<0.001
PKAcatB	PKA-RIIβ	0.822016333	4.5834160E-01	1.19E+00	3.00E-05	**** p<0.0001
PKAcatA	PKA-RIα/β	0.759781	3.9610620E-01	1.12E+00	7.46E-05	**** p<0.0001
PKAcatB	PKA-RIα/β	0.892499667	5.2882490E-01	1.26E+00	1.12E-05	**** p<0.0001
PKAcatB	PKAcatA	0.132718667	-2.3095610E-01	0.4963934	8.37E-01	

Appendix Table 8.2-6 Normality of cAMP affinity in HUVECs.

Condition	Shapiro Wilks (Normality test)		Figure
	p Value	W	
ETOH-NH	0.00154	0.824	Fig. 4.6. C
MYPT1	0.218	0.868	
PKA-RIIα	0.0847	0.787	
PKA-RIIß	0.368	0.894	
PKA-RIα/ß	0.972	1	
PKAcatA	0.994	1	
PKAcatB	0.866	0.995	

Appendix Table 8.2-7 Table of statistical test for cAMP affinity in HUVECs.

Group Comparison	Kruskal-Wallis rank sum test				Figure
ETOH, MYPT1, PKA-RIIα,PKA-RIIß,PKA-RIα/ß,	df	Kruskal Wallis Chi-	p-value	Significance Level	
	6	26.737	1.62E-04	**** p<0.0001	
Condition 1	Condition 2	Kruskal-Wallis multiple compairson		Significance Level	
		Z	P.unadjusted		
ETOH-NH	MYPT1	-0.22220904	8.2415116E-01		
ETOH-NH	PKA-RIIα	-2.83002077	4.6544982E-03	** p<0.01	
MYPT1	PKA-RIIα	-2.32477468	2.0084011E-02		
ETOH-NH	PKA-RIIß	-2.96208841	3.0556004E-03	** p<0.01	
MYPT1	PKA-RIIß	-2.44005277	1.4685117E-02		
PKA-RIIα	PKA-RIIß	-0.09983375	9.2047631E-01		
ETOH-NH	PKA-RIα/ß	-3.40935895	4.8237220E-04	*** p<0.001	
MYPT1	PKA-RIα/ß	-2.9011651	3.7177794E-03		
PKA-RIIα	PKA-RIα/ß	-0.49916874	6.1766051E-01		
PKA-RIIß	PKA-RIα/ß	-0.399335	6.8964638E-01		
ETOH-NH	PKAcatß	-2.30175023	2.1349262E-02	*p<0.05	
MYPT1	PKAcatß	-1.86366235	6.2369136E-02		
PKA-RIIα	PKAcatß	0.399335	6.8964638E-01		
PKA-RIIß	PKAcatß	0.49916874	6.1766051E-01		
PKA-RIα/ß	PKAcatß	0.89850374	3.6891705E-01		
ETOH-NH	PKAcatα	-0.89302878	3.7184176E-01		
MYPT1	PKAcatα	-0.63402946	5.2606160E-01		
PKA-RIIα	PKAcatα	1.46422832	1.4313158E-01		
PKA-RIIß	PKAcatα	1.56406207	1.1780299E-01		
PKA-RIα/ß	PKAcatα	1.96339706	0.049600055		
PKAcatβ	PKAcatα	1.06489332	0.286924208		

Fig. 4.6. C

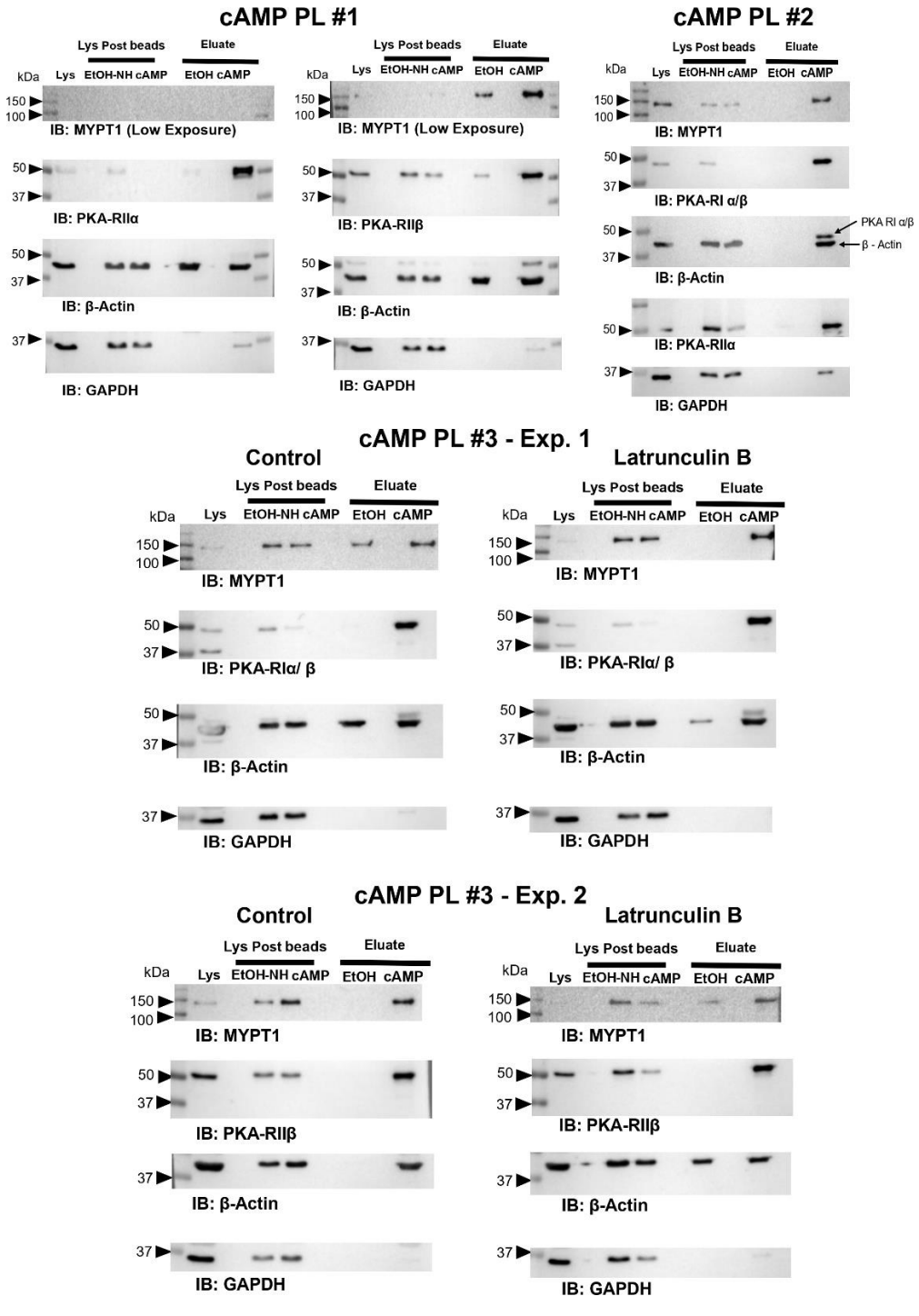

Appendix Figure 8.2-8 cAMP affinity pull-down in washed platelets. Independent experiments of cAMP Pull down in washed platelets. Lysates were incubated with 8-AHA-cAMP (cAMP) or control ethanolamine (EtOHN) agarose beads. Complexes were examined by western immunoblot for the presence of MYPT1 and PKA subunits. Beta-actin (β-actin) was used as a loading control for lysates. Lys- lysate; EtOH-NH (Ethanolamide).

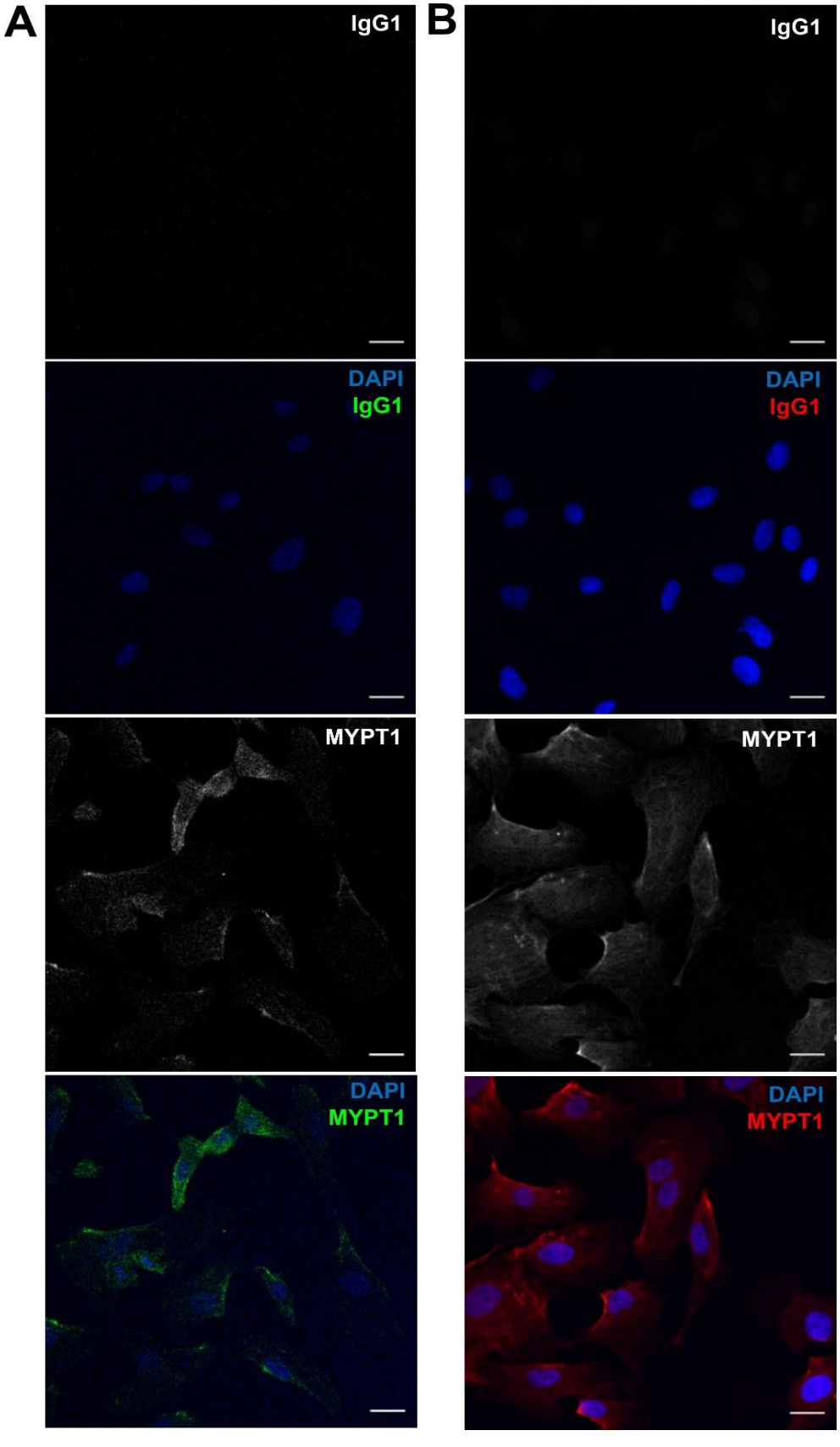

Appendix Figure 8.2-9 MYPT1 expression in HUVECs.(A) HUVECs were fixed with 4% PFA, permeabilised and stained with rabbit anti-MYPT1 antibody or isotype matching IgG1 followed by species-specific Alexa fluor 488 (green) conjugated secondary antibody. Nuclei were counterstained with DAPI. **(B)** HUVECs were processed as in A but a species-specific Alexa fluor 568(red) conjugated secondary antibody was used. Images were acquired with a ZEISS LSM 710 confocal laser scanning microscope equipped with a 20× objective. Scale bar represents 20 µm.

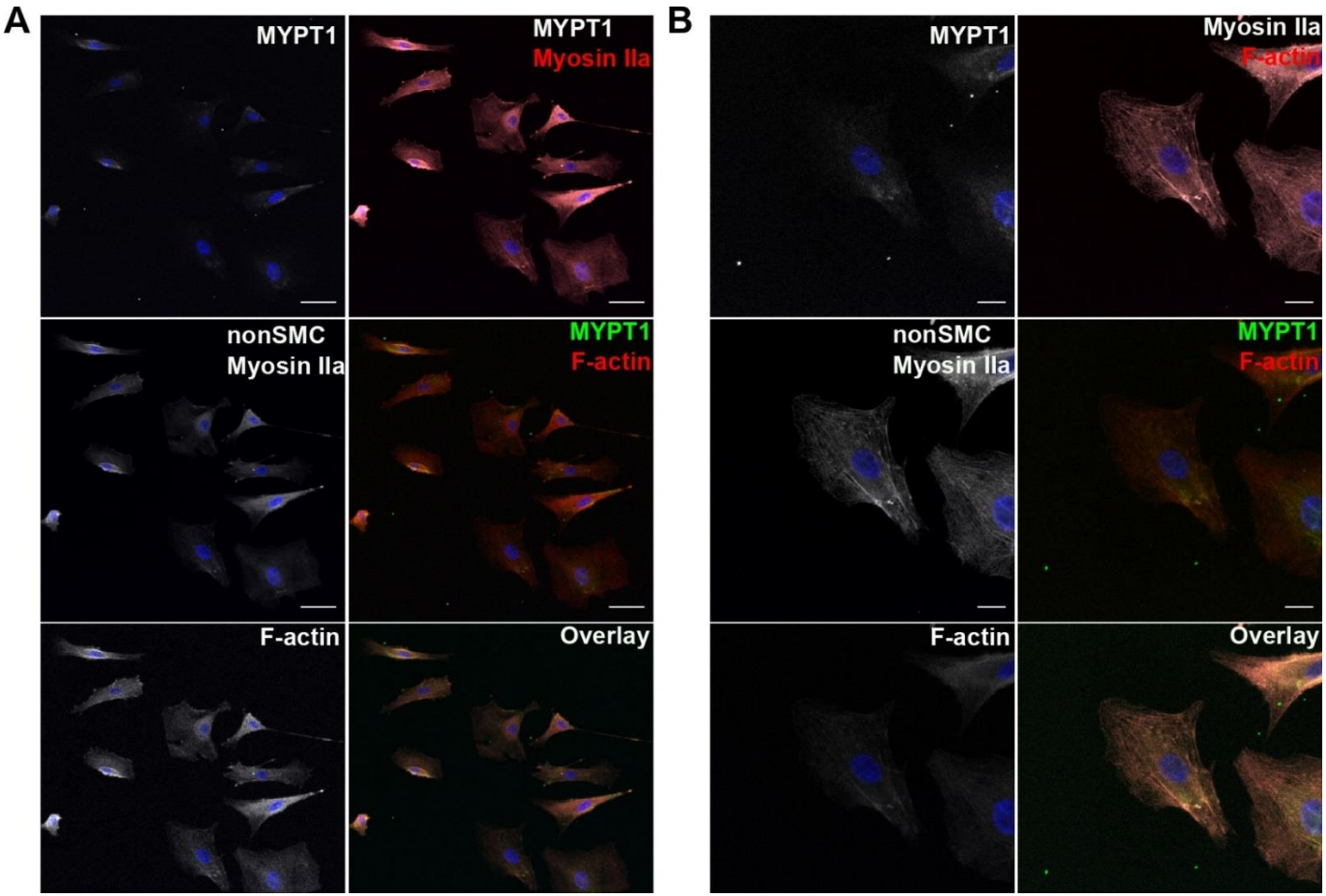

Appendix Figure 8.2-10 Triple fluorescence staining of MYPT1, non-muscle myosin IIa and actin in HUVECs. Cells were fixed, permeabilised and incubated with mouse MYPT1, rabbit non-muscle myosin IIa antibodies followed by species-specific Alexa Fluor 568 (red) or Alexa Fluor 488 (green) conjugated secondary antibodies. Actin was stained with phalloidin conjugated with a far-red tag. Nuclei were counterstained with DAPI. Images were acquired with a ZEISS LSM 710 confocal laser scanning microscope equipped with a 20× objective. Scale bar represents 20 µm.

Appendix Table 8.2-8 Normality for co-localisation of MYPT1 with PKA subunits in HUVECs.

Condition	Shapiro Wilks (Normality test)		Figure
	p Value	W	
Control	0.562	0.971	Fig. 4.10. B
PKA-RIα/β	0.525	0.969	
PKA-RIIα	0.084	0.939	
PKA-RIIβ	0.22	0.954	

Appendix Table 8.2-9 Statistical test used for co-localisation of MYPT1 with PKA subunits in HUVECs.

Group Comparison	One Way ANOVA						Figure
Control, PKA-RIα/β, PKA-RIIα, PKA-RIIβ	df	Sum sq	Mean Sq	F Value	Pr (>F)	Significance Level	Fig. 4.10. B
	3	11.53670749	3.85E+00	555.3861	<2.22e-16	**** p<0.0001	
Condition 1	Condition 2	One Way ANOVA with tukey post hoc test					
		diff	lwr	upr	p.adjusted	Significance Level	
PKA-RIα/β	Control	0.649233333	5.9322890E-01	7.05E-01	2.11E-15	**** p<0.0001	
PKA-RIIα	Control	0.815266667	7.5926223E-01	8.71E-01	2.11E-15	**** p<0.0001	
PKA-RIIβ	Control	0.6214	5.6539557E-01	6.77E-01	2.11E-15	**** p<0.0001	
PKA-RIIα	PKA-RIα/β	0.166033333	1.1002890E-01	2.22E-01	2.59E-11	**** p<0.0001	
PKA-RIIβ	PKA-RIα/β	-0.027833333	-8.3837765E-02	2.82E-02	5.68E-01		
PKA-RIIβ	PKA-RIIα	-0.193866667	-2.4987110E-01	-1.38E-01	6.72E-14	**** p<0.0001	

Appendix Table 8.2-10 Normality test for PLA quantified data by area.

Condition	Shapiro Wilks (Normality test)		Figure
	p Value	W	
IgGR+IgG1km	0.00000181	0.686	Fig 4.12. B
IgGR+IgG2bm	0.00307	0.848	
MYPT1+PKA-RIα/β	0.192	0.96	
MYPT1+ PKA-RIIα	0.0012	0.883	
MYPT1+PKA-RIIβ	0.0424	0.892	
MYPT1R+MYPT1M	0.774	0.965	
MYPT1R+PKAcat	6.04E-08	0.553	

Appendix Table 8.2-11 Statistical test and comparison between groups PLA quantified by area.

Group Comparison	Kruskal-Wallis rank sum test				Figure
IgGR+IgG1km, IgGR+IgG2bm, MYPT1+PKA-RIα/β, MYPT1+ PKA-RIIα, MYPT1+PKA-RIIβ, MYPT1R+PKAcat,MYPT1R+MYPT1M	df	Kruskal Wallis Chi-squared	*p* Value	Significance Level	
	6	147.73	<2.2e-16	**** p<0.0001	
Condition 1	Condition 2	Kruskal-Wallis multiple comparison			
		Z	*p* .unadjusted	Significance Level	
IgGR+IgG1km	IgGR+IgG2bm	0.00693259	9.4473020E-01		
IgGR+IgG1km	MYPT1+PKA-RIα/β	-8.5357008	1.3930840E-17	**** p<0.0001	
IgGR+IgG2bm	MYPT1+PKA-RIα/β	-8.0091078	1.1554360E-15	**** p<0.0001	
IgGR+IgG1km	MYPT1+ PKA-RIIα	-3.7460875	1.7961390E-04	*** p<0.001	
IgGR+IgG2bm	MYPT1+ PKA-RIIα	-3.5610643	3.6935470E-04	*** p<0.001	
MYPT1+PKA-RIα/β	MYPT1+ PKA-RIIα	5.0819557	3.7356860E-07	**** p<0.0001	
IgGR+IgG1km	MYPT1+PKA-RIIβ	-5.6570134	1.5402970E-08	**** p<0.0001	
IgGR+IgG2bm	MYPT1+PKA-RIIβ	-5.439397	5.3431190E-08	**** p<0.0001	Fig 4.12. B
MYPT1+PKA-RIα/β	MYPT1+PKA-RIIβ	1.4568579	1.4515560E-01		
MYPT1+ PKA-RIIα	MYPT1+PKA-RIIβ	-2.6504162	8.0392660E-03	** p<0.01	
IgGR+IgG1km	MYPT1R+MYPT1M	-7.6101698	2.7373600E-14	**** p<0.0001	
IgGR+IgG2bm	MYPT1R+MYPT1M	-7.3310889	2.2829010E-13	**** p<0.0001	
MYPT1+PKA-RIα/β	MYPT1R+MYPT1M	-1.0138058	3.1067540E-01		
MYPT1+ PKA-RIIα	MYPT1R+MYPT1M	-4.8519833	1.2223290E-06	**** p<0.0001	
MYPT1+PKA-RIIβ	MYPT1R+MYPT1M	-2.0766222	3.7836440E-02	* p<0.05	
IgGR+IgG1km	MYPT1+PKAcat	-1.5588724	1.1902660E-01		
IgGR+IgG2bm	MYPT1+PKAcat	-1.5327177	1.2534540E-01		
MYPT1+PKA-RIα/β	MYPT1+PKAcat	6.7756159	1.2387740E-11	**** p<0.0001	
MYPT1+ PKA-RIIα	MYPT1+PKAcat	2.056107	3.9772210E-02	* p<0.05	
MYPT1+PKA-RIIβ	MYPT1+PKAcat	4.2346681	2.2888950E-05	**** p<0.0001	
MYPT1R+MYPT1M	MYPT1+PKAcat	6.2558085	3.9546100E-10	**** p<0.0001	

Appendix Table 8.2-12 Normality for the PLA quantified by dots.

Condition	Shapiro Wilks (Normality test)		Figure
	p Value	W	
MYPT1R+MYPT1M	0.0371	0.929	Fig 4.12. B
IgGR+IgG1km	0.000000474	0.815	
IgGR+IgG2bm	0.696	0.968	
MYPT1+PKAcat	0.363	0.969	
MYPT1+PKA-RIα/β	0.0037	0.904	
MYPT1+ PKA-RIIα	0.000000333	0.818	
MYPT1+PKA-RIIβ	0.13	0.95	

Appendix Table 8.2-13 Statistical analysis for the PLA quantified by dots.

Group Comparison	Kruskal-Wallis rank sum test				Figure
MYPT1, PKAcat, IgG1, IgG2b, PKA-RIα/β, PKA-RIIα, PKA-	df	Kruskal Wallis Chi-squared	*p* Value	Significance Level	
	6	253.49	<2.2e-16	**** p<0.0001	
Condition 1	Condition 2	Kruskal-Wallis multiple compairson			
		Z	*p* .unadjusted	Significance Level	
MYPT1+PKAcat	IgGR+IgG1km	3.6587824	2.5341630E-04	*** p<0.001	
MYPT1+PKAcat	IgGR+IgG2bm	2.2093692	2.7148970E-02	* p<0.05	
IgGR+IgG1km	IgGR+IgG2bm	-0.6394456	5.2253310E-01		
MYPT1+PKAcat	MYPT1R+MYPT1M	-7.5188527	5.5259010E-14	**** p<0.0001	
IgGR+IgG1km	MYPT1R+MYPT1M	-11.6598598	2.0437870E-13	**** p<0.0001	
IgGR+IgG2bm	MYPT1R+MYPT1M	-8.5627716	1.1018610E-17	**** p<0.0001	
MYPT1+PKAcat	MYPT1+PKA-RIα/β	-7.2063275	5.7481060E-13	**** p<0.0001	
IgGR+IgG1km	MYPT1+PKA-RIα/β	-11.5397914	8.3126590E-31	**** p<0.0001	
IgGR+IgG2bm	MYPT1+PKA-RIα/β	-8.2906583	1.1262340E-16	**** p<0.0001	
MYPT1R+MYPT1M	MYPT1+PKA-RIα/β	0.5783223	5.6304640E-01		Fig 4.12. B
MYPT1+PKAcat	MYPT1+ PKA-RIIα	-3.2791569	1.0411770E-03	** p<0.01	
IgGR+IgG1km	MYPT1+ PKA-RIIα	-7.858747	3.8799510E-15	**** p<0.0001	
IgGR+IgG2bm	MYPT1+ PKA-RIIα	-5.0529304	4.3508250E-07	**** p<0.0001	
MYPT1R+MYPT1M	MYPT1+ PKA-RIIα	5.1600845	2.4683840E-07	**** p<0.0001	
MYPT1+PKA-RIα/β	MYPT1+ PKA-RIIα	4.7351973	2.1884210E-06	**** p<0.0001	
MYPT1+PKAcat	MYPT1+PKA-RIIβ	-5.3363697	9.4825980E-08	**** p<0.0001	
IgGR+IgG1km	MYPT1+PKA-RIIβ	-9.3254038	1.1056180E-20	**** p<0.0001	
IgGR+IgG2bm	MYPT1+PKA-RIIβ	-6.7008924	2.0715050E-11	**** p<0.0001	
MYPT1R+MYPT1M	MYPT1+PKA-RIIβ	2.1532347	3.1300230E-02	* p<0.05	
MYPT1+PKA-RIα/β	MYPT1+PKA-RIIβ	1.6480511	9.9342180E-02		
MYPT1+ PKA-RIIα	MYPT1+PKA-RIIβ	-2.7399976	6.1439630E-03	** p<0.01	

8.3. Appendix C

Determination of GST and His-Tag protein purity as described in section 2.4.7.1.

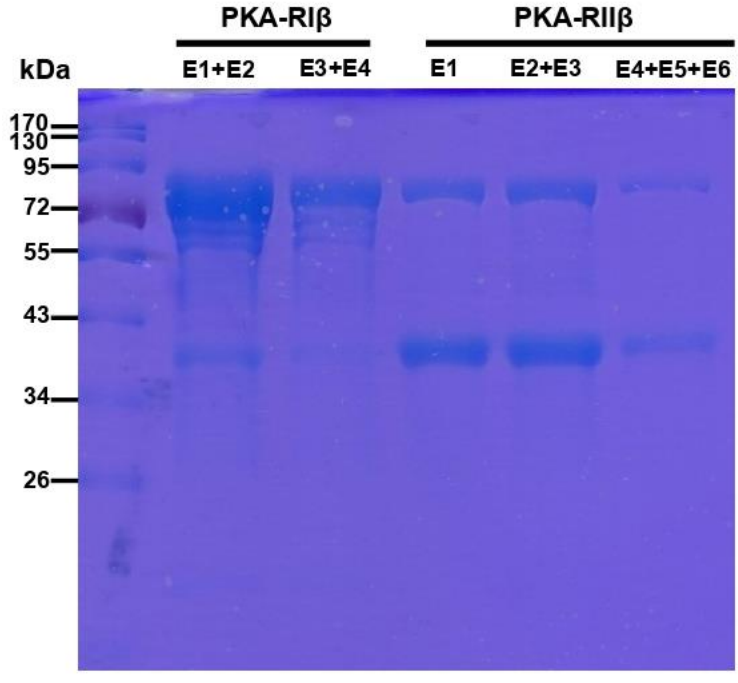

Appendix Figure 8.3-1 Purified GST tagged PKA RIß and PKA RIIß. (A) In this panel it is represented both proteins that were quantified to eliminate the amount of protein that is degraded. E, eluates.

Appendix Table 8.3-1 Determination of GST-tagged PKA RIß and RIIß total and intact protein concentration

Protein	Fraction	Total protein concentration (µg/µL)	% intact protein	Intact protein concentration (µg/µL)
PKA RIß	E1+E2	6.659	71%	4.741
	E3+E4	3.909	55%	2.147
PKA RIIß	E1	3.496	29%	1.003
	E2+E3	3.629	30%	1.104
	E4+E5+E6	3.573	38%	1.341

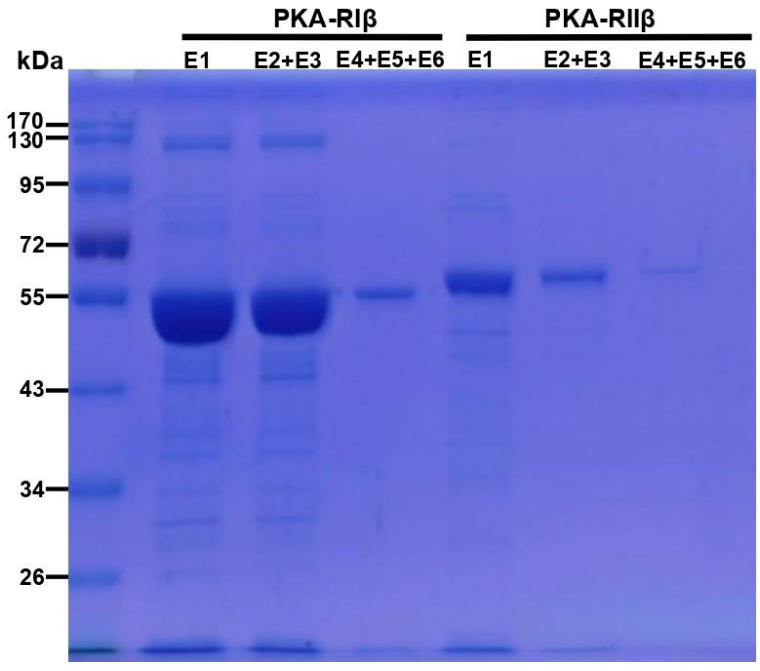

Appendix Figure 8.3-2 Purified GST tagged PKA RIß and PKA RIIß. In this panel it is represented both proteins that were quantified to eliminate the amount of protein that is degraded. E, eluates.

Appendix Table 8.3-2 Determination of total PKA RIß and RIIß His-tagged proteins and intact proteins concentrations.

Protein	Fraction	Total protein concentration (µg/µL)	% intact protein	Intact protein concentration (µg/µL)
PKA RIß	E1	2.689	83%	221.82
	E2+E3	2.491	82%	204.80
	E4+E5+E6	1.373	80%	109.43
PKA RIIß	E1	1.040	83%	86.18
	E2+E3	1.245	87%	108.86
	E4+E5+E6	1.264	47%	59.77

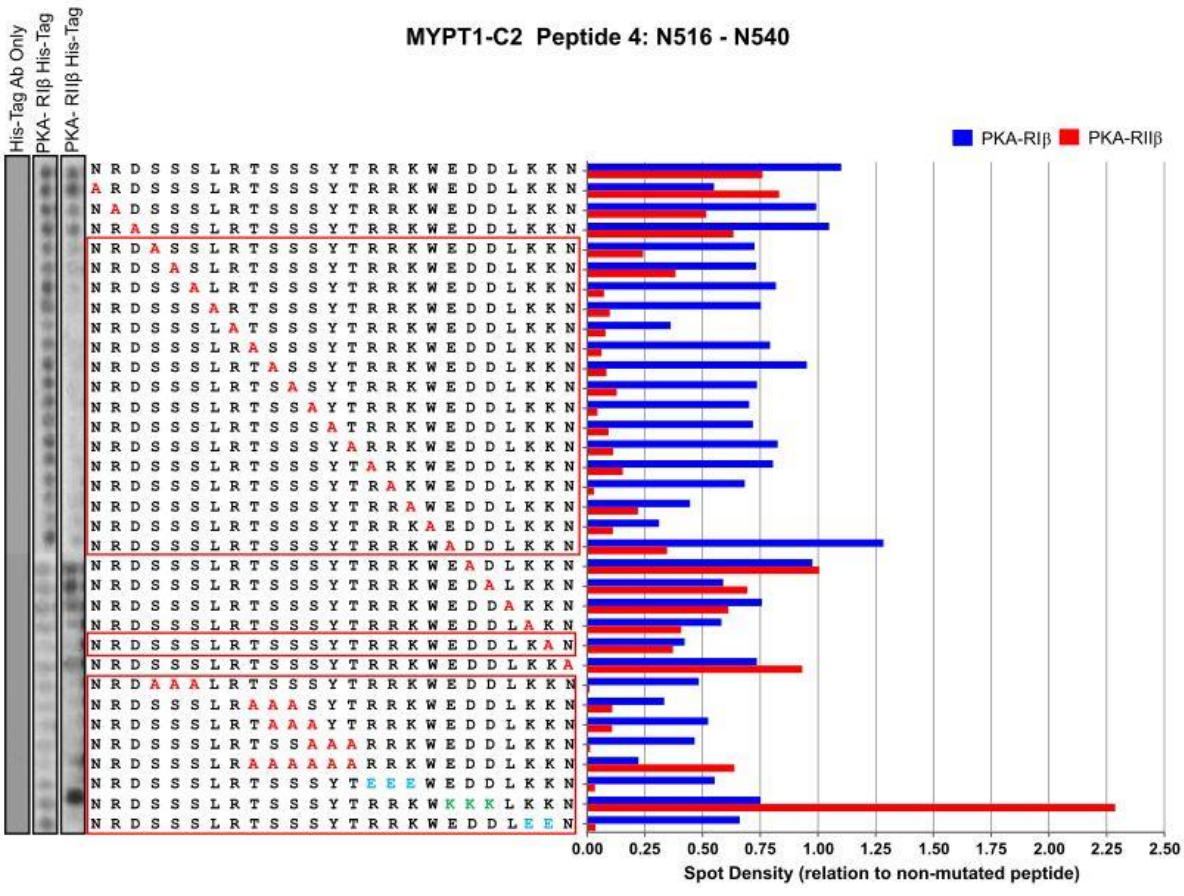

Appendix Figure 8.3-3 Peptide array substitution analysis of MYPT1-C2 peptide 4. Key MYPT1-C2 hot spots were identified by single, dual, or multiple alanine substitutions by opposite charge residue substitutions. The red box highlights a peptide where a substitution resulted in complete loss of binding. Spot densities are shown relative to the non-mutated peptide after subtraction of the antibody only control (Peptide microarray experiment carried out in George Baillie's laboratory).

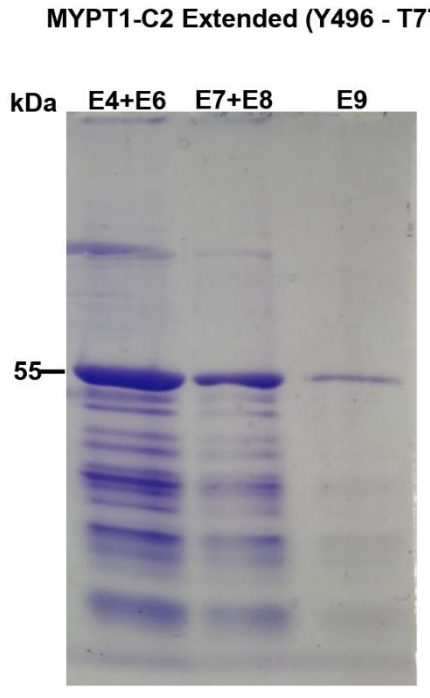

Appendix Figure 8.3-4 MYPT1-C2 his tagged protein. In this figure it is observed the eluates recovered from dialysis and some of protein degradation.

Appendix Table 8.3-3 Determination of total MYPT1-C2Ext His-tagged protein and intact protein concentration.

Protein	Fraction	Total protein concentration (µg/µL)	% intact protein	Intact protein concentration (µg/µL)
MYPT1-C2-Ext	E4+E5+E6	3.974	33%	1.32
	E7+E8	1.671	23%	0.39
	E9	0.499	20%	0.10